AN ABSTRACT OF THE DISSERTATION OF

Vincent Michele Rossi for the degree of Doctor of Philosophy in Physics presented on December 11, 2015.

Title: Digital Fourier Holographic Microscopy and Potential Applications Towards the Design of Photodynamic Therapy of Osteosarcoma

Abstract approved:

Steven L. Jacques

This work entails both imaging and therapeutic applications of biomedical optics. In both contexts, an understanding of light transport in tissues is necessary. An overview of optical transport in tissues is given, including scattering theory. Digital Fourier holographic microscopy is introduced and applied as a means of metrology via optical scatter imaging. The later portion of this work focuses on the clinical application of photodynamic therapy of osteosarcoma. A 3D Monte Carlo model is developed as a predictive model of clinical applications of photodynamic therapy in treating osteosarcoma within the medullary cavity of long bones. Prior to compiling the Monte Carlo model, optical properties of bone tissues are determined via diffuse reflectance spectroscopy.

Digital Fourier Holographic Microscopy and Potential Applications Towards the Design of Photodynamic Therapy of Osteosarcoma

by

Vincent Michele Rossi

A DISSERTATION

submitted to

Oregon State University

in partial fulfillment of
the requirements for the
degree of

Doctor of Philosophy

Presented December 11, 2015
Commencement June 2016

Doctor of Philosophy dissertation of Vincent Michele Rossi presented on December 11, 2015

APPROVED:

Major Professor, representing Physics

Chair of the Department of Physics

Dean of the Graduate School

I understand that my thesis will become part of the permanent collection of Oregon State University libraries. My signature below authorizes release of my thesis to any reader upon request.

Vincent Michele Rossi, Author

ACKNOWLEDGEMENTS

The work presented in this thesis is the culmination of numerous years of research and multiple lines of inquiry. In addition, much of the work carried out has challenged and expanded the author's knowledge base beyond fundamental physics by incorporating elements of chemistry, biology, computational modeling and image processing. As such, the list of individuals who have been detrimental to the author's growth and understanding is substantial. A large group of collaborators deserve individual recognition for their contributions to this work and the author's understanding.

First, I want to begin by thanking my wife, Tracy. I never would have had the courage or confidence to begin down this long path had it not been for her confidence in me, encouragement, and support. Thank you for your patience and strength.... I know this has been a long time coming.

I would also like to acknowledge the members of my committee for their guidance and patience. In particular, I thank Steve Jacques of Oregon Health and Science University Departments of Biomedical Engineering and Dermatology. Considering that I am a student at Oregon State University, Steve had no obligation to serve as my head advisor or mentor. I greatly appreciate that he was willing to work with me as a non-traditional graduate student. I have gained a great deal of knowledge from working with Steve, beyond the scope of this thesis. Beyond his support and optics help, I thank him in particular for the broad skills he has taught me in computational modeling and analysis. I would like to recognize Henri Jansen (OSU Department of Physics) for his guidance in developing a quantum mechanical description of PDT and Oksana Ostroverkhova (OSU Department of Physics) for her review of the DFHM optical design. Scott Gustafson (formerly of the OSU College of Veterinary Medicine and currently working privately at Surgery 4 Pets) was a great resource in introducing me to PDT, both in general and in clinical applications. On a personal note, he was also able to extend our dog, Baxter's life by five years via surgery and PDT. For that, he has the gratitude of my entire family.

Members of Steve's research group have made significant contributions to this work over the years. I would like to give a special thanks to Ravi Samatham for his particular help in designing and using the LabVIEW computer interface for the operation of the DFHM and subsequent data collection. His help on this expedited my research. Tracy Petrie has been instrumental in helping me with the ins and outs of image processing. I could always count on Tracy for a general sanity check when going through post processing, and even to help get over particular image processing and general computational blocks along the way. Niloy Choudhury, formerly of Steve's group at OHSU, was also helpful in discussing the DFHM system when I built and improved upon the earliest incarnations of the DFHM system.

Sergey Alexandrov (NUI Galway) spent a few days snowed in the lab at OHSU with me a few years back. His advice and tutelage in the alignment of the DFHM system over

those days was paramount to my understanding. Donald Duncan (Portland State University Department of Electrical and Computer Engineering) also advised me with respect to the heterodyne filtering of digital holograms. In addition, Nada Boustany (Rutgers Department of Biomedical Engineering) was helpful via correspondence in incorporating OSI capabilities in the DFHM.

I received support from the faculty and staff at Pacific University while teaching physics there for three years. In particular, I would like to thank James Butler and Andy Dawes (Department of Physics) for their general support via the use of lab space and equipment. This work has been unfunded, and their generosity helped me get the imaging components of this project started. In addition, I worked closely on the *in vitro* PDT experiment with Paige Baugher (Pacific University Biology Department) and two of her undergraduate students, Mariko Newton and Brad White. I would like to thank each of them for their contributions to this work and their collaboration. I gained the majority of my biological knowledge from this work and from sitting in on her Cancer Biology course. In addition, I thank Paige for teaching me tissue culture practices—which have been useful to me beyond my time at Pacific.

I would like to thank John Mata (OSU College of Veterinary Medicine) and Bernard Seguin (formerly of OSU College of Veterinary Medicine and currently at the Colorado State University Flint Animal Cancer Center). Along with Scott Gustafson, I was able to work with both John and Bernard on a couple of PDT and related veterinary projects. The work I did with them is the foundation of my knowledge of PDT and clinical applications.

Lastly, when I first started investigating the optical properties of bone tissues, Russell Turner and Urszula Iwaniec (OSU College Of Public Health and Human Sciences) gave me training and guidance with respect to bone tissues and bone related biology. In addition, they gave me open access to their lab. Their collaboration was greatly appreciated.

TABLE OF CONTENTS

TABLE OF CONTENTS (Continued)

LIST OF FIGURES

LIST OF FIGURES (Continued)

LIST OF FIGURES (Continued)

LIST OF FIGURES (Continued)

LIST OF FIGURES (Continued)

LIST OF TABLES

DEDICATION

To my wife, Tracy, for her endless patience, support and encouragement.

And to our son, Dylan, who conducts physics experiments in projectile motion and momentum on a daily basis.

PREFACE

The work presented in this dissertation draws from a broad set of disciplines. For this reason, I have dedicated a great deal of discussion towards the introduction of the fundamental principles upon which this work is built. In order to assist the reader in the demarcation between background information and my own work, I have included this preface. Here I mention specifically my own novel contributions to the field of biomedical optics.

To begin, in (chapter 2.) I discuss the design, calibration and application of a digital Fourier holographic microscope. I then go on to describe its application towards optical scatter imaging as a means of determining particle size in a given sample. Both digital Fourier holographic microscopy and optical scatter imaging have been reported extensively in the literature. However, these two imaging modalities have not been combined in a thorough manner. A good portion of this dissertation focuses on the use of the digital Fourier holographic microscope I've built for optical scatter imaging. In addition, the work that has been reported on digital Fourier holographic microscopy has been carried out in reflectance mode. I have built my system in transmission mode, which allows for the collection of forward scattered light, as opposed to the obtuse angles of scattering captured in reflectance. We are interested in using the system for imaging biological samples which tend to undergo strong forward scattering. Working in transmission affords us the opportunity to collect light around the forward scattering direction and therefore receive increased signal in comparison to working in reflection. I go through a detailed description of the system, its calibration and applications including pilot studies of its use for optical scatter imaging of cells *in vitro* and tissue slices.

I then move on (chapter 3.) to discuss the work done in the optical characterization of bone tissues using diffuse reflectance spectroscopy. Bone tissues have been characterized for absorption and scattering more sparingly than soft tissues. I use diffuse reflectance spectroscopy in order to determine the absorption and scattering properties of bone tissues. I then go on to incorporate those results into a Monte Carlo model simulating the use of photodynamic therapy in treating osteosarcoma *in silico* (chapter 4.). I model the geometries of a canine model of osteosarcoma. The simulation gives results that are in agreement with the small sample of clinical cases of treating canine osteosarcoma in the literature. Based upon the agreement between the model and clinical reports, Monte Carlo should be useful in helping design future clinical trials for photodynamic therapy of osteosarcoma.

Lastly, I present the work done in collaboration with Dr. Paige Baugher at Pacific University in order to show that ALA-mediated photodynamic therapy can be used effectively to kill human osteosarcoma cells *in vitro* (chapter 5.).

DIGITAL FOURIER HOLOGRAPHIC MICROSCOPY AND POTENTIAL APPLICATIONS TOWARDS THE DESIGN OF PHOTODYNAMIC THERAPY OF OSTEOSARCOMA

1. INTRODUCTION

This body of work takes the author's foreknowledge in physics and optics and tailors that work towards applications of biomedical optics. Generically speaking, biomedical optics can involve imaging technologies or clinical applications. The body of work here looks at both imaging and clinical applications of biomedical optics—specifically digital Fourier holographic microscopy (DFHM) and photodynamic therapy (PDT). As such, this work draws from a diverse set of disciplines including cell and molecular biology, oncology, biochemistry, and fields specific to physics including atomic and molecular theory, optics and electromagnetic theory. This introductory chapter serves just the purpose its name implies—to introduce the reader to the background and assumed knowledge that will be needed in order to put the remaining chapters into context.

Before engaging in a thorough discussion of digital holography, optical scatter imaging, photodynamic therapy or photoactivation, it will be necessary to cover some of the basic principles of biomedical optics—namely scattering theory and light-tissue interactions. Absorption and scattering are of fundamental importance when considering light transport in tissues, and scattering theory will also be required for later chapters. For this reason, this introduction will lead with an overview of scattering theory followed by general transport theory as applied to light-tissue interactions.

The focus will then shift towards a rigorous description of digital holography. In the third section, general digital holography and its principles are introduced. Based upon these fundamental concepts, we then shift to a description of Fourier optics and digital Fourier holographic microscopy. In closing, the second section will follow with an introduction to optical scatter imaging (OSI) and propose the use of the DFHM system for such an application.

Ultimately, a fair amount of discussion is required with regard to PDT. This will be addressed in the third section, covering the general photobiology, photochemistry and photophysics of PDT and then more detailed specifics of 5-aminolevulinic acid (ALA) induced PDT. A general overview of osteosrcaoma will be given including incidence and epidemiology as well as current therapies and the use of canine models. This section will close with a review of using PDT towards treating bone cancers.

Lastly, this introduction will close with a final section introducing each of the methods of inquiry employed in this thesis, namely the use of digital Fourier holographic microscopy for optical scatter imaging, the optical characterization of bone through diffuse reflectance spectroscopy, a 3D Monte Carlo model of a clinical application of ALA-mediated PDT *in silico* and an *in vitro* application of ALA-mediated PDT of human osteosarcoma cells.

1.1. Biomedical Optics

As with the interaction of light with any form of matter, light-tissue interactions are subject to the effects of reflection, refraction, absorption and scattering. We begin by outlining the basic principles of optical scattering of light by objects whose size are on the order of the wavelength of light. This regime of optical scattering is defined as Mie scattering, and is an appropriate scale for scattering in light-tissue interactions as we are most concerned with the scattering of visible light ($\lambda \sim 0.5\mu m$) by subcellular objects with diameters in the range of $0.1 \lesssim d \lesssim 1\mu m$. Beyond needing a basic understanding of scattering theory for the discussion of light-tissue interactions, it will also be required in order to have a deeper discussion of Optical Scatter Imaging later in this thesis.

We lead this section with a discussion of scattering because it is of fundamental importance with respect to the propagation of light in tissues. In addition, the light-tissue intertaction section will look at absorption and general reflection and refraction effects in describing a basic theory of optical transport. A general description of optical transport will be needed in order to reach a greater understanding of measuring the optical properties of tissues and simulating a clinical application of PDT of osteosarcoma *in silico*.

1.1.1 A Review of Scattering Theory

A good portion of this thesis is concerned with the metrology of objects sized at the same order of magnitude as visible wavelengths. In particular, imaging applications of biomedical optics are concerned with detecting and measuring subcellular objects. When light interacts with such objects, two typical effects occur—the absorption and scattering of light. While both of these occurrences will be dealt with somewhat generically in the following section, a bit more detailed description of scattering theory is warranted and so will be dealt with here.

Mie Theory describes scattering by spherical particles whose size is on the order of the incident light's wavelength. A complete description of Mie theory is well beyond the scope of this thesis, so the reader is referred to the works by van de Hulst and Bohren and Huffman for a more thorough description of scattering theory.[1,2] While the application of Mie Theory is accurate for spherical particles, it can also serve as a good first-order approximation for non-spherical particles of the same range of sizes.[2] As such, Mie Theory is appropriate for modeling scattering by polystyrene microspheres and will also be used to approximate scattering by subcellular particles throughout this chapter.

At its essence, scattering theory is concerned with determining the scattered field emitted by some particle, given some incident field (Figure 1.1). In addition to the resulting scattered field, an internal field is also generated within the object itself. The solution to this problem revolves around determining the resulting scattered and internal fields by forcing boundary conditions at the particle surface—the interface between the two media, that of the particle and of its surroundings. This process entails finding a solution to the

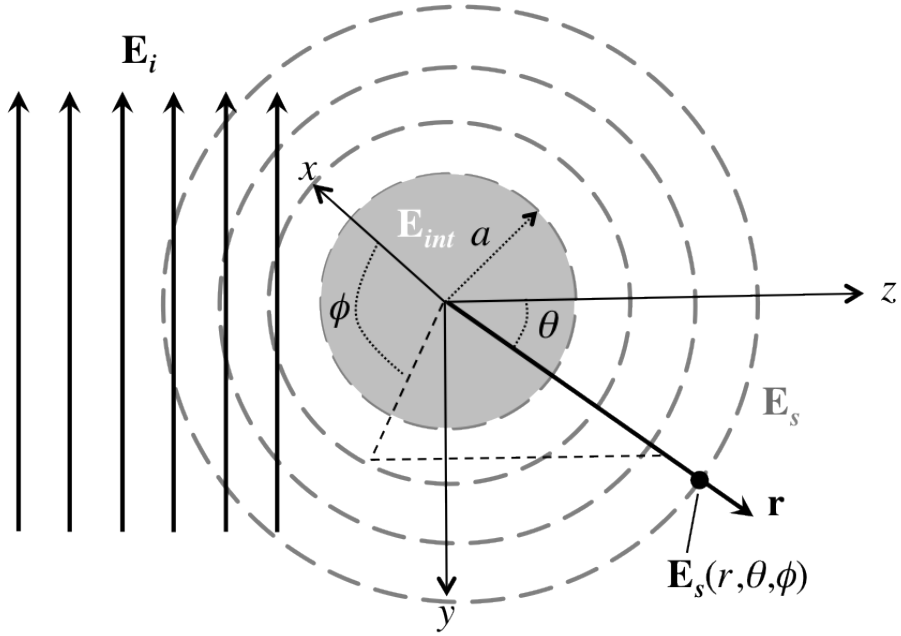

FIGURE 1.1: A plane wave is incident on a spherical particle. The plane of scattering is defined relative to the polarization of the incident field and its direction of propagation ($y - zplane$). Internal (E_{int}) and scattered (E_s) fields are generated as a result of the particle's interaction with the incident field. The scattered field $E_s(r, \theta, \phi)$ is defined as a function of the radial position (r), scattering (θ) and azimuthal (ϕ) angles. This figure naively insinuates that the scattered field has a spherically symmetric distribution.... Don't be fooled by this generic figure, as this is not the case for extended objects.

scalar wave equation in spherical coordinates,

$$\frac{1}{r^2}\frac{\partial}{\partial r}\left(r^2\frac{\partial\psi}{\partial r}\right) + \frac{1}{r^2 sin\theta}\frac{\partial}{\partial\theta}\left(sin\theta\frac{\partial\psi}{\partial\theta}\right) + \frac{1}{r^2 sin\theta}\frac{\partial^2\psi}{\partial\phi^2} + k^2\psi = 0, \tag{1.1}$$

where ψ represents the scalar wave.[1,2] Spherical coordinates are used for the scalar wave and therefore (1.1) due to the assumed spherical symmetry of the particle. The solution to the spherical wave equation is determined via the separation of variables, where the spatial dependencies of the function are broken into three separate functions,

$$\psi(r, \theta, \phi) = R(r)\Theta(\theta)\Phi(\phi), \tag{1.2}$$

where $R(r)$, $\Theta(\theta)$ and $\Phi(\phi)$ represent the radial, polar and azimuthal functions, respectively. The solution to this equation entails Legendre polynomials and spherical Bessel functions, given the spherical symmetry.[1,2]

Now that the scattering problem is established, we move on to the established solution to this problem, given by Mie theory. The scattered field will have two transverse components,[1,2]

$$\vec{E}_{s/\!/} = \vec{E}_o\frac{e^{ikr}}{-ikr}cos\phi S_2(cos\theta) \tag{1.3}$$

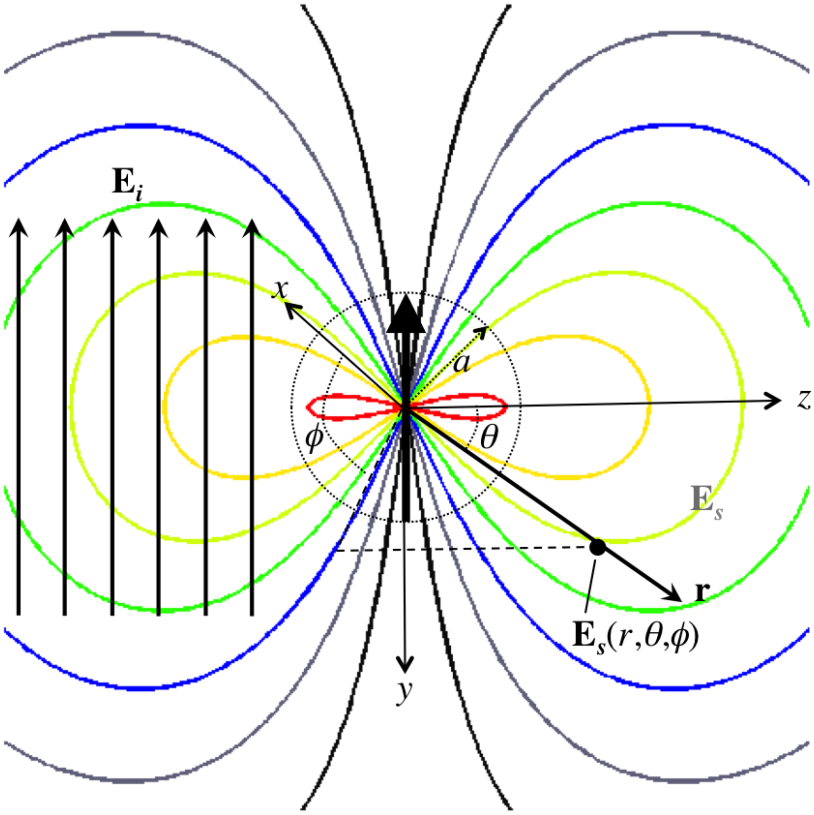

FIGURE 1.2: A plane wave is incident on a spherical particle, represented now as a dipole. The resulting scattered field $E_s(r, \theta, \phi)$ from the extended object will have a complex structure, taking the form of dipole radiation. Note, the displayed dipole is not to scale with the dipole field superimposed over the figure. This figure is presented solely for descriptive purposes.

and

$$\vec{E}_{s\perp} = \vec{E}_o \frac{e^{ikr}}{-ikr} sin\phi S_1(cos\theta) \tag{1.4}$$

where the e^{ikr}/r dependence of these functions tell us these will be radially outwardly directed spherical waves. However these spherical waves are modulated by additional factors, having polar and azimuthal angle dependencies (Figure 1.2). The polar angle, θ, is in fact termed the "scattering angle".

The terms S_1 and S_2 from (1.3) and (1.4) are the scattering amplitudes,

$$S_1 = \sum_n \frac{2n+1}{n(n+1)} (a_n \pi_n + b_n \tau_n) \tag{1.5}$$

and

$$S_2 = \sum_n \frac{2n+1}{n(n+1)}(a_n\tau_n + b_n\pi_n). \tag{1.6}$$

where the previously mentioned Bessel functions are buried within the scattering coefficients a_n and b_n. The Legendre polynomials are arguments of the angle-dependent functions π_n and τ_n.[1,2]

These Bessel functions ultimately are functions of the size parameter

$$x = \frac{2\pi n_{med} a}{\lambda} \tag{1.7}$$

and the relative index of refraction between the particle and medium,

$$n_{rel} = \frac{n_{part}}{n_{med}}, \tag{1.8}$$

where a represents the particle radius, λ the wavelength of incident light, n_{part} the index of refraction of the particle and n_{med} that of the medium.[1,2]

The problem of generating the scattered field from an incident field can be represented via acting on the incident field with a scattering matrix, of which the scattering amplitudes are elements,

$$\begin{pmatrix} \vec{E}_{/\!/s} \\ \vec{E}_{\perp s} \end{pmatrix} = \frac{e^{ik(r-z)}}{-ikr} \begin{pmatrix} S_2 & 0 \\ 0 & S_1 \end{pmatrix} \begin{pmatrix} \vec{E}_{/\!/i} \\ \vec{E}_{\perp i} \end{pmatrix} \tag{1.9}$$

where the z-axis is defined by the direction of propagation of the incident field and $z = 0$ is located at the center of the scattering sphere.[1,2]

As an example of the application of these results, the scattering function for parallel polarized light,

$$P(\theta) = |S_2|^2, \tag{1.10}$$

is plotted for microspheres in mounting media (Figure 1.3).[3] The scattering function is a dimensionless quantity, having units of scattered irradiance per unit incident irradiance. These example curves were modeled based on polystyrene microspheres ($n_{part} = 1.59$) embedded in mounting media ($n_{med} = 1.46$, Aqua-Poly/Mount®, Polysciences, Inc., Warrington, PA). Microsphere diameters plotted are in the range of $0.36\mu m - 2.90\mu m$.

A few characteristics of these scattering plots (Figure 1.3) are noteworthy. First, the larger diameter spheres scatter stronger in the forward direction ($\theta = 0^o$) than smaller spheres, while the smaller spheres have greater scattering at broader scattering angles. In addition, the scattering functions for the smaller spheres tend to have long, smooth oscillations, whereas those of the larger spheres tend towards more rapid oscillations as a function of scattering angle. This is a consequence of the Bessel functions, whose arguments are the size parameter (1.7). With the $2\pi/\lambda$ dependence, we can think of the size parameter as analogous to a spatial frequency. Therefore, as the particle radius a

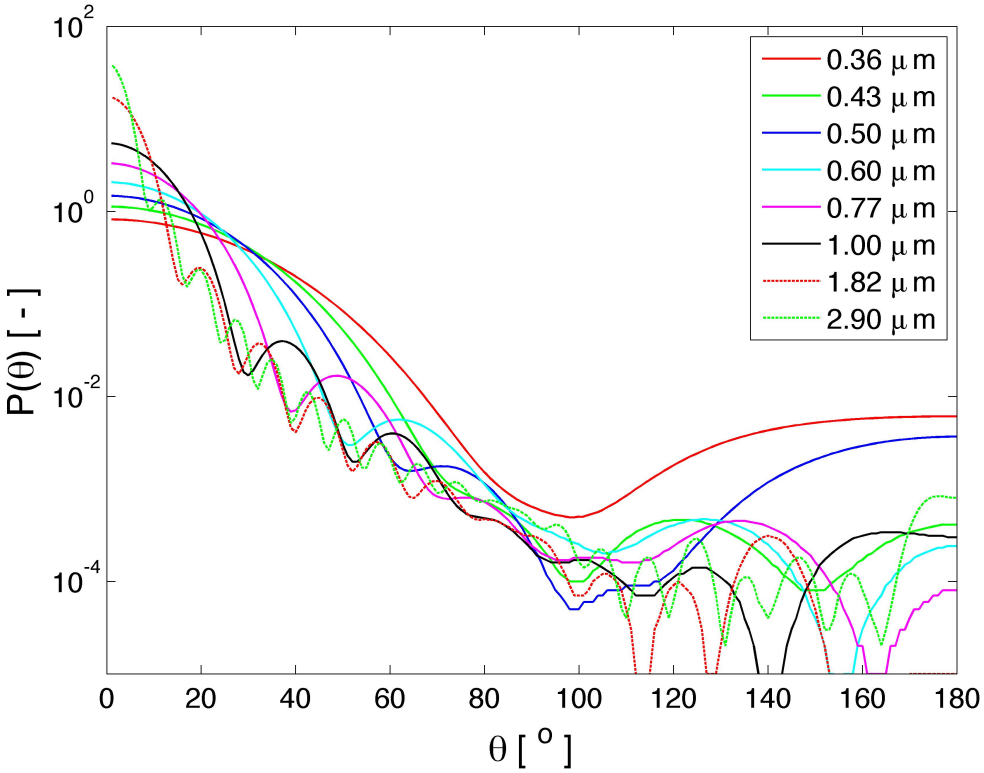

FIGURE 1.3: A log-scale plot of the scattering functions $P(\theta)$ for multiple polystyrene microspheres ($n_{part} = 1.59$) in mounting media ($n_{med} = 1.46$).[3] The oscillatory nature of these functions due to their dependencies on Bessel functions is apparent.

increases, the frequency of oscillation of the Bessel function increases, leading to the observed increased oscillation for larger particles. Similarly, increasing the relative index of refraction between the particle and media can have a similar effect, as some of the Bessel functions are dependent upon the product of (1.7) and (1.8).[1,2]

Relating these observations back to the dipole scattering picture (Figure 1.2), we can come to the same conclusions based upon superposition arguments. A true point source, with no appreciable extension compared to the wavelength of incident light, would scatter light equivalently in all directions, resulting in a smooth, flat scattering function $P(\theta)$. As we increase the particle size, and thereby add additional point sources, the superposition of their respective scattering fields comes into play. The superposition of two such point sources would lead to the classic dipole radiation field, which pinches in along the ends of the dipole and radiates outward in front of and behind the dipole. Increasing the size of the scattering sphere is equivalent to increasing the strength of the dipole, such that the loss of an isotropic field becomes more apparent and accentuated. Ultimately, large particles would need be represented by a long sequence of point sources. The superposition of their respective scattered fields would therefore be flatter in the forward direction, as edge effects would become less influential. In addition, regions of constructive and destructive interference between these superimposed fields will occur at greater frequency, giving rise to the observed oscillatory nature of the scattering functions of larger particles. These arguments explain the stronger forward directed scattering of larger particles as well as their increased oscillatory nature, without needing to make arguments with respect to the Bessel functions the fields ultimately entail.

Lastly, we can take the scattering function $P(\theta)$ from the polystyrene microsphere examples and allow them to revolve around the azimuthal angle. The result is a map of the scattering function, projected onto a forward directed plane. The same data is represented in both color and gray scale figures in order to accentuate different features. The color figures (Figure 1.4) do a better job of representing the change in intensity for smaller particles along the relatively smooth field, however the fluctuations found in the scattered field by larger particles aren't as apparent. The gray scale figure of the same data (Figure 1.5) is given in order to accentuate the fluctuations in the scatterd fields by the larger particles. This concept is of importance to this thesis as this projection of the scattered field onto a forward plane is ultimately the representation of the scattered field which will be measured.

When applying scattering theory to biological samples, the predominant subcellular contributors to scattering come from nuclei and mitochondria. Nuclei are generally spherical such that the application of Mie theory to nuclear scattering is directly applicable. Mitochondria however tend to be elongated and tubular. That said, the use of Mie theory for describing scattering due to mitochondria is not accurate, but meant to be used as a first order approximation. A polar plot of the scattering functions due to nuclei and mitochondria is presented for reference.[4] As will be discussed, mitochondria can swell in response to certain stimuli, so the figure includes scattering functions for the larger and

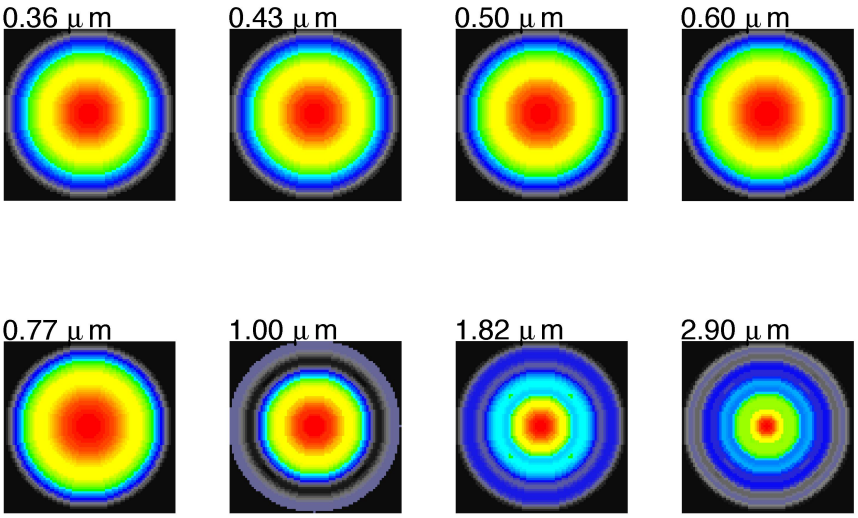

FIGURE 1.4: A log-scale plot of the scattering functions $P(\theta)$ for multiple polystyrene microspheres ($n_{part} = 1.59$) in mounting media ($n_{med} = 1.46$).[3] Particle diameters are displayed atop their respected plots.

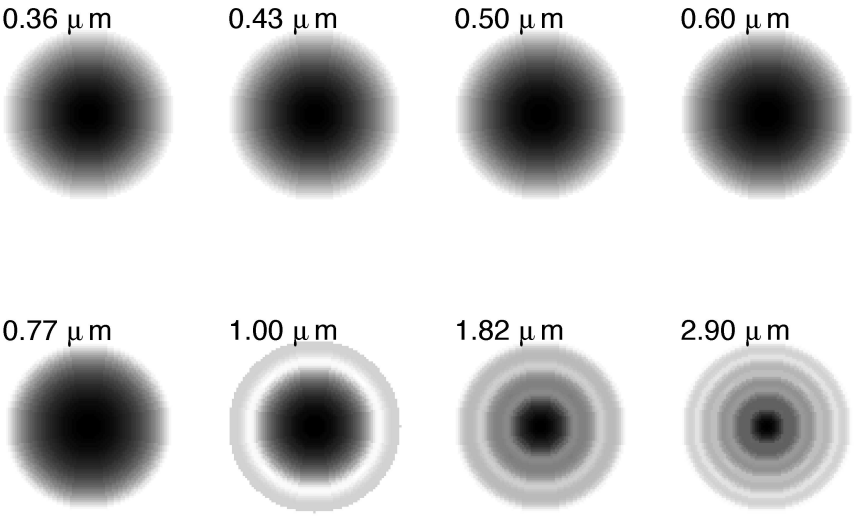

FIGURE 1.5: The same log-scale data as in (Figure 1.4) is presented again here in gray scale in order to accentuate the oscillatory nature of the scattered field from larger particles due to their dependencies on Bessel functions.

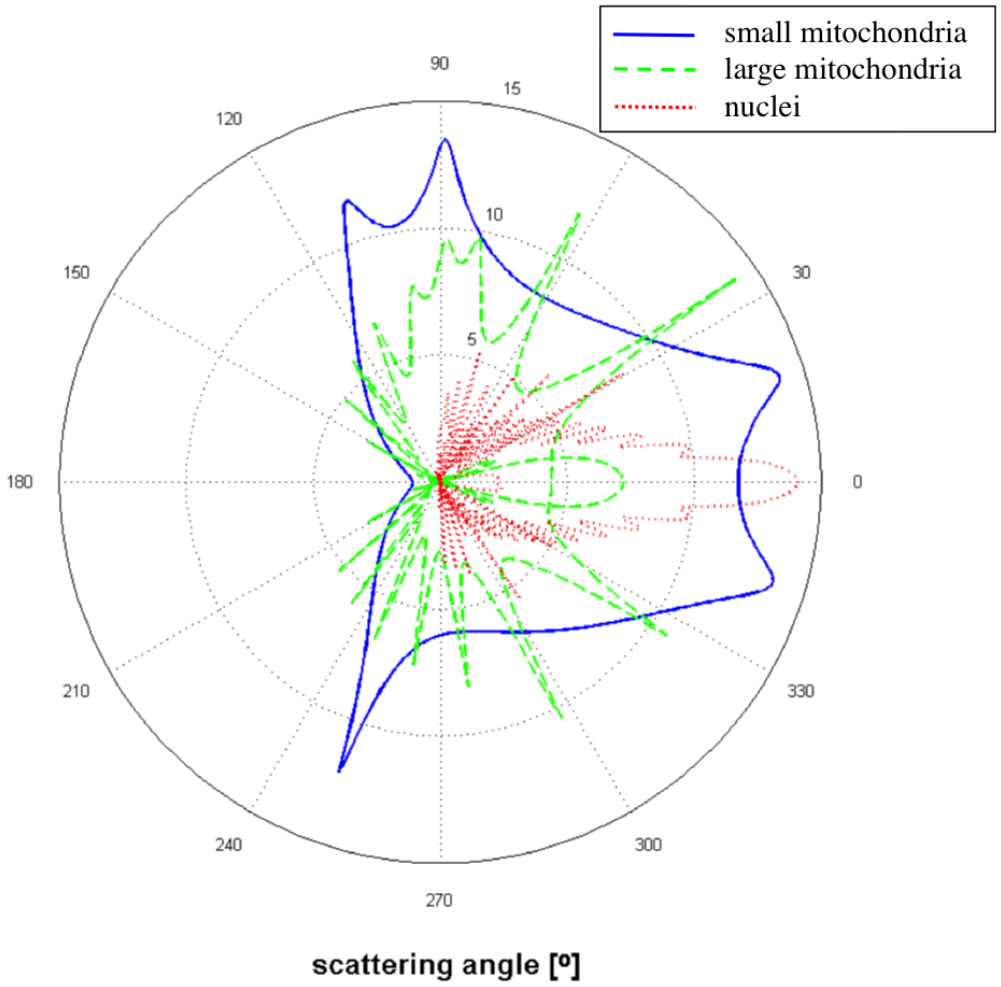

FIGURE 1.6: The dominant contributors to scattering in cells comes from the nuclei and mitochondria. The scattering functions for nuclei and two sizes of mitochondria are given in the form of a log-scale polar plot. The asymmetry to this plot is due to the fact that scattering by parallel polarized light is given in the top half of the plane and that of perpendicularly polarized light in the lower half.

smaller scales of mitochondrial size. Nuclear scattering is modeled here using a relative index of refraction $n_{rel,mit} = 1.04$ and a radius of $2.5\mu m$. Mitochondrial scattering is modeled here using a relative index of refraction $n_{rel,mit} = 1.02$ and radii of $0.25\mu m$ and $1.0\mu m$.[5–9] We see that nuclei will be strongly forward scattering, dominating scattering over the first $8 - 10^o$. Mitochondria will have broader angular scattering. As will be described later, the ability to filter the scattered field from cells will allow the ability to differentiate not ust between nuclear and mitochondrial scattering, but also between scattering from mitochondria of different sizes.

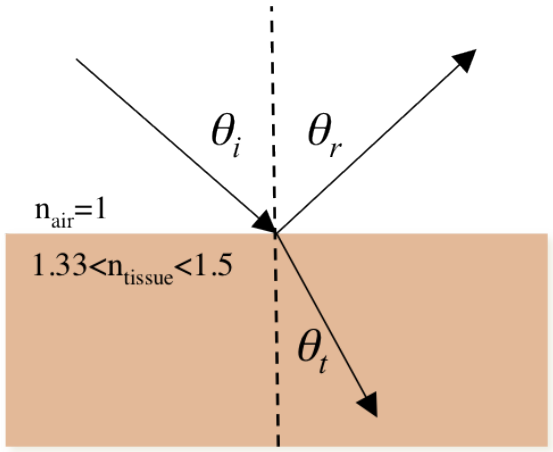

FIGURE 1.7: The simple geometry of the Law of Reflection and Snell's Law of refraction at an air-tissue interface.

1.1.2 Light-Tissue Interactions

Tissues are largely composed of water, such that the wavelength-dependent index of refraction for tissues lies in the range $1.33<n_{tissue}<1.5$. At $\lambda = 633nm$, $n = 1.37$ is a typical index of refraction for tissues.[10] Given an air-tissue interface (a typical scenario for dermatologic cases and skin cancers), specular reflectance will result (Figure 1.7). This specular reflectance is governed by Fresnel's Law (Figure 1.8),

$$r = \frac{1}{2}\left(\frac{tan^2(\theta_i - \theta_t)}{tan^2(\theta_i + \theta_t)} + \frac{sin^2(\theta_i - \theta_t)}{sin^2(\theta_i + \theta_t)}\right), \tag{1.11}$$

where θ_i and θ_t represent the angles of incident and transmitted (refracted) light at the interface, respectively.[10] For normal incidence ($\theta_i = 0^o$) and making use of Snell's Law (Figure 1.7),

$$n_i sin\theta_i = n_t sin\theta_t, \tag{1.12}$$

Fresnel's Law reduces to the simplified relationship

$$r = \frac{(n_i - n_t)^2}{(n_i + n_t)^2}, \tag{1.13}$$

where n_i and n_t represent the indicies of refraction for the materials corresponding to the incident and transmitted regions of light, respectively. We see that reflectances are on the order of 5% for normal incident light on tissue.

The fraction of light that penetrates beyond the surface of the tissue will be the total incident light multiplied by the transmission, or equivalently by multiplying by the difference between unity and the reflectance,

$$t = 1 - r. \tag{1.14}$$

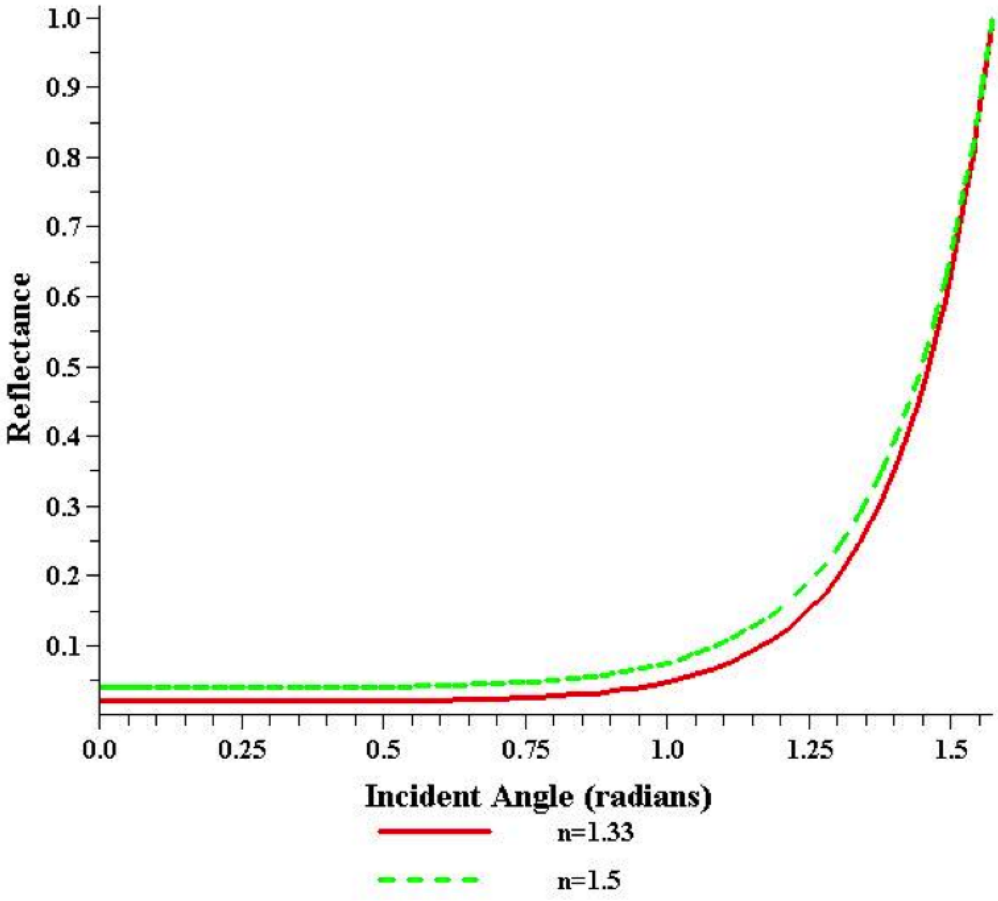

FIGURE 1.8: The resulting reflectances as a function of incident angle for an air-tissue interface. Resulting reflectances are displayed for the low (red, solid) and high (green, dashed) values of index of refraction for tissues.

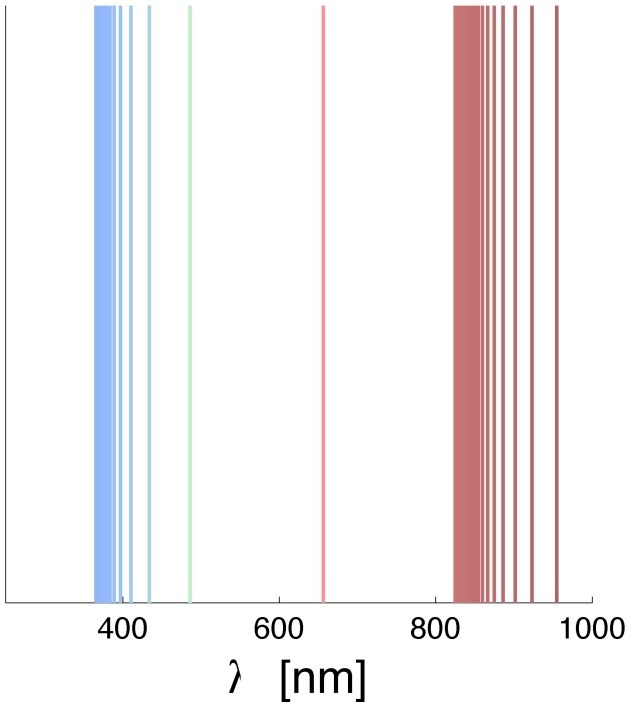

FIGURE 1.9: The discrete absorption lines of the hydrogen atom.[11] *Note, the coloring of these spectral lines is not meant to be indicative of actual colors in the visible spectrum, but merely as a reference to the visible spectrum*

Therefore, when a fluence ψ_o is incident on a tissue surface, the amount of light that just breaches the surface by some infinitesimal depth ϵ will be $\psi(\epsilon) = \psi_o t$. However this term only accounts for specular reflection and transmission across an index of refraction mismatch.

Before we let the light actually pass any deeper into the tissue, we need to consider the make-up of the tissue. Tissues are macroscopic biological structures, built up from countless biochemicals, intercellular and intracellular (subcellular) structures. Each of these components and their molecular make-up will be associated with molecular energy structures, such that they absorb electromagnetic radiation. Generally speaking, the more complex the structure, the broader the absorption bands of the structure. For instance, consider the discrete absorption spectra of the hydrogen atom (Figure 1.9)—the simplest of electronic structures—versus the broad, continuous absorption spectra of water (Figure 1.10) and oxygenated and deoxygenated hemoglobin (Figure 1.11), some of the more dominant chromophores in tissues.[11–13] With increased complexity follows an increase in atomic or molecular energy levels and the increased overlap between those levels. This results in the broadening, and ultimately overlapping of energy bands such that the more complex molecules have more continuous absorption spectra.

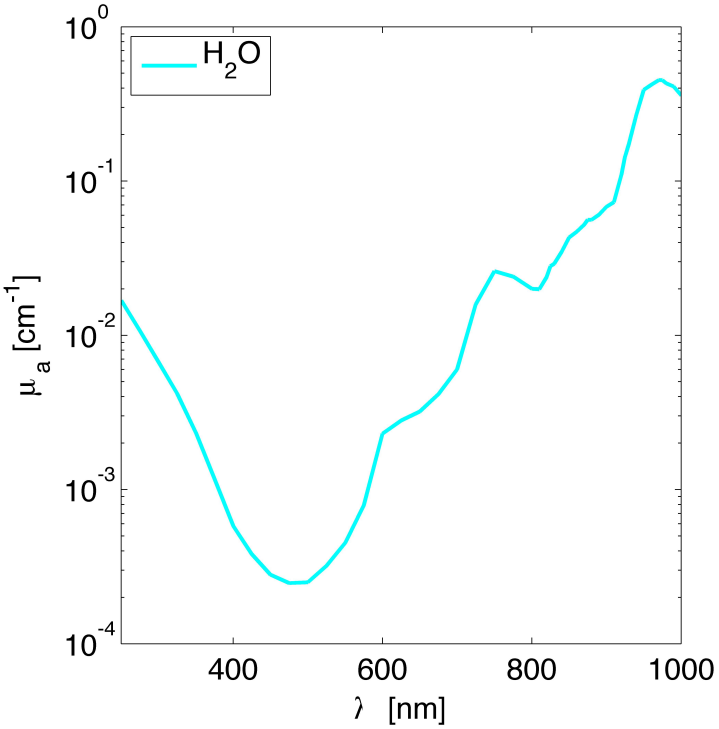

FIGURE 1.10: The absorption coefficient for water as a function of wavelength.[13]

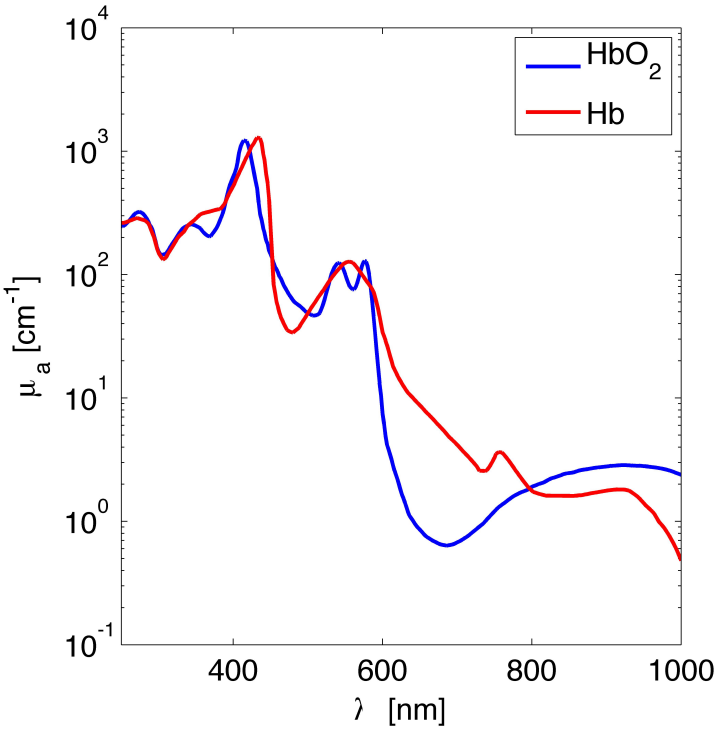

FIGURE 1.11: The absorption coefficients for oxygenated hemoglobin (HbO_2) and deoxyhemoglobin (Hb) as a function of wavelength. Absorption coefficients are calculated from the respective extinction coefficients, assuming 150 gHb/L whole blood.[12]

We must be able to characterize how these chromophores absorb light as a function of wavelength in order to construct a theory of optical transport relative to tissues. In tissue optics, this is achieved via the absorption coefficient, μ_a, which is the inverse of the mean-free path before absorption occurs in a given bulk chromophore.[14] Just as tissues are composed of a complex and dynamic set of structures and biochemical constituents, the absorption coefficient of a given tissue will be cumulative with respect to the absorption coefficients of its constituents. As mentioned, the two dominant chromophores in tissues under the visible spectrum are water and oxygenated and deoxygenated hemoglobin. A good approximation of the bulk absorption coefficient in tissues can then be determined by the sum of those respective absorption coefficients, weighed by their respective concentrations in the tissue,

$$\mu_a(\lambda) = B\Big(S\mu_{a,oxy}(\lambda) + (1-S)\mu_{a,deoxy}(\lambda)\Big) + W\mu_{a,H2O}(\lambda), \tag{1.15}$$

where B, S and W represent the concentrations of blood, oxygen saturation and water present in the tissue, respectively.[15,16] Of course, $\mu_{a,oxy}(\lambda)$, $\mu_{a,deoxy}(\lambda)$ and $\mu_{a,H2O}(\lambda)$ represent the absorption coefficients of oxygenated and deoxygenated hemoglobin and water, respectively. The wavelength dependence of the absorption coefficients of water, oxygenated and deoxygenated hemoblobin were used to introduce the broad, continuous spectral properties of complex molecules, (Figure 1.10) and (Figure 1.11). Typical absorption coefficients for red light in tissues are around $\mu_a \sim 0.3cm^{-1}$, such that its mean-free path would be 3.3 cm.[14]

Absorption works to decrease fluence levels exponentially as a function of depth. Think of an extinction curve for photons as a function of depth—the deeper we look within the tissue, the less photons will be present because they will have undergone greater absorption (and therefore extinction) along the way. This is in essence an exponential decay process.

Before we can put this all together though, we need to lastly consider scattering effects in tissues, which are substantially turbid due to optically large structural elements of varying indicies of refraction. Just as the absorption coefficient was defined as the inverse of the mean-free path before absorption, a scattering coefficient, μ_s, will be defined as the inverse of the mean-free path between scattering events in tissue. Scattering is typically dominant over absorption is tissues, thereby having typical scattering coefficients some two orders of magnitude larger than for absorption. Scattering coefficients in tissue tend to fall in the range of $\mu_s \sim 300cm^{-1}$. This is a very broad approximation, simply to give the reader an idea of a typical scattering value. Compendiums of optical properties of various tissues can be found for more precise values.[10]

Scattering also works to cause extinction of photons as they travel to greater depths in tissues. For example, if the tissue acts as a completely isotropic scatterer—scattering photons in all directions without bias—then only half of the photons incident at a point in the tissue will scatter with some forward directed component, and the other half would

only have a backward directed component. Therefore, for an isotropic medium, half of the light would cease to move with some component of their trajectories in the forward direction, causing extinction with greater and greater depths. Scattering therefore adds to the extinction of photons with depth in a tissue, and can also be modeled as an exponential decay function.

An interesting side note based on backscattering in tissues.... Fluence levels observed just below the surface of a tissue can be observed to be greater than that which was incident on the tissue itself. Assuming unity fluence is incident on the tissue, accounting for small losses due to specular reflection (Figure 1.8), the light that reaches just below the surface of the tissue will be supplemented by backscattered light from deeper in the tissue, such that the total fluence just below the surface of the tissue will be greater than unity.[14]

Conversely to isotropic scattering, if a tissue works to scatter light strongly in the forward direction, then this extinction effect would be slight, if substantial at all. For example, when light does not scatter in a medium, it continues along the same path as it is directed, throughout the entire transport process. In such a case, there is no extinction effect due to scattering. So long as absorption is not present in such a medium, one would anticipate the fluence anywhere along the path of a collimated beam would be measured to be the same.

As argued, the direction of scattering will play a significant role in the extinction effect of light as it propagates deeper into tissues. We can account for such discrepancies between tissues based on a term called anisotropy, g, which quantifies the directional bias of scattering in a tissue. The formal definition of anisotropy is given as the expectation value of the angle of scattering θ projected in the forward direction,

$$\begin{aligned} g &= \langle cos\theta \rangle \\ &= \int_{-1}^{1} p(cos\theta) cos\theta d(cos\theta), \end{aligned} \tag{1.16}$$

where for tissues, the probability density function can be adequately approximated by the Henyey-Greenstein function,[10]

$$p(cos\theta) = \frac{1 - g^2}{2(1 + g^2 - 2gcos\theta)^{3/2}}. \tag{1.17}$$

When a tissue scatters isotropically, its anisotropy has a value of $g_{isotropic} = 0$. When a tissue is biased towards complete forward scattering, its anisotropy has a value of $g_{forward} = 1$. In the context of complete backscattering, anisotropy would have a value of $g_{forward} = -1$. While anisotropy values can fall within the range $-1 \leq g \leq 1$, tissues tend to be strongly forward scattering, having anisotropies around $g \sim 0.9$ for visible light. The anisotropy factor is used to then scale the scattering coefficient, giving the reduced scattering coefficient

$$\mu_s'(\lambda) = \mu_s(\lambda)(1 - g), \tag{1.18}$$

where both the scattering and therefore the reduced scattering coefficients have wavelength dependence. Effectively, isotropic scattering is 100% efficient in randomly distributing scattered light and leading to extinction, while strongly forward-directed scattering tissues are much less effective in causing extinction. A typical anisotropy of $g \sim 0.9$ thereby only brings about a 10% efficiency in leading to extinction and would correspond to a typical reduced scattering coefficient of $\mu_s' \sim 30cm^{-1}$ for visible light in tissues.[14] Even with the anisotropy coming into consideration for the reduced scattering coefficient, it is clear that tissues tend to be scattering dominant (as compared to the typical $\mu_a \sim 0.3cm^{-1}$ over the same wavelengths).

The effect of the absorption coefficeint, scattering coefficient and anisotropy in a tissue can all be tied together into a single term called the penetration depth,

$$\delta = \frac{1}{\sqrt{3\mu_a(\mu_a + \mu_s(1-g))}}, \tag{1.19}$$

as defined by diffusion theory. This penetration depth is equivalent to the depth of transmission at which the fluence has been attenuated by a factor of $1/e$.[10,14,17]

Having condensed all of the factors that play a role in the extinction of light during propagation through an absorbing, turbid tissue, into a single term (1.19), the extinction of light can be determined as a function of depth via Beer's Law,[10,14,17]

$$\psi(z) = \psi_o k e^{-z/\delta}, \tag{1.20}$$

where the term k scales the fluence to account for basckscattered light and has been empirically determined to be

$$k = 3 + 5.1R_d - 2e^{-9.7R_d}. \tag{1.21}$$

The factor R_d from (1.21) represents the diffuse reflectance, or light that leaves the tissue after backscattering back through the tissue surface from deeper within. The diffuse reflectance can be approximated as

$$R_d \approx e^{-8\mu_a\delta}, \tag{1.22}$$

and will play a a crucial role in the later part of this thesis when Diffuse Reflectance Spectroscopy is used in order to measure the optical properties of bone tissues.[14]

1.2. Digital Holography

Given a plane wave of monochromatic light incident on a nonuniform, nearly transparent object (weak absorption), the transmitted wave will undergo a phase shift (Figure 1.12). This resulting phase shift is spatially dependent upon the depth of the sample and

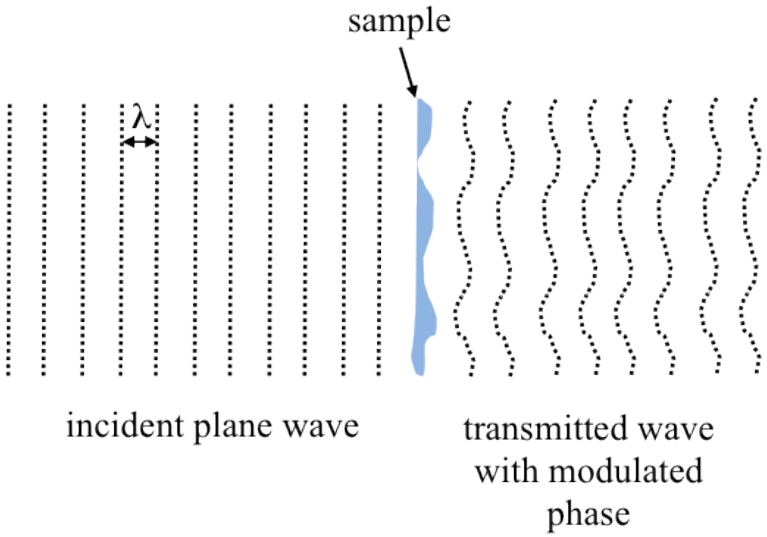

FIGURE 1.12: A plane wave incident upon a thin, weakly absorbing sample carries away information of the sample's depth and index of refraction, which is encoded in the resulting phase distribution of the transmitted wave.

the spatial distribution of its index of refraction. Phase through a thin medium in general is dependent upon both these factors—depth of sample, $d(x, y)$, and index of refraction, $n(x, y)$,[18,19]

$$\Phi(x, y) = \frac{2\pi d(x, y)}{\lambda} n(x, y). \tag{1.23}$$

Imaging systems traditionally measure the intensity of light that is incident on the sensor, such as a CCD camera. As an electromagnetic wave, light carries both amplitude and phase. In measuring the intensity of light from an object, the phase information is lost. Holography is a method of measuring both the amplitude and phase of light from a source, giving information of the "whole" field. Hence, the name holography was coined by Gabor for its ability to measure the whole electromagnetic field. An introduction to two methods of recovering a sample's phase via digital holography will be given—digital holographic microscopy and digital Fourier holographic microscopy. These introductions are accompanied by simulated examples.

1.2.1 Digital Holographic Microscopy

Digital holographic microscopy (DHM) is a means of recapturing the phase of light leaving an object at its image plane. Considering the image plane of a sample is a convenient introduction to digital holography in that the reconstructed phase from the image plane will directly correlate to the physicality of the sample. Describing the holographic process in the image plane therefore serves as a natural starting point for an introduction

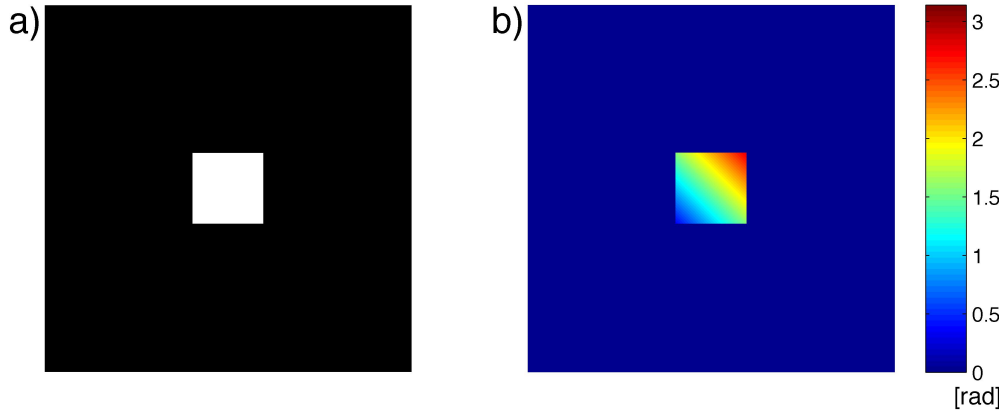

FIGURE 1.13: a) Amplitude and b) phase of a simulated sample.

to digital holography.

Recovery of Phase Information

Begin with a phase object (Figure 1.13) whose transmitted field is of the form

$$\vec{s}(x,y) = s(x,y)e^{i\Phi_s(x,y)}, \tag{1.24}$$

where $s(x,y)$ represents the amplitude and $\Phi_s(x,y)$ the phase of the sample field.

A CCD camera captures an intensity based image, such that no phase information is available. Digital holographic microscopy can be employed in order to recover the required phase information needed for image reconstruction. This method recovers phase information via the interference pattern resulting at the plane of the CCD due to the mixing of the scattered field with a reference field.

In order to recover phase information from the sample, three images are generally collected at the image plane via a CCD. The first image collected is the intensity of the scattered field, $S(x,y)$, from the sample only. This image will appear equivalent to that given in (Figure 1.13a). The second image collected is the intensity of the reference field, $R(x,y)$ (Figure 1.14). The third image is the intensity image of the hologram itself, $H(x,y)$ (Figure 1.15)—a result of the interference pattern between the scattered and reference fields.[18,20,21] If we start with the field nature of light incident upon the CCD via the sample and reference paths, we can illustrate the means of recovering the phase information lost in the intensity values captured via the CCD.

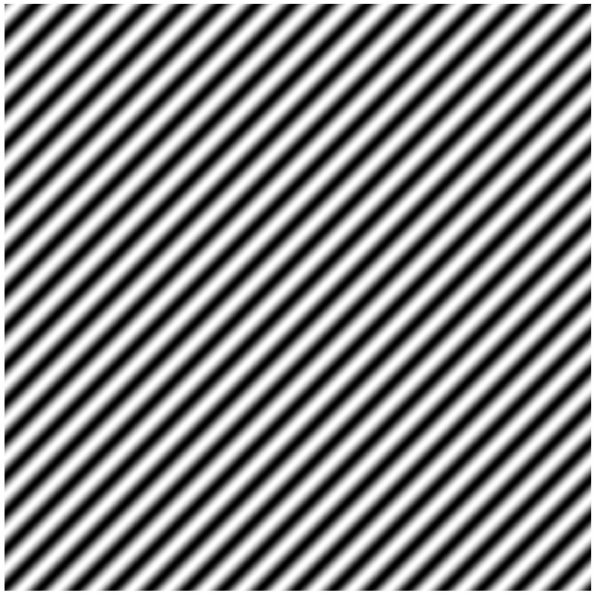

FIGURE 1.14: The phase of the reference beam alone, collected at the CCD. The image given here is used as an example of the phase of the reference field across the CCD due to the angle of incidence. The incident angle used in the actual simulation was greater, resulting in a frequency some 50 times greater than that seen in this image—and therefore not visually perceptible in the figure.

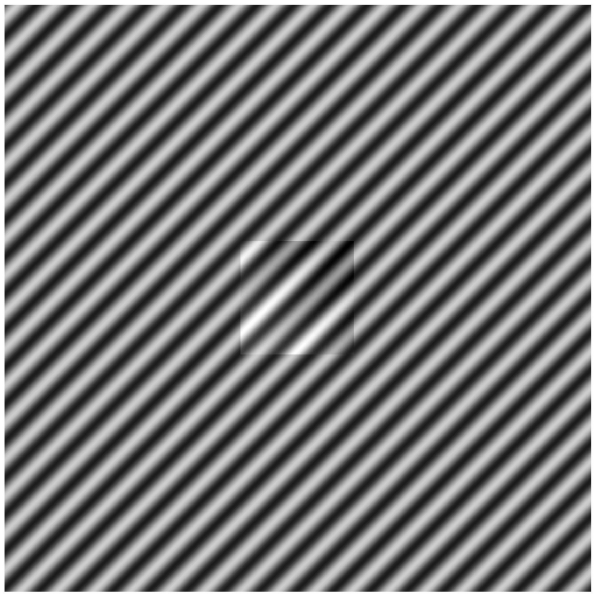

FIGURE 1.15: The interference pattern between the sample and reference beams, (1.33), collected at the image plane. That the reference signal is stronger than that of the sample is of no small consequence—the reference signal can be used to amplify the sample signal via heterodyne amplification, (1.33). As with (Figure 1.14), the image given here is used as an example since the resulting fringes of the reference field are not visually perceptible in the applied simulation.

Define the reference field as

$$\vec{r}(x,y) = r(x,y)e^{i\Phi_r(x,y)}, \tag{1.25}$$

where $r(x,y)$ represents the amplitude and $\Phi_r(x,y)$ the phase of the reference field. The measured intensities of the sample and reference fields are then given by the complex squares of their respective fields,

$$S(x,y) = \vec{s^*}(x,y)\vec{s}(x,y) = |s|^2, \tag{1.26}$$

$$R(x,y) = \vec{r^*}(x,y)\vec{r}(x,y) = |r|^2, \tag{1.27}$$

which correspond to the simulated images given in (Figure 1.13a) and (Figure 1.14), respectively. The superposition of the sample and reference fields at the CCD results in the combined hologram field,

$$\vec{h}(x,y) = s(x,y)e^{i\Phi_s(x,y)} + r(x,y)e^{i\Phi_r(x,y)}, \tag{1.28}$$

which is in turn measured as an intensity by the CCD (Figure 1.15).

Taking the complex square of the hologram field, we can determine the measured intensity to be

$$\begin{aligned} H &= |se^{i\Phi_s} + re^{i\Phi_r}|^2 \\ &= (s^*e^{-i\Phi_s} + r^*e^{-i\Phi_r})(se^{i\Phi_s} + re^{i\Phi_r}) \\ &= |s|^2 + |r|^2 + s^*re^{i(\Phi_r - \Phi_s)} + sr^*e^{-i(\Phi_r - \Phi_s)}, \end{aligned} \tag{1.29}$$

where the notation indicating the $x-$ and $y-$dependence has been suppressed. We can assume the amplitudes of both the sample and reference fields are both real, such that their amplitudes are their own complex conjugates. In addition, using the identity for the cosine function

$$\cos\Phi = \frac{e^{i\Phi} + e^{-i\Phi}}{2}, \tag{1.30}$$

we can simplify the measured intensity of the hologram as measured by the CCD to be represented by[18,20,21]

$$H = |s|^2 + |r|^2 + 2sr\cos\Phi, \tag{1.31}$$

where the phase of the hologram is defined as the difference between those of the sample and reference fields

$$\Phi = \Phi_r - \Phi_s. \tag{1.32}$$

The intensity (1.31) can be interpreted as the sum of intensities from the sample and reference fields plus a cross-term. This cross-term is the product of the reference and sample field amplitudes, modulated by the cosine of their respective phase differences (1.32).

In applications, an increased reference amplitude will therefore amplify the intensity of the holographic image. Looking back at (1.29), if the first two terms can be interpreted as the intensities of the sample and reference fields, this cross-term comes from the later two terms which are known as the "twin images".[18,20–22]

Subtracting the measured intensities of the sample (1.26) and reference (1.27) waves from the measured intensity of the hologram (1.31), as imaged by the CCD, therefore isolates the interference pattern due to the superposition of the two fields,

$$\begin{aligned} E &= |s|^2 + |r|^2 + 2sr\cos\Phi - |s|^2 - |r|^2 \\ &= 2sr\cos\Phi. \end{aligned} \tag{1.33}$$

Upon taking the Fourier transform of (1.33),

$$\mathcal{E}(k_x, k_y) = \mathcal{F}[E(x, y)], \tag{1.34}$$

the phase information for the hologram is recovered, where k_x and k_y represent coordinates of spatial frequency resulting from the Fourier transform.[18,20–25] Computationally, (1.34) will be a complex array with the amplitude and phase encoded in its real and imaginary terms, respectively.

In the holographic reconstruction process, a two dimensional Fourier transform is carried out, resulting in two mirrored Fourier transforms centered around a DC term (Figure 1.16). One of the two twin frequency spectra can then be selected and cropped for further analysis (Figure 1.17). Once separated via the digital Fourier transform, we select a region of pixels around a single twin image and recenter the localized array, thereby separating it from the other twin image and DC component. This process is referred to as heterodyne filtering because we are essentially shifting the high frequency components of the selected twin image to the central DC location. We now refer to the isolated twin image as $\mathcal{E}'(k_x, k_y)$. Having isolated a single twin image, we are ready for additional image processing. In this sense, (1.34) now represents a piece of the hologram specific to an isolated twin image, having removed the DC signal and other twin image.

The importance of the periodicity of the reference beam as it crosses the CCD is determined by the beam's wavelength, as well as it's incident angle, θ_R, with respect to the normal to the CCD (Figure 1.18). For a fixed wavelength, λ, the peak-to-peak distance of the reference wave's intensity as it crosses the plane of the CCD is inversely proportional to the $sin\theta_R$,

$$d_{pp} = \frac{\lambda}{sin\theta_R}, \tag{1.35}$$

such that increasing the reference angle increases the carrier frequency imparted on the hologram by the reference beam. For a fixed wavelength, the reference beam's angle of incidence is the determining factor for the carrier frequency it imparts, and therefore the separation of the twin frequency spectra. This is of no small consequence, as can be

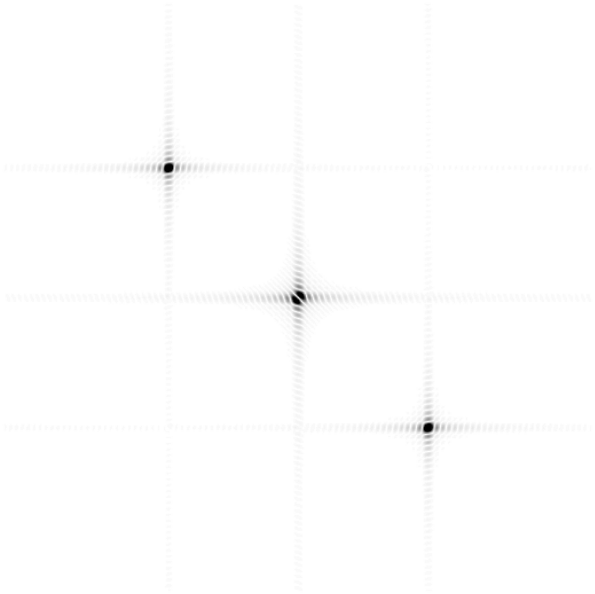

FIGURE 1.16: The Fourier transform of (1.31), (Figure 1.15). The twin frequency spectra are offset from the central DC component as a result of the carrier frequency incorporated by the reference field. From this reconstruction, one of the two twin frequency spectra can be isolated for further analysis.

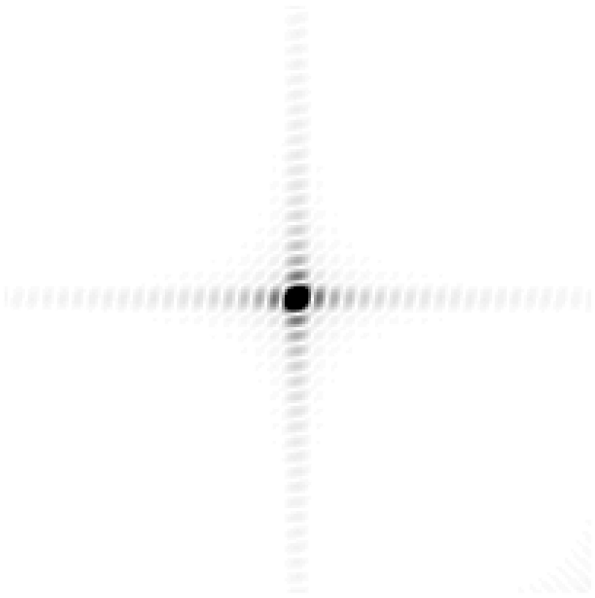

FIGURE 1.17: One of the twin frequency spectra is isolated and recentered computationally from its twin spectrum and the DC components shown in (Figure 1.15). Isolation of this single frequency spectrum allows reconstruction of a single hologram upon employing an inverse Fourier transform—by cutting out one of the twin frequency spectra, one of the twin images will also be eliminated as a result.

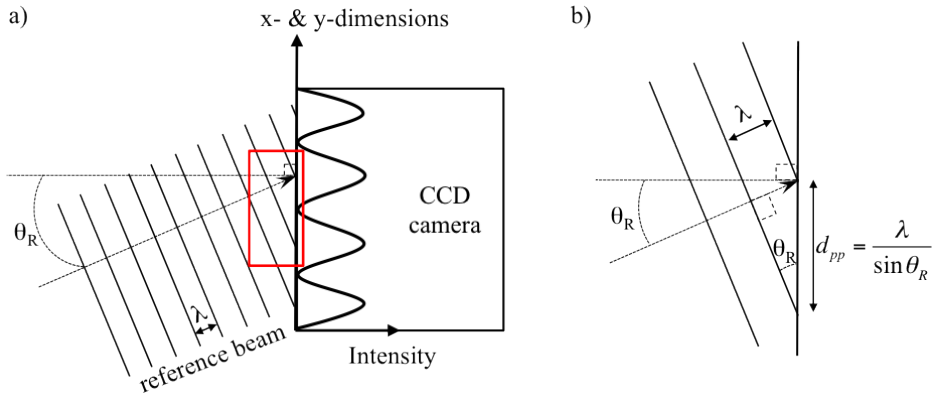

FIGURE 1.18: a) The geometry between the reference beam and plane of the CCD camera affects the periodicity of the reference field's intensity across the CCD and therefore the carrier frequency it imparts on the hologram. b) A zoomed in view of the critical geometry between the reference beam and CCD camera, as indicated by the red box in a).

demonstrated via simulation. As seen in (Figure 1.19), reference angles too small do not adequately resolve the twin frequency spectra (images) from the DC component. Similarly, too steep of a reference angle with respect to the CCD separates the twin frequency spectra (images) too dramatically such that they leave the field of view and wrap to the opposite corner. Either of these two extreme scenarios is detrimental to the isolation and analysis of a single twin frequency spectrum (image).

Having successfully removed the DC component and isolated a single twin frequency spectrum, we can take a two-dimensional inverse Fourier transform of the cropped version of (1.34), $\mathcal{E}'(k_x, k_y)$, in order to recover the hologram of the sample in the image plane,

$$E'(x, y) = \mathcal{F}^{-1}[\mathcal{E}'(k_x, k_y)]. \tag{1.36}$$

Notice from the simulated data that the phase of the original (Figure 1.13b) and reconstructed (Figure 1.20b) samples are not identical. An identical match of phase at this point of the holographic reconstruction process is not to be expected because the recovered phase of the object will be computationally bound in the range of $-\pi$ to π (or for other algorithms, from $-\pi/2$ to $\pi/2$). Although it is not the case in the given simulation, the recovered phase can be wrapped in order to reach a phase beyond this range. Two dimensional phase unwrapping algorithms would then need be used in order to recover an absolute phase as a function of position in the recovered object.[26] When the phase difference (or the number of wrapped cycles) across an object matches that across the original object, phase recovery is successful.

Once the phase of the object is recovered (and unwrapped if necessary), we can take advantage of (1.23) in order to solve for the sample depth. To do this, we must know the relative index of refraction between the sample and surrounding medium. Then, by using the relative phase difference between that of the sample and a reference point outside of

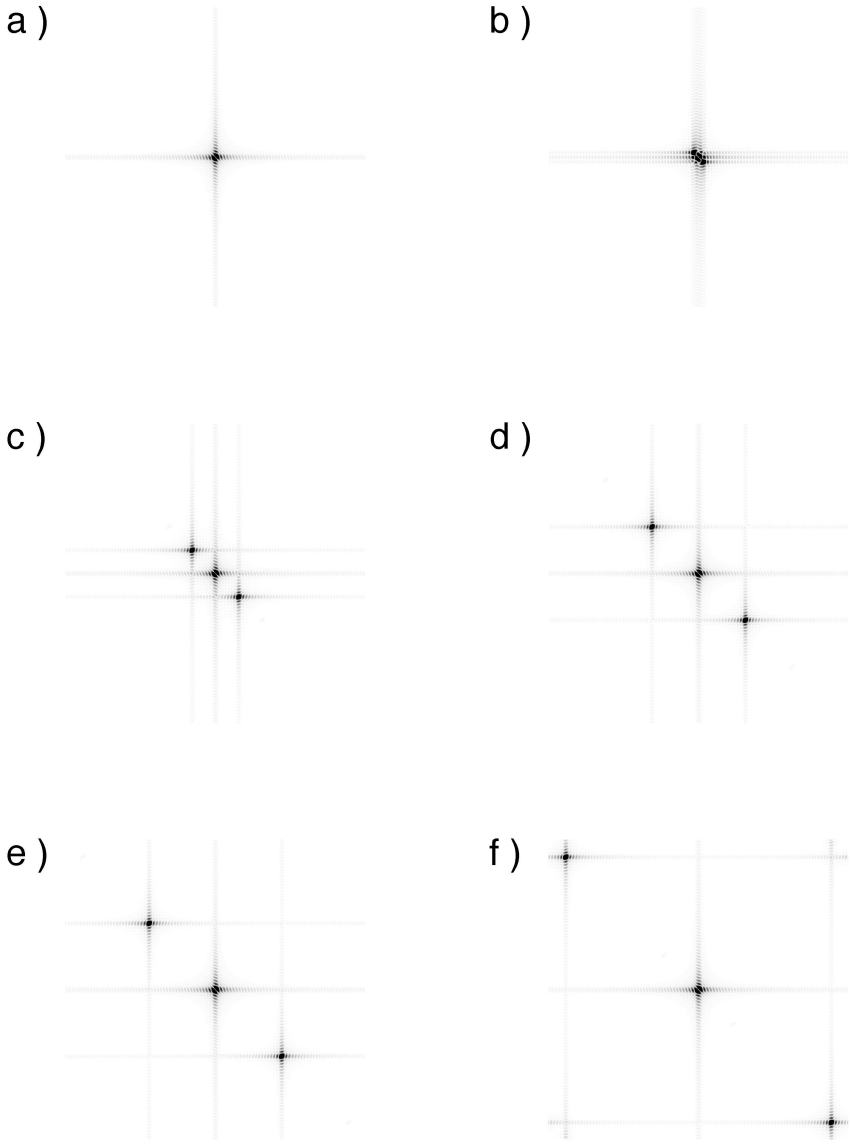

FIGURE 1.19: Dependence of the separation of twin frequency spectra (images) on the carrier frequency imparted by the reference field is demonstrated. a) For normal incidence, the twin frequency spectra are neither resolved from each other nor from the DC spectrum. b - e) Increasing the angle of incidence of the reference beam increases the separation of the twin frequency spectra from each other and the DC spectrum. f) Too large of an incident angle results in too great of a separation between the twin frequency spectra, pushing them out of the field of view and causing them to wrap to their opposite corners.

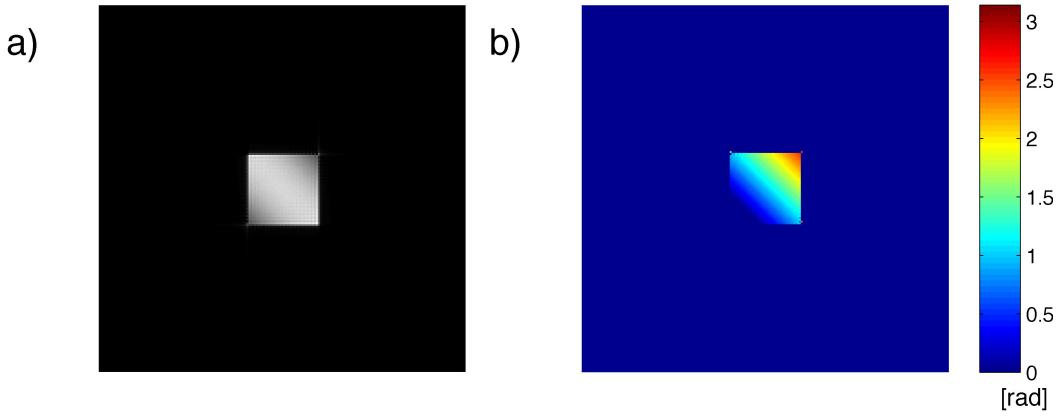

FIGURE 1.20: The inverse Fourier transform of (Figure 1.17) results in a single reconstructed hologram of the sample. The twin image is effectively removed. a) Amplitude and b) phase of a single reconstructed hologram.

the sample, $\Delta\Phi(x, y)$, we can solve (1.23) for the depth of sample[18,27,28]

$$d(x, y) = \Delta\Phi(x, y)\frac{\lambda}{2\pi n(x, y)}. \tag{1.37}$$

Assuming the sample used in the simulation is etched glass with an index of refraction of 1.5, a 3D reconstruction is generated (Figure 1.21). Notice that the resolution of this reconstruction is subwavelength ($\lambda = 533$ nm for the simulation). This is because the reconstructed phase is continuous, and by definition gives resolution to parts of a wavelength.[18,27,28] The resolution achieved via quantitative phase imaging is subwavelength and limited only by the continuum of the reconstructed phase and choice of reference phase.

1.2.2 Digital Fourier Holographic Microscopy

We now consider the application of collecting the hologram of an object at its Fourier plane—digital Fourier holographic microscopy (DFHM). This is accomplished experimentally by moving the camera from an image plane to a Fourier plane. As opposed to DHM, the reconstructed phase from a given pixel in the Fourier plane will no longer directly correlate to the physicality of the sample, as the entirety of the sample's spatial distribution is mapped to the Fourier plane via a point spread function. Having already established

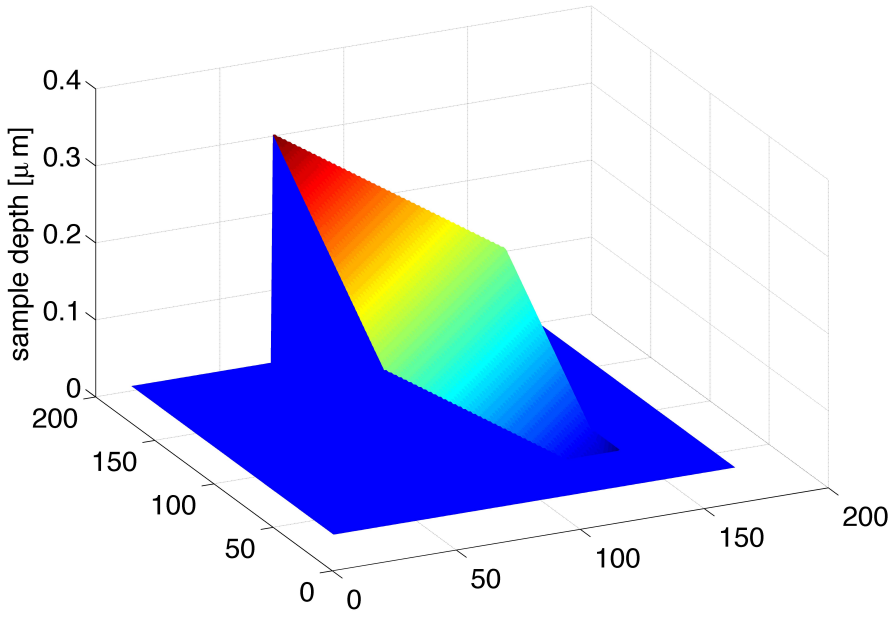

FIGURE 1.21: A 3D surface plot of the sample used in the simulation, assuming it to be etched glass.

digital holographic principles in the simpler context of DHM, we now transition towards describing the more complex DFHM system. While this incarnation of digital holography may be more complex by choosing to work directly in the Fourier plane, we will find that there are clear advantages to this method of imaging and that the additional labor involved is well worth the reward.

The digital signal collected at the conjugate Fourier plane can then be put through an inverse Fourier transform in order to recreate a hologram in the image plane. As described in the previous section, in order to take the inverse Fourier transform of the image collected at the conjugate Fourier plane, we require information of both the amplitude and phase of the scattered field at the imaging plane (Figure 1.13).

Recovery of Phase Information

The CCD captures an intensity based image, such that no phase information is available. Digital Fourier holographic microscopy can be employed in order to recover the required phase information needed for image reconstruction via the inverse Fourier transform. This method recovers phase information via the interference pattern resulting at the plane of the CCD due to the mixing of the scattered field with a reference field.

In the case of Fourier holography, the sample intensity is in actuality the Fourier transform of the sample (Figure 1.22). In this section, when referring to the "sample field"

or "scattered field" we are in fact referring to the Fourier transform. In order to differentiate between the sample fields in holographic microscopy versus Fourier holographic microscopy, the Fourier transform of the sample field and intensity will now be defined respectively as

$$\vec{f}(x,y) = f(x,y)e^{i\Phi_f(x,y)} \tag{1.38}$$

and

$$F(x,y) = \vec{f^*}(x,y)\vec{f}(x,y) = |f|^2, \tag{1.39}$$

where $f(x,y)$ represents the amplitude and $\Phi_f(x,y)$ the phase of the Fourier transform of the sample field.

Experimentally, the Fourier transform of the sample is created via an optical Fourier transform. In this section, the figures shown will be based on a computational simulation of the Fourier holographic process.

Similar to the methodology described in subsection 1.2.1, in order to recover phase information from the sample via Fourier holography, three images are collected at the conjugate Fourier plane via a CCD. The first image collected is the intensity of the scattered field, $F(x,y)$ (Figure 1.22), from the sample only. The second is again the intensity of the reference field, $R(x,y)$ (Figure 1.23). The reference field and intensity will be defined as in (1.25) and (1.27), respectively. The third image is the intensity image of the hologram, $H(x,y)$ (Figure 1.24), due to the interference pattern between the scattered and reference fields. All three of these intensities are collected at a conjugate Fourier plane for Fourier holography.

Following the same math as outlined previously, the superposition of the sample and reference fields at the CCD results in the combined hologram field,

$$\vec{h}(x,y) = f(x,y)e^{i\Phi_f(x,y)} + r(x,y)e^{i\Phi_r(x,y)}, \tag{1.40}$$

which is measured by the CCD as an intensity (Figure 1.24). We determine the measured intensity by taking the complex square of the hologram field,

$$\begin{aligned} H &= |fe^{i\Phi_f} + re^{i\Phi_r}|^2 \\ &= (f^*e^{-i\Phi_f} + r^*e^{-i\Phi_r})(fe^{i\Phi_f} + re^{i\Phi_r}) \\ &= |f|^2 + |r|^2 + f^*re^{i(\Phi_r - \Phi_s)} + fr^*e^{-i(\Phi_r - \Phi_f)}, \end{aligned} \tag{1.41}$$

again suppressing the $x-$ and $y-$dependencies. Assuming the amplitudes of both the sample and reference fields are both real, their amplitudes are their own complex conjugates. Applying the identity for the cosine function (1.30) again, we can simplify the measured intensity of the hologram as measured by the CCD as

$$H = |f|^2 + |r|^2 + 2fr\cos\Phi, \tag{1.42}$$

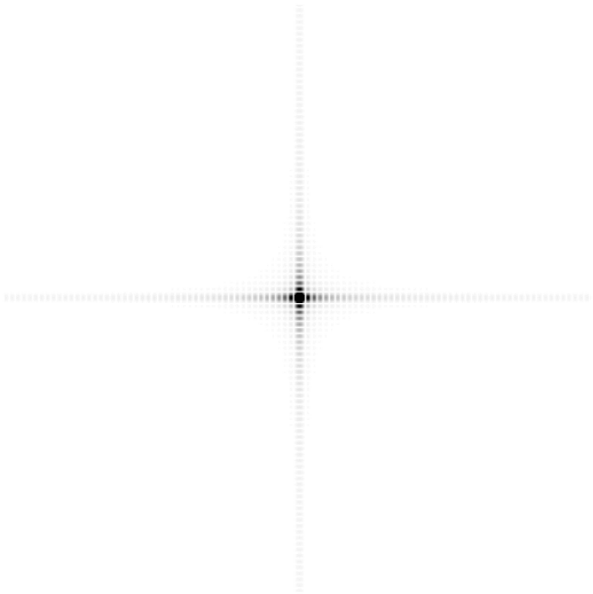

FIGURE 1.22: The Fourier transform of the sample from (Figure 1.13), collected at the CCD.

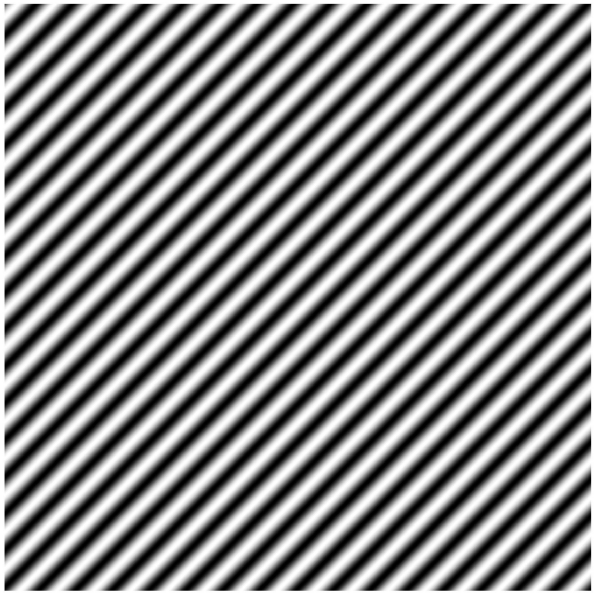

FIGURE 1.23: The phase of the reference beam alone, collected at the CCD. The image given here is used as an example of the phase of the reference field across the CCD due to the angle of incidence. The incident angle used in the actual simulation was greater, resulting in a frequency some 50 times greater than that seen in this image—and therefore not visually perceptible in the figure.

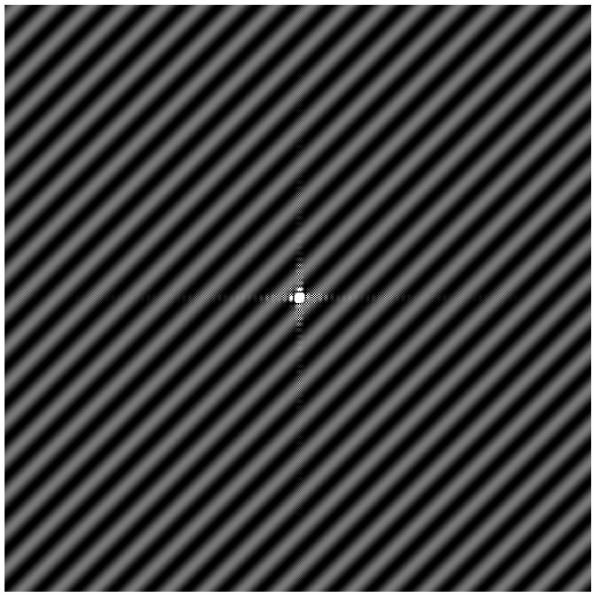

FIGURE 1.24: An image of the interference pattern between the sample's Fourier transform and reference beam, (1.33), collected at the Fourier plane. As with (Figure 1.23), the image given here is used as an example since the resulting fringes of the reference field are not visually perceptible in the applied simulation. Heterodyne amplification ($R(x, y) > F(x, y)$) is used experimentally in order to boost the sample signal via the cross term from (1.42). The sample field should therefore be nearly imperceptible in this figure. Although still faint here, the sample field in this figure has been boosted by a multiplicative factor and the color scale has been manipulated in order to bring out the features of the sample field for the sake of visualization.

with the hologram's phase defined as

$$\Phi = \Phi_r - \Phi_f. \tag{1.43}$$

Similar to (1.29), the first two terms of (1.41) are the intensities of the sample and reference fields. The cross-term comes from the later two terms, again creating "twin images" upon taking the inverse Fourier transform of (1.42). Again, it is critical that the angle of incidence of the reference beam be such that it clearly resolves the twin images from each other and the DC component upon undergoing an inverse Fourier transform (Figure 1.25). As in the holographic reconstruction process, two mirrored, twin images are reconstructed via Fourier holography from this cross term via an inverse Fourier transform (Figure 1.26). One of the two twin images can then be isolated for further analysis.

Again, subtracting the measured intensities (1.39) and (1.27) from (1.31) recovers the phase information for the hologram

$$\begin{aligned}\mathcal{E}(k_x, k_y) &= |f|^2 + |r|^2 + 2fr\cos\Phi - |f|^2 - |r|^2 \\ &= 2fr\cos\Phi.\end{aligned} \tag{1.44}$$

To this point, we have assumed an $x - y$ coordinate system based upon the pixels of the CCD. Since the hologram in Fourier holography is captured at the conjugate Fourier plane, it is actually a function of spatial frequencies k_x and k_y and is explicitly stated as such from here on, where $k_x = 2\pi x/\lambda$ and $k_y = 2\pi y/\lambda$. Computationally, $\mathcal{E}(k_x, k_y)$ will have its amplitude and phase encoded in its real and imaginary terms upon undergoing an inverse Fourier transform, respectively.

As (1.44) is the Fourier transform of scattered light from the sample plane, its inverse Fourier transform will now return a hologram of the sample plane,

$$E(x, y) = \mathcal{F}^{-1}[\mathcal{E}(k_x, k_y)], \tag{1.45}$$

which will be a complex array with both amplitude and phase encoded in its real and imaginary parts, respectively. Upon taking the inverse Fourier transform to generate (1.45), one of the twin images is cropped and centered via heterodyne filtering. This method of isolating a single twin image is the same as described in the previous section (section 1.2.1). The cropped twin image is passed through a low-pass filter in order to remove high spatial frequencies from cropped edges that would result upon undergoing a Fourier transform. The heterodyne filtered Fourier transform of a single twin image is then ready for further image processing.

The simulated data for the phase of the original (Figure 1.13) and reconstructed (Figure 1.26) samples are again not identical. The recovered phase will again be bound in the range of $-\pi$ to π and phase wrapping is again a possibility in order to account for greater phase differences beyond this range.

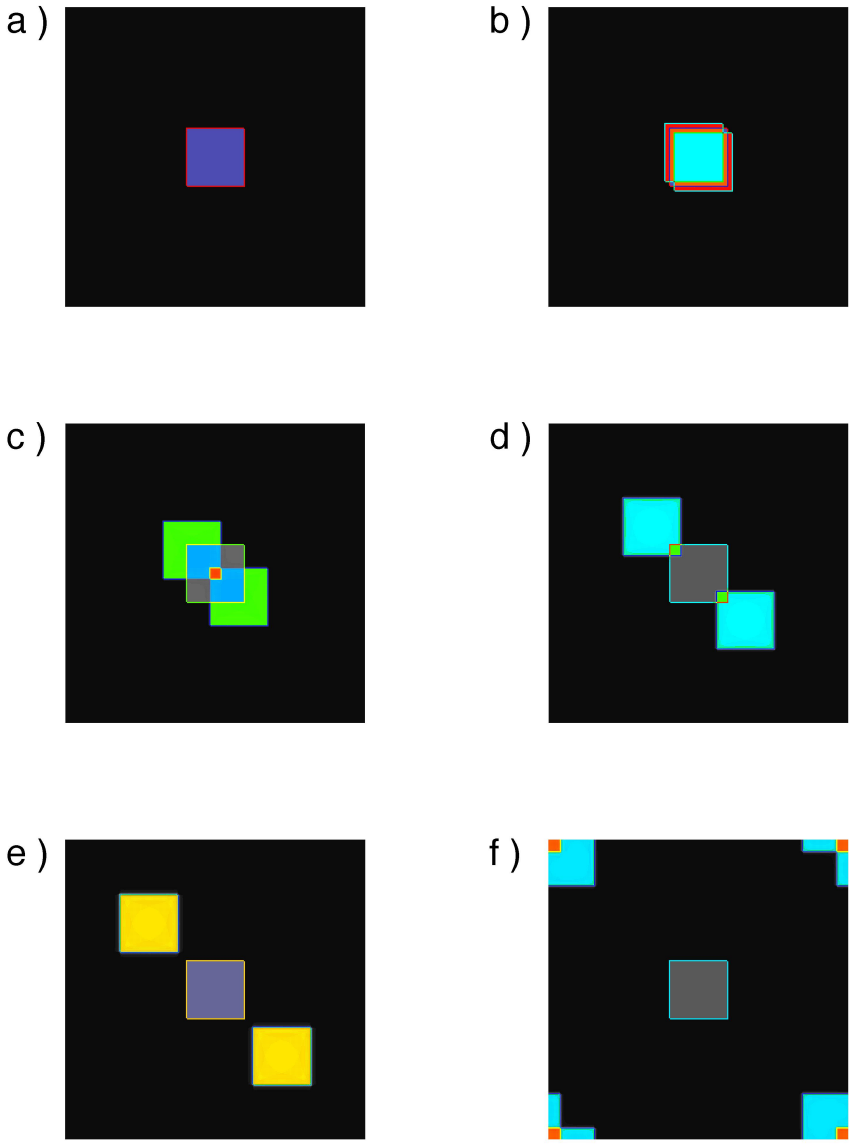

FIGURE 1.25: The "twin images" are offset from the central DC component as a result of the carrier frequency incorporated by the reference field. Figures a - f show the increased offset with increased θ_{ref}. As previously seen, too small of a θ_{ref} will not resolve the "twin images" from the DC component, whereas too large of a θ_{ref} will cause the reconstructed "twin images" to wrap around the spatial frequency plane. Upon an appropriate reconstruction (e), one of the two twin images can be isolated for further analysis.

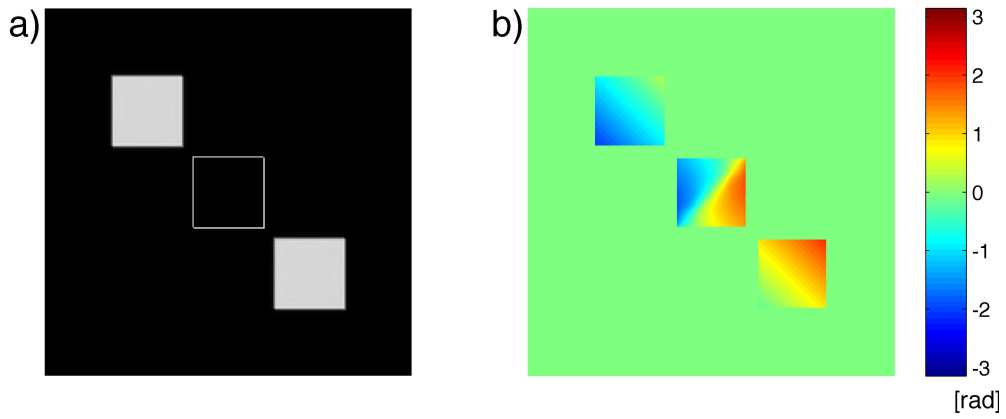

FIGURE 1.26: a) Amplitude and b) phase of the recovered sample via the inverse Fourier transform of (1.45), (Figure 1.24). The "twin images" are offset from the central DC component as a result of the carrier frequency incorporated by the reference field. From this reconstruction, one of the two twin images can be isolated for further analysis.

Image Reconstruction & Numerical Refocusing

The twin images resulting from the last inverse Fourier transform (Figure 1.26) will actually project to focal planes away from the plane of the hologram. Notice in (Figure 1.26) that the upper left twin image has a positive phase, while that of the lower right twin image is negative by the same magnitude. The occurrence of positive and negative phases in the twin images as a result of a spatial Fourier transform stems from the same mechanism from which a temporal Fourier transform results in positive and negative values in frequency space.

For a fixed wavelength and constant speed of light, a difference in phase translates physically to a difference in path lengths. Physically, this is analogous to the upper left twin image in (Figure 1.26) having propagated further in space beyond the plane of the DC reconstruction. The negative phase of the lower right twin image would by analogy have come into focus before the plane of reconstruction.

Although the twin images determined via the simulation have phases of opposite sign, they both are still in focus in the image. In an optical Fourier transform however, one twin image will come to a focus behind the plane of the hologram—the optical Fourier transform lies exactly one focal length behind the lens, as does the optical inverse Fourier transform. The other twin image will come into focus in front of the hologram plane by the same distance. In traditional holography, where photographic film was used to encode the amplitude and phase information, a second reference beam was then needed in order to reconstruct the images from the film. The resulting twin image reconstructed downstream from the film was a real image, whereas that falling upstream of the film was a virtual image.

That both the amplitude and phase are encoded in the resulting holographic image (1.45) is of fundamental importance to digital holography—we can vary the phase as a function of axial depth in order to numerically refocus the holographic image to the plane of one of the twin images. In addition, as the plane of reconstruction is varied, incrementally approaching the plane of focus and then moving beyond it, we can reconstruct a 3-D image of the sample.[18,29]

Numerical reconstruction can be explained starting with the Rayleigh-Sommerfield Solution to the Huygen's-Kirchoff Principle

$$E(\vec{\rho}, z) = \frac{-ik}{2\pi} \int\int E(\vec{\rho}_o, 0) \frac{e^{ikR}}{R} \cos\theta d^2\rho_o, \tag{1.46}$$

where $E(\vec{\rho}_o, 0)$ represents the incident field at it originating depth $z = 0$ and $E(\vec{\rho}, z)$ represents the field downstream at a reconstructed depth z.[20,30,31] The $x-$ and $y-$dependence has been grouped into the vector $\vec{\rho}_o$ at the sample plane ($z = 0$) and $\vec{\rho}$ at some nonzero depth in the corresponding $z-$plane. This geometry is demonstrated in (Figure 1.27). This notation is used to simplify the the mathematics in this section, where we ultimately need take a Taylor series for R in terms of the transverse $x-$ and $y-$coordinates. Since

both of the $x-$ and $y-$ transverse coordinates maintain radial symmetry in the $x-y$ plane, it is a simpler notation to combine them into a single radial component, $\vec{\rho}$ for the sake of the following mathematics. Using typical notation in holography texts,

$$\rho = \sqrt{x^2 + y^2} \tag{1.47}$$

at some $z-$depth of propagation. Similarly, in the sample plane

$$\rho_o = \sqrt{\xi^2 + \eta^2}, \tag{1.48}$$

where we let ξ and η represent the $x-$ and $y-$ coordinates in the sample plane.

We are reminded in (1.46) that this is a two-dimensional integral over the sample plane via the $d^2\rho_o$ factor. Aside from $E(\vec{\rho}_o, 0)$ and $E(\vec{\rho}, z)$, the remaining terms in (1.46) are those of the "impulse response",

$$H(\vec{\rho}, z) = \frac{-ik}{2\pi} \frac{e^{ikR}}{R} \cos\theta. \tag{1.49}$$

By Huygen's Principle, the incident field, $E(\vec{\rho}_o, 0)$ can be divided into infinitesimal units, each acting as an individual point, or secondary, source.[32] Observation of the field downstream is then the result of the interference between the waves from each of these secondary sources. Integrating over the $x-y-$plane then is equivalent to summing over each of these infinitesimal, outwardly propagating waves in order to reconstruct the resulting field downstream at depth z. Each secondary source is then a point source with an outgoing spherical wave, such that in (1.49) the factor $\frac{e^{ikR}}{R}$ represents the propagation of a spherical wave. In addition, the $\cos\theta$ term in (1.49) accounts for the direction of propagation from each secondary source and the remaining coefficient $\frac{-ik}{2\pi}$ accounts for the time variation and phase of the wave at the $z-$ plane in comparison to that of the incident, $z = 0$ plane.

Applying the Paraxial (or small angle) approximations

$$\cos\theta \to 1 \tag{1.50}$$

and

$$R \to z \tag{1.51}$$

to the impulse response (1.49), we are able to relax the R and θ dependence of the function. However, the latter approximation is not valid when applied to the exponential term. Instead, we must apply a Taylor Series for R.[31] Based on the geometry of (Figure 1.27) and the Pythagorean Theorem, R can be defined as

$$\begin{aligned} R &= \sqrt{z^2 + (\rho - \rho_o)^2} \\ &= z\left[1 + \left(\frac{\rho - \rho_o}{z}\right)^2\right]^{1/2}. \end{aligned} \tag{1.52}$$

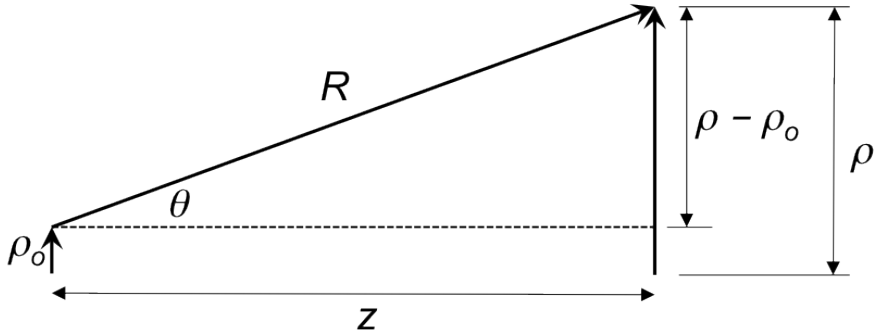

FIGURE 1.27: The secondary source is located in the incident plane at a location ρ_o from center and is propagated along R to the point of observation ρ from center in the $z-$plane. The reader is reminded of the definitions of ρ and ρ_o as defined by (1.47) and (1.48), respectively.

When $\rho - \rho_o << z$, we can use the Binomial series for $|x| < 1$

$$(1+x)^{\alpha} = \sum_{n=0}^{\infty} \frac{\alpha(\alpha-1)...(\alpha-n+1)}{n!} x^n, \tag{1.53}$$

such that

$$\left[1 + \left(\frac{\rho - \rho_o}{z}\right)^2\right]^{1/2} \approx 1 + \frac{1}{2}\left(\frac{\rho - \rho_o}{z}\right)^2, \tag{1.54}$$

keeping only the zeroth and first order terms. With this approximation, (1.52) can be reduced to a simpler $z-$dependence[31]

$$\begin{aligned} R &\approx z\left[1 + \frac{(\rho - \rho_o)^2}{2z^2}\right] \\ &\approx z + \frac{(\rho - \rho_o)^2}{2z}. \end{aligned} \tag{1.55}$$

Making approximation (1.55) within the exponential term of the impulse response (1.49), along with those from the Paraxial approximation, (1.50) and (1.51), we can then approximate the impulse response as[31]

$$H(\vec{\rho}, z) = \frac{-ik}{2\pi z} e^{ik\left[z + \frac{(\rho-\rho_o)^2}{2z}\right]}, \tag{1.56}$$

thereby simplifying the Rayleigh-Sommerfield Solution to the Huygen's-Kirchoff Principle (1.46) to

$$E(\vec{\rho}, z) = \frac{-ik}{2\pi z} \int\int E(\vec{\rho}_o, 0) e^{ik\left[z + \frac{(\rho-\rho_o)^2}{2z}\right]} d^2\rho_o. \tag{1.57}$$

This equation can be further simplified by multiplying through the $(\rho - \rho_o)^2$ terms within the exponential and separating the ρ and z terms outside of the integral, giving

$$E(\vec{\rho}, z) = \frac{-ik}{2\pi z} e^{ikz} e^{ik\frac{\rho^2}{2z}} \int\int E(\vec{\rho}_o, 0) e^{-\frac{ik}{z}\rho\cdot\rho_o} e^{ik\frac{\rho_o^2}{2z}} d^2\rho_o. \tag{1.58}$$

If we now make the notation changes $\rho^2 = x^2 + y^2$ and $\rho_o^2 = \xi^2 + \eta^2$ in the propagated and originating planes, respectively, (1.58) becomes

$$E(x, y, z) = \frac{-ik}{2\pi z} e^{ikz} e^{ik\frac{(x^2+y^2)}{2z}} \int\int \left[E(\xi, \eta, 0) e^{ik\frac{(\xi^2+\eta^2)}{2z}} \right] e^{-\frac{ik}{z}(x\xi+y\eta)} d\xi d\eta. \tag{1.59}$$

By the definition of the Fourier transform, the integral within (1.59) is the 2-D Fourier transform of the term in brackets—the field at the originating plane multiplied by a quadratic phase factor.[31] We can now express the propagation term by the factors prior to the integral

$$H(x, y, z) = \frac{-ik}{2\pi z} e^{ikz} e^{ik\frac{(x^2+y^2)}{2z}}. \tag{1.60}$$

All together, (1.59) can be interpreted as a convolution of the incident field and propagation term in order to determine the reconstructed wave downstream from its originating plane,

$$E(x, y, z) = [H(x, y, z) \otimes E(\xi, \eta, 0)]. \tag{1.61}$$

By the Convolution Theorem of Fourier Theory, the Fourier transform of a convolution is equivalent to the product of the Fourier transforms of the individual functions being convolved[20]

$$\mathcal{F}[H(x, y, z) \otimes E(\xi, \eta, 0)] = \mathcal{H}(k_x, k_y, z)\mathcal{E}(k_x, k_y, 0), \tag{1.62}$$

where k_x and k_y represent the spatial frequencies in the $x - y-$plane,

$$\mathcal{H}(k_x, k_y, z) = \mathcal{F}[H(x, y, z)] \tag{1.63}$$

and

$$\mathcal{E}(k_x, k_y, 0) = \mathcal{F}[E(\xi, \eta, 0)]. \tag{1.64}$$

Employing the Convolution Theorem, (1.62), thereby eliminates the need for a convolution integral, (1.46), in favor of simply multiplying two Fourier transforms together. For the present application then, this process simplifies to

$$\mathcal{F}[E(x, y, z)] = \mathcal{H}(k_x, k_y, z)\mathcal{E}(k_x, k_y, 0), \tag{1.65}$$

such that the inverse Fourier transform of (1.65) returns the field at the desired image plane[20,31,33]

$$E(x, y, z) = \mathcal{F}^{-1}[\mathcal{H}(k_x, k_y, z)\mathcal{E}(k_x, k_y, 0)]. \tag{1.66}$$

Wanting to take advantage of the simplicity afforded by the Convolution Theorem (1.62), we now work towards taking the 2-D Fourier transform of (1.60)

$$\begin{aligned}\mathcal{H}(k_x,k_y,z) &= \mathcal{F}[H(x,y,z)] \\ &= \int\int \left[\frac{-ik}{2\pi z}e^{ikz}e^{ik\frac{(x^2+y^2)}{2z}}\right] e^{-i(k_x x+k_y y)}dxdy \\ &= \frac{-ik}{2\pi z}e^{ikz}\int\int e^{ik\frac{(x^2+y^2)}{2z}}e^{-i(k_x x+k_y y)}dxdy \\ &= \frac{-ik}{2\pi z}e^{ikz}\int\int e^{i\pi\frac{(x^2+y^2)}{\lambda z}}e^{-i(k_x x+k_y y)}dxdy, \end{aligned} \tag{1.67}$$

where the definition of the wave number, $k = 2\pi/\lambda$ was used in the last line.[31] Further, letting $a^2 = b^2 = 1/\lambda z$, (1.67) becomes

$$\mathcal{H}(k_x,k_y,z) = \frac{-ik}{2\pi z}e^{ikz}\int\int e^{i\pi(a^2x^2+b^2y^2)}e^{-i(k_x x+k_y y)}dxdy. \tag{1.68}$$

Using the solution of integrals of this form,

$$\mathcal{F}\left[e^{i\pi(a^2x^2+b^2y^2)}\right] = \frac{i}{|ab|}e^{-i\pi\left(\frac{k_x^2}{a^2}+\frac{k_y^2}{b^2}\right)}, \tag{1.69}$$

we can evaluate (1.68) as[31]

$$\mathcal{H}(k_x,k_y,z) = \frac{-ik}{2\pi z}e^{ikz}(i\lambda z)e^{-i\pi\lambda z(k_x^2+k_y^2)}. \tag{1.70}$$

The definition $k\lambda = 2\pi$ can be used to eliminate the factor of 2π in the equation, leading to the simplified solution[31]

$$\mathcal{H}(k_x,k_y,z) = e^{ikz}e^{-i\pi\lambda z(k_x^2+k_y^2)}. \tag{1.71}$$

Finally then, the scattered field can be determined at a subsequent $z-$plane by substituting (1.71) into (1.66)

$$E(x,y,z) = \mathcal{F}^{-1}[e^{ikz}e^{-i\pi\lambda z(k_x^2+k_y^2)}\mathcal{E}(k_x,k_y,0)]. \tag{1.72}$$

For the Fourier transform of a captured field, $\mathcal{E}(k_x,k_y,0)$, we can then numerically bring the desired image into focus by varying the depth of focus (z) within the Fourier transform of the propagation term (Figure 1.28).[29,31] This numerical reconstruction method can also be used for varying depths of focus approaching the focal plane of the image and beyond in order to reconstruct a 3-D reconstruction of an extended sample.[34,35]

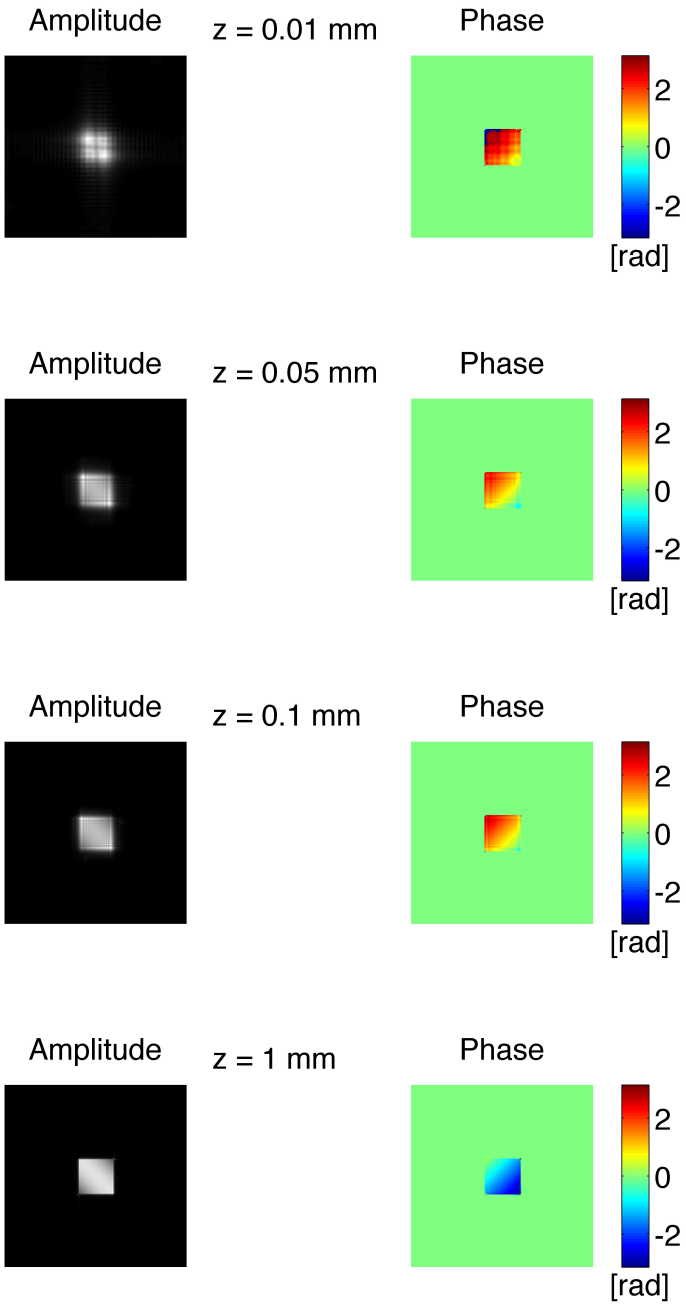

FIGURE 1.28: The numerically refocused amplitude and phase results for (Figure 1.20) at depths of $z = 0.01, 0.05, 0.1$, and $1mm$.

1.2.3 Optical Scatter Imaging

The optical scatter imaging (OSI) method outlined by Boustany, et. al.[9] maps the scattered light from a sample to a conjugate Fourier plane for spatial filtering. The filtered signal is then reimaged downstream via a CCD camera. The spatial filter employed uses a beam-block at the central focal spot of the field in order to filter out the background, DC signal (Figure 1.29). Use of the central beam-block alone is a form of dark-field imaging, where directly transmitted light is blocked from reaching the camera. In this fashion, only scattered light, which passes around the central beam-block is remapped to the imaging plane.[36] The OSI system goes beyond simply blocking ballistic photons, and uses a variable iris in order to create a maximum range of accepted scattered light.

The combination of the DC beam-block and outer iris comprises an annulus of variable outer radius for spatial filtering. The collection of and ratio between two different spatial filters leads to an index termed the optical scatter imaging ratio (OSIR),

$$OSIR = \frac{\int_{\phi=0}^{2\pi} \int_{\theta_{block}}^{\theta_{max}} F(\theta,\phi) sin\theta d\theta d\phi}{\int_{\phi=0}^{2\pi} \int_{\theta_{block}}^{\theta_{min}} F(\theta,\phi) sin\theta d\theta d\phi}, \tag{1.73}$$

where $F(\theta,\phi)$ represents the scattering function, or intensity distribution of scattered light, as a function of the scattering θ and azimuthal ϕ angles. The scattering angle is measured between the direction of propagation of incident light and the direction of scattered light.[1,2,9]

Numerically, or computationally, (1.73) reduces to a simple pixel-by-pixel ratio between images,

$$OSIR(x,y) = \frac{HNA(x,y)}{LNA(x,y)}, \tag{1.74}$$

where $HNA(x,y)$ and $LNA(x,y)$ stand for high- and low-numerical aperture images, referring to the images collected via the larger and smaller annuli, respectively. Pixels are represented in the camera plane via the cordinates (x,y). As the HNA filter includes the range of the LNA spatial filter, the OSIR will always fall in the range $OSIR \geq 1$. In Boustany's initial report on OSI, angles of $\theta_{block} = 2^o$, $\theta_{min} = 10^o$ and $\theta_{max} = 67^o$ were used.[9]

Based on Mie theory, the OSIR has been shown to be an effective measure of particle size in polystyrene microspheres suspended in water. This proof-of-principle sizing of known particles translates to the ability to make claims with respect to the sizing of subcellular components, namely mitochondria.[9,37,38] In both the mitochondrial and microsphere applications, Boustany uses Mie theory in order to generate a continuous OSIR curve as determined by the scattering parameter,

$$x = \frac{\pi a n_{med}}{\lambda} \tag{1.75}$$

and relative index of refraction between the scattering particle and medium,

$$n_{rel} = \frac{n_{particle}}{n_{medium}}, \tag{1.76}$$

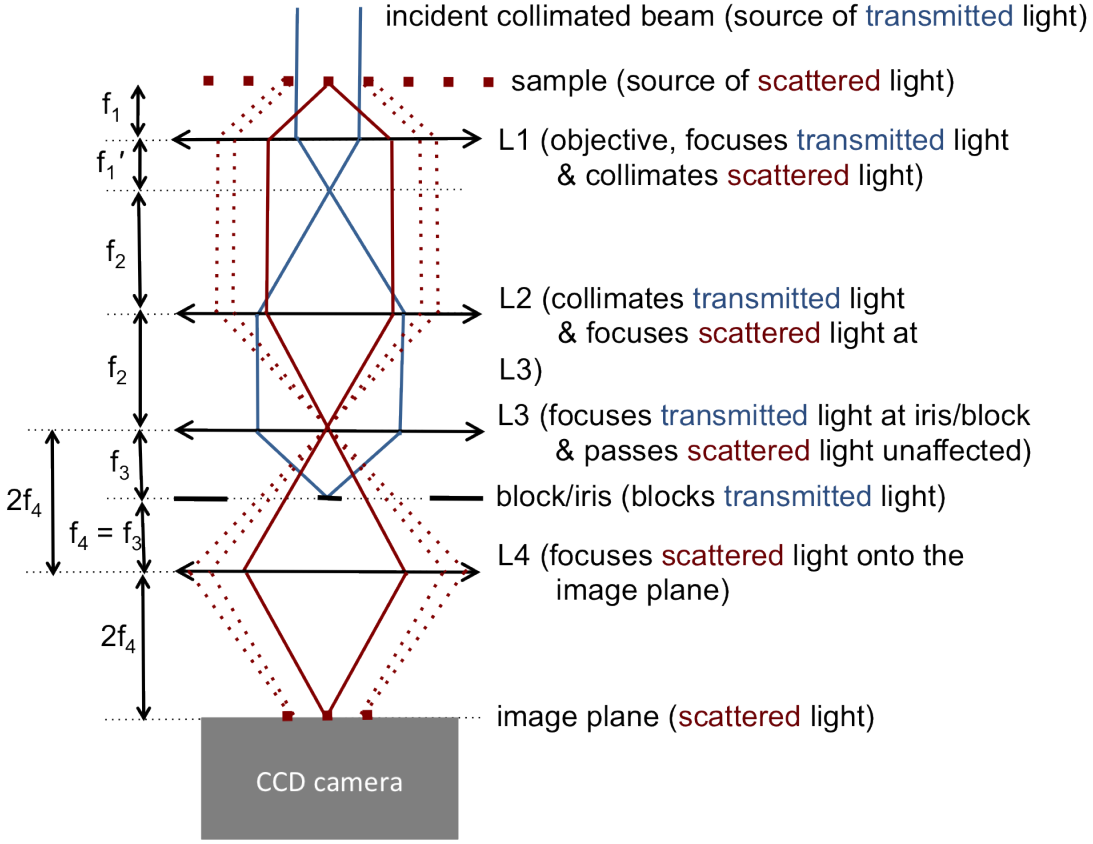

FIGURE 1.29: A schematic of Boustany's OSI system is recreated here in order to map the optical paths of scattered versus ballistic photons as a means of isolating scattered light for OSI.[9]

where a represents the particle diameter, λ is the wavelength of incident light, and n_{part} and n_{med} represent the indicies of refraction of the particle and medium, respectively.[1,2,9] Using an appropriate set of HNA and LNA spatial filters, the OSIR curve will fall off smoothly as it transitions from smaller to larger particle diameters and can therefore be used as a single "look-up function" for determining particle size.

Examples of scattered fields from two different particle sizes are given, along with a demonstration of the geometry employed in HNA and LNA filtering in the conjugate Fourier plane (Figures 1.30 and 1.31). Note the changes in the angular distribution of the scattered fields between these two particles. This characteristic difference between scattered fields is fundamental to the ability to use OSI in order to determine particle sizes. The scattered field of a given particle is unique to it and its family of identical particles. In order to identify a particle's size would require matching its scattered function to one from a database of unique scattering functions of known particles. Instead, the ratio of the two filtered images makes use of those unique scattered fields in order to generate a "look-up" function that can be used to determine particle sizing based upon a single data point, the OSIR.

Using the parameters outlined by Boustany in her initial paper outlining the OSI system, a recreation of the predictive curves for polystyrene microspheres (Figure 1.32) and mitochondria (Figure 1.33) are given. These OSIR curves were generated using Mie theory, and accurately match those reported in her work.[4,9] As can be seen, the high numerical aperture of her system allows for a dynamic range of OSIR values over particle diameters up to roughly $2\mu m$. This was arranged by design, as mitochondria in their normal state are typically on the scale of $0.5 - 1.0\mu m$. Whereas upon swelling at the onset of apoptosis, they can swell up to $\sim 2\mu m$. Above the $2\mu m$ diameter, the OSIR of mitochondria will be ~ 1, such that precise sizing would not be possible, however the goal is only to see swelling up to the range of $2\mu m$, such that this predictive curve is sufficient for the experimental design.

The two parameters (1.75) and (1.76) are typically multiplied together as arguments of the Bessel functions used in determining the solution to the scattered field using Mie theory.[1,2,4] As a result, the relative index of refraction scales the frequency between oscillations in the resulting Bessel function. When the particle and medium index of refraction are similar, $n_{rel} \sim 1$, the lowest frequency of oscillation is achieved in the Bessel function. When there is a distinct disparity between the particle and medium indicies of refraction, scattering is accentuated and the product of these two arguments results in an increased frequency of oscillation of the Bessel functions.

The presence of these oscillations is exemplified via the OSIR curves (Figures 1.32 and 1.33). We see no oscillatory characteristics (or bumps) in the curve for mitochondira since $n_{rel,mit} = 1.06$ (Figure 1.33), whereas the polystyrene microspheres in water have a larger $n_{rel,ps} = 1.20$ such that a bump in its OSIR curve is found around a $3\mu m$ diameter (Figure 1.32). Boustany's OSI work was not only able to experimentally match the drop-off of the OSIR curve for increasing polystyrene microsphere diameters, but was also able

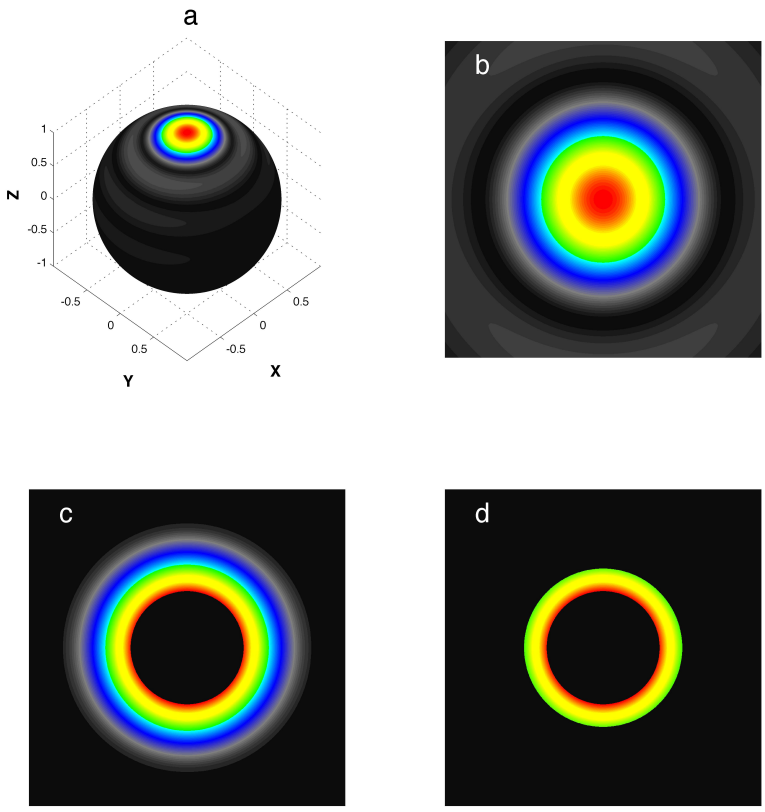

FIGURE 1.30: The resulting scattered field from a $1\mu m$ diameter polystyrene microsphere in water, given unpolarized incident light at $\lambda = 532nm$. The scattered field is a) mapped onto a unit sphere, b) projected onto a plane in the forward direction, and then spatially filtered by a c) high numerical aperture and d) low numerical aperture annuli. Note that these annuli displayed (c and d) are merely demonstrative and do not correspond to those used in Boustany's OSI system.

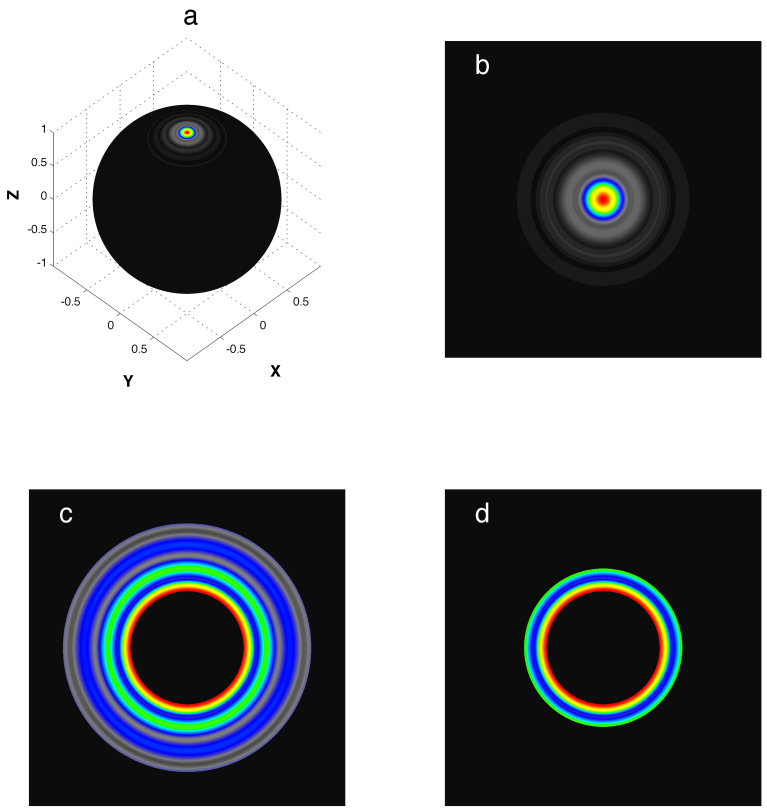

FIGURE 1.31: The resulting scattered field from a $4\mu m$ diameter polystyrene microsphere in water, given unpolarized incident light at $\lambda = 532nm$. The scattered field is a) mapped onto a unit sphere, b) projected onto a plane in the forward direction, and then spatially filtered by a c) high numerical aperture and d) low numerical aperture annuli. Note that these annuli displayed (c and d) are merely demonstrative and do not correspond to those used in Boustany's OSI system.

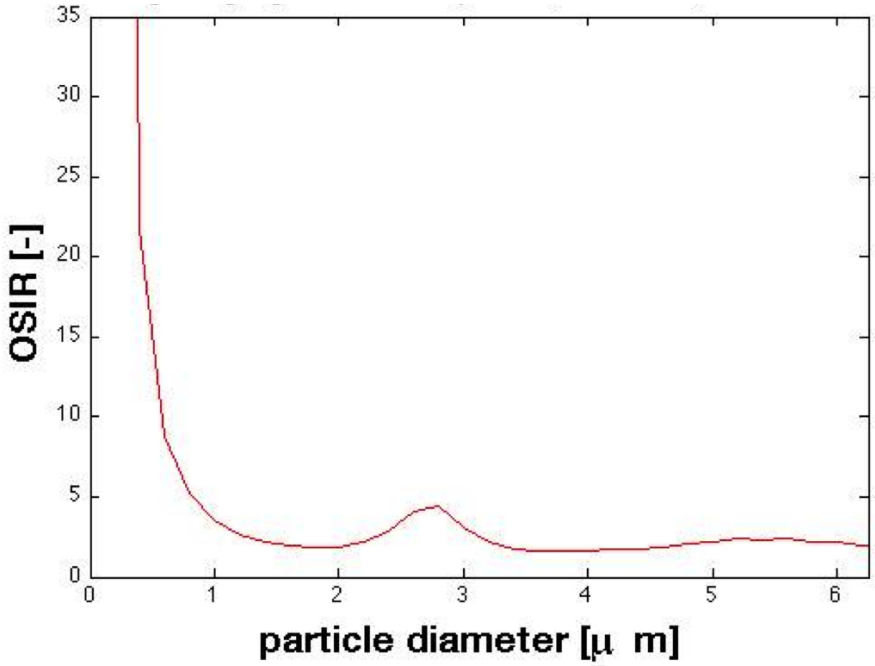

FIGURE 1.32: The OSIR falls off with increased particle diameter for polystyrene microspheres. This serves as a predictive curve for polystyrene microsphere particle sizing. This is a recreation of the same curve given by Boustany, et. al., using Mie theory and the given parameters of the OSI system outlined in her work.[4,9]

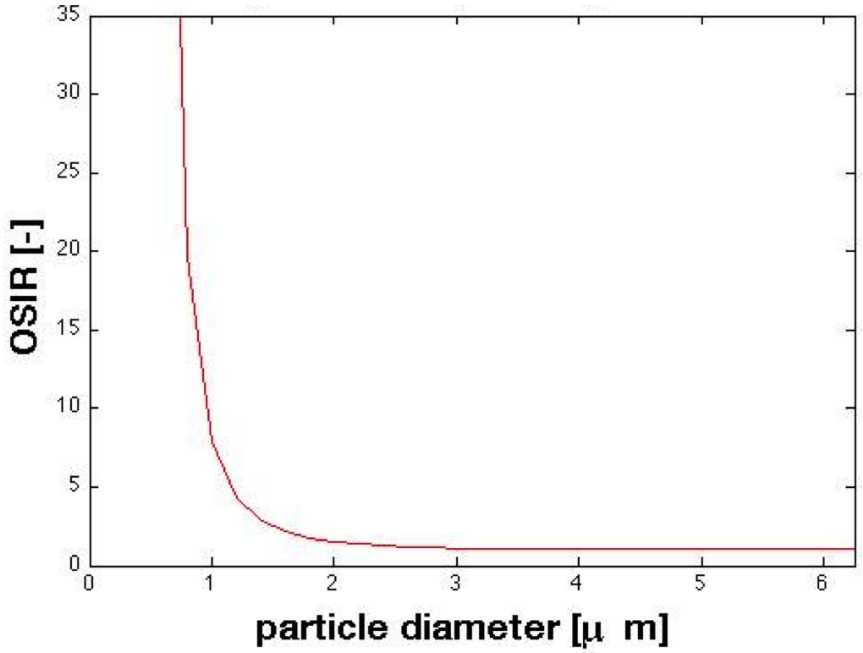

FIGURE 1.33: The OSIR falls off with increased particle diameter for mitochondria. This serves as a predictive curve for polystyrene microsphere particle sizing. This is a recreation of the same curve given by Boustany, et. al., using Mie theory and the given parameters of the OSI system outlined in her work.[4,9]

to pick out this bump in the OSIR curve as well.[9]

Newer generations of the OSI system constructed by Boustany and her group have included the use of a digital micromirror device in the conjugate Fourier plane.[39] Such a device allows for greater accuracy in creating the spatial filter, as well as other spatial filter geometries due to the fine resolution and flexibility permitted via electric tuning of the device. Since this is a mirrored device, the filtered light is then reflected off-axis to a camera-lens system for image capture, as opposed to the previous in-line arrangement of the system. The use of the micromirror device still requires a series of images be captured in order to determine the OSIR (1.74) because the varied digital spatial filters are still changed sequentially. Since the filtering is done upstream from the camera, one image corresponds to one set of static data. In order to gain additional data would require the acquisition of additional images.

When imaging dynamic systems, which is the case for cellular targets, there is no guarantee that the target will remain static between image acquisitions. Variation in the sample between collection of HNA and LNA images can lead to artifacts and variations in the OSIR. A better approach would only require a single data acquisition that could be spatially filtered by countless variations during post-processing.

The DFHM system outlined in the previous section and described physically in greater detail later in this work uses a 4-f system of lenses in order to map the Fourier

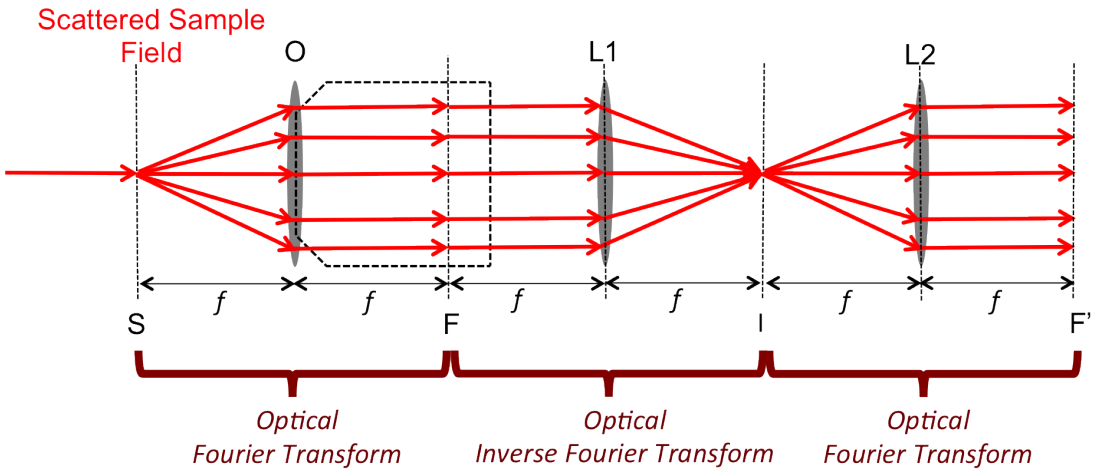

FIGURE 1.34: A diagram illustrating the geometry between the scattered field of a particle originating in the sample plane (S) and its resulting optical Fourier transform in the Fourier plane (F). The Fourier plane lies within the housing of the microscope objective, and needs to be remapped to a conjugate Fourier plane (F') via a 4-f optical system.

transform of the scattered field (Figure 1.34), which lies within the housing of the objective lens, directly to the conjugate Fourier plane. A 4-f optical system is measured in length from the sample to image planes to be equal to the four focal lengths of the two lenses (front and back focal lengths from two lenses). The OSI systems constructed by Boustany do not use a 4-f system, and as such the field mapped to the conjugate Fourier plane is not a true Fourier transform of the sample.[9,40] Instead of using spatial frequencies, or angle of scattering in the Fourier plane, to guide spatial filtering in their OSI system, Boustany's group uses simple geometric optics in order to map the angles of acceptance at the plane of their spatial filter (Figure 1.35).

As an alternative to physically spatially filtering the scattered light at the conjugate Fourier plane, spatial filtering can be done digitally by moving the CCD upstream to the conjugate Fourier plane (Figure 1.36). This method is advantageous in that a single image captured via the physical spatial filtering method are unique to the specific spatial filter employed at the conjugate Fourier plane prior to imaging with the CCD. However, imaging the Fourier transform at the conjugate Fourier plane directly allows a single image, or sample, to be used with countless variations of the digital spatial filter applied. This makes for a more robust system. In addition, the alignment and calibration of physical spatial filters in the conjugate Fourier plane can be tenuous, whereas employing these filters digitally allows greater ease.

Again, in order to recreate an image of the sample we must take the inverse Fourier transform of the field reconstructed at the conjugate Fourier plane, implying that we require information of both the amplitude and phase of the scattered field (Figure 1.13). Boustany's foundational work in OSI was done in the simple transmission mode of a

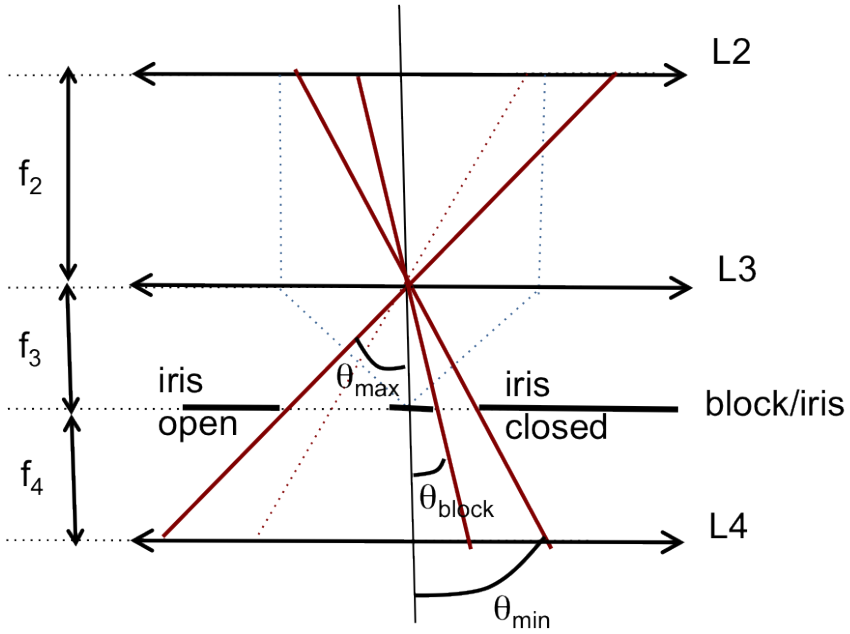

FIGURE 1.35: The geometry of Boustany's OSI system is demonstrated here as a means of determining the various angles of acceptance at the spatial filter.[9]

microscope and her use of Fourier and inverse Fourier transforms was achieved optically, thereby the collection of phase was not required.

The construction of a system capable of employing spatial filtering digitally at the conjugate Fourier plane with the goal of more robust and broad OSI applications does require phase information since it is the Fourier transform that is collected at the CCD. As a result, only the intensity of the signal is collected in a normal imaging mode, such that the true digital Fourier transform would not be achievable without the sample's true phase information. Without phase information, the use of an inverse Fourier transform, will not result in a true reconstructed image of the sample plane. The need to collect information of both the field's phase and amplitude in the conjugate Fourier plane leads naturally to the construction of the DFHM system.

Such a DFHM system employed for OSI has been reported by Seet, et al. briefly in the literature.[41] However, the full capabilities of the system were not explored beyond this cursory report. In their paper, Seet, et. al. collect the Fourier transforms of two different samples—one of $2\mu m$ spheres in solution and the other of $5\mu m$ spheres in solution. They then take the ratio of these two collected Fourier transforms in order to create a spatial filter that is then imposed on a third sample, which is a mixture of the two particles sizes together. Applying the spatial filter returns an image where the relative intensities of the two particle sizes are different, illustrating the ability to qualitatively distinguish between different size objects in their system. The use of "qualitative" is intentional here, in that the resulting relative intensities are not founded in, or tied to any predictive,

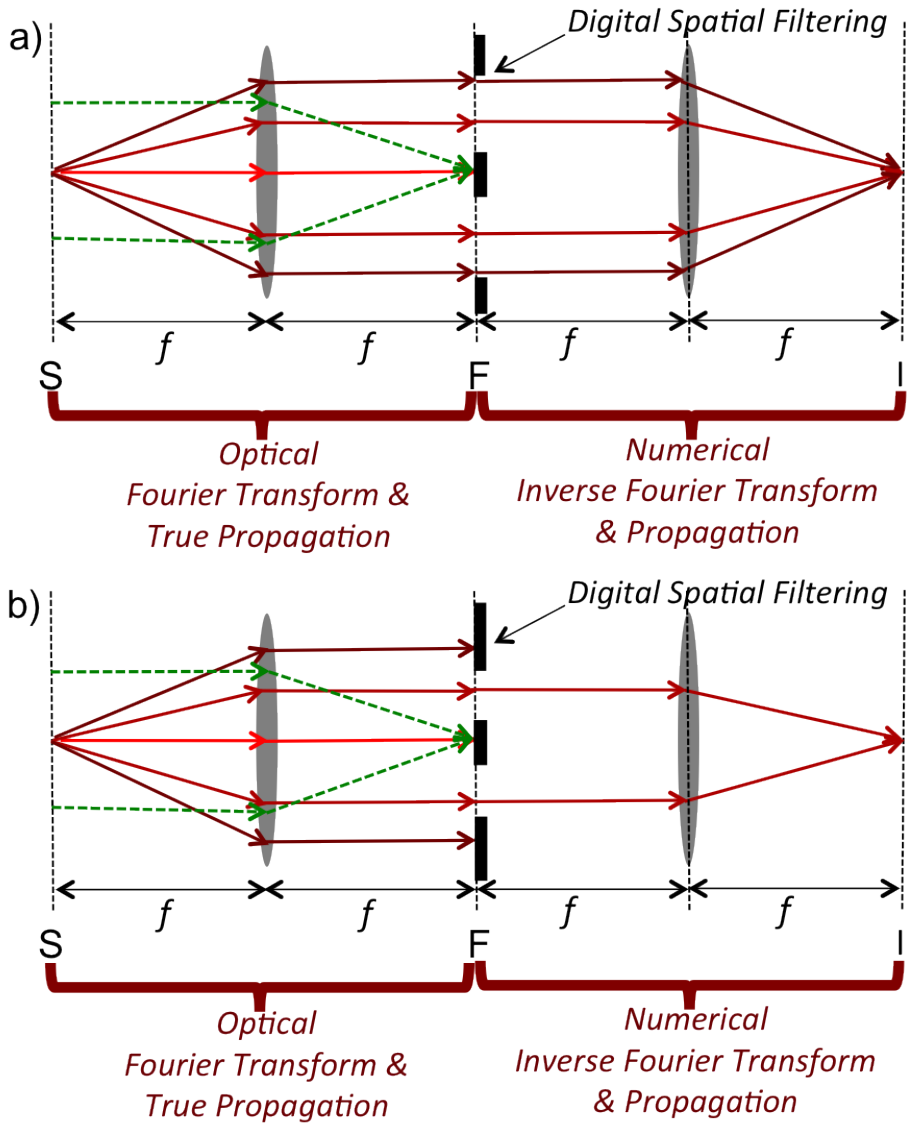

FIGURE 1.36: The geometry of the DFHM is displayed in reference to OSI. a) The geometry of the High Numerical Aperture (HNA) reconstructed image allows more light to be remapped to the image plane via a digital inverse Fourier transform. b) The geometry of the Low Numerical Aperture (LNA) reconstructed image further restricts the amount of light to be remapped to the image plane via a digital inverse Fourier transform. In both scenarios, the light truly propagates to the Fourier plane, while undergoing an optical Fourier transform along the way. Digital spatial filtering is applied during post processing, as well as the numerical propagation and digital inverse Fourier transforms of the HNA and LNA filtered light. In both cases, we see that the directly transmitted, DC signal (dashed, green) is blocked via a digitally applied central beam block.

theoretical model. Without such a reference scale by which to interpret the results, there is no measure of true particle size, only the presence of differing particle sizes.

A critique of that paper is that their work assumes empirical data *a posteriori*. Furthermore, their work can be grossly simplified as taking the image of an object and using that image to pick out the same object in later images. To use the system in this means requires that the user know the object they are looking for in order to distinguish it from other known objects. To use the system in this fashion would essentially require an infinite database of "look-up images".

A better approach would be to use Mie theory in conjunction with the DFHM as a theoretical, predictive source for particle sizing of unknown particle diameters. This is the same approach used by Boustany, and has proven to be more robust than the example given by Seet, et. al. A large component of this thesis works to use a DFHM system in order to create a more robust means of using OSI to determine particle sizes.

1.3. Photodynamic Therapy

Photodynamic therapy (PDT) operates on the principles included under the generic classifications of photobiology, photochemistry and photophysics.[14,42–45] This section will recount some of the main aspects of these principles, as applied towards understanding the functionality and application of PDT.

Unlike chemotherapy, the systemic treatment paradigm, photodynamic therapy (PDT) is a localized and selective therapy. Selectivity and localization of damage to cancerous tissues is two-fold in PDT, due to pharmokinetics and optical transport. Photodynamic therapy requires three ingredients—a photosensitizer (PS), light, and oxygen—in order to induce photochemical damage to tissues. Localization and selectivity achieved through PDT are both direct results of these three components. In short, the PS is administered to the patient and after an appropriate time interval, the targeted region of tissue is illuminated with light of an appropriate wavelength to be absorbed by the PS. Upon excitation by light of appropriate energy, the excited PS interacts with endogenous oxygen supplied by the vasculature in order to create reactive oxygen species (ROS). These ROS then interact with neighboring subcellular bodies, creating oxidative damage to the cells.[42–45]

A PS can be administered to the patient in a number of possible means, depending on the nature of the therapy and targeted cancer. In treating superficial cancers, such as melanoma, the PS can be diluted in a topical solution which can be applied directly to the surface of the targeted region, where the PS is then absorbed into the tissue. For larger or deeper tumors, the diluted PS can be injected directly into the target, where it will then diffuse and distribute throughout the region. Lastly, the PS can also be administered systemically in the case of internal cancers. In this last scenario, the PS can either be

administered orally or intravenously.

Already approved by the FDA for specific soft tissue cancers (i.e. esophageal cancer), PDT can be applied as a single modality or as a component of more aggressive treatment plans with multiple modalities.[45] In particular, in the case of limb sparing surgery, PDT can be used to clean the margins of resection in order to assure removal of all cancerous tissues. PDT has been investigated in treating bone metastases and is anticipated to be an effective palliative treatment of osteosarcoma, reducing pain and increasing quality of life for patients.[46–48,48–50,50]

1.3.1 Photophysics and Photochemistry

Once the PS is administered, an appropriate time interval needs to pass before light is incident on the targeted region. For obvious reasons, this time interval is commonly referred to as the drug-light interval. The drug-light interval employed in a given therapy will be dependent upon the PS used and means of administration, where the pharmokinetics resulting from these criteria will dictate the appropriate drug-light interval.

As mentioned, the selectivity achieved in PDT is a result of the components. Firstly, typical PS employed in PDT have greater affinities towards and greater retention times within cancerous versus healthy tissues. Greater affinity and retention of PS within cancerous tissues can be due to a number of factors, including greater cell proliferation in cancers, increased HDL and LDL receptors along the cell walls of cancer cells or lower pH within cancerous tissues.[45,51,52] Specific pharmokinetic explanations of affinities and retentions of a particular PS will be tied to the transport of that individual PS.

While a PS will have a greater affinity towards cancerous cells, in each of the means of administering the PS described above, some portion of the PS will be introduced to healthy tissues and cells. The appropriate drug-light interval for a given therapy will then account for time of delivering the PS to the targeted region along with the time necessary for the PS to clear healthy tissues. Due to the greater PS retention within cancerous cells over healthy cells, an appropriate drug-light interval will be long enough to allow the PS to clear healthy cells while being brief enough for the PS to remain localized in and therefore available for activation within the cancerous tissues.

The PDT process is only activated when the PS absorbs light of an appropriate energy, raising it to an excited state. For this reason, additional localization is achieved in PDT through the ability to administer light in targeted tissues, sparing healthy tissues from photochemical insult. Upon excitation, the PS interacts with endogenous oxygen to create ROS, which are ultimately responsible for cellular damage.

Absorbed photons transfer discrete energies to the PS, raising it from the singlet ground state (^1PS) to an excited singlet state ($^1PS^*$),

$$^1PS + h\nu \rightarrow ^1 PS^*, \tag{1.77}$$

where the product of Planck's constant (h) and the frequency of light absorbed (ν) represents the addition of energy via absorption. The PS may then fluoresce back to its ground

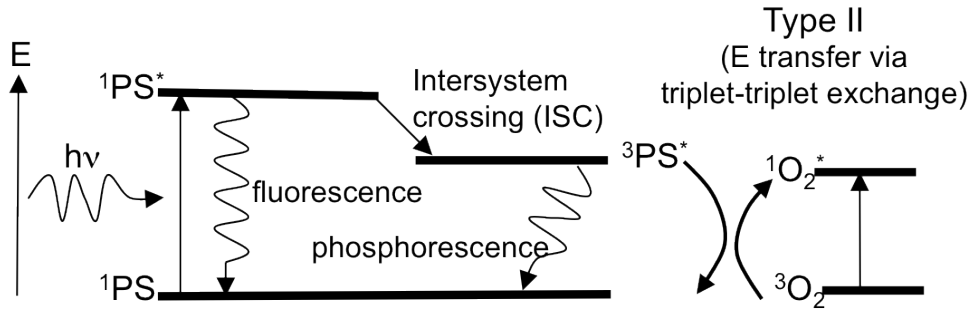

FIGURE 1.37: The process leading to the preferred Type II path to photodamage starts when the PS is excited by incident light of energy $h\nu$. The PS then relaxes via ISC to an excited triplet state, whereby it can transfer energy to molecular oxygen via a triplet-triplet electron transfer.

state. Preferably, the PS in its excited singlet state will transition to its excited triplet state ($^3PS^*$) through Intersystem Crossing (ISC),

$$^1PS^* \rightarrow ^3 PS^*. \tag{1.78}$$

Once in the excited triplet state, the photosensitizer may then decay back to its ground state through one of two mechanisms. The first of which, called the Type I pathway to photodamage in PDT, involves the PS in its excited triplet state interacting with the surroundings, thereby losing energy and creating free radicals. The resulting free radicals may then react with endogenous oxygen to form cytotoxic species such as OH^-.[14,36,51,53–55]

The Type II pathway to photodamage (Figure 1.37) in PDT entails a direct interaction between the PS in its excited triplet state and molecular oxygen in its triplet ground state ($^3O_2$) supplied by the vascular system. Such interactions, termed a Triplet-Triplet Exchange, can also cause the PS agent to decay back to its singlet ground state, in turn raising the molecular oxygen to an excited singlet state ($^1O_2^*$),

$$^3PS^* + ^3 O_2 \rightarrow ^1 PS + ^1 O_2^* \tag{1.79}$$

The excited singlet state of molecular oxygen (ROS) can then cause damage to its surroundings. Due to the long lifetime of the excited triplet oxygen, sufficient time is allowed for interactions with endogenous oxygen. For this reason, the Type II pathway is generally accepted as the most common pathway to photodamage in PDT.[14,36,42,43,51,53–55]

Each of the transitions outlined (Figure 1.37) will have an associated rate constant, the cumulative effect of which will determine the overall quantum yield of singlet oxygen, or efficiency of this process. Let k_{PS^*} represent the rate constant for the excitation of the PS to the excited singlet state with units of $(\mu gPSmL^{-1})(cm^2W^{-1})hr^{-1}$, k_{PO} the rate constant dictating the conversion of the PS to singlet oxygen with units of hr^{-1} and k_{P-}

the degredation, or photobleaching, of PS in units of $(cm^2W^{-1})hr^{-1}$. Based on these rate constants, we can represent the change in PS per unit time as

$$\frac{dC_{PS}}{dt} = \Big[(k_{PS^*} - k_{P-})I - k_{PO}\Big]C_{PS}, \tag{1.80}$$

where C_{PS} represents concentration of PS ($\mu gPSmL^{-1}$). The excitation and photobleaching of the PS will be light dependent, such that k_{PS^*} and k_{P-} must be multiplied by the irradiance, I in units Wcm^{-2}.

Assuming an initial concentration of PS, C_{PSo} at time $t_o = 0$, the concentration of PS can be determined as a function of time by solving the differential equation (1.80),

$$C_{PS}(t) = C_{PSo}e^{[(k_{PS^*}-k_{P-})I-k_{PO}]t}. \tag{1.81}$$

Ultimately, photobleaching of the PS works to reduce the concentration of PS as a function of time.

Given a broad spectral dependency of the irradiance ($I(\lambda)$), area of illumination (A), and extinction coefficient of the PS as a function of wavelength ($\varepsilon_{PS}(\lambda)$), we can determine the power absorbed by the PS as a function of time

$$P_{abs}(t) = \int I(\lambda)A\varepsilon_{PS}(\lambda)C_{PS}d\lambda. \tag{1.82}$$

This absorbed power can then be used to determine the equivalent power necessary to achieve the same result from a different source by equating the integral (1.82) for the new source to these results. For instance, assuming a 633 nm helium-neon laser with a negligible FWHM, the integral reduces to the product of the laser's power with the concentration and extinction coefficient of PS at that wavelength, such that

$$P_{633}(t)\varepsilon_{PS}(633)C_{PS} = \int I(\lambda)A\varepsilon_{PS}(\lambda)C_{PS}d\lambda. \tag{1.83}$$

Therefore, dividing both sides by the concentration and extinction coefficient of the PS at 633 nm, we can determine the equivalent power necessary to achieve the same results as found using a broader spectral source[56]

$$P_{633}(t) = \frac{\int I(\lambda)A\varepsilon_{PS}(\lambda)C_{PS}d\lambda}{\varepsilon_{PS}(633)C_{PS}}. \tag{1.84}$$

Assuming tissue densities similar to that of water ($1gmL^{-1}$), we can convert the concentration of PS from $\mu gPSmL^{-1}$ to $\mu gPSg^{-1}_{tissue}$. Via an integration of either (1.82) or (1.84) with respect to time, we can determine the total energy absorbed by the PS during the course of PDT

$$\begin{aligned} E_{abs} &= \int\int I(\lambda)A\varepsilon_{PS}(\lambda)C_{PS}d\lambda dt \\ &= \int I(\lambda)At_{exp}\varepsilon_{PS}(\lambda)C_{PS}d\lambda, \end{aligned} \tag{1.85}$$

where t_{exp} represents the total time of exposure. Lastly, if we then divide (1.85) by the energy per photon

$$E_\gamma = \frac{hc}{\lambda}, \tag{1.86}$$

where h is Planck's constant and c is the speed of light, it is possible to determine the photodynamic dose (D_{PDT}) as the number of photons absorbed by the PS per gram of tissue

$$D_{PDT} = \int I(\lambda) t_{exp} \frac{\lambda}{hc} A \varepsilon_{PS}(\lambda) C_{PS} d\lambda. \tag{1.87}$$

PDT dosages of $10^{17} - 10^{20}$ photons absorbed per gram of tissue are typically required in order to achieve sufficient photoactivation of cell death.[57]

Incorporating (1.20) into (1.87), we can associate the photodynamic dose with an achievable depth of induced death in tissues, z_D.[58] We begin by redefining the photodynamic dose in terms of a number of photons absorbed by the PS and converted to singlet oxygen

$$\begin{aligned} D_{PDT} &= \Phi \mu_{aPS} \frac{\lambda}{hc} \psi(z) \\ &= \Phi \mu_{aPS} \frac{\lambda}{hc} \psi_o k e^{-z_D/\delta}, \end{aligned} \tag{1.88}$$

where Φ defines the quantum efficiency of the generation of singlet oxygen, μ_{aPS} is the absorption coefficient of the PS at the given wavelength and the remainder of variables carry the definitions outlined in (section 1.1.2). Solving for z_D, we find

$$z_D = -\delta ln\left[\frac{D_{PDT}}{\Phi \mu_{aPS} \frac{\lambda}{hc} \psi_o k}\right]. \tag{1.89}$$

Of significant importance from this result, we find that while the depth of tissue death is linearly dependent upon the penetration depth, δ (1.19), it has a log-scale dependence on all other factors. While we have no control over the tissue properties which determine δ, we do have the ability to control the design of PDT protocol in order to achieve greater tissue death. For instance, we can choose an appropriate PS in order to increase μ_{aPS} and Φ. Similarly, we can control the applied fluence rate, ψ_o, for the incident light.[17]

Given the typical Type II pathway achieved via PDT, we will focus on the effects of the excited singlet oxygen ROS on its environment. Due to the intracellular lifetime of the excited singlet oxygen ROS ($\tau_\Delta = 3\ \mu s$) and its diffusion coefficient ($D \approx 2 - 4 \times 10^{-6} cm^2 s^{-1}$), the ROS will only be available for interaction and insult within a narrow region of space.[59] Starting with Fick's Law,[59,60]

$$\frac{N}{A\Delta t} = D \frac{N \backslash V}{\Delta x}, \tag{1.90}$$

where N is the number of ROS particles, A is the cross sectional area of interaction, and the volume (or region) of interaction is approximated by

$$V \approx A\Delta x \tag{1.91}$$

we can solve for the approximate diffusion length of the ROS

$$\Delta x \approx \sqrt{D\Delta t}. \tag{1.92}$$

Using the conservative value of $D \approx 4 \times 10^{-6} cm^2 s^{-1}$ as the diffusion constant for singlet oxygen in tissue, and permitting the singlet oxygen to travel for up to three lifetimes ($3\tau_\Delta \approx 9\ \mu s$), we find that upon excitation, the ROS will travel at most some

$$\Delta x \approx \sqrt{(2 \times 10^{-6} cm^2 s^{-1})(9 \times 10^{-6} s)} \approx 60nm \tag{1.93}$$

prior to extinction. Therefore, the diffusion length of the excited singlet oxygen ROS is some three orders of magnitude less than the size of a cell (tens of microns). Thereby, upon activation via PDT, the excited singlet oxygen ROS will only interact with and have damaging effects within the immediate cellular and subcellular environments. This narrow region of interaction is a third component to the localization of damage invoked through PDT.

While low concentrations of ROS in cells has been associated with increased cell proliferation, an excess of ROS can stress cells. The ROS primarliy target DNA, lipids and proteins within subcellular structures, thereby disrupting cellular function. Such disruptions can lead to growth arrest and senescence or ultimately cell death via apoptosis or necrosis.[61–65] Cancer cells are generally characterized by failure to undergo the normal process of apoptotic cell death and by increased metabolisms and proliferation rates. The goal of PDT is to increase the production of ROS—namely excited singlet oxygen via the Type II pathway—in order to counteract the increased proliferation rates within cancerous cells and their failure to undergo apoptosis.

1.3.2 A Quantum Mechanical Description of PDT

We will consider a basic quantum mechanical example of a generic photosensitizer (PS) interacting with molecular oxygen as part of the desired Type II pathway to photodamage achieved in PDT (1.3.1). Both the PS and molecular oxygen can be approximated as two-electron molecules. For example, molecular oxygen forms via the covalent bond between two oxygen atoms, each needing a pair of $2p$ electrons in order to fill the $2p$ shell.[63] This pair of shared $2p$ electrons will therefore be considered as those undergoing the transitions that follow during the PDT process. The same assumption will be made of the PS, considering that the exchange of energy between the PS and molecular oxygen comes in the form of electron exchange between a pair of two electron systems.

In quantum mechanics, we are concerned with eigenvalue problems where we can determine the given set of eigenstates corresponding to a given set of eigenvalues. The eigenstate of a system corresponds to the wavefunction of the system, or generically speaking, the state of the system. The eigenvalue corresponds to some physically measureable quantity, or characteristic of the system, such as its energy, spin or angular momentum.

As alluded to here, the characteristics of a quantum state can have spatial and spin dependencies, such that their corresponding wavefunctions must also incorporate spatial and spin states. Using the separation of variables, we can break the overall wavefunction, $\Psi(\vec{r}, m_s)$, into the product of the two functional dependencies,

$$\Psi(\vec{r}, m_s) = \Phi(\vec{r})\chi(m_s), \tag{1.94}$$

where $\vec{r}$ represents the three dimensional spatial dependence of the spatial wave function $\Phi(\vec{r})$ and m_s is the spin quantum number, representing the spin dependence of the spin wavefunction $\chi(m_s)$. In this context of atomic and molecular physics, the wavefunction represents the overall state of an electron. Since electrons are Fermions, their overall wavefunctions must be antisymmetric.

When looking specifically at the context of PDT, we are dealing with a system of two electron molecules. Therefore, the overall wavefunction (1.94) for both the PS and molecular oxygen must be modified to reflect a two electron system,

$$\Psi(\vec{r}_1, m_{s1}; \vec{r}_2, m_{s2}) = \Phi(\vec{r}_1, \vec{r}_2)\chi(m_{s1}, m_{s2}), \tag{1.95}$$

where the subscripts 1 and 2 represent the two separate electrons.

From the requirement for electrons to have antisymmetric wavefunctions follows the definition of the singlet and triplet states, which refer specifically to the spin wavefunction, $\chi(m_{s1}, m_{s2})$, of the two electron system. A combination of these two electrons in the spin state lead to a set of three possible symmetric wavefunctions,

$$\chi(m_{s1}, m_{s2}) = \begin{cases} \chi_{++} \\ \frac{1}{\sqrt{2}}(\chi_{+-} + \chi_{-+}) \\ \chi_{--} \end{cases} \tag{1.96}$$

where the $+$ and $-$ refer to the different combinations of spin up ($m_s = +\frac{1}{2}$) and spin down ($m_s = -\frac{1}{2}$) states, respectively. This state is specifically called the (spin) triplet state because there is a set three possible symmetric combinations for the two electron system. Similarly, there is only a single antisymmetric combination of spins,

$$\chi(m_{s1}, m_{s2}) = \frac{1}{\sqrt{2}}(\chi_{+-} - \chi_{-+}), \tag{1.97}$$

which is therefore referred to as the (spin) singlet state.[66]

One of the spin sates from (1.96) or (1.97) can therefore be applied directly within the overall two electron wavefunction (1.95) for either the PS or molecular oxygen. This leaves us to more thoroughly define the spatial state of the system.[66] Resolving the spatial wavefunction will be based upon the quantum mechanical rules for dealing with systems

of identical particles and the assumption that we can start from the model of the most simple of two electron systems—the helium atom. Under this premise, the spatial wave function can undergo a swap of electrons such that,

$$\Phi(\vec{r}_1, \vec{r}_2) = \frac{1}{\sqrt{2}}\Big[\psi_{100}(\vec{r}_1)\psi_{nlm}(\vec{r}_2) \pm \psi_{100}(\vec{r}_2)\psi_{nlm}(\vec{r}_1)\Big], \tag{1.98}$$

where the wavefunctions ψ_{100} and ψ_{nlm} refer to electrons in the ground and possible excited states, respectively. The two states $\psi_{100}(\vec{r}_1)\psi_{nlm}(\vec{r}_2)$ and $\psi_{100}(\vec{r}_2)\psi_{nlm}(\vec{r}_1)$ account for a change of state via exchange of identical particles—changing the configuration of the system by exchanging the states of two electrons translates to a change of state. However, the total spatial state (1.98) is the superposition of these two states, which can be gained either by the addition or subtraction of the two combinations. The addition of these two spatial states results in a symmetric spatial wave function. Conversely, the subtraction of the two states results in an antisymmetric spatial wave function.

Now that the symmetric and antisymmetric representations of the spatial and spin states are defined, we look to their possible combinations for the overall wavefunction of the two electron system.[66] Since the electron wavefunction must have overall antisymmetry, the antisymmetric spin singlet state (1.97) must pair with the symmetric spatial state (1.98), giving the overall antisymmetric singlet state,

$$\begin{aligned}\Psi_{singlet}(\vec{r}_1, m_{s1}; \vec{r}_2, m_{s2}) =& \frac{1}{\sqrt{2}}\Big[\psi_{100}(\vec{r}_1)\psi_{nlm}(\vec{r}_2) + \psi_{100}(\vec{r}_2)\psi_{nlm}(\vec{r}_1)\Big] \\ &\times \frac{1}{\sqrt{2}}(\chi_{+-} - \chi_{-+}).\end{aligned} \tag{1.99}$$

Similarly, the symmetric spin triplet (1.96) must pair to the antisymmetric spatial wavefunction (1.98), giving the overall antisymmetric triplet state,

$$\begin{aligned}\Psi_{triplet}(\vec{r}_1, m_{s1}; \vec{r}_2, m_{s2}) =& \frac{1}{\sqrt{2}}\Big[\psi_{100}(\vec{r}_1)\psi_{nlm}(\vec{r}_2) - \psi_{100}(\vec{r}_2)\psi_{nlm}(\vec{r}_1)\Big] \\ &\times \frac{1}{\sqrt{3}}\Big[\chi_{++} + \frac{1}{\sqrt{2}}(\chi_{+-} - \chi_{-+}) + \chi_{--}\Big].\end{aligned} \tag{1.100}$$

The system can be described in terms of the quantum numbers for orbital angular momentum (l), magnetic quantum number (m_l), spin angular momentum (s), and spin quantum number (m_s). In addition to the before mentioned quantum numbers comes the principle quantum number (n), which is associated with the energy of the electron orbital. Starting with the principle quantum number, which can take any nonzero, positive integer value ($n = 1, 2, 3, ...$), we are able to define the allowed values of the angular momentum and magnetic quantum number as follows:[67]

$$l = 0, 1, 2, ..., (n-1) \tag{1.101}$$

$$m_l = -l, -l+1, ..., 0, 1, 2, ..., +l. \tag{1.102}$$

In addition to the limitations placed on the possible states of angular momentum and the corresponding magnetic quantum numbers, there are quantum rules for the combining angular momenta. The reasons for adding angular momenta at the quantum level could entail the need to consider multiple particles within a system, or even the combination of different forms of angular momenta. Both of these scenarios will affect our quantum mechanical discussion of PDT. If we begin by defining a generic angular momentum term, j, two angular momenta (j_1 and j_2) can be added to reach the following permitted values:

$$j_{min} = |j_1 - j_2| \tag{1.103}$$

$$j_{max} = j_1 + j_2. \tag{1.104}$$

Based on these maximum and minimum values of total angular momenta,

$$j = |j_1 - j_2|, ..., j_1 + j_2 \tag{1.105}$$

is the range of acceptable total angular momenta values.[67] When dealing with the addition of angular momenta, the range of

$$m_j = -(j_1 + j_2), , ..., 0, ..., j_1 + j_2 \tag{1.106}$$

follows from (1.105) and (1.106).

These allowed values for the quantum numbers are based on the solution for the spatial wavefunction of the hydrogen atom in spherical coordinates by separating radial and angular dependencies

$$\Phi(r, \theta, \phi) = R(r)Y_l^{m_l}(\theta, \phi), \tag{1.107}$$

where $R(r)$ represents the radial wavefunction and $Y_l^{m_l}(\theta, \phi)$ the spherical harmonics. Of key importance is the orthonormality of these special functions. Stating the wavefunction in terms of the given quantum numbers via subscripts, Φ_{nlm_l}, taking the inner product of two such wavefunctions (or equivalently, integrating the product of the two wave functions over all space) returns

$$\langle \Phi_{n'l'm_l'} | \Phi_{nlm_l} \rangle = \delta_{nn'}\delta_{ll'}\delta_{m_l m_l'}, \tag{1.108}$$

where any given delta function takes the value of zero when the respective indices differ and unity when they are the same.[67]

As an example illustrating the principle of conservation of energy, since the quantum number n is tied to the energy of a state, the inner product of the final ($\Phi_{n'l'm_l'}$) and initial (Φ_{nlm_l}) states will be zero if $n' \neq n$, meaning the system cannot transition spontaneously and unperturbed between the two states. The result will be unity if $n' = n$, such that the transition between the two states does not violate the conservation of energy. The only way to change the energy of the system between the initial and final states is to operate on them by doing work on the system, or by letting the system itself do work. Since there is no operator acting on the energy of these functions, the energy of the system must remain the same between the final and initial states.

Similarly, the conservation of angular momentum is thus upheld in reference to the angular momentum quantum number l between the two states. A transition from Φ_{nlm_l} directly to $\Phi_{n'l'm_l'}$ is forbidden unless $l' = l$. This is of fundamental importance for the following discussion, as we shall see that the angular momentum of the PS goes from $l = 0$ to $l = 1$ during activation in PDT. This transition is however perfectly acceptable as the PS is being acted on by the incident light—by absorbing a photon (which carries an angular momentum of $l = 1$), the PS gains angular momentum in addition to energy. Later, this angular momentum will be transferred to molecular oxygen along with energy in order to elicit a phototoxic effect. Ultimately, when operating on one quantum state in order to cause it to transition to another quantum state, the operator acting on the system will invoke a set of selection rules as to which quantum transitions are allowed versus forbidden.

One further note should be made on the notation employed. The spin angular momentum (s) and spin quantum number (m_s) have been left out of the above conversation. However, as the name suggests, spin angular momentum is another form of angular momentum, or at least behaves quantum mechanically in the exact fashion as does angular momentum. The addition of spin angular momenta therefore abides the general rules for addition of angular momenta (1.105). The spin angular momentum of an electron is $s = \frac{1}{2}$, such that the associated spin quantum numbers are $m_s = \pm\frac{1}{2}$. Since both the PS and molecular oxygen of interest can each be considered two electron systems, their respective spin angular momenta can take values of $s = 0, 1$ via the rules for addition of angular momenta. Therefore, the spin quantum numbers for each of these individual molecules can take the values $m_s = 0, \pm 1$. The photon carries no spin angular momentum ($s = 0$, $m_s = 0$).

To begin our formal discussion of the quantum mechanical processes involved in PDT, we can use the addition of angular momenta in order to determine the state of each of the molecules using the condensed the notation

$$|\Psi\rangle_{molecule} = |l, s; m_l, m_s\rangle. \tag{1.109}$$

In this notation, the total state of the system is the product of the two molecular states

$$\begin{aligned} |\Psi\rangle_{system} &= |\Psi\rangle_{PS} \otimes |\Psi\rangle_O \\ &= |l, s; m_l, m_s\rangle_{PS} \otimes |l, s; m_l, m_s\rangle_O, \end{aligned} \tag{1.110}$$

where again PS and O refer to the photosensitizer and molecular oxygen, respectively.

Initially, both the PS and oxygen reside in their ground states—the PS in a spin singlet and the molecular oxygen a spin triplet (Figure 1.38a)—such that

$$|\Psi\rangle_i = |l = 0, s = 0; m_l = 0, m_s = 0\rangle_{PS} \otimes |l = 0, s = 1; m_l = 0, m_s = 0\rangle_O. \tag{1.111}$$

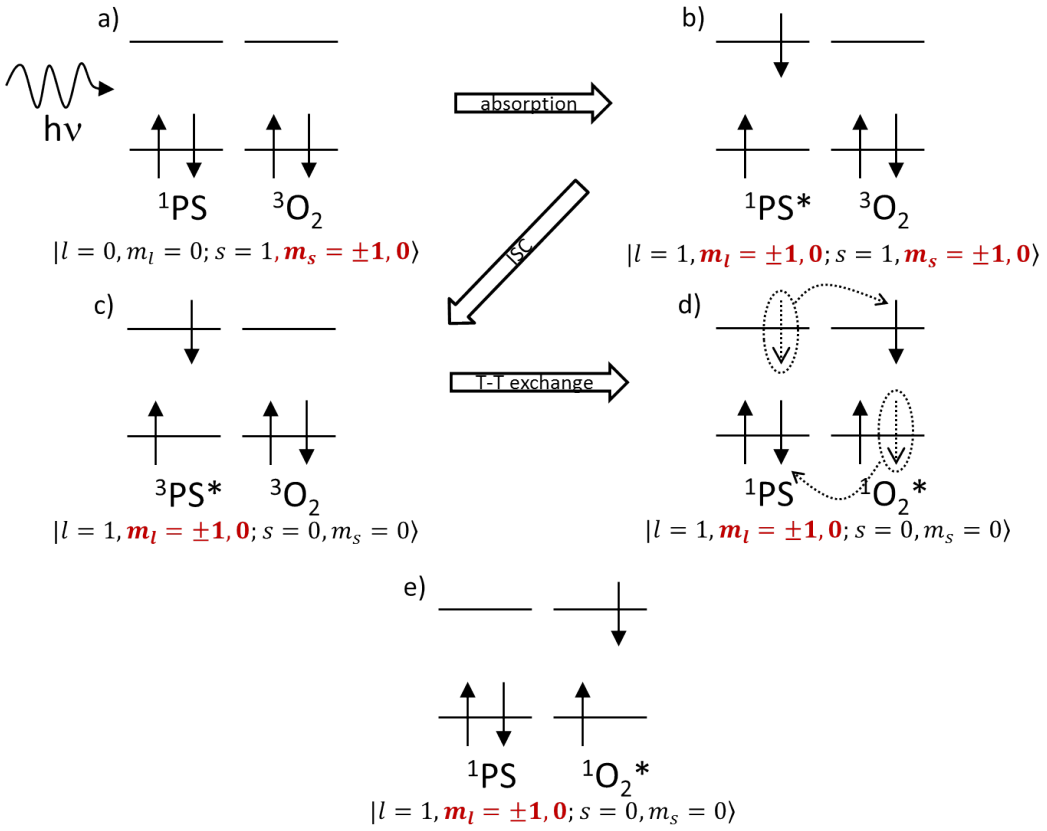

FIGURE 1.38: Energy level diagrams of the PDT process leading to the creation of singlet oxygen. a) The initial states of the PS and molecular oxygen. b) Transition of the PS to an excited spin singlet state via absorption. c) Transition of the PS to an excited spin triplet state via Intersystem Crossing. d) Triplet-Triplet electron exchange between the PS and molecular oxygen, leading to e) the final state of the system where the excited spin singlet state of oxygen is ready to create oxidative damage in surrounding organisms.

Again using the addition of angular momentum, this time between the two molecules, the overall initial state given in terms of the same quantum numbers becomes

$$|\Psi\rangle_i = |l=0, s=1; m_l=0, m_s=0, \pm1\rangle. \tag{1.112}$$

When the PS absorbs light of the appropriate wavelength, it transitions to an excited singlet state (Figure 1.38b). Since the photon carries a quantum angular momentum of $l=1$, this transition corresponds to an increase in orbital angular momentum of $\Delta l=+1$ within the PS. The state of molecular oxygen remains unchanged during this process.

Upon absorption, the system transitions to the state

$$|\Psi\rangle_{abs} = |l=1, s=0; m_l = 0, \pm 1, m_s = 0\rangle_{PS} \otimes |l=0, s=1; m_l = 0, m_s = 0\rangle_O, \tag{1.113}$$

where again the addition of angular momentum between molecules gives the overall state

$$|\Psi\rangle_{abs} = |l=1, s=1; m_l = 0, \pm 1, m_s = 0, \pm 1\rangle. \tag{1.114}$$

Once in the excited state, the PS can either transition back to its ground state via fluorescence, or undergo a nonradiative transition to a spin triplet state. The later process is desirable for the PDT process, allowing the PS in its excited triplet state to interact with molecular oxygen. The nonradiative process by which the PS moves from an excited spin singlet to an excited spin triplet state is known as Intersystem Crossing, whereby the spin of the excited electron is no longer paired to that of the electron in the ground state (Figure 1.38c).[44] Due to the conservation of spin angular momentum, the transition from a singlet to a triplet state is a quantum mechanically forbidden transition. However, Intersystem Crossing is made possible by spin-orbit coupling, where the orbital and spin angular momenta are combined to give possible total angular momenta given in (1.105). This nonradiative transition relies upon the overlap of the vibrational states of the initial and final states of the electron.[44,66–68] Again, molecular oxygen remains in its ground state during this process. Via Intersystem Crossing, the system transitions to the state

$$|\Psi\rangle_{ISC} = |l=1, s=1; m_l = 0, \pm 1, m_s = 0\rangle_{PS} \otimes |l=0, s=1; m_l = 0, m_s = 0\rangle_O. \tag{1.115}$$

The addition of angular momentum between molecules gives the possible states

$$\begin{aligned} |\Psi\rangle_{ISC} = &|l=1, s=0; m_l = 0, \pm 1, m_s = 0\rangle \\ &+ |l=1, s=1; m_l = 0, \pm 1, m_s = 0, \pm 1\rangle \\ &+ |l=1, s=2; m_l = 0, \pm 1, m_s = 0, \pm 1, \pm 2\rangle, \end{aligned} \tag{1.116}$$

where the states $s = 0, 1, 2$ are allowed along with their corresponding $-s \leq m_s \leq s$ values. Although the excited spin triplet state of the PS may phosphoresce back to its ground state, this state has a long-lived life time such that interaction with molecular oxygen becomes more likely.[59]

The PS in its excited triplet state interacts with the molecular oxygen in its ground state (spin triplet) via a Triplet-Triplet Exchange of electrons (Figure 1.38d). In this process, the excited electron of the PS transitions to the molecular oxygen and the electron with matching spin in the ground state of molecular oxygen transitions to the ground state

of the PS. Along with this swapping of electrons comes an exchange of energy, such that the PS returns to its ground (spin singlet) state and the molecular oxygen transitions to an excited (spin singlet) state (Figure 1.38e).[44,69,70] The Triplet-Triplet Exchange is also referred to as a Dexter Exchange, based upon the seminal work "A Theory of Sensitized Luminescence in Solids" written by D.L. Dexter, which thoroughly explains this process. While the focus of this section is to simply give a general description of the quantum states of the PS and molecular oxygen during the stages of PDT, the reader is referred to Dexter's work for a more rigorous and thorough description of the exchange.[69]

Continuing with the same quantum numbers, the corresponding wave function for the system becomes

$$|\Psi\rangle_{TT} = |l=0, s=0; m_l=0, m_s=0\rangle_{PS} \otimes |l=1, s=0; m_l=0, \pm 1, m_s=0\rangle_O. \tag{1.117}$$

The addition of angular momentum between molecules gives the state

$$|\Psi\rangle_{TT} = |l=1, s=0; m_l=0, \pm 1, m_s=0\rangle. \tag{1.118}$$

Given that the final state of this system must remain unchanged from that of (1.116) during this process, we can conclude that after the PS underwent Intersystem Crossing the system must have been in the first of those states listed in (1.116),

$$|\Psi\rangle_{ISC} = |l=1, s=0; m_l=0, \pm 1, m_s=0\rangle. \tag{1.119}$$

From this conclusion, it follows that after the PS undergoes Intersystem Crossing, the system must be described by the individual molecular states

$$|\Psi\rangle_{ISC} = |l=1, s=1; m_l=0, \pm 1, m_s=0\rangle_{PS} \otimes |l=0, s=1; m_l=0, m_s=0\rangle_O. \tag{1.120}$$

A summary of the states of the $PS - O_2$ system based upon the transitions and physical processes described would look as follows:

1. The PS and molecular oxygen begin in their ground states, the PS in a spin singlet and the molecular oxygen a spin triplet,

$$|\Psi\rangle_i = |l=0, s=0; m_l=0, m_s=0\rangle_{PS} \otimes |l=0, s=1; m_l=0, m_s=0\rangle_O. \tag{1.121}$$

2. Upon absorption of a photon, the PS is raised to an excited spin singlet state, while the molecular oxygen goes unaffected,

$$|\Psi\rangle_{abs} = |l=1, s=0; m_l=0, \pm 1, m_s=0\rangle_{PS} \otimes |l=0, s=1; m_l=0, m_s=0\rangle_O. \tag{1.122}$$

3. The PS undergoes a nonradiative transition from the excited spin singlet to an excited spin triplet via Intersystem Crossing, while the state of the molecular oxygen again remains unchanged in its spin triplet ground state,

$$|\Psi\rangle_{ISC} = |l = 1, s = 1; m_l = 0, \pm 1, m_s = 0\rangle_{PS} \otimes |l = 0, s = 1; m_l = 0, m_s = 0\rangle_O. \quad (1.123)$$

4. Finally, the molecular oxygen is raised from its ground spin triplet state to an excited spin singlet state as the PS simultaneously relaxes back from its excited spin triplet state to its spin singlet ground state,

$$|\Psi\rangle_{TT} = |l = 0, s = 0; m_l = 0, m_s = 0\rangle_{PS} \otimes |l = 1, s = 0; m_l = 0, \pm 1, m_s = 0\rangle_O. \quad (1.124)$$

Again, a summary of these processes and states is also depicted in (Figure 1.38), where the overall wavefunction of the system at each step is listed with the corresponding energy diagram.

Simply put, energy from the excitation light is absorbed by the PS. Following some internal transitions, the PS is then able to transfer the added energy to the molecular oxygen. The final state of the $PS - O_2$ system leaves the molecular oxygen in an excited state, ready to unleash oxidative stress on its immediate surroundings, ultimately causing photodamage as a result of PDT.[61,62,64,65]

1.3.3 5-Aminolevulinic Acid induced PDT

Applications of photodynamic therapy entail the introduction of an exogenous photosensitizing agent to the targeted tissue or tumor. Many PS, such as the industry standard PS Photofrin®, are excited at wavelengths near 400 nm in order to induce a phototoxic effect. However, light below 600 nm is strongly absorbed by hemoglobin (Figure 1.11).[12,45,71] As such, these PS are not effective beyond superficial applications as they are greatly attenuated and therefore deliver insufficient light toward the activation of deeply accumulated PS. Longer wavelengths generally have greater penetration depths within tissues until the absorption of the NIR and IR wavelengths due to water becomes appreciable (Figure 1.10).[13,72] However, due to the inverse relationship between the wavelength and energy of a photon, wavelengths above 900 nm do not have sufficient energies for the production of singlet oxygen.[45] This work looks at 5-aminolevulinic acid (ALA) mediated PDT, with illumination at either 633 nm or 636 nm, depending on the application.

Rapidly dividing cells, as is the case for cancer cells, generally results in an increased accumulation of PS administered for PDT. While the exact transport mechanisms attributing to greater accumulation of ALA in neoplastic over normal cells are not clear, it

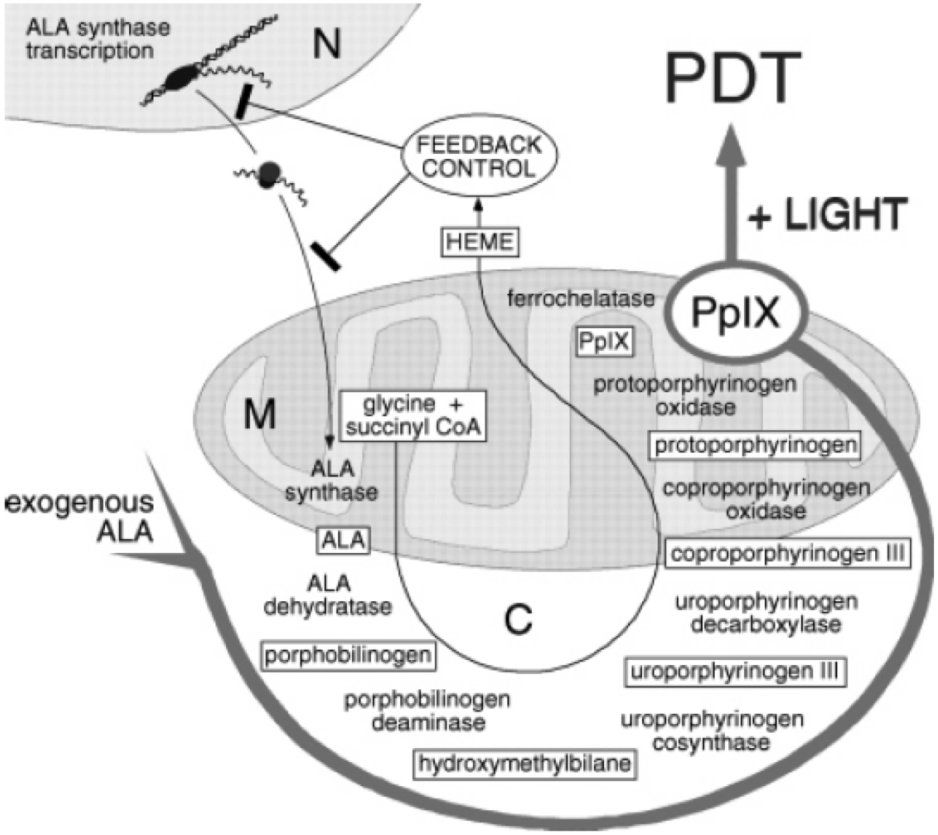

FIGURE 1.39: ALA is a precursor for PpIX in the heme production pathway. As illustrated in this figure, introduction of exogenous ALA leads to an over expression of PpIX. Once endogenous iron is quenched by binding with PpIX via ferrochelatase, excess PpIX remains ambient in the subcellular environment for the photoproduction of singlet oxygen. This figure is taken (with permission) from Figure 34.6 in Tayyaba Hasan's book chapter "Photodynamic therapy of cancer".[45]

has been suggested that transport of ALA is due to uptake by carrier systems related to the transport of β-amino acids, β-alanine and taurine, and γ-aminobutyric acid.[73] Additionally, the PEPT1 and PEPT2 transporters have also been associated with the transport of ALA.[74] Upon cellular uptake, ALA is converted to the photosensitizer protoporphyrin-IX (PpIX) via the heme pathway (Figure 1.39).[45,73,75] Exogenous ALA is administered in order to override the negative feedback control in this process due to haem, thereby increasing an accumulation of PpIX in ALA mediated PDT.[76] Furthermore, high porphobilinogen deminase (PBGD) and low ferrochelatase (FeC) activity along with low iron concentrations may also play a role in the decreased conversion of PpIX to haem in tumors, leading to higher concentrations of PpIX than in healthy tissues.[76–78] The resulting surplus of PpIX in the subcellular environment then stands ready for photoactivation and the ultimate production of singlet oxygen via PDT.

Production of PpIX occurs within the mitochondria–any photo-activated PpIX within the vicinity of the mitochondria that interacts with nearby oxygen would then create singlet oxygen in that region (1.93). Combined with the short diffusion length of singlet oxygen in intracellular media, it is anticipated that mitochondria will suffer significant oxidative damage via ALA-mediated PDT, thereby triggering apoptotic cell death.[79] Alternatively, PpIX activated away from mitochondria would then interact with oxygen in order to create general necrosis.

Beyond the activation of singlet oxygen follows a complex and intricate series of biochemical reactions that must be set into motion prior to the activation of apoptosis. Molecular activation and deactivation can be summarized in three basic types of physical processes, namely cleavage of, bonding of and conformal changes to the molecule. All of these changes are fundamentally related back to the electromagnetic structure of the molecule. These three effects cause physical changes to the molecule that can cause receptors to either be exposed or suppressed. Such changes to activation and binding sites within the molecule therefore render the molecule either active or inactive, as the situation dictates.

The onset of apoptosis via ALA-mediated PDT is a cascading process of biomolecular activation and deactivation (Figure 1.40). Already present throughout the cytosol are XIAP, caspase-9 and the apoptotic protease activating factor 1 (APAF1). Caspase-9 (an initiator caspase, with respect to the onset of apoptosis) binds with APAF1 in order to form (in part) an apoptosome. The apoptosome is responsible for the initiation of the executioner caspases-3 and -7, which also act to activate a third such caspase, caspase-6. All three of these executioner caspases are also present continuously throughout the cytosol. The executioner caspases are enzymes that serve the purpose of cutting proteins internally via their substrates. The cleavage of proteins (such as DNA) by these executioner caspases causes the cell to shut down its function and dismantle into small apoptotic bodies that can be cleared away. Due to the mechanistic nature by which a cell undergoes apoptotic cell death, apoptosis is also termed “programmed cell death”.

While the three executioner caspases are continually present within the cytosol, they lie dormant as inactive dimers until they are cleaved and become activated monomers. Caspases-3 and -7 must be cleaved and activated by the apoptosome. Upon activation, caspases-3 and -7 can cleave the substrate directly or they can also act to cleave and thereby activate caspase-6. This said, cytochrome-c is the third factor necessary to bind with APAF1 and caspase-9 within the cytosol in order to form the apoptosome and activate the executioner caspases. In addition, the inhibitor XIAP also resides in the cytosol and acts to inhibit caspase-9 from binding to form the apoptosome. Therefore, before apoptosis can be set into motion, cytochrome-c must be introduced into the cytosol and XIAP must iteslf be inhibited, thereby freeing caspase-9 to bind to form the apoptosome with the already present APAF1 and newly introduced cytochrome-c.

During ALA-mediated PDT, once singlet oxygen is created via interactinos with excited PpIX, oxidative attacks addressed to the outer mitochondrial membrane (OMM)

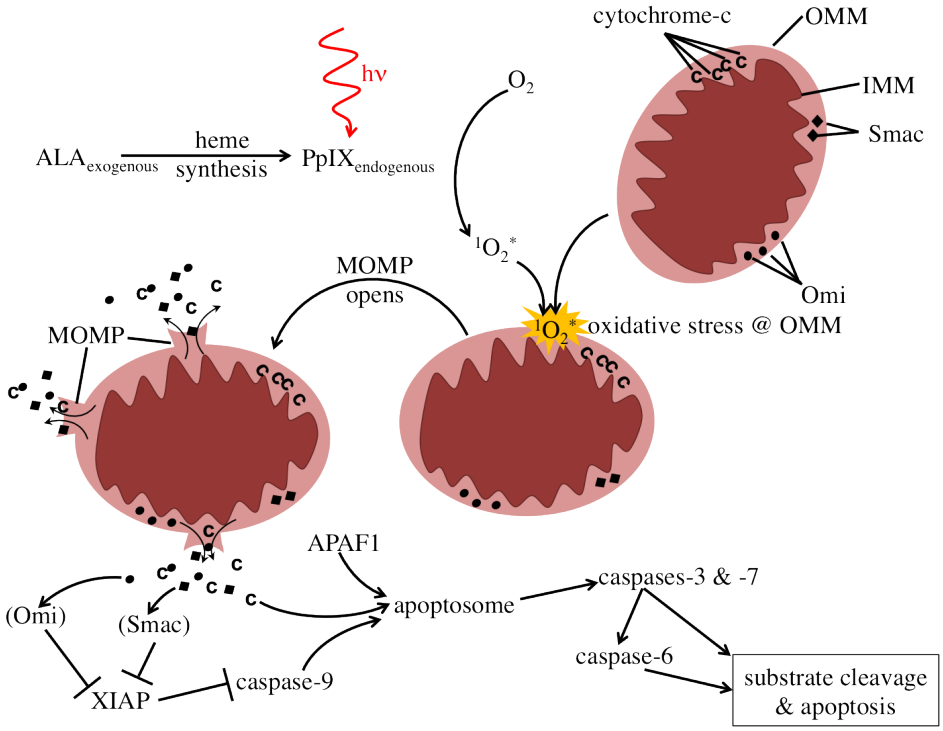

FIGURE 1.40: Exogenous ALA converts to PpIX via the heme synthesis pathway. A surplus of PpIX results, and is activated by the absorption of light of the appropriate energy ($h\nu$). Upon activation, PpIX interacts with endogenous molecular oxygen in order to create singlet oxygen ($^1O_2^*$), which then disrupts the OMM via oxidative stress. Trauma to the OMM causes the MOMP to open, releasing cytochrome-c, Smac and Omi from the mitochondria into the cytosol. The release of these factors leads to the activation of caspase-9, which binds with cytochrome-c and APAF1 (already present in the cytosol) to form the apoptosome. Executioner caspases (caspases-3 , -7 and indirectly, -6) are generated by the apoptosome, whereby they cleave the substrate and apoptosis follows.

cause the OMM to open pores via mitochondrial outer membrane permeabilization (MOMP). The factors cytochrome-c, Smac and Omi reside between the OMM and inner mitochondrial membrane (IMM) and are thereby released into the cytosol via diffusion. Smac and Omi both serve as inhibitors of XIAP, thereby freeing caspase-9 to form the apoptosome with endogenous APAF1 and the cytochrome-c that is released from the MOMP. By causing oxidative stress to the OMM, singlet oxygen thereby sets in action apoptotic pathway by blocking inhibitor factors while simultaneously releasing initiator factors related to apoptosis.[80]

1.3.4 Osteosarcoma

Osteosarcoma is a primary bone cancer. This means the first site osteosarcoma develops is within the bone itself, as opposed to secondary bone cancers which originate elsewhere in the body and migrate to the bone via malignancies. Leading examples of secondary bone cancers originate from primary breast, prostate, lung, thyroid and kidney cancers.[81] The bones are typically the first site of development for secondary cancers when other primary cancers metastasize. About two thirds of the primary breast and prostate cancers that spread to other parts of the body spread to the bones, creating a secondary bone cancer. This is also the case for about one third of the lung, thyroid and kidney cancers that become malignant.[82]

The overwhelming majority (95%) of osteosarcoma cases diagnosed are classified as conventional central osteosarcoma, meaning the majority of osteosarcoma cases are medullary osteosarcomas, forming within the medullary cavity of long bones.[83] Starting within the medullary cavity, osteosarcoma grows outward towards the hard shell of cortical bone. The knee and upper arm are the most common sites for the development of osteosarcoma in humans, principally around the knee joint in the lower femur or upper tibia, or near the shoulder in the upper humerus. Osteosarcoma initially presents itself through pain in the bone. Because osteosarcoma develops in the bone marrow, encased within cortical bone, swelling and lumps external to the bone usually don't present until more advanced stages.[84] In addition, in advanced stages the affected bone may break without an associated trauma. These later symptoms of osteosaroma occur as the tumor has degraded the internal structure of the bone, and in the case of lumps, when the mass has grown to the point of breaching the medullary cavity and protruding out beyond the dense cortical bone. Upon an initial diagnosis, osteosarcoma is confirmed via medical imaging such as x-ray or MRI.

Incidence and Epidemiology

Although most bone cancers found in humans are secondary cancers, caused by malignancies originating in different organs, osteosarcoma is the leading primary, malignant bone cancer, accounting for an estimated 800 cases in the U.S. per year. Osteosarcoma can manifest itself at all ages, but is most common in children (8th leading cancer in chil-

dren under 15 years at 2.6%) and adolescents and young adults between the ages of 10-30 years. This accounts for an estimated 400 cases in children and adolescents in the U.S. per year. Individuals of advanced age are the next group at greatest risk for osteosarcoma, with around 10% of cases found in adults over the age of 60. In addition, osteosarcoma is more commonly diagnosed in males than females.[83–85]

That osteosarcoma is most prevalent in adolescents, is generally found at earlier ages in females than males, and in adolescents that are somewhat tall for their age suggests that its development is related to rapid bone growth. Lifestyle related risk factors, such as body weight, use of tobacco and diet have not been linked to osteosarcoma. The only additional risk factor that may contribute to the development of osteosarcoma is the application of radiation therapy in treatment of other cancers.[86]

For localized (non-metastatic) osteosarcoma, the 5-year survival rate for patients lies around 60-80%. The 5-year survival rate for patients with metastatic osteosarcoma are dramatically lower, between 15-30%. In either case, the prognosis improves if the entire tumor (and secondary tumors, when applicable) have been completely resected via surgery.[87]

Current Therapies

Cancer therapies and treatments can generically be classified as surgical, chemotherapy and radiation therapy. Surgical treatment of osteosarcoma includes the complete amputation of the limb where the tumor is present and limb sparing surgery, where only the immediate region surrounding and including the tumor is resected. In the later case, the limb can be saved and functionality can be maintained via the use of prosthetics or implants. Chemotherapy has been found to be effective in treating osteosarcoma, and can be given prior to surgery (neoadjuvant chemotherapy), post surgery (adjuvant chemotherapy), or both. Radiation therapy is applied much less frequently in cases of osteosarcoma, as osteosarcoma cells are much more resistant to its affects.[88]

Traditionally, treatment for osteosarcoma consists of multiple modalities, including amputation or limb sparing surgery in combination with chemotherapy. This thesis is motivated towards an investigation of photodynamic therapy (PDT) as an additional modality of treatment for osteosarcoma. Beyond this work, it is anticipated that the application of PDT towards secondary bone cancers could also be beneficial.

Canine Model of Osteosarcoma

Canine cases of osteosarcoma serve as a good model for investigating osteosarcoma in humans. Findings in canine incidences of osteosarcoma can be informative of human cases of the disease. First, this is because the presentation, diagnosis, biologic behavior, and risk factors in canine and human cases are similar. Additionally, osteosarcoma is the most common form of primary bone cancer found in canines, occurring in more than 6000 dogs in the U.S. per year.[89]

Although the standard of care for osteosarcoma in a veterinary setting generally combines surgery and chemotherapy modalities, treatment lies at client (owner) discretion. Monte Carlo modeling of PDT in silico is carried out and discussed at the end of this thesis in the context of a canine model.

1.3.5 PDT of Bone Cancers

Although PDT has already been approved for the treatment of specific soft tissue cancers, only in recent years has it begun to be investigated and shown promise for use in treating general bone metastases.[45–49,90] Bone itself has shown resilience against PDT, whereas surrounding tissues were affected.[91] Beyond the treatment of tumor masses, PDT has also been suggested as a means of bone marrow purging in leukemia and non-Hodgkin's lymphoma.[92]

While the application of PDT towards treating osteosarcoma is still in the early stages of investigation, work has been done to look at the effects of combining PDT with other therapies in the treatment of osteosarcoma using *in vivo* models. PDT of osteosarcoma cells *in vitro* and animal models *in vivo* using acridine orange have shown to be effective.[93,94] Used in combination with $1-5Gy$ X-ray irradiation, PDT using acridine orange was shown to cause significantly greater necrosis in a mouse model of osteosarcoma.[95] ALA-mediated PDT was also shown to be effective in combination with hyperthermia in mouse models of osteosarcoma, where NIR wavelengths were administered via a fiber optic probe in order to raise the tumor temperature simultaneously with the activation of PpIX via $\sim 630nm$ light.[96,97]

Most recently, the PS mTHPC was shown to successfully treat a mouse model of the metastatic human osteosarcoma cell line 143B. Using $2.5-10J/cm^2$ of $652nm$ light, the PDT pathway was shown to induce apoptosis via the activation of caspases-3, -7 and -9.[98]

The only published use of PDT in canine cases of osteosarcoma as a primary tumor reports administering $0.4mg/kg$ of BPD-MA and illumination with $690nm$ light up to $500Jcm^{-1}$ at an irradiance of $200-250mW/cm^2$. A cylindrical diffusing tip was used at the end of an optical fiber in order to deliver light within the tumors, all located in the distal radius. In each of these cases, the osteosarcoma was then removed via amputation 48hrs after PDT treatment, whereupon the tumors were inspected and showed a necrotic effect throughout the tumor masses.[48,50]

In these clinical studies of PDT of canine osteosarcoma, the osteosarcoma was illuminated for fixed times in order to achieve a total light delivered via the diffusing fiber tip. These studies serve as the initial inspiration for the later part of this thesis, aimed at a better understanding of light propagation in bone as applied towards PDT of osteosarcoma.[16,56] While a positive response was achieved by causing necrosis in the tumors, there is the opportunity to improve upon the light dosimetry involved in such clinical applications in order to better guide such applications and perhaps increase their efficacy

and efficiency. If nothing else, a model of light propagation in bone tumors would serve to explain the effects observed.

1.4. Development of Novel Technology & Applications

This thesis incorporates applications of biomedical optics including scattering theory, optical transport in tissues, PDT and digital holographic imaging. Some of these applications stand alone, while others are applied directly towards an investigation of PDT of osteosarcoma. The former work revolves around the development and deployment of the DFHM system and its application towards OSI. The later, work is motivated towards a comprehensive understanding of the fundamental principles involved with the use of ALA-mediated PDT in the treatment of osteosarcoma.

1.4.1 DFHM: Development of Novel Technology

The largest component of this thesis works to use a DFHM system in order to create a more robust means of using OSI to determine particle sizes (chapter 2.). To begin, the design and functionality of the DFHM system is detailed (section 2.1.). The means of characterizing the system is then described and calibration results are given (section 2.3.). Reconstructed images of standard optical targets are created via the DFHM system to illustrate its functionality. Polystyrene microspheres of known sizes are then imaged via the DFHM-OSI system as a means of validating its use for particle sizing (section 2.4.). In addition to particle sizing, the robust, holographic nature of the DFHM system allows for additional applications including quantitative phase imaging (QPI) and 3D imaging.

1.4.2 DFHM: Applications

Upon calibration and completion of proof-of-principle experiments using polystyrene microspheres in suspension, the constructed DFHM-OSI system is used in pilot studies to image cells in culture and tissue samples (section 2.5.). Cell images are interested in looking at subcellular structure, while the tissue images given are interested in identifying tissue structures, such as collagen. A combination of OSI, QPI and 3D imaging results are given between these applications.

1.4.3 PDT Related Work

The second line of inquiry explored in this thesis looks at the particulars of treating osteosarcoma in a clinical, veterinary setting for canine cases. In order to do so, Diffuse Reflectance Spectroscopy is carried out in order to first characterize the optical properties of bone tissue (chapter 3.). Once determined, those optical properties are incorporated

into a 3D Monte Carlo model in order to predict the efficacy of ALA-mediated PDT in a geometry similar to that of canine osteosarcoma (chapter 4.).

Lastly, an *in vitro* investigation of the subcellular effects of ALA-mediated PDT is explained as a supplement to the above mentioned PDT of osteosarcoma work (chapter 5.).

2. DIGITAL FOURIER HOLOGRAPHIC MICROSCOPY

The basic principles of digital Fourier holographic microscopy (DFHM) were previously introduced in some detail, along with simulated examples (section 1.2.2). This chapter now turns towards a description of the physical design and calibration of such a system. Applications of the system include quantitative phase imaging (QPI) and optical scatter imaging (OSI). Goniometric and OSI results are given for known polystyrene microspheres in suspension as a means of system validation. Biological applications of the DFHM system are then presented as examples.

2.1. DFHM System Design

In describing the construction of the digital Fourier holographic microscope (DFHM), a system schematic (Figure 2.1) and image (Figure 2.2) of the microscope can be referred to for clarity throughout this section.

In building the system, a helium-neon laser (Melles Griot, 25-LGP-193-249, $\leq 5mW$) with $\lambda = 543.5nm$ is first leveled and aimed at a target fixed at the opposite end of the optical bench. The beam path of the laser is also centered over a continuous row of screw holes in the bench in order to keep all of the following optical elements aligned. Optical elements are added to the system sequentially, starting with the laser and ending with two CCD cameras. Each time an optical element is added to the beam path, the elements are oriented such that the beam remains directed above the row of screw holes and centered about the original target. When a beam splitter is placed in the system, additional targets are placed at the periphery of the system, maintaining the same height as the original target. These additional targets also maintain the beam's path centered above a continuous row of screw holes in the optical bench in order to assure proper alignment of each beam after insertion of each additional optical element.

All electronic components of the system (namely cameras and shutters) are controlled via a Labview program (Figure 2.3) designed to efficiently synchronize timing of the elements, collect and save data. The Labview program controls the cameras and shutters via a combination of NI USB-6221 DAQ and firewire/USB3 cables. The field of view of CCD2 is displayed on the left, showing the image plane for focusing purposes and the collection of a brightfield image for reference. The display on the right is that of the conjugate Fourier plane, mapped to CCD1. Below each output image is a set of controls for gain and shutter time (exposure). On the far left, buttons are present for manual control of shutters in the sample and reference arm, along with the acquisition button. The user is also able to set frame rates for the cameras and define folder and file names when acquiring data.

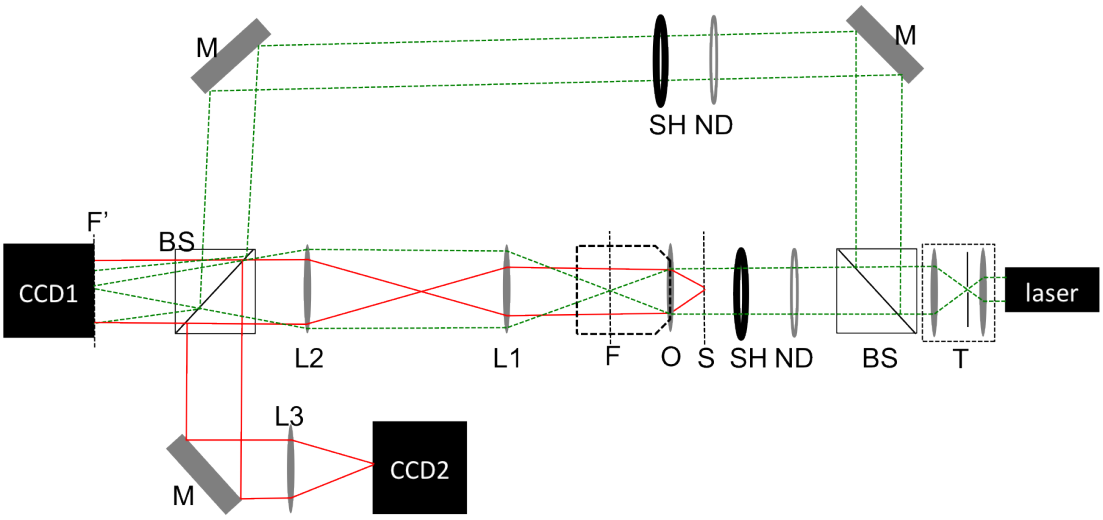

FIGURE 2.1: A schematic of the Digital Fourier Holographic Microscope with elements: telescoping system (T), cube beam splitters (BS), variable neutral density filters (ND), electronic shutters (SH), microscope objective (O), lenses (L1, L2, L3), and mirrors (M). Planes of importance are also indicated: sample plane (S), Fourier plane (F) and conjugate Fourier plane (F′). Cameras CCD1 and CCD2 are used to capture the optical Fourier transform (1.41) and image (1.26) of the sample, respectively. The incident beam is indicated by a dashed, green outline. Light scattered by the sample is indicated by a solid, red outline. Light unscattered (or directly transmitted) by the sample, as well as the reference beam are indicated by a continuation of the dashed, green outline.

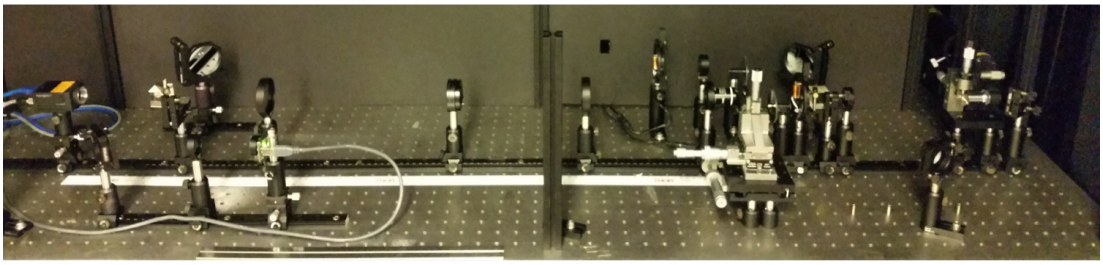

FIGURE 2.2: An image of the Digital Fourier Holographic Microscope.

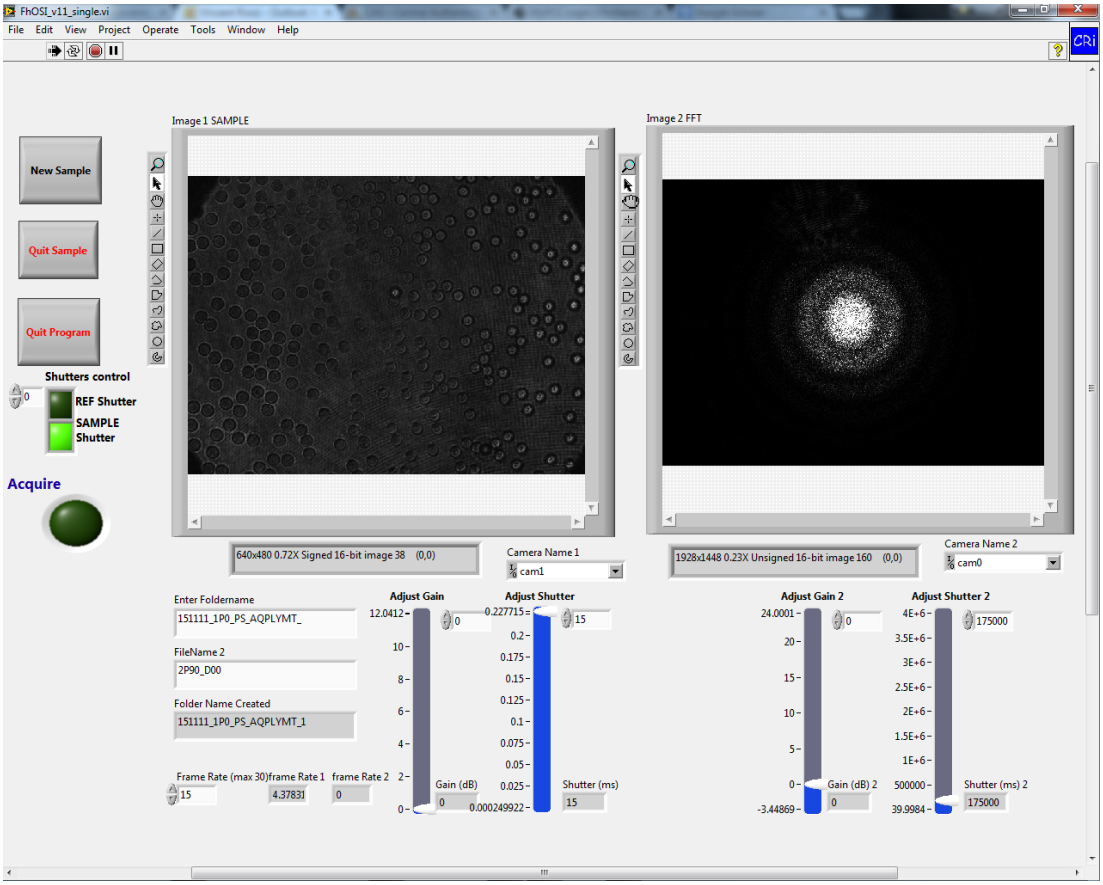

FIGURE 2.3: A screen shot of the open Labview progam used to control the DFHM system. The FOV of CCD2 (image plane) is displayed on the left, while that of CCD1 (conjugate Fourier plane) is displayed on the right. Controls for each camera's gain, shutter time (exposure) and frame rate are displayed and easily adjusted in real time. Control of shutters in the sample and reference arms, along with the acquisition button are also included. User defined file and folder names are also given for ease of data cataloging.

Following the laser, a telescoping system is aligned in order to expand and clean the beam diameter. The telescoping system consists of a 3-axis spatial filter (Newport 900) with a 10X objective lens and $50\mu m$ pinhole (Newport 900 PH-50) placed in series with a bi-convex lens ($f = 100mm$). After leaving the telescoping system, the beam is then passed through a 50/50 cube beam splitter in order to create a reference arm for the interferrometric system.

Staying along the reference arm, the split beam is directed along a path parallel to the sample arm via a mirror before being reintroduced to the sample field via a second mirror and beam splitter combination. Along the reference arm, a variable neutral density filter (Thorlabs, NDC-50C-4-A) is used to control the intensity of the reference beam. In addition, an electric shutter (Melles Griot, UT24340-A) is kept open when collecting reference and interferrence images and closed during collection of the sample intensity.

Returning to the sample arm, the split beam is then passed through a variable neutral density filter (Thorlabs, NDC-50C-4-A) and an electric shutter (Melles Griot, UT24340-A). The controllers for both electric shutters (Melles Griot, 25580) are controlled via the Labview program (Figure 2.3) to be open when collecting sample and interferrence images and closed during collection of the reference image.

The sample plane follows the electric shutter in the sample arm of the system. A 3D translation stage with slide holder is used in order to bring the sample into focus before a microscope objective (100X Olympus Plan Fluorite Oil Immersion Objective, ∞-corrected, 1.30 NA, 0.20 mm WD). When the sample is in focus, scattered light diverges and is collimated by the objective, creating an optical Fourier transform of the sample at the Fourier plane. This optical Fourier transform is encased within the body of the objective itself. The remaining elements in this system are used in order to map the sample's Fourier transform to a conjugate Fourier plane that can be accessed via a CCD camera. Light which goes unscatterd by the sample will remain collimated and therefore converge to a focus at the Fourier plane upon entering the objective. The unscattered light will then be divergent upon leaving the back aperture of the objective.

A plano-convex lens ($f = 200mm$) follows the microscope objective and is placed one focal length downstream from the back aperture of the objective. This lens therefore enacts an inverse Fourier transform on the collimated beam of scattered light, thereby creating an image of the sample at its back focal plane. This lens acts as the tube lens for the objective, and maintains the 100X magnification of the objective as it is designed for use with a $f = 200mm$ tube lens. A variable iris (not shown in Figure 2.1) is placed at this image plane in order to help control distortion in the field and block much of the (now collimated) unscattered, DC signal.

A second plano-convex lens ($f = 300mm$) is placed one focal length downstream from the image plane (iris). This lens combines with the previous lens to create a 4-f system, the optical system used in order to map the sample's Fourier transform from within the microscope objective to a conjugate Fourier plane that is accessible via a CCD camera. Light scattered by the sample will therefore be collimated upon leaving this

second lens and light which goes unscattered by the sample will again be brought to a focus. This second lens thereby creates an optical Fourier transform of the image plane one focal length downstream. Being brought to a focus, the unscattered light thereby contributes to the DC component of the optical Fourier transform, as should be expected.

Before the optical Fourier transform of the sample is mapped to the conjugate Fourier plane, a second 50/50 beam splitter is placed along the sample arm in order to reincorporate the reference beam for interferrometric purposes. The angle of this beam splitter is carefully aligned in order to keep the sample arm on its true path, while slightly offsetting the reference beam. This has the effect of controlling the angle of incidence of the reference beam, θ_{ref}. Achieving an appropriate offset of the twin images in the holographic reconstruction process is greatly dependent upon the fine tuning of θ_{ref}, as previously described (sections 1.2.1 and 1.2.2).

A CCD camera (Point Grey, Grasshopper USB3, GS3-U3-28S4M-C, 2.8MP, 14bit, 1928x1448, $\delta x = 3.69\mu m$) is then placed at the conjugate Fourier plane in order to acquire images of the sample's Fourier transform, reference beam, and the interference pattern between the two. The intensity of the optical Fourier transform of the scattered field, (1.64) is then experimentally equivalent to a hologram (1.33) upon recovering the phase.

As the second beam splitter will split the sample arm into two paths, advantage is found in collecting the path not directed towards the conjugate Fourier plane. The light directed along this path, which was scattered by the sample, can be passed through an additional optical inverse Fourier transform via a bi-convex lens ($f = 100mm$) and mirror combination. This third lens, along with the second lens, comprises a second 4-f system that maps the image plane (at the iris) to a second CCD camera (Point Grey, Firefly MV, FFMV-03M2M-CS, 640x480, $\delta x = 6\mu m$). The real-time image acquired by this second camera aids in alignment and focusing of the sample, as well as giving sample images for comparison to the reconstructed hologram.

The reference beam passed along this final arm by the beam splitter is not incident upon the second CCD. This is due to a combination of the focusing effect of the final lens and due to the angle of the beam splitter used to obtain an appropriate θ_R in the other arm. As such, this beam has been omitted completely from the schematic (Figure 2.1).

2.2. DFHM Holographic Reconstruction

Upon aligning the reference and sample arms of the system to be normally incident at the center of the CCD in the conjugate Fourier plane, it is then necessary to slightly shift the angle of incidence of the reference arm, θ_{ref}. As shown previously (Figure 1.25), this is necessary in order to sufficiently separate the twin images from each other and the DC component. We can adjust θ_{ref} by slightly and incrementally adjusting the mirrors in the reference arm. At each step, the separation of the "twin images" from each other and

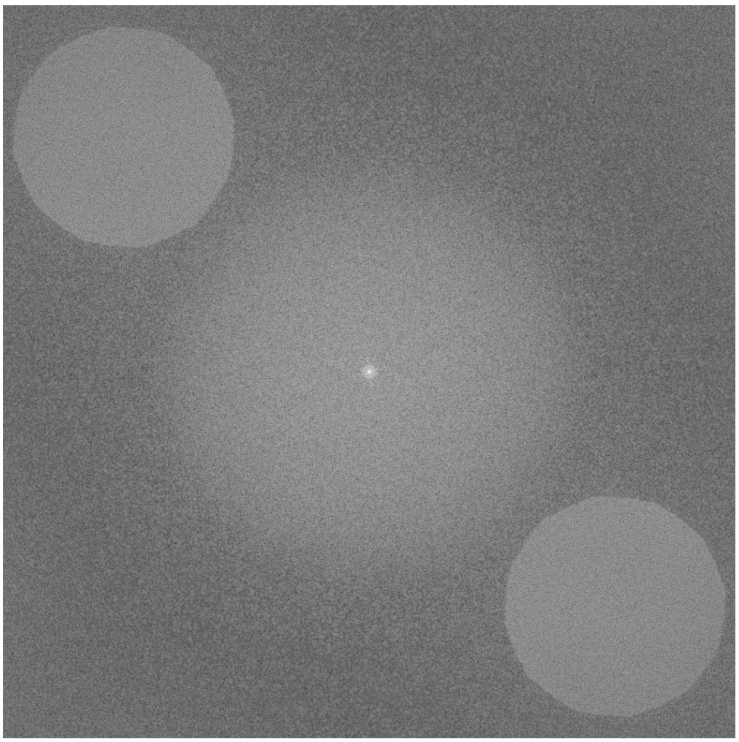

FIGURE 2.4: Upon aligning both the sample and reference arms within the DFHM, the angle of incidence of the reference beam at the CCD is adjusted in order to completely separate the twin images from the DC signal. As seen here, the DC component is the large, centrally located circular field of view. The twin images are resolved in their upper left and lower right hand corners, respectively.

the DC component can be viewed upon reconstruction via an inverse Fourier transform. This is an iterative process that can be done until sufficient separation is achieved (Figure 2.4).

We now describe step by step the entire holographic reconstruction process for the DFHM, beginning with the interference pattern between the sample and reference arms (1.44). Previously, we removed the sample and reference intensities from (1.44) by subtracting them individually. Experimentally, this would require the capture of the interference pattern created via the superposition of the sample and reference fields, followed by the capture of the individual sample and reference intensities. Exposure times of $\sim 200\mu s$ are necessary for each image collected. Accounting for the automation of the system—controlling the timing of shutters, cameras and saving data—collection of a single set of

images for holographic reconstruction takes anywhere from $1 - 2s$. Considering that the aim of the DFHM system will be to ultimately investigate biological samples *in vitro*, this is a significantly long time of acquisition. Even if the interference image between the sample and reference arms and the individual sample intensity were collected immediately one after the other, some $\sim 400\mu s$ would have passed between the initial acquisition of the first image and the end of acquisition of the later. This minimum achievable time between images is significantly long compared to the timescale of biological action. Due to the possibility of motion or changes within the sample between the collection of these two images, motion artifacts could arise when subtracting the sample intensity form the interference pattern.

There is however a work around for the issue of motion artifacts. When the intensity of the reference field is significantly greater than that of the sample field, we can approximate the intensity of the sample field (1.39) as[18]

$$F \approx \frac{(H-R)^2}{2(H+R)}, \tag{2.1}$$

where H represents the intensity of the superposition between the sample and reference fields (1.42) and R represents that of the reference field (1.27). The DFHM satisfies the condition that the intensity of the reference field be much greater than that of the sample field because we are already making use of heterodyne amplification, using the reference intensity to amplify the weaker sample intensity. Therefore, we can isolate the interference pattern between the sample and reference fields by substituting (2.1) into (1.44),

$$\begin{aligned}\mathcal{E}(k_x, k_y) &= |f|^2 + |r|^2 + 2fr\cos\Phi - |r|^2 - \frac{(H-R)^2}{2(H+R)} \\ &= 2fr\cos\Phi. \end{aligned} \tag{2.2}$$

Using this method of holographic reconstruction, we need only collect the interference pattern between the sample and reference fields and an image of the reference field intensity, thereby avoiding the risk of motion artifacts that could result due to the collection of an additional sample image. We don't care about the time delay between the collection of the interference pattern and reference intensities because the reference intensity will be in a steady state and independent of the sample.

Imaging static samples can be used as a control group of sorts in order to test holographic reconstruction via (2.2) since there is no motion within the sample. Reconstructing the hologram from a static sample independently via (1.44) and (2.2) and comparing their results tests the accuracy of the approximation (2.1). Comparisons of these two methods of holographic reconstruction show no difference in the final results when imaging static samples. We therefore trust the use of (2.2) as an accurate method of holographic reconstruction which has the added benefit of avoiding any possible motion artifacts due to sample dynamics.

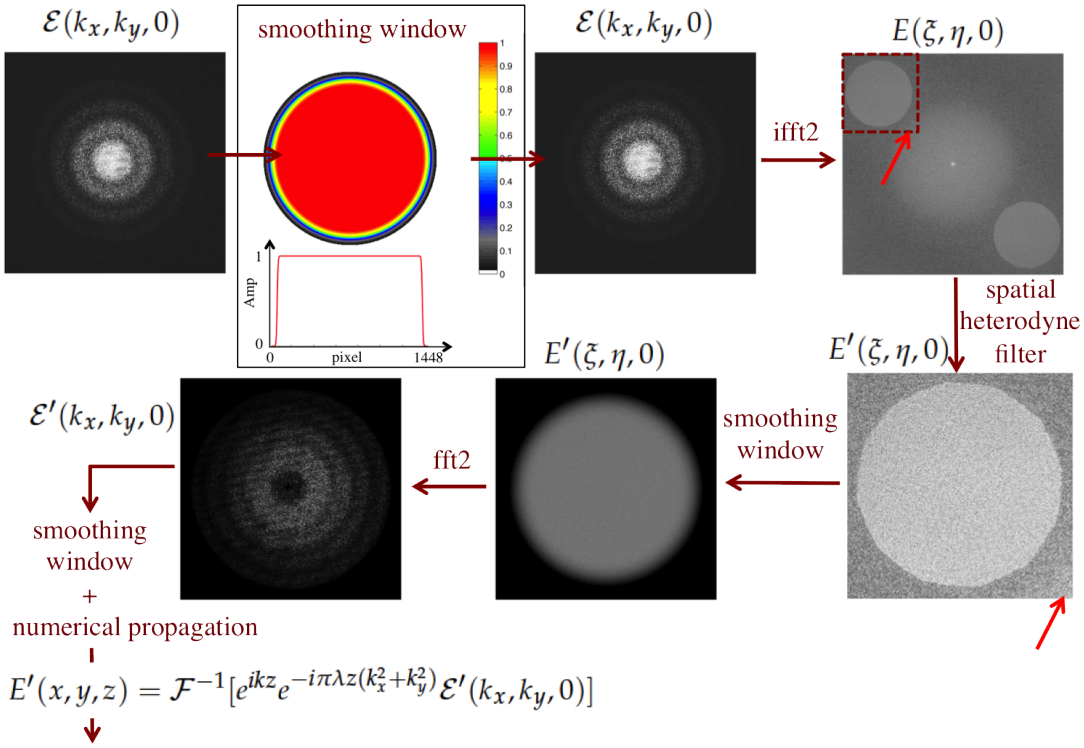

FIGURE 2.5: Upon aligning both the sample and reference arms within the DFHM, the angle of incidence of the reference beam at the CCD is adjusted in order to completely separate the twin images from the DC signal. As seen here, the DC component is the large, centrally located circular field of view. The twin images are resolved in their upper left and lower right hand corners, respectively. The scales on the vertical and horizontal axes indicate pixel numbers.

Having described the isolation of the interference patterns between the sample and reference fields via (2.2), we take $\mathcal{E}(k_x, k_y, 0)$ as our starting point for the rest of the holographic reconstruction process associated with the DFHM. This process is described via a series of experimental images associated with each step of image processing (Figure 2.5). We first pass (2.2) through a smoothing window, which eliminates high frequency noise associated with the sharp edge of the image.[99] Zero-padding the image prior to taking its inverse Fourier transform will have a similar effect. However, we will need to use the smoothing window throughout image processing and at times where zero-padding will not be effective. Therefore, we use the smoothing window exclusively throughout image processing.

After smoothing $\mathcal{E}(k_x, k_y, 0)$, we take its inverse Fourier transform (1.45) in order to move to the sample plane, $E(\xi, \eta, 0)$, (Figure 2.5). Notice again the separation of the twin images from each other and the DC component. A single twin image $E'(\xi, \eta, 0)$ is then cropped from the remainder of $E(\xi, \eta, 0)$ and centered, as indicated by the red dashed box in (Figure 2.5). Although the twin images have been sucessfully separated from the DC

component, the DC component may still invade the field of view of $E'(\xi, \eta, 0)$ as indicated via the red arrows. This is a situation where zero-padding will not effectively remove the overflow of the DC term into the $E'(\xi, \eta, 0)$ field of view. Instead, we must again pass $E'(\xi, \eta, 0)$ through a smoothing filter. This will have two effects. First, the smoothing window will attenuate the overflow of the DC component into the field of view. And as before, the smoothing window will soften the hard edge of the field of view. Both of these consequences are apparent (Figure 2.5).

While the twin image has at this point been isolated and smoothed, it is not yet brought into focus. Think back to the optical Fourier and inverse Fourier transfers (Figure 1.34), where light must actually propagate in order to go through these transforms. Simply taking the digital Fourier transform (or digital inverse Fourier transform, as the case is here) does not lead to an automatic propagation of the field. Instead, we need to propagate the field numerically, as described in (section 1.2.2). We ultimately make use of the Convolution Theorem, which says the propagated field can be achieved by the inverse Fourier transform of the product between the sample's Fourier transform—which we just so happen to have recovered experimentally (2.2)—and the Fourier transform of a propagation factor (1.72). Therefore, we take an additional Fourier transform of the smoothed $E'(\xi, \eta, 0)$, giving

$$\mathcal{E}'(k_x, k_y, 0) = \mathcal{F}[E'(\xi, \eta, 0)]. \tag{2.3}$$

This resulting Fourier transform can now be passed through an additional smoothing filter and numerically propagated to the image plane via

$$E'(x, y, z) = \mathcal{F}^{-1}[e^{ikz} e^{-i\pi\lambda z(k_x^2 + k_y^2)} \mathcal{E}'(k_x, k_y, 0)]. \tag{2.4}$$

This is also the appropriate time to digitally employ spatial filtering for optical scatter imaging. Notice in this final Fourier transform, $\mathcal{E}'(k_x, k_y, 0)$ (Figure 1.34), that the bright central DC component has been lost. This is a direct consequence of the heterodyne filtering, where a twin image in $E(\xi, \eta, 0)$ was cropped. The DC component was physically separated and removed from the twin image. This can take the place of the central beam block applied in OSI, however the width of the central DC signal removed in this fashion varies with exposure. Employing a known central beam block is advisable, eliminating any variability or uncertainty in the actual beam block.

2.3. DFHM System Calibration

Once the reference arm is appropriately aligned, the system is ready for imaging and holographic reconstruction. However, since the intent is to use the DFHM system for metrology based upon scattering, an additional level of calibration is required. In order to spatially filter the collected Fourier hologram digitally, we need to map scattering angle

space to the conjugate Fourier plane. This is achieved by imaging the diffraction pattern from a known diffraction grating. For a given grating spacing and incident wavelength (adjusted for index of refraction of the medium), we can relate the observed angles of diffraction to the scattering angle space of the CCD via the diffraction equation[32]

$$\frac{m\lambda}{n_{med}} = dsin\theta_m, \tag{2.5}$$

where $m = 0, 1, 2, ...$ indicates the order of diffraction and d indicates the spacing between lines on the grating (Figure 2.6). Solving for the $m^{th} - order$ diffraction angle,

$$\theta_m = sin^{-1}\left(\frac{m\lambda}{dn_{med}}\right), \tag{2.6}$$

we then have an angle space to relate to pixel space on the CCD. This results in a scaling factor of $pixels/degree$ that is computationally incorporated into image processing for digital spatial filtering.

Beyond determining the scaling term relating angle to pixel space at the conjugate Fourier plane, it is also possible to use the numerical aperture of the objective

$$NA = n_{oil}sin\theta_{max} \tag{2.7}$$

in order to determine the maximum scattering angle of detection

$$\theta_{max} = sin^{-1}\frac{NA}{n_{oil}}, \tag{2.8}$$

where n_{oil} refers to the index of refraction of the immersion oil coupled to the objective. Since $n_{oil} > 1$, the use of an oil-immersion objective works to increase the angle of acceptance.

While high-NA objectives are designed for large angles of acceptance in order to improve resolution and collect more light from the sample, the angle of acceptance will be slightly skewed via Snell's Law (1.12) due to the multiple interfaces between the sample and objective. For instance, when imaging cells *in vitro*, there are interfaces between the cell media and coverglass, followed by the coverglass and immersion oil of the objective (Figure 2.6).

This work generally focuses on the use of the DFHM system for imaging polystyrene microspheres suspended in mounting media (Aqua-Poly/Mount, $n_{AQP} = 1.457$) and cells in culture ($n_{H2O} = 1.33$, that of water). Depending on the scenario, the predicted angles of scattering or diffraction would then need be mapped to the actual angles observed in the conjugate Fourier plane via the application of Snell's Law at each of these interfaces,

$$n_{med}sin\theta_{med} = n_g sin\theta_g \tag{2.9}$$

$$n_g sin\theta_g = n_{oil}sin\theta_{oil}, \tag{2.10}$$

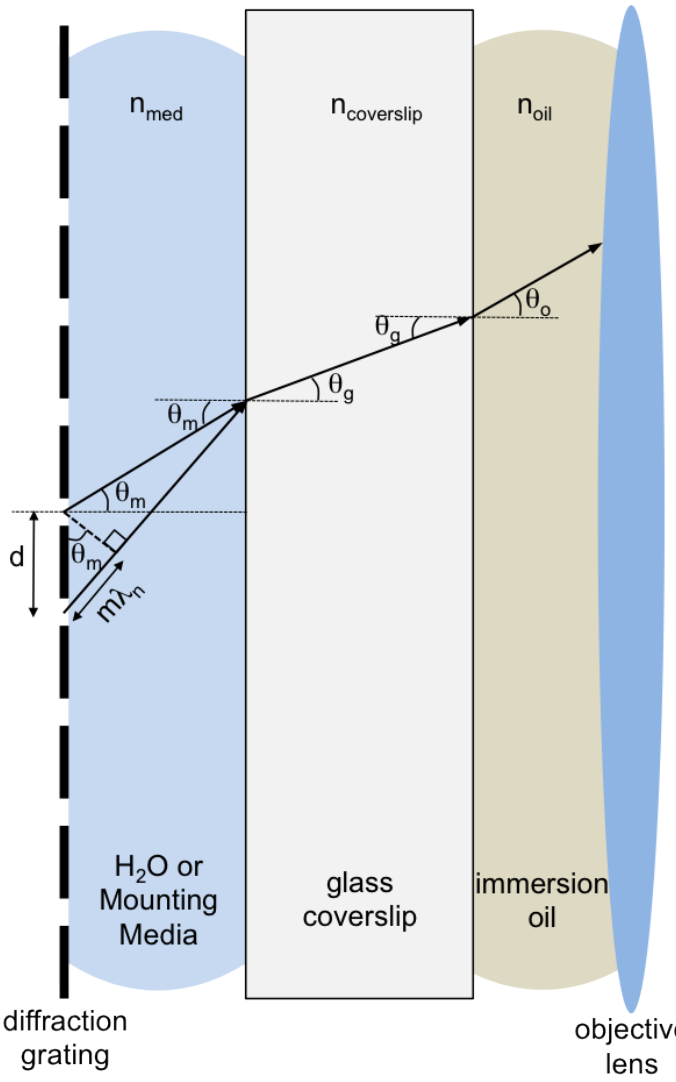

FIGURE 2.6: The presence of varying media along the optical path between the sample and objective will result in a change in scattering angles collected due to Snell's Law. This figure shows the geometry used in order to correct for the angle of acceptance to the objective θ_o, as compared to the m^{th}-order angle of diffraction, θ_m.

where the subscripts *med*, *g* and *oil* represent the sample medium, coverglass and immersion oil, respectively. The relationship between the sample medium and immersion oil can be directly related via elimination of the coverglass contributions found in both (2.9) and (2.11), such that

$$n_{med} sin\theta_{med} = n_{oil} sin\theta_{oil}. \tag{2.11}$$

Solving for the actual angle of acceptance by the objective,

$$\theta_{oil} = sin^{-1}\left(\frac{n_{med}}{n_{oil}} sin\theta_{med}\right), \tag{2.12}$$

we find the relationship between the expected and actual angles of scattering or diffraction. Typically, $n_{med} < n_{oil}$, such that the actual observed angles of diffraction or scattering in the conjugate Fourier plane will be less than those anticipated by diffraction or scattering (Mie) theory, respectively. The right hand side of (2.17) can therefore be used in image processing and analysis as a scaling factor in order to appropriately reflect the multiple interfaces and the resulting refraction en route to the objective of the DFHM system.

Similarly, the maximum angle of acceptance by the objective will be slightly diminished from that predicted based solely on the NA of the objective (2.8),

$$\theta_{o,max} = sin^{-1}\left(\frac{n_{med}}{n_{oil}} sin\theta_{max}\right). \tag{2.13}$$

As an example, the predicted maximum angle of acceptance by the objective in the DFHM system as determined by (2.8) is $\theta_{max,pred} = 58.9^o$. However, when incorporating (2.13), the maximum angles of acceptance are diminished to $\theta_{max,AQP} = 55.3^o$ and $\theta_{max,H2O} = 48.6^o$ for Aqua-Poly/Mount and cell media when imaging polystyrene microspheres and cells, respectively.

The overall scaling of the observed angles of diffraction (or scattering) are represented in (Figure 2.7). We see that refraction across the Aqua-Poly/Mount-glass-immersion oil interfaces will slightly diminish observed angles in the conjugate Fourier plane. This result will be accentuated for the cell media-glass-immersion oil interface due to the greater waiter-oil index of refraction mismatch.

Due to the effects of refraction on the angles of accepted light by the objective, the calibration process using a diffraction grating (as described above) needs be carried out for each imaging scenario—namely with water or Aqua-Poly/Mount as the medium in which the scattering particles are immersed. Diffraction patterns are therefore collected at the conjugate Fourier plane of the DFHM system after placing a drop of media directly on the diffraction grating, followed by a coverglass and a drop of immersion oil. In the case of imaging polystyrene microspheres, the media used is the before mentioned Aqua-Poly/Mount designed by the manufacturer specifically for polystyrene microspheres (Figure 2.8). When imaging cells in tissue culture media, the same effect is achieved by using a drop of water directly on the diffraction grating (Figure 2.9).

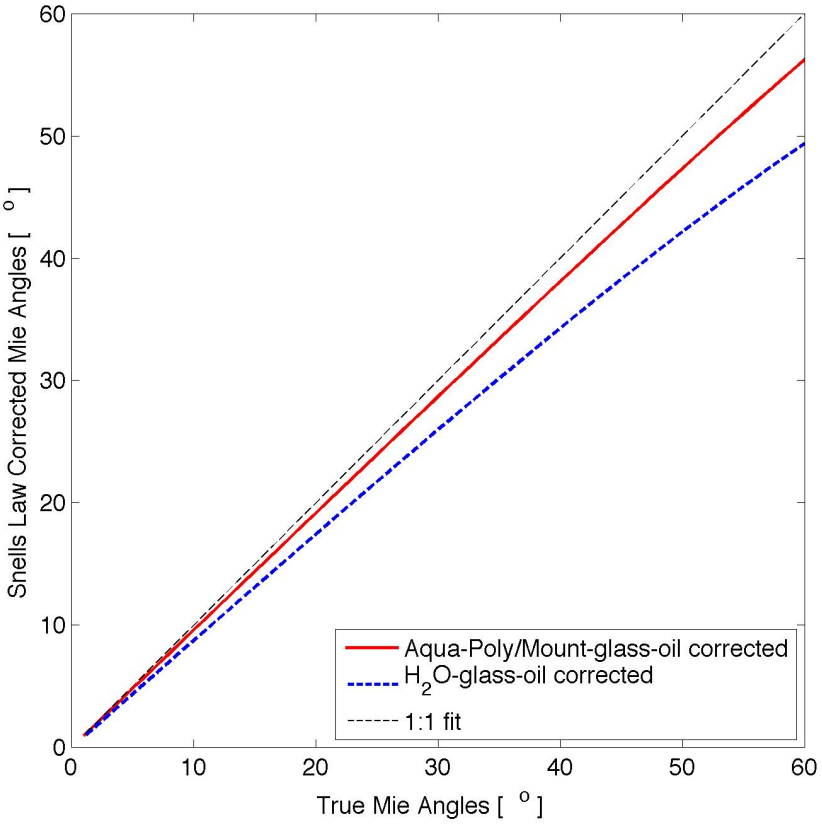

FIGURE 2.7: The angles of acceptance predicted via Snell's Law are plotted against the true scattering (or uncorrected) angles. A thin black, dashed line of linear proportion is plotted. As can be seen, light passing through both media-glass-oil and water-glass-oil interfaces will be collected by the objective at smaller angles of acceptance than their true values upon leaving the sample. The effect is more dramatic in water due to a greater water-oil index of refraction difference than that of mounting media-oil.

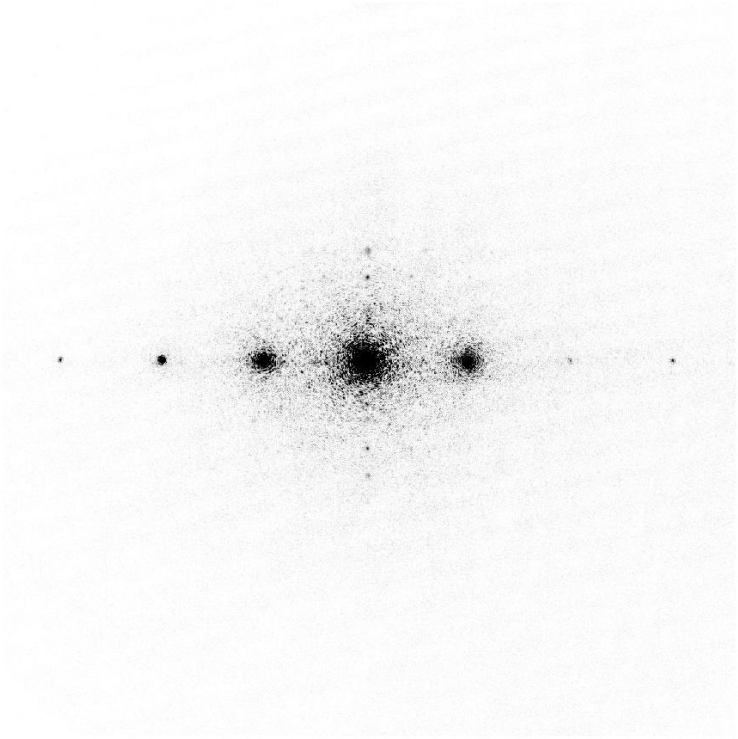

FIGURE 2.8: The diffraction pattern measured from a $500 lines/mm$ diffraction grating for calibration using an Aqua-Poly/Mount-glass-oil interface. The first three orders of diffraction are obvious across the figure, leaving a strong signal that can be used for calibration of the pixels per angle of scatter in Fourier space.

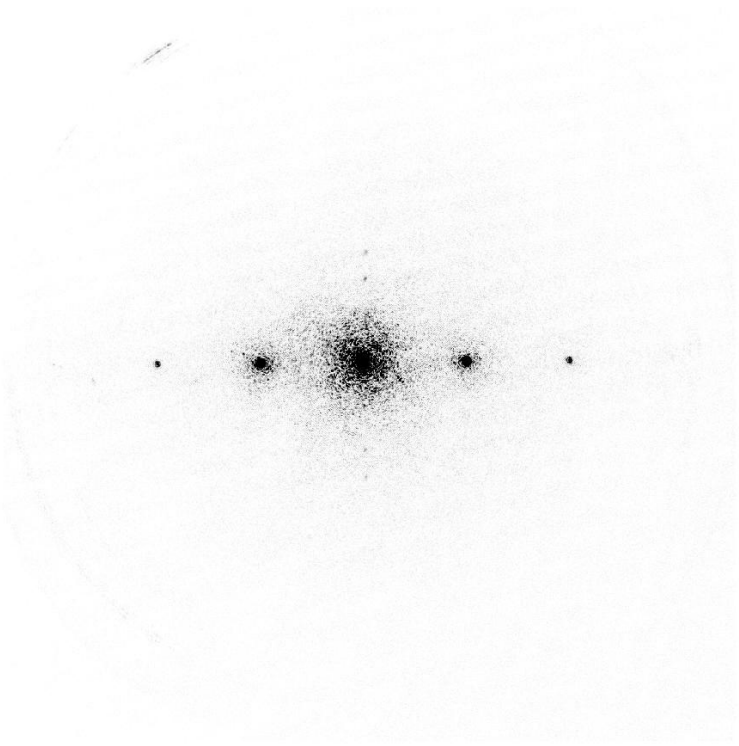

FIGURE 2.9: The diffraction pattern measured from a $500 lines/mm$ diffraction grating for calibration using a water-glass-oil interface. The first two orders of diffraction are obvious across the figure, leaving a strong signal that can be used for calibration of the pixels per angle of scatter in Fourier space.

After collecting the diffraction patterns from a known diffraction grating, the central maxima from each image are registered and used in order to determine the $pixels/degree$ scaling factors for each imaging scenario. For imaging polystyrene microspheres in the Aqua-Poly/Mount mounting media, a scaling factor of $18.6 pixels/degree$ and maximum angle of acceptance of 38.9^o are determined (Figure 2.10). Similarly, a scaling factor of $19.4 pixels/degree$ and maximum angle of acceptance of 37.4^o are determined for imaging cells in tissue culture media (Figure 2.11).

The respective diffraction patterns undergo image thresholding and morphological operations in order to bring out the edges between the diffraction peaks and regions of destructive interference in order to achieve a clean line-scan across the diffraction pattern for display purposes (Figures 2.10 and 2.11).[99,100]

A summary of the calibration results is given for both Aqua-Poly/Mount and tissue culture media (Table 2.1). Note that the observed maximum angles of acceptance are far below the anticipated values based on the NA of the objective. This is in large part because the final lens proceeding the CCD in the conjugate Fourier plane was originally used for a lower NA objective and therefore is currently overfilling the CCD. Ultimately, this lens would need to be replaced with a lens with a smaller focal length in order to reduce the beam diameter of the collimated scattered light and therefore fit the full range of the angular spectrum onto the CCD. While the use of the current lens will reduce the dynamic range of spatial filtering in the conjugate Fourier plane, it is still sufficient for the purposes of this work.

TABLE 2.1: Parameters and results from the calibration of the DFHM system, where Aq-Pol/Mnt refers to the microsphere mounting media, $[pix/deg]$ the scaling factor, $\theta_{max,th}$ the theoretical maximum scattering angle of acceptance based on the NA of the objective, and $\theta_{max,exp}$ is the actual observed maximum angle of acceptance for the objective.

Sample	Media	$n_{med}[-]$	$[pix/deg]$	$\theta_{max,th}[^o]$	$\theta_{max,exp}[^o]$
ps μspheres	Aq-Pol/Mnt	1.457	18.6	55.3	38.9
cells	H_2O	1.33	19.4	48.6	37.4

In determining a $pixels/degree$ scaling factor at the conjugate Fourier plane, a linear relationship was assumed. Pixel locations of the observed diffraction peaks are plotted against a linear fit function based on the $pixels/degree$ scaling factors in order to test the validity of this assumption. For both the Aqua-Poly/Mount (Figure 2.12) and water (Figure 2.13) media, this assumption proves to be valid as there is good correlation between the observed and predicated diffraction peaks. These results are corrected for refraction effects as previously described by (2.17).

As a further check on the calibration of the angle-to-pixel space correlation, upon determining the $pixels/degree$ scaling factor from a given diffraction grating, two addi-

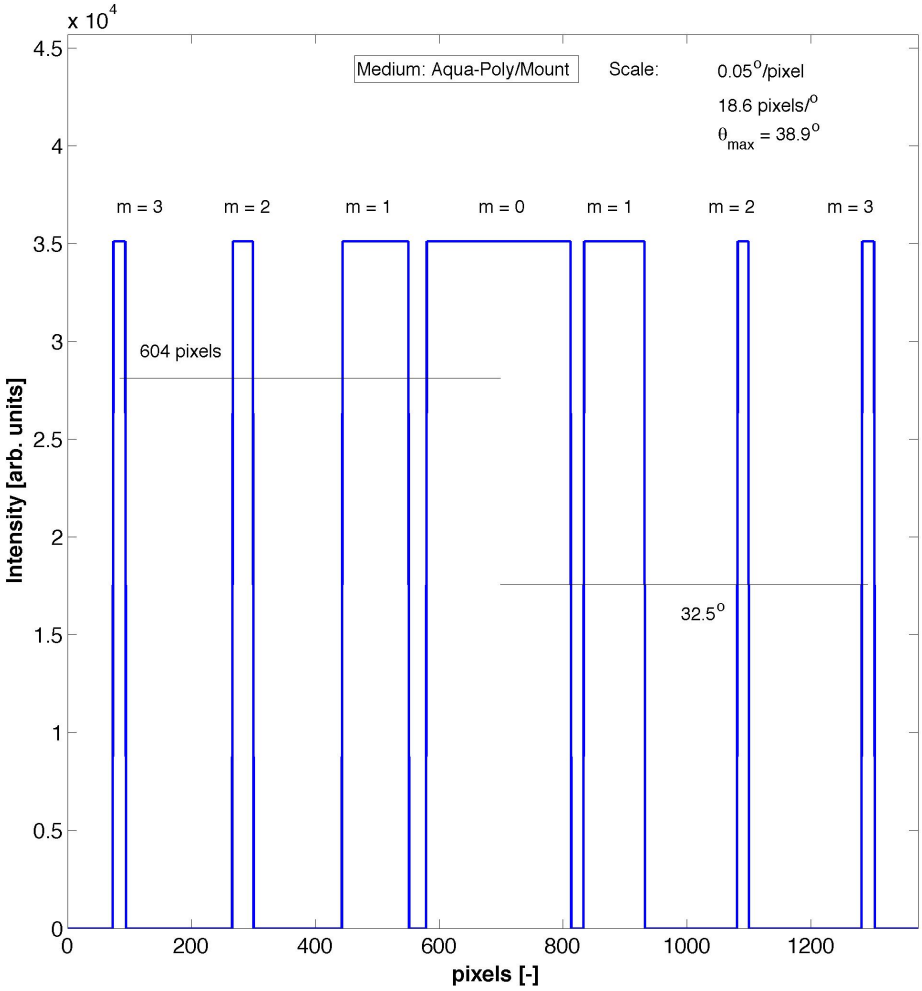

FIGURE 2.10: The diffraction pattern from a $500 lines/mm$ diffraction grating is analyzed in order to pick out the diffraction peaks, which are compared to the known angles of diffraction in order to determine a pixels/degree scaling factor in the conjugate Fourier plane. This scale factor is used for determining the appropriate windows for digital spatial filtering of polystyrene samples suspended in mounting media.

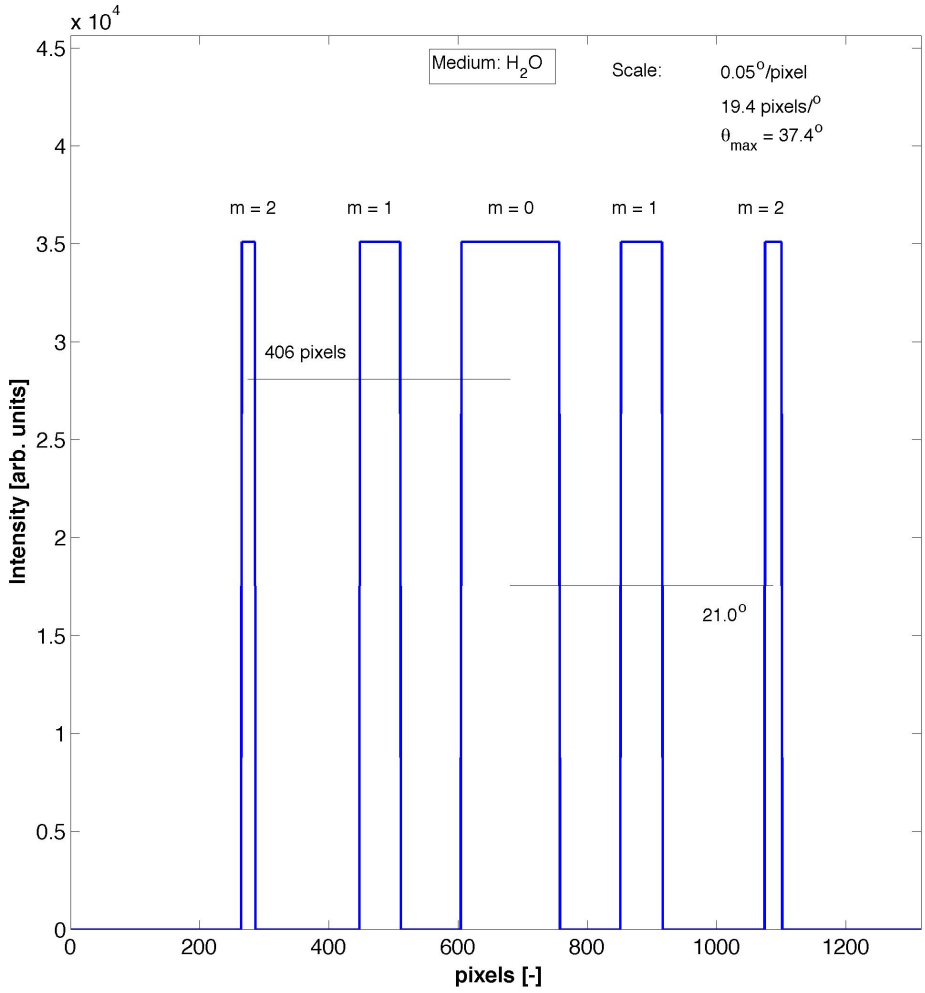

FIGURE 2.11: The diffraction pattern $500 lines/mm$ diffraction grating is analyzed in order to pick out the diffraction peaks, which are compared to the known angles of diffraction in order to determine a pixels/degree scaling factor in the conjugate Fourier plane. This scale factor is used for determining the appropriate windows for digital spatial filtering of cells in culture media.

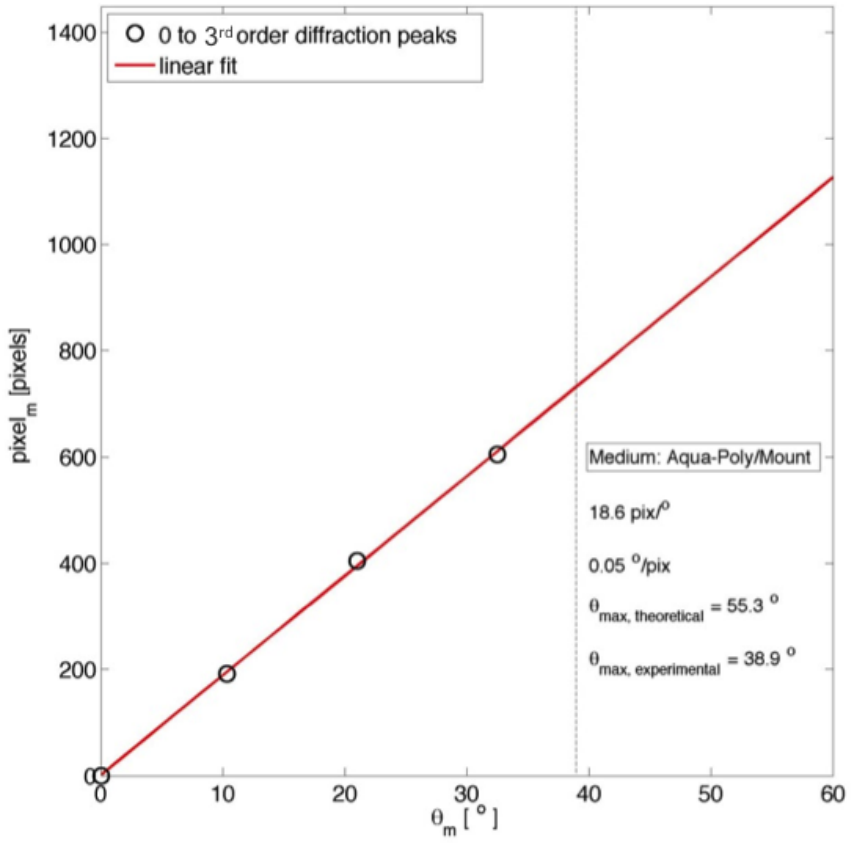

FIGURE 2.12: Upon adjusting for Snell's Law across the sample holder, scaled points of diffraction peaks are plotted against a linear fit function for a mounting media-glass-oil interface. The experimental data points match nicely with the linear pixels per degree slope, indicating that a linear fit across the CCD is appropriate.

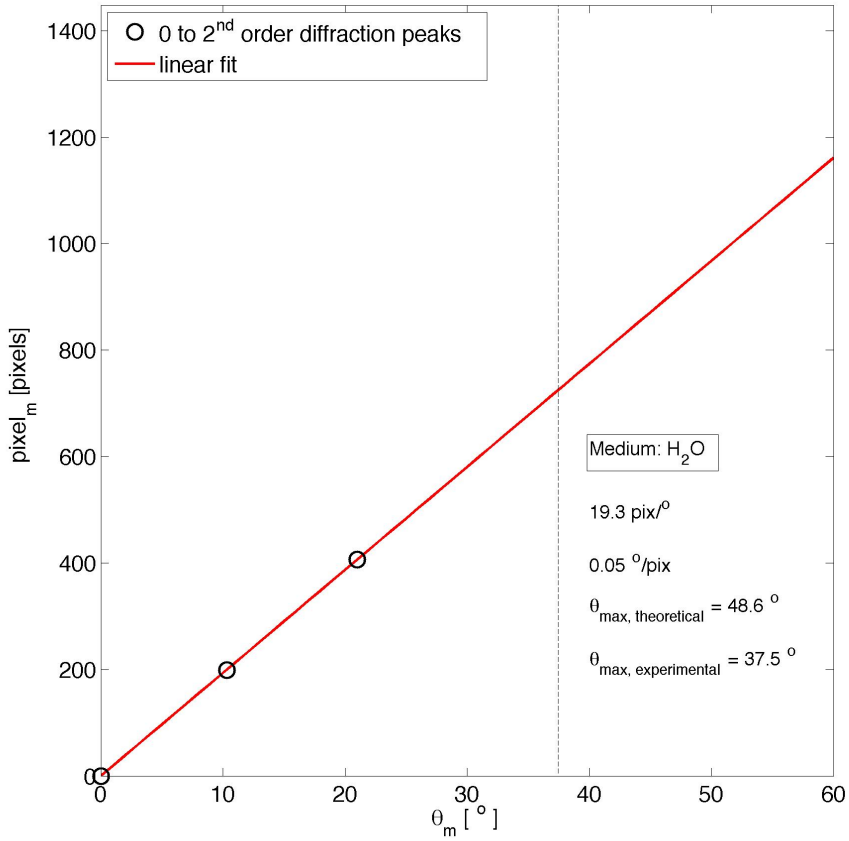

FIGURE 2.13: Upon adjusting for Snell's Law across the sample holder, scaled points of diffraction peaks are plotted against a linear fit function for a water-glass-oil interface. The experimental data points match nicely with the linear pixels per degree slope, indicating that a linear fit across the CCD is appropriate.

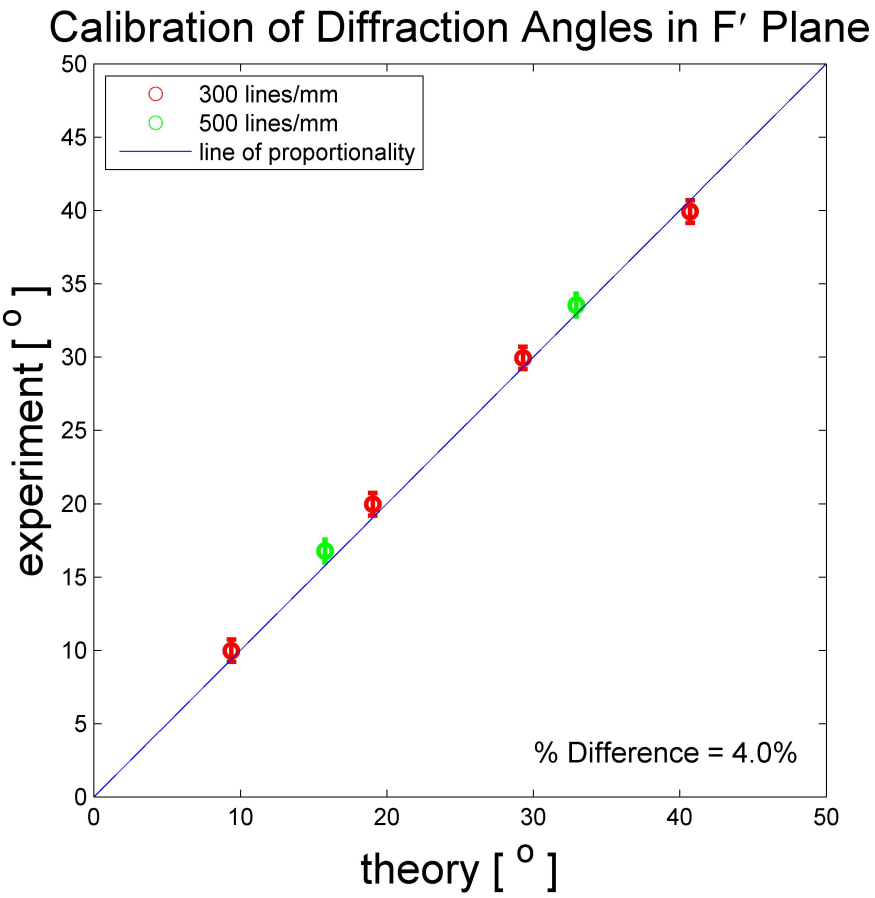

FIGURE 2.14: The calibration of pixel to angle space in the conjugate Fourier plane was originally carried out with a 1000 lines per mm grating. Based upon the resulting scaling, experimental angles of diffraction were then plotted against theoretical predicted angles of diffraction for both 300 and 500 lines per mm gratings. Their resulting points of diffraction were within 4% of the predicted values, further demonstrating the appropriate linear scaling of the conjugate Fourier plane.

tional diffraction gratings are imaged via the DFHM system and their known diffraction patterns are plotted against the scaled angle space (Figure 2.14). In this figure, the scaling was initially carried out using a $1000 lines/mm$ grating, and the diffraction peaks from additional $500 lines/mm$ and $300 lines/mm$ gratings were plotted against the predicted values based upon that $1000 lines/mm$ scaling. Good agreement is demonstrated between all three diffraction patterns, averaging only a 4% difference from predicted values. Beyond verifying the validity of the linear scaling between pixel and angle space, these results also affirm the accuracy of this scaling.

2.4. DFHM System Validation

As discussed, Mie theory is an accurate model of scattering for spherical particles on the same size scale as the wavelength of visible light.[1,2] As such, we will look to Mie theory as a means of validating the DFHM system. Polystyrene microspheres ($n_{ps} = 1.59$ at $\lambda = 543.5nm$), Polysciences, Inc., Warrington, PA) with diameters in the range of $0.36\mu m \leq d \leq 2.90\mu m$ are mounted on glass coverslips via the Aqua-Poly/Mount media ($n_{AQP} = 1.457$ at $\lambda = 543.5nm$) developed by the manufacturer specifically for these particles. Mounting in the manufacturer's media has advantage over mounting the spheres in water because there is a lesser index of refraction mismatch between the particles and media than would be achieved if mounting in a water/agar gel ($n_{agar} \approx 1.33$). We want to have an index of refraction mismatch between the particles and media so as to have scattering, but we want that mismatch to be slight so as to be similar to that seen in cells ($n_{media} = 1.33$, $1.35 \leq n_{subcell} \leq 1.38$). Mounting the polystyrene microspheres in epoxy would result in an even smaller index of refraction mismatch ($n_{epoxy} \approx 1.55$), however the polystyrene microspheres can actually absorb epoxy, thereby swelling and no longer serving as reliable size standards. Use of the manufacturer's mounting media thereby serves as a passable solution, giving a bit more of an index of refraction mismatch than would be seen in subcellular components, however its use guarantees reliable particle sizing.

Using the Oregon Medical Laser Center (OMLC) Mie Calculator website, scattering functions are generated for the particular particles in mounting media (Figure 1.3).[3] Those scattering functions, which give scattering intensity as a function of the scattering angle θ, are then revolved around 2π to generate two dimensional scattering functions, $P(\theta, \phi)$ (Figures 1.4 and 1.5). The resulting scattering functions will be symmetric with respect to the azimuthal angle ϕ. Aside from some scaling to account for intensity, these scattering functions should be identical to those measured from single a particle at the conjugate Fourier plane of the DFHM system. We therefore want to compare the experimentally measured scattering functions with those generated via Mie theory as a means of validating the DFHM system.

However, scattering from a single particle will result in a weak scattered intensity in the DFHM. The ability to find a single microsphere in the roughly $100\mu m \times 100\mu m$ field of view of the DFHM would be tenuous and tedious. In addition, the control over concentrations of microspheres in sample preparation is limited since we are mixing an aqueous solution of microspheres into a viscous mounting media and the resulting distribution of microspheres will not be uniform. The ability to assuredly have a single microsphere isolated in the field of view would not be guaranteed. Instead, the microspheres are mixed at roughly a 1% concentration by volume, such that there will be multiple microspheres visible in a single field of view, but not so densely packed so as to cause aggregation and effectively increasing the overall particle sizes detected.

Since we want to compare the theoretical scattering function of a single particle with the experimentally measured scattering function from many identical particles, we make use of the Array and Convolution Theorems. The convolution Theorem states that the superposition of signals from multiple identical sources can be reconstructed by convolving the point spread function of a single particle with a two dimensional distribution of delta functions,

$$S(x,y) = [P(x,y) \otimes A_\delta(x,y)]. \tag{2.14}$$

where $S(x,y)$ represents the superposition of the individual fields $P(x,y)$ and each delta function in $A_\delta(x,y)$ represents the spatial positioning of a single particle.[20,32] This convolution is further simplified via the application of the Convolution Theorem, which states that the convolution of two functions is equivalent to taking the inverse Fourier transform of the product of the functions' individual Fourier transforms,[20]

$$[P(x,y) \otimes A_\delta(x,y)] = \mathcal{F}^{-1}[\mathcal{P}(x,y)\mathcal{A}_\delta(x,y)]. \tag{2.15}$$

Therefore, combining (2.14) and (2.15) gives a simplified solution to the superposition of fields from multiple sources,

$$S(x,y) = \mathcal{F}^{-1}[\mathcal{P}(x,y)\mathcal{A}_\delta(x,y)]. \tag{2.16}$$

Therefore, a two dimensional, random array of delta functions is generated and convolved with the predicted scattering functions generated via Mie theory via (2.16) in order to generate modeled samples of polystyrene microspheres suspended in Aqua-Poly/Mount (Figure 2.15). Taking the two dimensional Fourier transform of these modeled samples gives a theoretical prediction for the scattering functions from multiple particles (Figure 2.16) for comparison to the experimentally determined scattering functions with the DFHM (Figure 2.17).

While a qualitative match between theoretical and experimental scattered fields (Figures 2.16 and 2.17) is visually satisfying, a more quantitative approach is required for validating the use of the DFHM for scattering measurements. We turn to goniometry for such a quantitative approach to particle sizing.[7,8,101–104] As the scattering functions generated via Mie theory (Figure 1.3) were revolved around 2π in order to generate a two dimensional scattered field, the two dimensional scattered fields measured experimentally in the DFHM (Figure 2.17) can be integrated over the range $0 \leq \phi \leq 2\pi$ in order to return experimental one dimensional scattering functions, $P(\theta)$.

We begin by normalizing the theoretical and experimental scattering functions (in order to account for intensity differences) and correcting the experimental scattering functions to account for the shift in angular dependence as a result of refraction through the mounting media-coverglass-immersion oil interfaces. This later step is the reverse process as described in (2.17), where instead of solving for the observed angle of scattering as a function of relative index of refraction and expected scattering angles, we solve for the

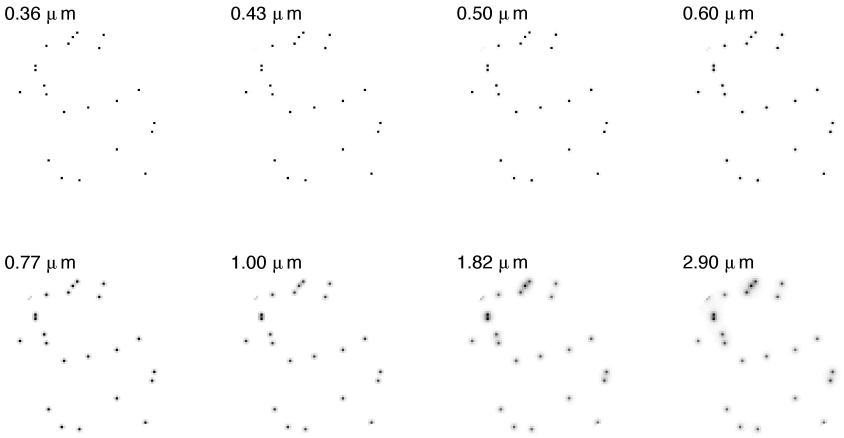

FIGURE 2.15: Random distributions of polystyrene microspheres ($0.36\mu m \leq d \leq 2.90\mu m$) embedded in Aqua-Poly/Mount are generated in the sample plane. The two dimensional Fourier transform of these modeled samples will return a theoretical model of the scattered fields which will be measured in the conjugate Fourier plane of the DFHM.

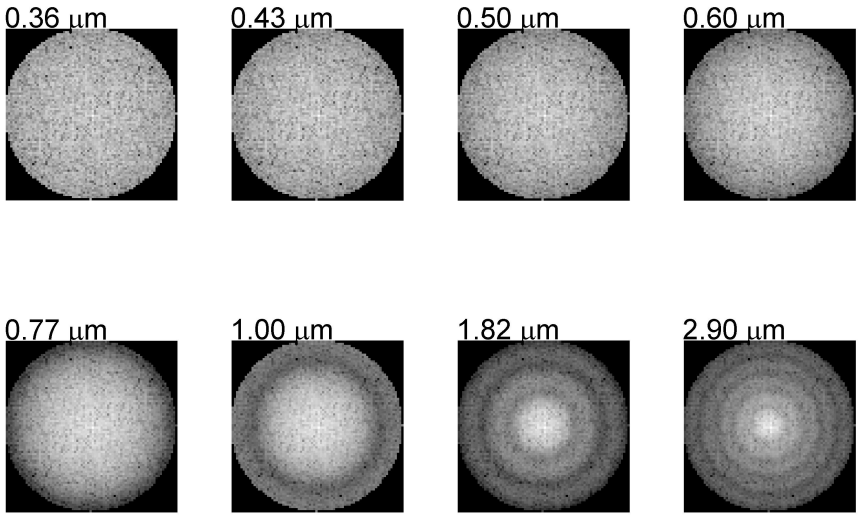

FIGURE 2.16: The two dimensional Fourier transforms (log scale) of random distributions of polystyrene microspheres ($0.36\mu m \leq d \leq 2.90\mu m$) embedded in Aqua-Poly/Mount (Figure 2.15) give theoretical models of the scattered fields which will be measured in the conjugate Fourier plane of the DFHM.

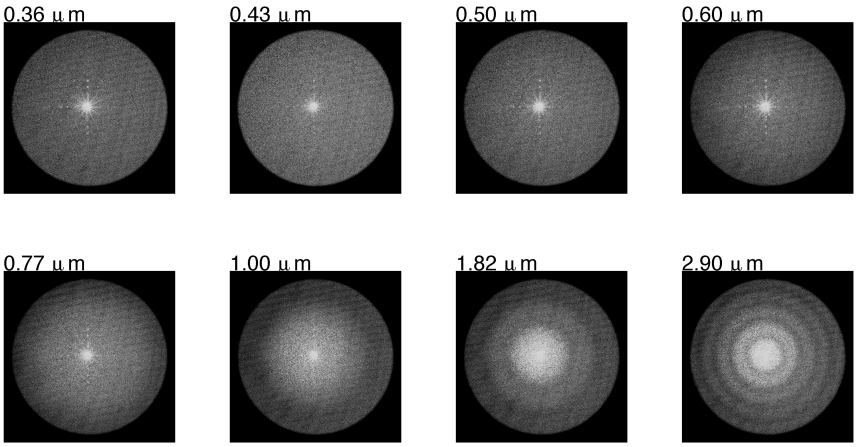

FIGURE 2.17: The scattered fields (log scale) from polystyrene microspheres ($0.36\mu m \leq d \leq 2.90\mu m$) embedded in Aqua-Poly/Mount, as measured experimentally in the conjugate Fourier plane of the DFHM. Agreement between the predicted (Figure 2.16) and experimental results is visually notable, in particular for the larger particle diameters, where concentric rings of diffraction match.

true scattering angles as a function of those measured and relative index of refraction,

$$\theta_{true} = sin^{-1}\left(\frac{n_{oil}}{n_{AQP}} sin\theta_{exp}\right), \tag{2.17}$$

where we now let θ_{exp} represent the angle of scattering as measured by the DFHM, $n_{oil} = 1.518$ for the immersion oil and $n_{AQP} = 1.457$ for the Aqua-Poly/Mount mounting media.

Upon carrying out the normalization and correction of the experimental data to account for refraction effects, we find that the experimental results closely match the theoretical predictions over the range of $8^o \lesssim \theta \lesssim 39^o$ (Figure 2.18), thereby confirming the ability of the DFHM to resolve scattering functions accurately in the conjugate Fourier plane. A comparison is given between the theoretical goniometric curves predicted via Mie theory (solid black lines) for these spheres and those measured (green circles).

The upper limit to the angle of measurement is in agreement with the previously determined maximum angle of scattering as determined via the calibration and scaling process (2.13). This upper limit was not possible for all particle diameters though. Looking at the larger particle diameters, $d \geq 1.0\mu m$, scattering strength falls off considerably for large angles. This is expected as large particles tend to be strongly forward scattering. This drop off for larger angles generally causes the broad scattering signal from larger particles to fall within the noise of the DFHM system.

Prior to generating each of these scattering functions, the background signal (as measured via a blank Aqua-Poly/Mount only coverglass in the DFHM) was subtracted out in order to remove background noise from the data. In doing so, the strong, central

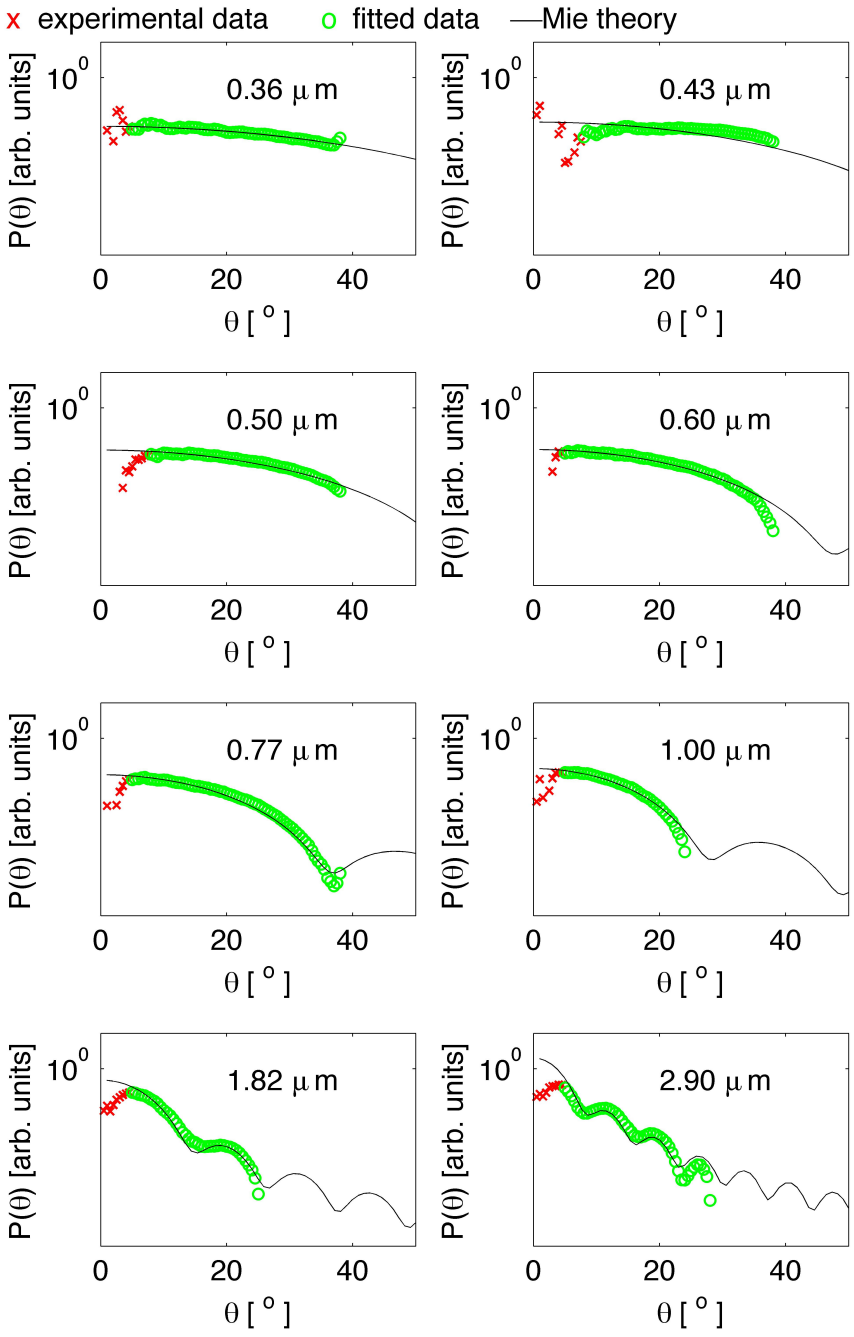

FIGURE 2.18: The DFHM is able to accurately discern fine details of the goniometry curves for the particles in suspension and therefore is correctly interpreting angle space at the conjugate Fourier plane.

DC component of the scattering fields was removed, depleting the signal in the forward direction of each scattering function. At best, this DC term only affects the first $1.8^o \pm 0.3^o$ of scattering when capturing images with short exposure times. However, at such short exposure times, scattering strength at broad angles is diminished and therefore imperceptible above the background noise. In order to bring up the signal from broadly scattered light, exposure times are increased. This has the effect of removing the DC component out as far as $\sim 8^o$, which accounts for the minimum range of efficacy in resolving the goniometric scattering functions in (Figure 2.17). Data falling below this range is indicated via red x's for each experimental curve in the figure.

A related note should be made with respect to the central dark spot located in the end product of the scattered field via image processing (Figure 2.5). This central dark spot was explained as a result of the removal of the DC component via heterodyne filtering. In fact, the ranges of the scattering angles removed in this fashion are exactly those mentioned with respect to the goniometry curves (Figure 2.17)—removal of the first $1.8^o \pm 0.3^o$ of scattering when capturing images with short exposure times, up to the removal of the first $\sim 8^o$ of scattering when using longer exposure times.

In addition to using goniometry to validate the use of the DFHM for scattering measurements, we turn to optical scatter imaging (OSI). As described previously (section 1.2.3), the optical scatter image ratio (OSIR) created via spatial filtering scattered light can be used as a metric for particle sizing. As a means of evaluating the application of the DFHM towards OSI, a predictive model is creating by generating a random distribution of polystyrene microspheres *in silico*. These polystyrene microspheres are assumed to be suspended in Aqua-Poly/Mount mounting media (Polysciences, Inc, Warrington, PA) in the sample plane, with their positions determined via a random two-dimensional distribution of delta functions. The scattered field of a given particle size is generated via Mie theory.[3] Parameters for this calculation are wavelength of incident light ($\lambda = 543.5nm$) particle size ($0.36\mu m - 2.90\mu m$) and index of refraction ($n_{ps} = 1.59$) and that of the mounting media ($n_{ps} = 1.457$).

In order to model a distribution of particles with true scattered fields (Figure 2.15), the Array and Convolution Theorems are used between the two-dimensional array of delta functions representing particle locations and the scattered field of one such theoretical particle.[20,32] Fourier transforms of these particle distributions are generated modeling the DFHM system (Figure 2.16). The resulting Fourier transforms represent the scattered fields from the respective particle distributions. Using the same digital spatial filtering on these modeled fields as will be used for the experimental DFHM data will give a set of theoretical predictions for the OSIR values which will be measured for polystyrene microspheres in suspension using the DFHM.

As was explained (section 1.2.3), a set of apertures was created using a central beam block ($\theta_{block} = 8^o$), minimum ($\theta_{min} = 15^o$) and maximum ($\theta_{max} = 39^o$) angles of acceptance.[9] The combination of the beam block and minimum angle of acceptance returns an annulus that accepts scattered light over the range of $8^o \leq \theta \leq 15^o$. This

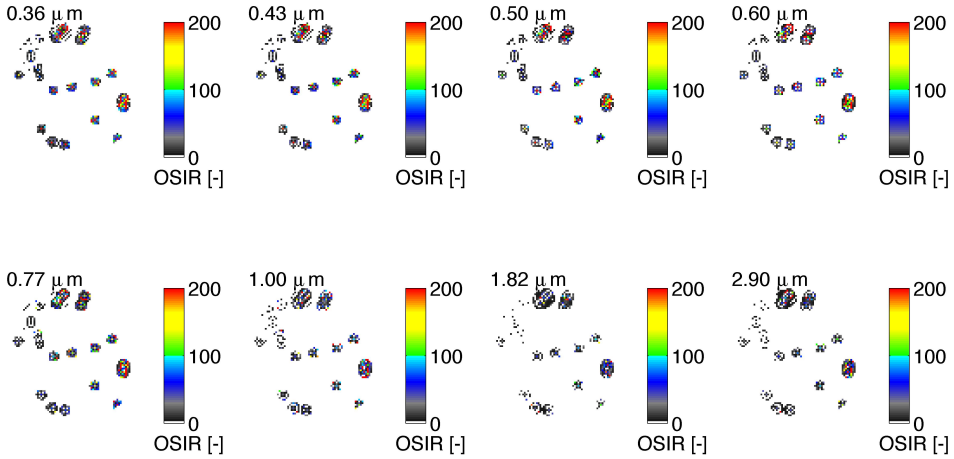

FIGURE 2.19: Passing the scattered fields (Figure 2.16) through the described HNA and LNA spatial filters and taking their ratios results in the predicted OSI false color image. Notice that the OSIR generally decreases with particle size.

annulus is called the low numerical aperture (LNA) filter. Similarly, a high numerical aperture (HNA) filter is generated over the range $8^o \leq \theta \leq 39^o$, where the beam block and upper angle of acceptance is determined by the experimental design of the DFHM. These filters are generated digitally as masks of unity value for pixels which are passed and zero for those which are blocked.

The pixel-by-pixel multiplication of the two spatial filters with the scattered fields (Figure 2.16) returns a set of HNA and LNA filtered Fourier transforms of the respective scattered fields. Taking an inverse Fourier transform of the spatially filtered fields returns spatially filtered images of the samples—one having undergone a high pass filter and the other a low pass filter. Again following the OSI method originally described, we now generate the Optical Scatter Imaging Ratio (OSIR) digitally via the pixel-by-pixel division between the HNA and LNA images (Figure 2.19)

$$OSIR(x,y) = \frac{I_{HNA}(x,y)}{I_{LNA}(x,y)}, \tag{2.18}$$

where $I_{HNA}(x,y)$ and $I_{LNA}(x,y)$ represent the pixel-by-pixel intensities of the HNA and LNA image planes, respectively.[9] The HNA filter includes the area of the LNA filter. Therefore, upon taking the ratio between the two, the resulting OSIR will always be greater than or equal to unity because the resulting HNA image contains all of the information included within the LNA image plus more.

By Mie theory, larger particles are expected to be predominantly forward scattering, while smaller particles are expected to have increased levels of side scattering as compared to their forward scattered light. As a result of this, the OSIR values are expected to be

greatest for the smallest particles and then drop off towards unity for larger particles. As seen in the modeled OSIR results (Figure 2.19), the false coloring of the particles based upon the OSIR is largest for the smallest particles and decreases with increasing particle size.

Due to its sharp edges, use of a digital spatial filter can generate high spatial frequency noise upon enacting the inverse Fourier transform. This noise can be detrimental to the model (and later experiment), but can be dealt with in a couple of fashions. First, the edges of the spatial filters can be smoothed via a smoothing window, such as the Hamming or Hann windows.[99] Alternatively, thresholding and morphological operations can be used in order to bring out the particle signal as compared to the noise and surroundings. The later was carried out in the modeled results presented here. The predominant reason for choosing the later method over the former is that the smoothing of the windows has the effect of removing information from the system prior to taking the inverse Fourier transform, such that the overall results will not accurately reflect the OSIR in the image plane.

This model was run a series of ten times in order to generate average OSIR values and the corresponding standard error of the mean for each particle size. These results serve as the scale for comparison to the experimental data generated by the DFHM.

The same methodology modeled above is then applied physically via the DFHM system. Particles in the range of $0.36 - 2.90\mu m$ were suspended in the manufacturer's Aqua-Poly/Mount mounting media (Polysciences, Inc, Warrington, PA). Particles were suspended in roughly $1M$ concentrations within the mounting media and a coverslip was placed over the top of the suspension to seal it in and supply a coupling surface for the objective's immersion oil. However, upon mixing with the microsphere solutions with the viscous mounting media, homogeneous concentrations were not able to be maintained.

For reference, the reconstructed hologram and OSI from the $d = 2.90\mu m$ polystyrene micropsheres are given (Figure 2.20). As with all of the polystyrene images and the resulting image processing, these images were filtered with a LNA filter of $8^o \leq \theta \leq 15^o$ and HNA filter over the range $8^o \leq \theta \leq 39^o$ in order to determine the experimental OSIR (2.18). As with the theoretically modeled data, these images did undergo some mild image thresholding in order to remove background noise, however all images were dealt with equivalently so as to maintain consistency in the image processing methods between samples.

After thresholding, the images were then used to create binary masks, which then were used to generate connected components using the `bwconncomp` command in MatLab. This allowed us the means of determining the average OSIR for each individual particle (or region of space, as was likely the case with the smaller particles). The resulting average OSIR values are plotted versus particle diameter for polystyrene microspheres in mounting media, as compared to resutls predicted from the Mie theory model implemented (Figure 2.21). The experimental and theoretical predictions for the OSIR versus particle diameter are in good agreement, ensuring confidence in the ability of the DFHM to be used for

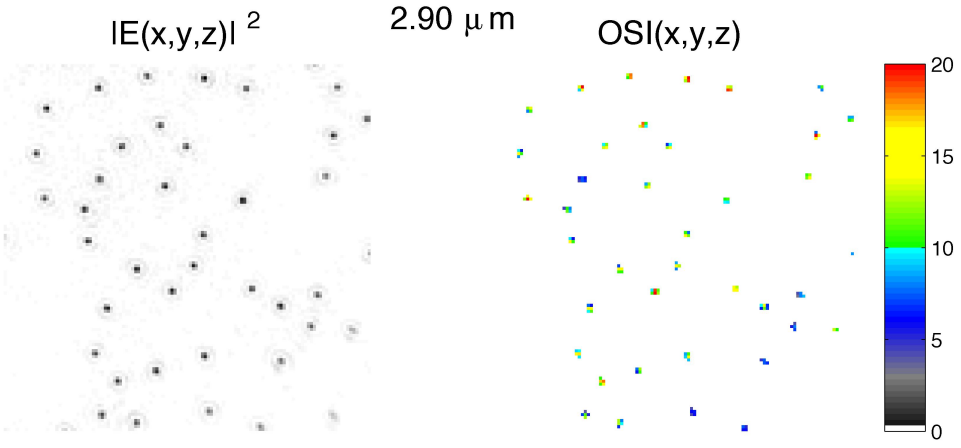

FIGURE 2.20: Experimentally determined OSI figures from the $d = 2.90\mu m$ polystyrene micropsheres are given. In addition, the reconstructed hologram is also given for reference.

particle sizing via OSI.

2.5. Experimental Results

As a demonstration of the functionality of the DFHM system, we begin by working with a 1951 USAF (negative) Test Target (R1DS1N, ThorLabs, New Jersey). The field of view imaged via CCD2 in the image plane is given for reference (Figure 2.22).

As a demonstration of the numerical focusing process, a tiled figure (Figure 2.23) is given where the depth of focus increases from $5mm$ to $21mm$ moving through the images from a) to d). This process is carried out for a single twin image. Were we to proceed with the numerical propagation beyond the depth of focus, the object would then move back out of focus.

Upon focusing the object to its focal plane, the resulting amplitude and phase images are given (Figure 2.24). The phase image is "wrapped" because phase is always computationally bound to the range of $-\pi$ to π. A magnified region of the USAF target is then displayed (Figure 2.25) displaying the amplitude, and wrapped and unwrapped phases of the target. The smallest groupings of lines are the group 7, element 6 lines, measuring $2.2\mu m$ in width. Having successfully demonstrated the functionality of the DFHM on a known calibration standard, we move on to the investigation of biological

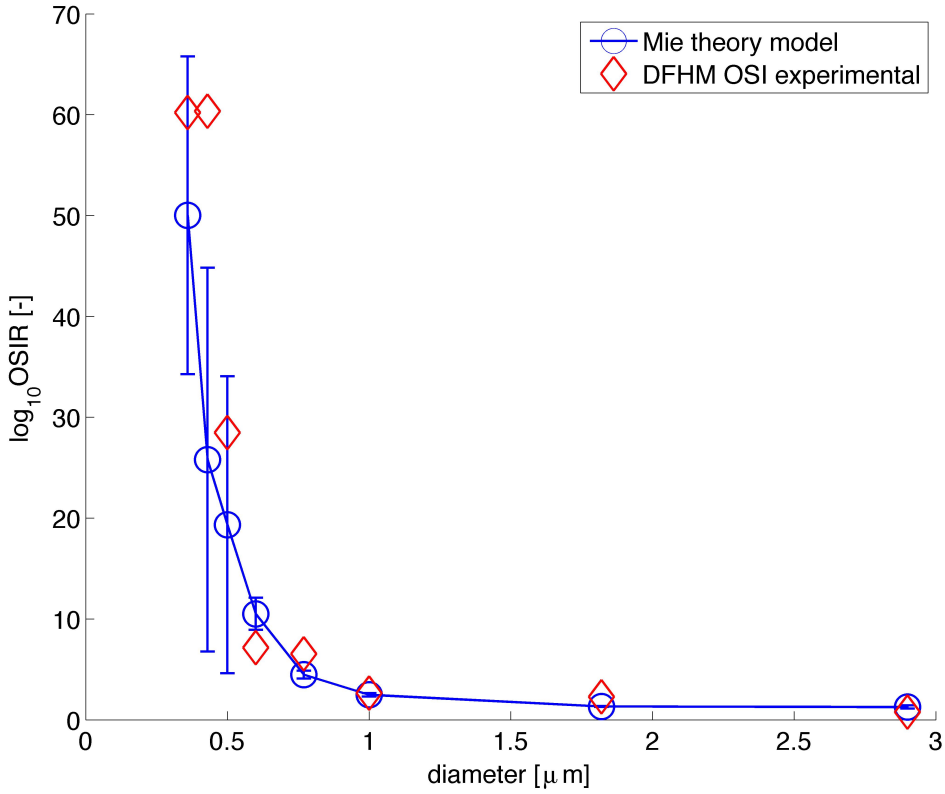

FIGURE 2.21: Polystyrene microspheres from 0.36 to 2.90μm in diameter were suspended in the manufacturer's mounting media and imaged with the DFHM. The collected scattering function is then spatially filtered and analyzed via optical scatter imaging using angles $\theta_{block} = 8^o$, $\theta_{min} = 15^o$ and $\theta_{max} = 39^o$. The expected OSIR was determined for each particle size based on the Mie theory model (blue) circles and solid curve with error bars. The average and standard deviation of the mean for the OSIR were determined from ten trials. Experimental results using the DFHM for OSI are displayed as (red) diamonds.

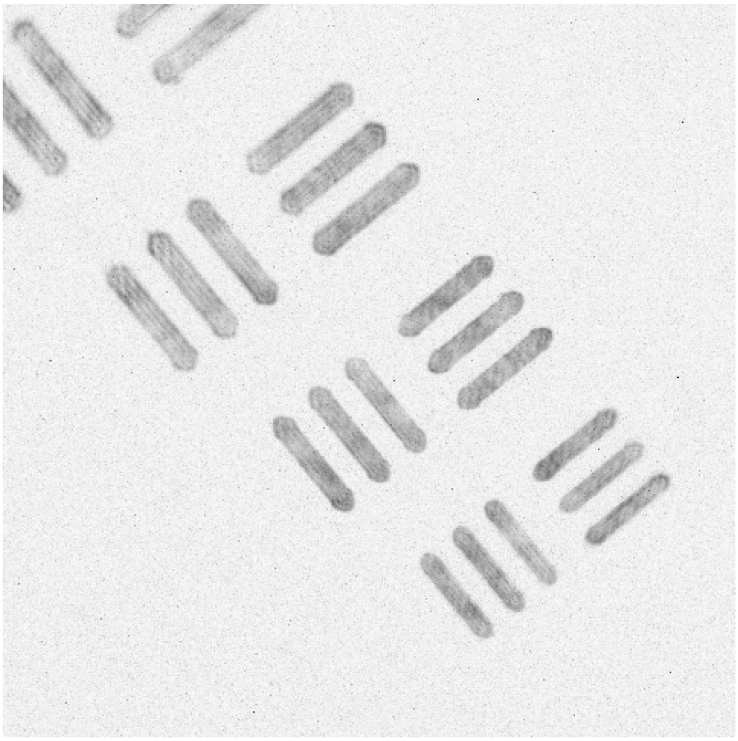

FIGURE 2.22: A 1951 USAF test target is imaged in the DFHM system. This particular target is a negative target, such the markings are etched and transparent, while the remainder of the target is masked. The smallest elements seen here are element 6 from group 7, 2.2μm in width.

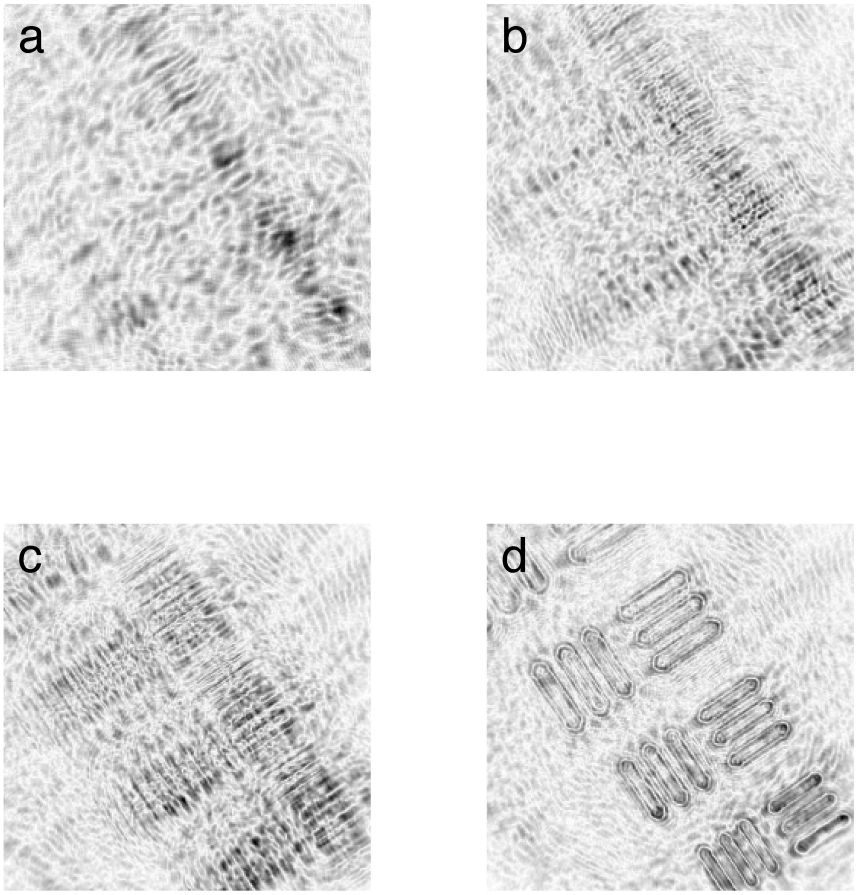

FIGURE 2.23: A 1951 USAF test target is imaged in the DFHM system. These tiles represent the numerical focusing process, where it is clear that the hologram is converging to a focus with increased depth of numerical refocus (a - d).

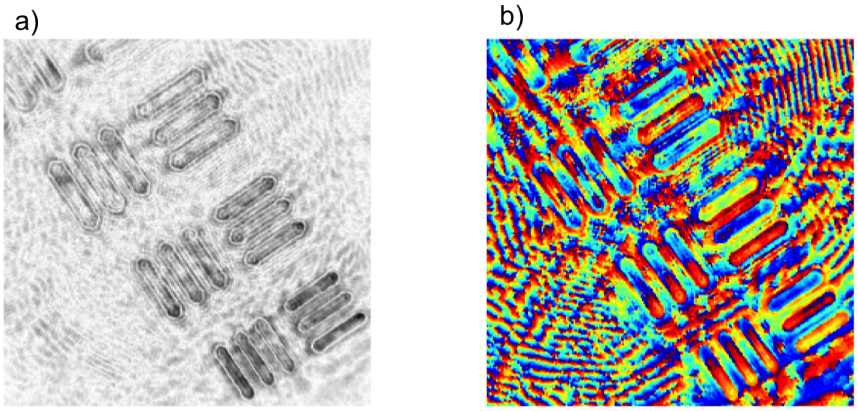

FIGURE 2.24: A 1951 USAF test target is imaged in the DFHM system. a) The amplitude and b) wrapped phase of the hologram.

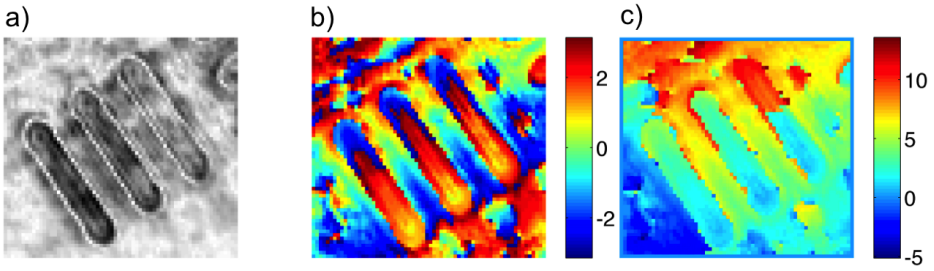

FIGURE 2.25: A magnified field of view is selected from the previous figure, and the corresponding a) amplitude, b) wrapped phase, and c) unwrapped phase are displayed.

samples.

The DFHM was also applied for the OSI of cells in culture. A glass culture chamber was made to hold cells in the DFHM for an extended period of time. This way, cells can be imaged in real time while undergoing some perturbation. A syringe is embedded at the bottom of the glass chamber so tissue culture media can be swapped out to add chemicals in order to elicit a physiological effect. The resulting time course of OSIR images could then be used to determine a time course of the physiological response, with respect to intracellular morphological changes.

In this fashion, human osteosarcoma MG63 cells were imaged in the DFHM over the course of an hour. Prior to imaging, cells were passaged and plated in the glass culture chambers and placed in the incubator at 37^oC and $5\%CO_2$ for three hours in normal tissue culture media (DMEM with 10% FBS, 1% l-glutamine, 1% pen/strep). After about a half hour, cells were mostly attached to the inner wall of the glass chamber, however it takes

a few hours for the cells to flatten and spread out on the glass. Due to the small size of the chamber (volume $\sim 120\mu L$) and poor circulation for oxygen exchange, the media was changed every hour in order to keep the cells alive. After three to four hours, cells had flattened and spread out on the glass coverslip and were ready for imaging in the DFHM.

First, a set of cells was imaged via OSI in normal tissue culture media as a time control group. This works as a test of whether or not the sustained presence of the cells in the DFHM was detrimental to their survival. Cells were imaged over the same field of view for 67 minutes and holographic images were taken at the zero and two minute time points and then every five minutes until reaching the final time point.

Afterwards, a second glass culture chamber with fresh cells was placed in the DFHM. A holographic image was collected at the zero time point while the cells were still in the normal tissue culture media. Upon collection of the zero time point, the media was quickly drawn out of the chamber via the syringe and new media was placed in the chamber. This new media was the same as the normal tissue culture media, but with the addition of $1\mu M$ staurosporine (STS), which is a chemical agent known to trigger the onset of apoptosis in cells, including this particular MG63 cell line.[105] As such, it was anticipated that the MG63 cells would undergo some morphological changes over the imaging time course—namely that swelling would result in the mitochondria with the onset of apoptosis. Holographic images were collected over the course of 70 minutes, collecting holographic images every minute for the first five minutes and then in two and finally three minute increments. The resulting OSI images were constructed via post-processing, an example of which is given for reference (Figure 2.26).

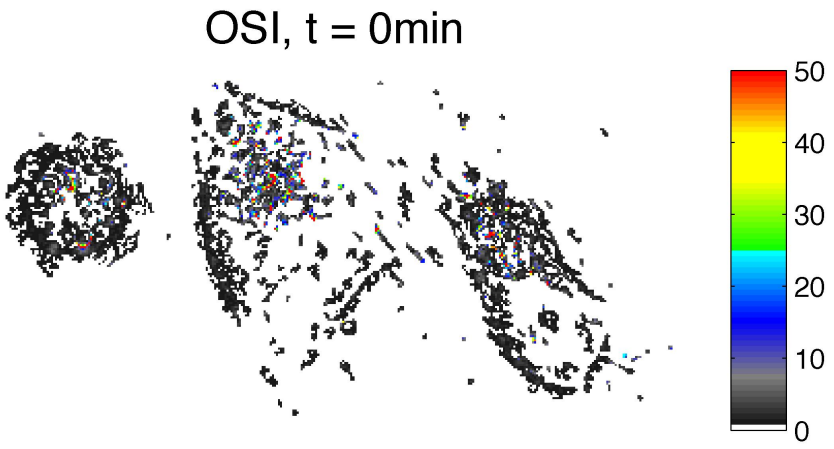

FIGURE 2.26: An example of the resulting OSI images of cells *in vitro*. The three distinct cells seen here are MG63 human osteosarcoma cells. This particular image is the zero time point from the STS experimental group. The colorbar represents the scale of the OSIR in the image.

2.6. Discussion

To this point, digital Fourier holographic microscopy has not be explored to its fullest. Two groups have posted work on DFHM in the literature, but much room for improvement has been left. As mentioned in the introduction, Seet, et. al demonstrated the use of a DFHM system in transmission, but did not attempt to rigorously calibrate the system or use it in conjunction with some quantitative metric, as is done here.[41]

More thorough work has been done with DFHM systems by Alexandrov, et. al., who have applied Mie theory for quantified particle sizing.[106–108] A difference between their systems and that presented in this work is that their systems work in reflectance, whereas this work presents the use of a DFHM in transmittance. The use of the DFHM has challenges associated with its design and implementation in transmission—namely the presence of the large DC component at the center of the conjugate Fourier plane, which can saturate and limit the dynamic range of the system (both spatially and in terms of pixel depth).

The systems built by Alexandrov, et. al. work around scattering angles in the range of $\theta \sim 135^o$. While there is sufficient information to descriminate between particle sizes at those more obtuse scattering angles (Figure 1.3), scattering amplitudes will generally be small. No matter the particle size over the range of interest, particles will still tend to have dominant scattering in the forward direction as compared to their respective levels of side scattering. In addition, as we've seen from the scattering functions for intracellular bodies (Figure 1.6), when considering scattering by cells we are predominantly interested in forward and acute angle scattering. The use of a DFHM in transmission mode gives us access to those more acute scattering angles and is only limited by the central DC component. In this sense, the DFHM used in transmission mode will be more capable of detecting scattering by intracellular objects such as mitochondria and nuclei.

Interpreting the OSI results for polystyrene microspheres (Figure 2.21), we see that the OSIR did a god job of falling off with increased particle diameter as expected. Looking at the predicted OSIR values based upon the Mie Theory model (blue circles), we see a great deal of variation at and below the $0.50\mu m$ particle diameter. Above this range, the OSIR values predicted via the theoretical model have small variations and the experimental results (red diamonds) are also in good agreement. While the experimental results also fall off with increasing particle diameter, the $0.43\mu m$ diameter particle failed to sit within the standard error of the mean as predicted via the theoretical model. Based upon this result and the overall uncertainties of the $0.50\mu m$ and smaller diameter microspheres, we cannot claim that the DFHM system can accurately determine the size of particles in this lower range via OSI. We can however see that the OSIR does fall off with increased particle size over the entire experimental range.

The theoretical limit to the resolution of this system is $d_{min} = 0.255\mu m$, as deter-

mined by

$$d_{min} = \frac{1.22\lambda}{2NA}, \tag{2.19}$$

where $\lambda = 543.5nm$ and $NA = 1.30$.[32] Based on the inability to use the OSIR in order to accurately measure particles at and below the $0.50\mu m$ diameter, it is likely that they fall below the actual resolution of the DFHM system.

Looking at the OSIR results generated via the DFHM system in more detail, the experimental resolution limit of the OSI analysis lies around $0.50\mu m$. Judging by the numerical aperture of the objective however, we anticipate that the system should measure out to a maximum angle of 55.3^o (when using the polystyrene microsphere mounting media) and have resolution down to $0.255\mu m$. At present the system does not meet these theoretical limits, having a maximum angle of acceptance at the CCD of 38.9^o and being unable to accurately resolve at or below $0.50\mu m$ diameter microspheres via the OSIR. The lower range of angles accepted at the CCD is a result of the final lens in the sample arm and immediately prior to the conjugate Fourier plane, which overly magnifies the Fourier transform. This overfills the CCD at present. Replacing that $f = 300mm$ bi-convex lens with a new lens with a focal length less than $168mm$ would allow the capture of the maximum angle of 55.3^o as predicted via the numerical aperture of the objective. A $f = 150mm$ bi-convex lens would adequately map the full range of angles to the CCD, while not causing too great a loss of resolution by underfilling the CCD. While this modification would improve the range of angles mapped to the CCD, it does not guarantee that the system would be able to resovle the $0.36\mu m$ polystyrene particles and get closer to the resolution limit set by the numerical aperture of the objective, but it should help.

An additional note should be mentioned with respect to the digital spatial filtering of the scattered field, as well as the isolation of the desired twin image. As discussed, each time we crop the digital image or Fourier transform, we impart hard edges on the spatial (frequency) distribution. Enacting on such a cut or filtered digital representation with the Fourier (inverse Fourier) transform will result in high frequency ringing. In order to limit this ringing effect, apodization can be used to smooth out the edges, thereby reducing or removing the high frequency noise that would otherwise result.[20] Common tools used for smoothing the spatial frequency window include the Hamming and Hann windows.[99] As an alternative, we use a modified version of the error function (`erf` in MatLab) in order to create a spatial frequency window which can be adjusted for width and the sharpness with which it drops off.

While the use of a smoothing spatial frequency window helps to remove high noise ringing upon Fourier (and inverse Fourier) filtering, it also has the effect of attenuating the signal from the sample at the edges of the sample or frequency space. This loss of signal will also cause the range of acceptance angles in Fourier space to be slightly decremented and can also be attributed with the low maximum angle of acceptance observed at the conjugate Fourier plane.

As an alternative to the use of smoothing windows, images can be reconstructed with the hard edges and the resulting high frequency noise can be cleaned up via image thresholding and morphological operations.[99] Use of these alternative tools comes with their own set of caveats, which generally reduce again to a loss of information. A combination of both of these techniques has been employed in generation of the OSI results presented here. Boustany's original OSI work gets around the noise generated by taking the pixel-by-pixel ratio of two images by binning pixels into larger pixel groups. Each bin is then averaged in order to determine the local average OSIR within the image.

While it would be ideal to be able to reach the minimum predicted resolution of the DFHM at $0.255\mu m$, minimum sizes of mitochondria are around $\sim 0.50\mu m$. Therefore, this system should be sufficient for detecting mitochondria in cells. Although the application of OSI via the DFHM has failed to accurately pick out and resolve the $0.36\mu m$ polystyrene microspheres, the goniometric analysis was still able to sufficiently match the theoretical predictions. This tells us that the scattering information from the $0.50\mu m$ diameter and smaller particles is accessible via the DFHM, however more work needs to be done to try and coax it out via the application of OSIR. Variations in spatial filters may be applied in order to maximize the OSIR signal for smaller particles in an attempt to reach the predicted limit to the resolution of the DFHM. The OSIR may also be enhanced by taking the autocorrelation between the experimentally determined scattering functions and those predicted via Mie theory. This could have the effect of amplifying the true scattering signal above the noise of the system or that generated via the Fourier transform.

In analyzing the application of the DFHM towards OSI of biological samples, the OSIR returns a false colored image meant to give information of the sample, not necessarily to improve its resolution. In order to evaluate the OSIR characteristics of a given sample, we can generate a histogram of the measured OSIR values across the sample. Given the varied and dynamic composition and geometries of biological samples, this histogram should generally represent a normal distribution. By assessing the maxima and broadness (FWHM) of histograms from different biological samples of similar type, it should be possible to determine a change in scattering and therefore size distributions within the samples via the OSIR. If an experimental group shifts its maximum towards lower OSIR values, this would indicate a general increase in particle size. A shift in maxima towards larger OSIR would indicate shrinkage of structures within the sample. In cells, these morphological changes can be attributed to the likes of mitochondria or other intracellular bodies. In the context of imaging skin samples, this can be indicative of collagen structures—whether there is an increase or decrease in the thickness of collagen bundles within the tissue.

Using this method of analysis, distributions of OSIR values were generated for both the time control (Figure 2.27) and experimental STS (Figure 2.28) groups for the MG63 cells. The histograms were normalized for each time point prior to comparison. To avoid cluttering the figures, histograms are not given for all time points. Instead, histograms are displayed for the first (blue) and final (red) few time points for comparison.

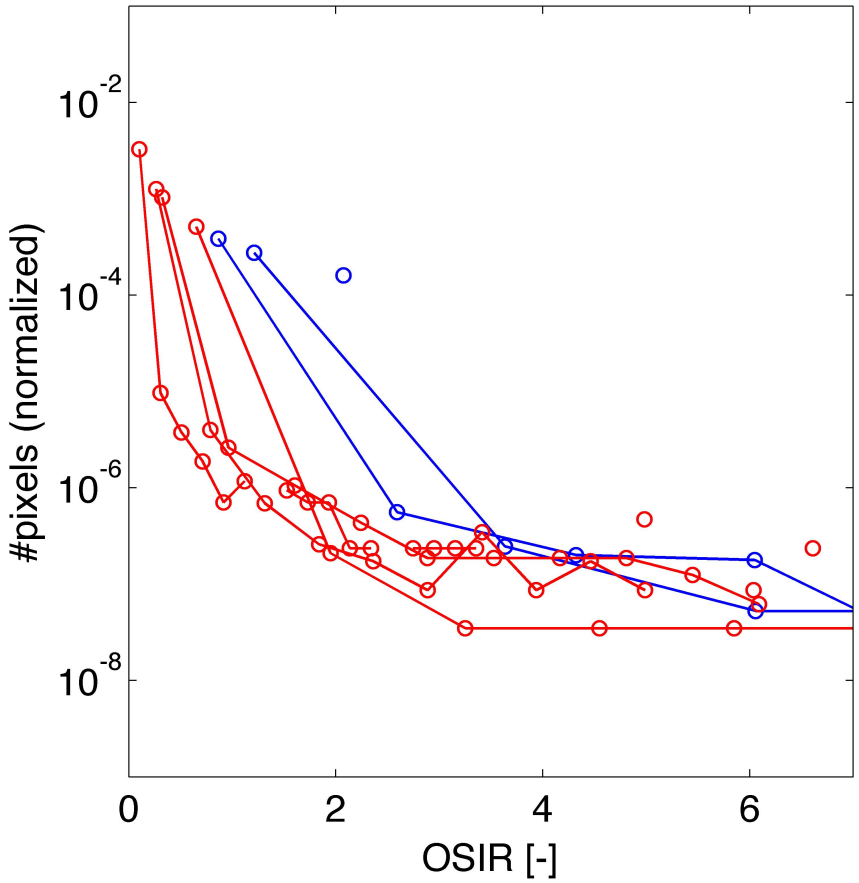

FIGURE 2.27: The OSIR values from the first (blue) and last (red) few time points in the control group are displayed. A definite shift towards lower OSIR values is seen in the time control group. This shift towards lower OSIR values is associated with an increase in particle sizes at the intracellular level. The physiological cause of this swelling is not understood at this time, but it is likely that the cells are not viable in the DFHM for such a long period of time.

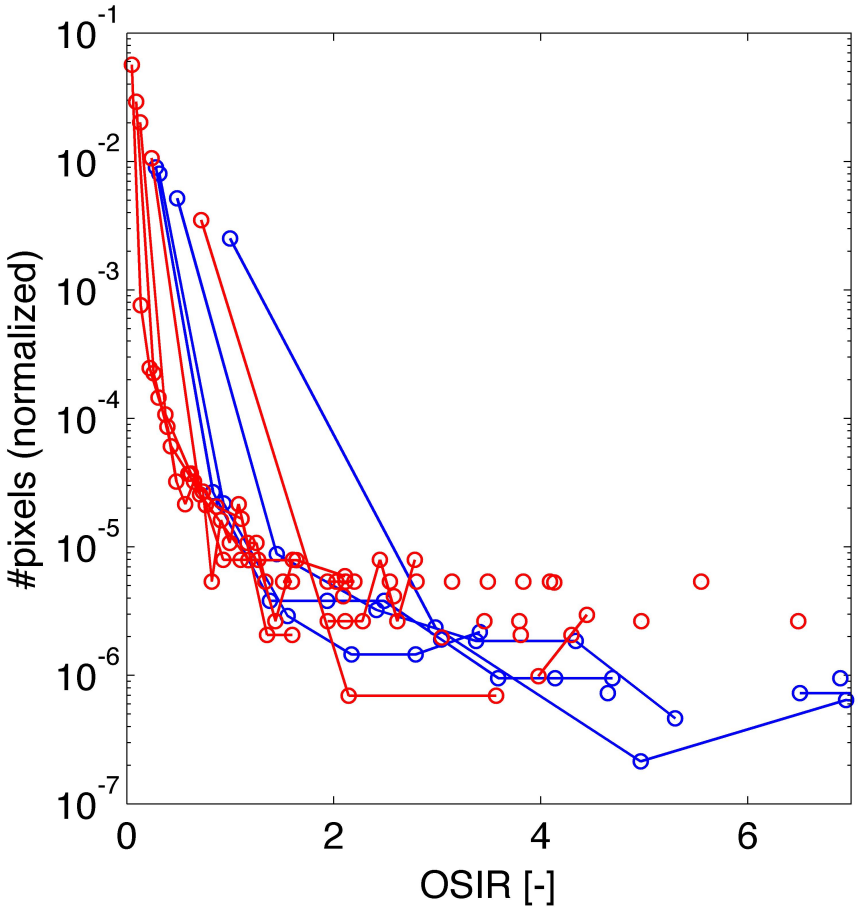

FIGURE 2.28: As with the time control group, we see a time dependent shift in the experimental STS group towards lower OSIR values. Because we see a similar shift in the time control group, we cannot attribute the shift in the experimental group to the swelling of the mitochondria and the onset of apoptosis.

While there is some variability, the experimental STS group of MG63 cells does tend towards a narrower distribution of OSIR with an increase in time (Figure 2.28). However, we see a similar shift towards lower OSIR values with increased time for the time control group as well (Figure 2.27). Since the results for the experimental and control groups in this experiment are similar, we cannot conclude that the shift towards lower OSIR values with time in the experimental STS group is associated with swelling of mitochondria and the onset of apoptosis. That there is variation measured in the OSIR as a function of time for both the experimental and control groups does suggest that OSI via DFHM can be used as an optical assay to detect morphological changes in subcellular structure.

A possible explanation for both the experimental and control groups having similar responses would be that the cells are not viable in the DFHM for an extended period of time. Ultimately, it would be prudent to continue this investigation by determining the specific effects on cells due to their protracted presence in the DFHM. Once that issue has been resolved or accounted for, further investigations in the onset of apoptosis can be made using the DFHM for OSI. Such experiments can again be related to the presence of STS or even carrying out PDT *in vitro* while cells are housed in the DFHM.

As an alternative to measuring the OSIR as the ratio of the HNA to LNA images, we can take the inverse relationship which would then accentuate forward scattering (LNA) over side scattering (HNA),

$$Fwd/Side = \frac{LNA}{HNA}. \tag{2.20}$$

Because this new metric is the inverse of the OSIR, as we move towards larger structures the $Fwd/Side$ ratio would therefore increase with increased size.

Images of thin ($\sim 10\mu m$ thick) tissue slices were imaged and analyzed using the $Fwd/Side$ metric via the DFHM. Samples were of the human dermis, and were acquired post-biopsy from the OHSU Dermatology clinic. Samples were biopsied under the standard of care for clinical reasons other than those of this project. In addition, since no patient data was associated with the samples, IRB approval was not required.

Varied fields of view were imaged over different samples, from separate patients. The use of the $Fwd/Side$ metric can be indicative of collagen structure and bundling within the dermis. Larger collagen strands are visible in the reconstructed holograms and are enhanced via the $Fwd/Side$ ratio (Figure 2.29).

From the skin sections imaged, histograms are generated for the distribution of $Fwd/Side$ ratios within each respective image (Figure 2.29). The resulting histograms show similar distributions for collagen structure and bundling in the first two images (a and b). The third and fourth samples (c and d) show an increasing predisposition towards lower $Fwd/Side$ ratios, indicating smaller overall structure. The histograms generated form these four data points corroborate these conclusions—the fourth field of view (d) shows smaller collagen structure in both the reconstructed hologram and $Fwd/Side$ images, and the corresponding histogram shows a distribution that is slightly shifted towards lower $Fwd/Side$ ratios.

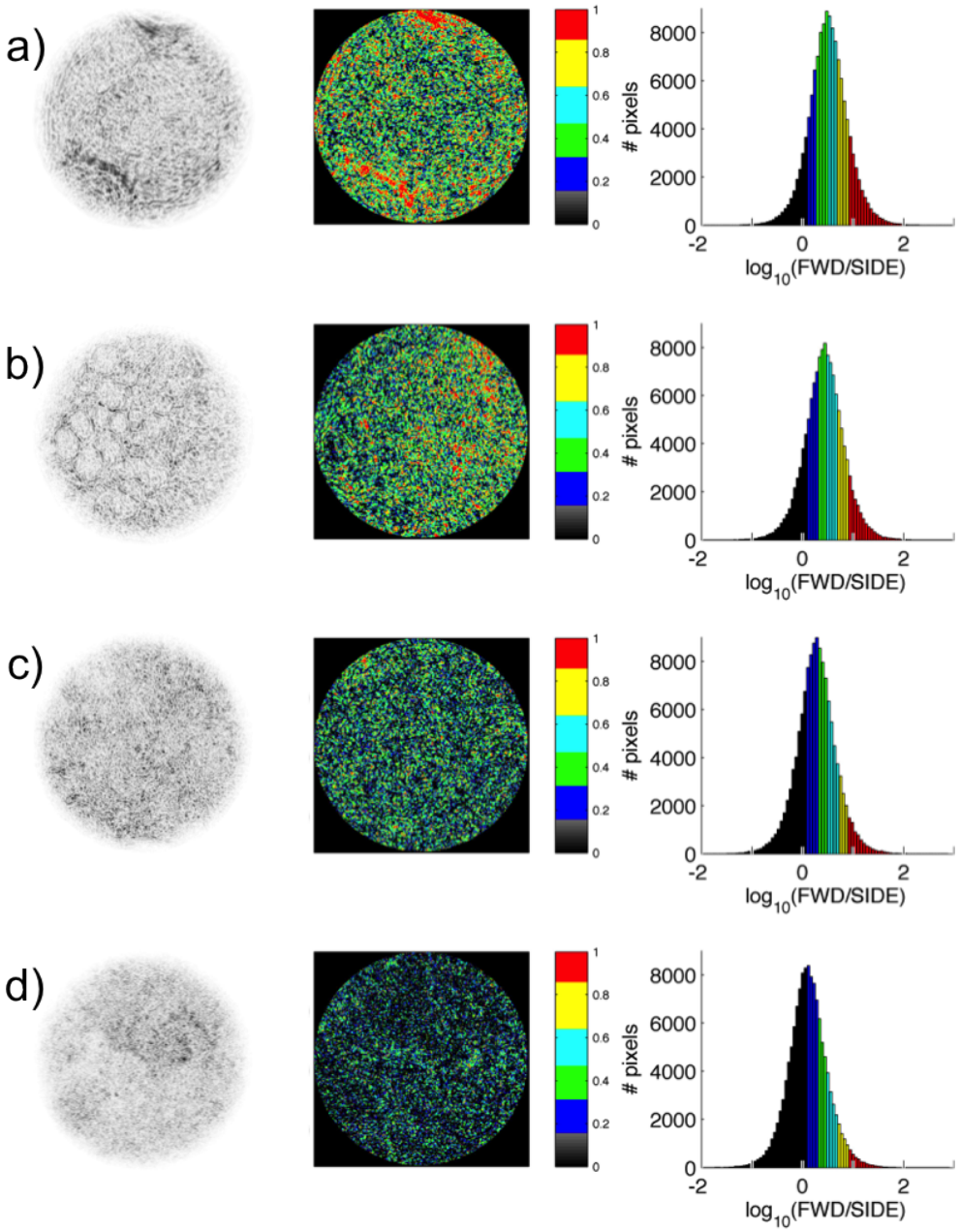

FIGURE 2.29: Images were collected of collagen in thin tissue slices with the DFHM. Image groups a-d are from different samples. Reconstructed holograms of each sample are in the left most column. The corresponding $Fwd/Side$ reconstructions are in the central column and their corresponding histograms are in the right column. We see that the $Fwd/Side$ images emphasize collagen structure within the samples and that variation between structures is apparent based upon the overall pixel values and the corresponding histograms. Note that the $Fwd/Side$ ratio can be less than unity, which was not the case for its inverse, the OSIR.

The use of the $Fwd/Side$ ratio via the DFHM system has shown the ability to resolve collagen structures within tissue slices and can generate quantitative data for analysis. Such data could be useful in determining relationships between different stimuli or conditions and collagen bundling in the dermis, such as hydration or aging effects.

Beyond the application of the DFHM towards OSI, additional functionality can be achieved from the numerical refocusing of the sample and the recovered phase information. Namely, the DFHM can be used for 3D imaging and quantitative phase imaging (QPI). As the scattered field is numerically refocused, a stack of image planes can be built up and translated into a voxel space. With the appropriate scaling along the z-axis (the direction of light propagation in the system), this stack of image planes could them be interpreted as a 3D image of the sample, illustrating its extension through a volume.

Alternatively, instead of projecting a sample's extension through space, numerical focusing and localized focusing metrics can be used in order to determine the best plane of focus for a localized region of the sample. Such metrics for automated focus detection include variance in amplitude, the Laplacian of Gaussian, phase and amplitude extrema detection as a function of depth.[18,109–112] Once the localized focus is determined for a sample, each region can then be numerically brought into focus simultaneously.[112]

As a demonstration of the means of bringing multiple objects from different depths of focus into focus simultaneously, the variance between pixels in a local region is evaluated across all reconstructed depths.[112] After constructing a 3D voxel space via numerical refocusing, the field of view is broken into localized 20×20 pixel regions. The variance in intensity is measured for each bin as a function of depth of focus. Bins that are void of objects ("blanks") are found by comparison to the median variance of all bins across all depths of focus. Additionally, bins that have uniform intensities and therefore minimum variance ("flats") are also identified. Flats occur when the object size is larger than the bin, such that the variance metric fails to identify the proper depth of focus because there is no variance index. In both the blank and flat scenarios, bins are then numerically propagated to the mean depth of focus determined from the surrounding bins. All other bins are numerically refocused to their respective depths of maximum variance—which coincides with an object being brought into focus (bright intensity) while the surroundings remain out of focus (low intensity). This leads to the maximum variance as a function of depth when an object in comes into focus.

Using this methodology, we are able to successfully bring objects at different depths into focus simultaneously. As an example, a sample of $2.90\mu m$ polystyrene microspheres is numerically refocused to a single depth such that a single microsphere remains in focus (Figure 2.30a). Upon applying the focus detection criteria, multiple microspheres are brought into focus simultaneously while the original particle remains in focus as well (Figure 2.30b), demonstrating that objects originally out of focus can be simultaneously brought into focus while objects at different focal planes maintain focus.

Looking now towards QPI, the phase measured across a sample (relative to some background phase) will be dependent upon the sample's optical path length OPL, which

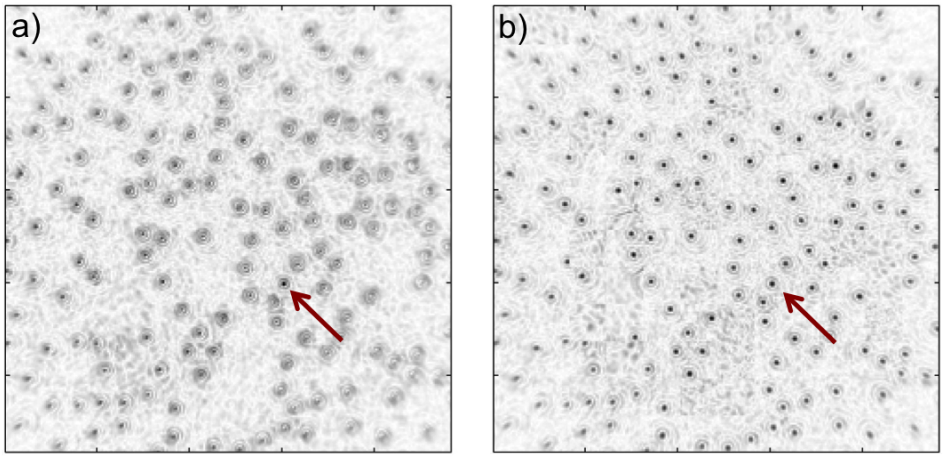

FIGURE 2.30: a) A sample of 2.90μm polystyrene microspheres in mounting media is numerically propagated to a plane out of focus for most particles. However, a single particle is resolved in this plane (red arrow). b) The numerical refocusing metric is applied for 20×20 pixel regions across the field of view and measured as a function of depth in order to determine the optimal numerical refocusing depth for each region. Multiple particles are then brought into focus in an automated fashion across the entire field of view, while the original particle in focus from (a) remains in focus (red arrow).

is a product of the sample's physical dimension d and index of refraction n,

$$OPL = dn. \tag{2.21}$$

Phase is indicative of the number of cycles the electromagnetic field has oscillated in traversing space.[113,114] Since a number of cycles may occur across a given object, the phase determined computationally will generally exist between $-\pi \leq \phi \leq \pi$ and therefore be "wrapped" (Figure 2.31b). Phase unwrapping algorithms can then be applied in order to reconstruct a continuous phase distribution across the sample and field of view (Figure 2.31c).[26,115] Note that the characteristic wave front is apparent in the wrapped phase image, and somewhat less so in the unwrapped phase image. If the spherical nature of the wave front is disruptive, it can be compensated for by using the phase distribution in order to determine the curvature of the wave front. The wavefront can then be flattened.[116]

The combination of the particle depth and index of refraction will work to slow the speed of the wave down (relative to some portion of the wave traveling through free space) when the wave enters the particle. From this, and assuming we know its index of refraction, we can determine the extension of an object by taking the difference between its unwrapped phase ϕ_{UW} and that of the background ϕ_{med},[18,19,27,113]

$$h = \frac{\lambda}{2\pi} \frac{\phi_{med} - \phi_{UW}}{n_{med} - n_{cell}} \tag{2.22}$$

The extension of an object's depth can therefore be surmised based upon the unwrapped phase distribution of the object and a known (or assumed) index of refraction (Figure

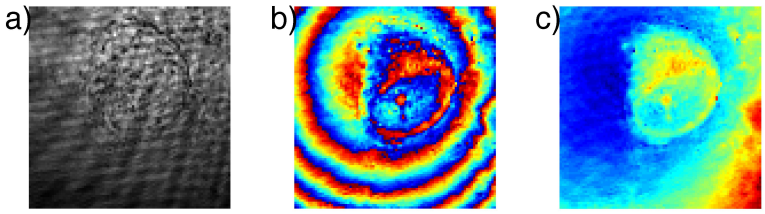

FIGURE 2.31: The a) amplitude, b) wrapped phase, and c) unwrapped phase based on the reconstructed hologram of an endothelial cell in media.

2.32). Similarly, if we were able to determine the size of a particle in another fashion, the phase distribution across the particle would be indicative of a distribution of index of refraction variations across the sample.

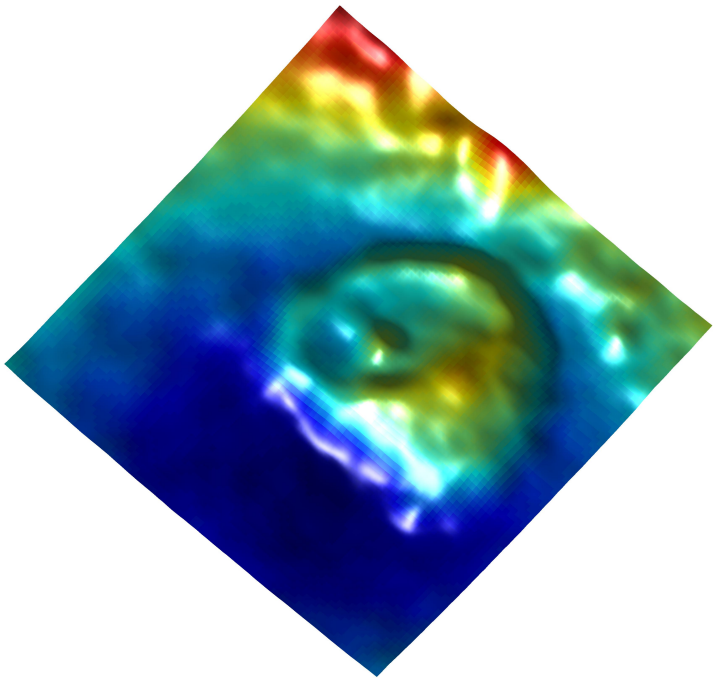

FIGURE 2.32: A 3D rendering of an endothelial cell, based on its unwrapped phase and (2.22) (Figure 2.31c).

3. OPTICAL CHARACTERIZATION OF BONE

In order to predict and control the delivery of light and elicit a photodynamic response for PDT of osteosarcoma, it is necessary to understand light transport in bone tissues. In particular, light transport can be classified by the absorption and scattering coefficients of bone tissues. Diffuse reflectance spectroscopic measurements are made using a source-collector set of optical-fibers. Measurements of the visible and near infrared spectrum are made over a range of source-collector separations. Measured spectra are then fit against Mie and Rayleigh scattering in order to determine the tissue's scattering coefficient. The measured spectra are also fit against absorption spectra for native absorbers. From the fitting routine, the tissue's percent composition by water and oxygenated and deoxygenated hemoglobin are then determined, from which the wavelength dependence of the tissue's absorption coefficient can be calculated.

3.1. Diffuse Reflectance Spectroscopy

Diffuse reflectance spectroscopic measurements are made on the cortical surface of two whole, ex vivo porcine femurs procured from a local butcher. Both bones were cleaned of periosteum and had an average outer radius of 14mm in the regions measured. A halogen source (Mikropack HL-2000-LL) is connected to the source fiber-optic cable (Figure 3.1). The collecting fiber-optic cable is connected to a spectrometer (Ocean Optics QE-65000) measuring in the visible and near-infrared spectra, however only measurements between $\lambda = 580 - 860nm$ are used for analysis in order to distinguish between absorption by hemoglobin and water. Absorption is high below and above this range, dominated by hemoglobin (Figure 1.11) and water (Figure 1.10), respectively. Greater absorption in these regions result in low spectral reflectance measurements, limiting the ability to adequately fit for hemoglobin and water content.

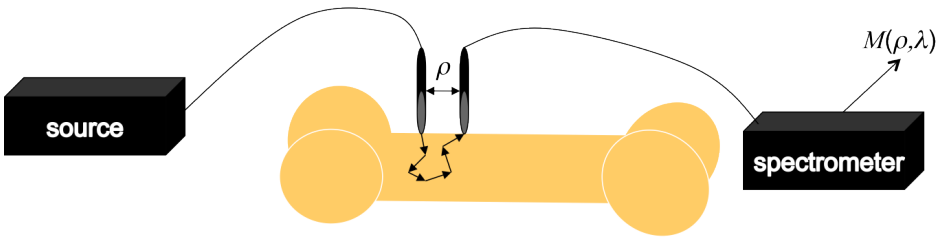

FIGURE 3.1: A diagram illustrating the system used for and geometry of Diffuse Reflectance Spectroscopy measurements. A source fiber is brought into contact with the bone, while a collection fiber attached to a spectrometer is used to measure the reflectance spectrum, $M(\rho, \lambda)$ for varying source-collector separation distances, ρ.

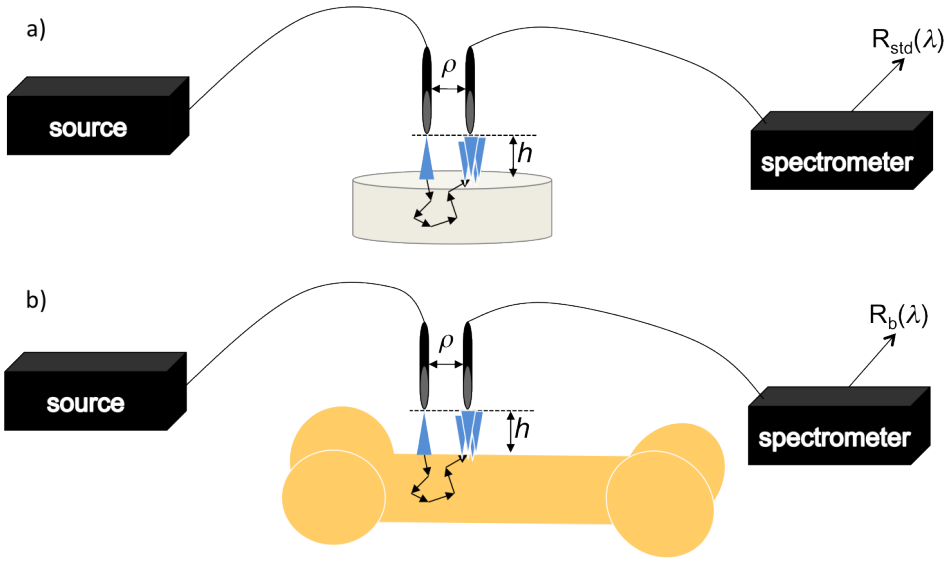

FIGURE 3.2: A diagram illustrating the system used for and geometry of reflectance measurements, which are used for calibration purposes. Source and collection fibers are fixed at a height of $h = 5mm$ above the object. The collection fiber is attached to a spectrometer and is used to measure the total reflectance spectrum, $R(\lambda)$ at a fixed source-collector separation distance of $\rho = 5mm$. Measurement of the a) 99% Spectralon reflectance standard and b) bone are made using the same geometries.

While water, oxygenated and deoxygenated hemoglobin are not the principle components of bone tissues, they are the dominant chromophores in bone tissues within the visible spectrum. The principle components of bone tissues are mineral (calcium phosphate-based hydroxyapatite) and protein (collagen) based, however these chromophores are not dominant absorbers in the visible region of the spectrum.[117–120] While their contributions to the absorption of visible wavelengths is negligible, they will be the dominant factors in scattering effects in bone tissues. Since we are concerned with the propagation of red wavelengths through bone tissues during PDT of osteosarcoma, we can limit the use of diffuse reflecance spectroscopy to determining the absorption coefficient of bone tissues over the visible spectrum. Therefore, the determined absorption coefficient will be reflective of small concentrations of the water and hemoglobin chromophores and not reflect concentrations of hydroxyapatite or collagen.

The system is first calibrated for each bone by determining the reflectance of each. The source-collector optical fiber pair is mounted with a separation of 5mm and height of 5mm above a sample mount (Figures 3.2 and 3.3a). A 99% Spectralon reflectance standard is held in place 5mm below the fiber pair and the reflectance is measured. The reflectance standard is then replaced by each femur, again 5mm from the fiber pair, and reflectances are acquired above a relatively flat portion of the femur.

Spectral measurements $M(\lambda)$ are dependent upon source $S(\lambda)$, material reflectance

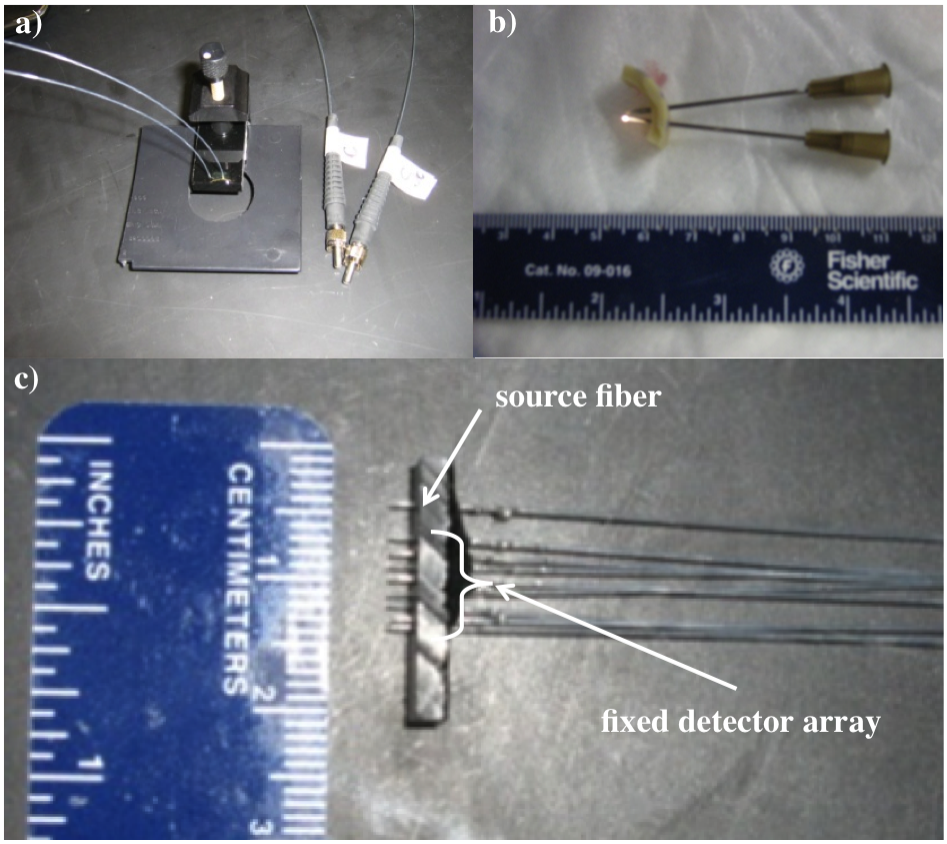

FIGURE 3.3: a) The fiber holder used for calibration in diffuse reflectance spectroscopy. b) A source-collector pair of fibers are held within a malleable rubber sleeve for adjustable measurements around the curvature of bone samples. The collecting fiber needs to be repositioned for different source-collector spacings. The use of hypodermic needles helps to guide the fiber tips through the rubber sleeve without damage. Once the fiber is in place, the needle can be removed and the rubber sleeve holds the fibers snugly in place. c) The fixed mount for the source-collector array, which can be used for diffuse reflectance spectroscopy over flat regions of bone where direct contact between all fibers and cortical bone is possible.

$R(\lambda)$, collection $C(\lambda)$, and detector $D(\lambda)$ factors as a function of wavelength,[15]

$$M(\lambda) = S(\lambda)R(\lambda)C(\lambda)D(\lambda). \tag{3.1}$$

Source and detector dependence will not change from sample to sample. By using a flat region of bone in the calibration measurements described above, the collection factor can also be assumed constant between bone and reflectance standard. Therefore, source, detector, and collection terms cancel in taking the ratio of bone to standard spectral measurements,

$$\begin{aligned} \frac{M_b(\lambda)}{M_{std}(\lambda)} &= \frac{S(\lambda)R_b(\lambda)C(\lambda)D(\lambda)}{S(\lambda)R_{std}(\lambda)C(\lambda)D(\lambda)} \\ &= \frac{R_b(\lambda)}{R_{std}(\lambda)}, \end{aligned} \tag{3.2}$$

where $M_b(\lambda)$ is the spectral measurement of the bone and $M_{std}(\lambda)$ is the measurement on the standard. Rearranging allows the total bone reflectance $R_b(\lambda)$ to be isolated and to be described in terms of the reflectance standard $R_{std}(\lambda)$ and spectral measurements of bone and standard,

$$R_b(\lambda) = \frac{M_b(\lambda)}{M_{std}(\lambda)} R_{std}(\lambda), \tag{3.3}$$

where $R_{std} = 0.99$ across all wavelengths in the range of measurement, as defined by the 99% Spectralon reflectance standard.

Diffuse spectral measurements are next taken for each bone, with the source and collecting fibers in direct contact with the cortical bone (Figure 3.1). Measurements are taken for varying source-collector separations of $\rho = 3 - 10mm$ at $1mm$ intervals (Figure 3.3c). With the fibers now in contact with the bone, the collection factor is no longer $C(\lambda)$ but instead is a fiber collection efficiency, $\eta(\lambda)$. Source and detector dependencies still cancel in taking the ratio of bone to standard reflectance measurements,

$$\begin{aligned} \frac{M(\rho,\lambda)}{M_{std}(\lambda)} &= \frac{S(\lambda)R(\rho,\lambda)\eta(\lambda)D(\lambda)}{S(\lambda)R_{std}(\lambda)C(\lambda)D(\lambda)} \\ &= \frac{R(\rho,\lambda)\eta(\lambda)}{R_{std}(\lambda)C(\lambda)}, \end{aligned} \tag{3.4}$$

where $M(\rho,\lambda)$ is the measurement on the bone at each source-collector separation ρ, and $M_{std}(\lambda)$ is the same total reflectance measured from the standard as in (3.2). By defining a calibration factor incorporating the collection factor and fiber collection efficiency,

$$cal(\lambda) = \frac{C(\lambda)}{\eta(\lambda)}, \tag{3.5}$$

we combine the two unknown factors in to a single, yet still unknown term. Rearranging (3.4) and making use of (3.5), we can solve for the reflectance as a function of source-collector separation,

$$R(\rho,\lambda) = R_{std}(\lambda)\frac{M(\rho,\lambda)}{M_{std}(\lambda)}cal(\lambda). \tag{3.6}$$

Although the factors $C(\lambda)$ and $\eta(\lambda)$, and therefore $cal(\lambda)$, are unknown, we can solve for the unknown constant based upon the calibration measurements with respect to the 99% calibration standard. We already define the total reflectance of the bone based upon calibration measurements taken above the surface of the bone and a reflectance standard (3.3). Similarly, were we to measure the reflectance of the bone at its surface and continuously increase the radial distance from the source fiber along a line, two-dimensional integration of these measurements in cylindrical coordinates would result in the same total reflectance of the bone,

$$\begin{aligned} R_b(\rho,\lambda) &= \int_0^{2\pi}\int_0^{\infty} R(\rho,\lambda)\rho d\phi d\rho \\ &= \int_0^{\infty} R(\rho,\lambda)2\pi\rho d\rho. \end{aligned} \tag{3.7}$$

Using (3.6), this integration becomes

$$\begin{aligned} R_b(\lambda) &= \int_0^{\infty} R(\rho,\lambda)2\pi\rho d\rho \\ &= cal\int_0^{\infty}\frac{M(\rho,\lambda)}{M_{std}(\lambda)}2\pi\rho d\rho, \end{aligned} \tag{3.8}$$

such that the previously unknown calibration factor can be determined as a function of wavelength,

$$cal(\lambda) = \frac{R_b(\lambda)}{\int_0^{\infty}\frac{M(\rho,\lambda)}{M_{std}(\lambda)}2\pi\rho d\rho}. \tag{3.9}$$

At this point, the experimental data at each wavelength are determined by incorporating the wavelength dependence of the calibration factor (3.9) back into (3.6). By applying this analysis to each wavelength of the spectral data, a final data set $R_b(\rho,\lambda)$ is generated and ready for analysis by least squares fitting with respect to scattering and absorption parameters.

The wavelength dependence of the tissue's absorption coefficient, μ_a, can be determined as a function of the absorption and concentration of native absorbers. In the visible spectral range, concentrations of blood (B), oxygen saturation in blood (S), and water (W) will be dominant, such that the total absorption of the tissue is defined as

$$\mu_a(\lambda) = B(S\mu_{a,oxy}(\lambda) + (1-S)\mu_{a,deoxy}(\lambda)) + W\mu_{aW}(\lambda), \tag{3.10}$$

where $\mu_{aW}(\lambda)$, $\mu_{a,oxy}(\lambda)$ and $\mu_{a,deoxy}(\lambda)$ are the wavelength dependent absorption coefficients of water, oxygenated and deoxygenated whole blood (hemoglobin = $150g/L$ for whole blood), respectively.[15] The reduced scattering coefficient is also a function of wavelength,

$$\mu_s' = a\left(\frac{\lambda}{635nm}\right)^{-b} + c\left(\frac{\lambda}{635nm}\right)^{-4}, \tag{3.11}$$

where the first and second terms on the right of (3.11) are associated with Mie and Rayleigh scattering, respectively.[15] In both the Mie and Rayleigh terms, the wavelength dependence is divided by a $635nm$ wavelength as a type of normalization and in order to cancel the units of wavelength (nm). For Mie scattering, the constant b in the exponent is approximately one, and therefore is fixed as such during least squares fitting.

By using the coefficients B, M, W, a, and c as fitting parameters, thereby varying μ_a and μ_s', a least squares fitting routine is used to fit the experimental diffuse reflectance spectra, $R(\rho, \lambda)$, to that predicted by diffusion theory via the method of images approach,[121]

$$R(\rho,\lambda) = \frac{1}{4\pi}\left[z_o\left(\mu_{eff} + \frac{1}{r_1}\right)\frac{e^{-\mu_{eff}r_1}}{r_1^2} + (z_o + 2z_b)\left(\mu_{eff} + \frac{1}{r_2}\right)\frac{e^{-\mu_{eff}r_2}}{r_2^2}\right], \tag{3.12}$$

where

$$\mu_{eff} = \sqrt{3\mu_a(\mu_a + \mu_s')}, \tag{3.13}$$

$$z_o = \frac{1}{\mu_a + \mu_s'}, \tag{3.14}$$

$$D = \frac{z_o}{3}, \tag{3.15}$$

$$r_i = -1.440n_{rel}^{-2} + 0.710n_{rel}^{-1} + 0.668 + 0.0636n_{rel}, \tag{3.16}$$

$$z_b = 2AD, \tag{3.17}$$

$$A = \frac{1 + r_i}{1 - r_i}, \tag{3.18}$$

$$r_1 = \sqrt{z_o^2 + \rho^2}, \tag{3.19}$$

$$r_2 = \sqrt{(z_o + 2z_b)^2 + \rho^2}. \tag{3.20}$$

In all of the above (3.12) - (3.20), the factor μ_{eff} is the effective attenuation coefficient, z_o defines the depth of the photon source, D is the diffusion constant, r_i a dimensionless internal reflection coefficient which has been determined experimentally, and n_{rel} is the ratio of the indices of refraction of tissue to air.[121] Assuming cortical bone to have an index of refraction similar to that of dentin ($n = 1.45$), the value $n_{rel} = 1.45$ was used throughout this analysis.[122–124] The term z_b is the distance between the true tissue surface and a plane of symmetry between the real and image sources, as indicated by the dashed line in (Figure 3.4).[121]

Equation (3.12) is a solution for the diffuse reflectance at an air/tissue interface using the method of images as a model, with a real source at r_1 and an image source located at r_2.[121] The fiber launches the light into the tissue, so the real source appears as a point source at depth z_o (3.14) within the tissue. For source-collector separations $\rho > z_o$, (3.12) yields predictions with $< 5\%$ accuracy. Below this range, diffusion theory breaks down as single scattering becomes dominant over multiple scattering events. Recent work has been done to overcome the failure of diffusion theory to model light transport

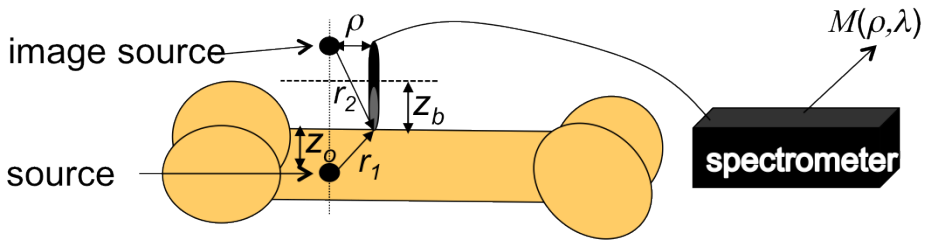

FIGURE 3.4: The geometry of the method of images approximation for a fiber-optic source, used for the solution to the diffusion of light in bone. The depth of the real source, z_o, is exaggerated in the drawing. Typically, $z_o \approx 1mm$ for near IR wavelengths, and $z_b \approx 2z_o$. In reality then, the image source is $\sim 5z_o$ above the tissue surface.

within the sub-diffusion range, however such work is beyond the scope of this thesis.[125,126] Traditionally, Monte Carlo modeling has been used in order to give a better understanding of light transport in the sub-diffusion regime, as will be the case in this work.[127]

The fitting routine varies the fitting parameters B, M, W, a, and c, passes them on to calculate μ_a (3.10) and μ_s' (3.11) and finally $R(\rho, \lambda)$ (3.12) based on those variations (Figure 3.5). The calculated reflectance (3.12) is then fit against the measured reflectance at a given source-collector separation. This process repeats for each source-collector separation measurement until the difference between the actual reflectance and fit function is minimized via a least squares fitting method. The fitting parameters are stored for each source-collector separation, and the average of these values is used to determine the absorption and reduced scattering coefficients of the bone. The determined absorption and reduced scattering coefficients are then input back into (3.12) in order to determine the functional fit of the reflectance versus source-collector separation in comparison to the actual measurements.

3.2. Experimental Results

As it has been described leading up to this point in this chapter, Diffuse Reflectance Spectroscopy was used in order to determine the optical properties of two porcine femurs (referred to as pb14 and pb15 throughout the remainder of this chapter). The least squares method used to fit a predicted reflectance (R_{fit}) to a measured reflectance (3.6) results in a set of coefficients representing absorption and scattering in the tissue (Figure 3.5). The resulting absorption and reduced scattering coefficients are then averaged for each bone for individual absorption and reduced scattering coefficients, as well as for both bones to determine average values for porcine femurs in general (Figure 3.6).

The average absorption and reduced scattering coefficients at $\lambda = 635nm$ were determined to be $0.0359mm^{-1}$ and $1.6160mm^{-1}$, respectively. These averaged results for the absorption and reduced scattering coefficient at 635nm are then input back into

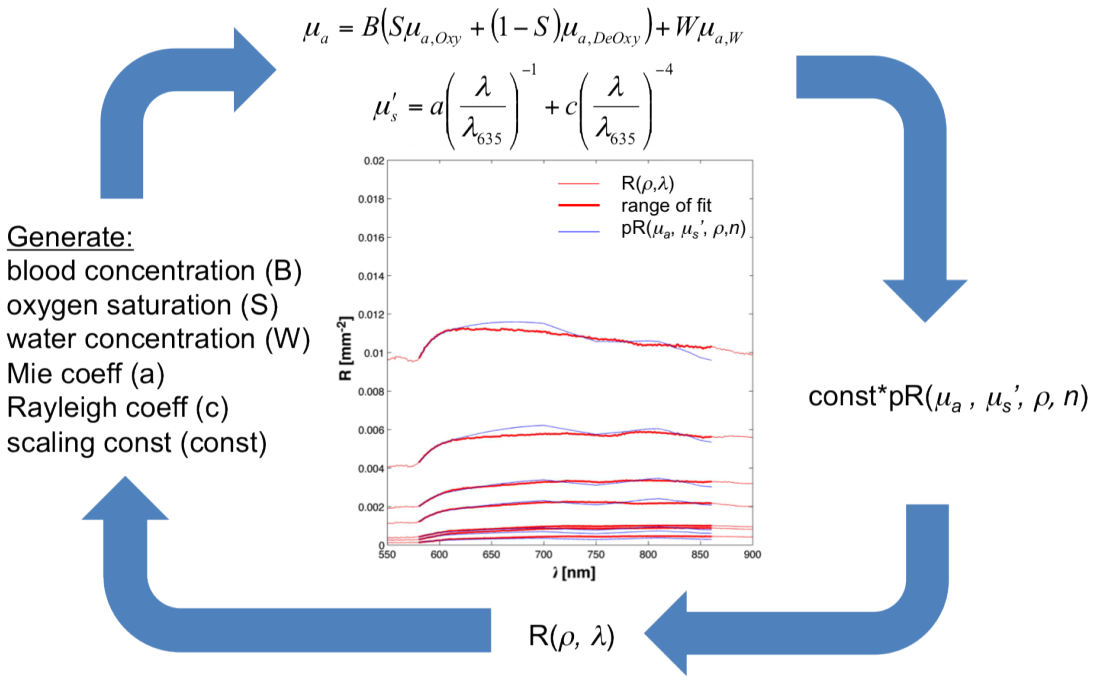

FIGURE 3.5: A flow chart of the least squares fitting routine as applied towards the solution for (3.12) and determination of optical characteristics μ_a and μ_s'. In the above, $pR(\mu_a, \mu_s', \rho, n)$ is the predicted reflectance as calculated using the chosen fitting parameters for each iteration. Since the arguments of the predicted reflectance are functions of wavelength, the predicted reflectance is also a function of wavelength. Eight predicted reflectances are simultaneously fit against the measured reflectances for eight given source-detector separations via the least squares method. The fit is only carried out over the specified range of wavelengths (bold red curve in the central figure, called the range of fit) in order to avoid regions where absorption is overwhelmingly dominated by water and hemoglobin.

(3.12) in order to determine the expected reflectance curve as a function of source-collector separation. The actual reflectances measured at 635nm are plotted against this fit curve, as well as a curve reflecting the expected values based on previous literature, measured using reflection and transmission measurements (Figure 3.7).[128]

The coefficients found in the literature were determined using reflection and transmission measurements from ex vivo bone samples of known thickness and assuming an anisotropy of $g = 0.8$. The work described throughout this chapter assumes a higher anisotropy for cortical bone, $g = 0.95$.[122] As such, the reduced scattering coefficient cited in the literature has been adapted to reflect the greater anisotropy assumed here. This calculation was made by reverting back from the reduced scattering coefficient to the scattering coefficient (μ_s) and then a forward calculation of the new reduced scattering coefficient reflecting the greater anisotropy. This calculation was based on the defining equation for the reduced scattering coefficient (3.11).

3.3. Discussion

In the application of diffuse reflectance spectroscopy towards measuring the optical properties of cortical bone, two assumptions have been made. First, it has been assumed that the multi-layered nature of the bone does not come into affect. Also, it has been assumed that the curvature of the bone around its central, cylindrical axis is negligible.

The solution to the diffusion equation (3.12) assumes a semi-infinite medium, meaning a medium that is flat across the surface and extends infinitely far along the surface and is infinitely deep, or at least sufficiently deep such that there is no light which leaves the other end of the tissue (Figure 3.8a). Bone is instead, roughly speaking, a cylindrical shell filled with a second medium (Figure 3.8b). If either of these two assumptions were not valid, the model used in order to solve for the optical properties of the bone would break down and its results would not be valid.

Were the light to penetrate beyond the outer layer of cortical bone and deeper into the cancellous bone and marrow, then the applied model would break down as the measured reflectances would carry information of both layers of the bone tissue. The cortical bone measured was on average $4mm$ thick, and therefore well beyond the source depth of roughly $1mm$ attributed via the method images, such that the assumption of a semi-infinite medium should be justified.

Similarly, if the curvature of the bone around its central axis were sufficiently large, the geometry of light leaving the surface would have an increasing divergence. As such, the reflectance would be lower than expected at a fixed source-collector separation distance. In this sense, the calculated reflectance would not be an adequate solution for that which was measured. This would result in overestimating the absorbance and scattering properties of cortical bone tissue.

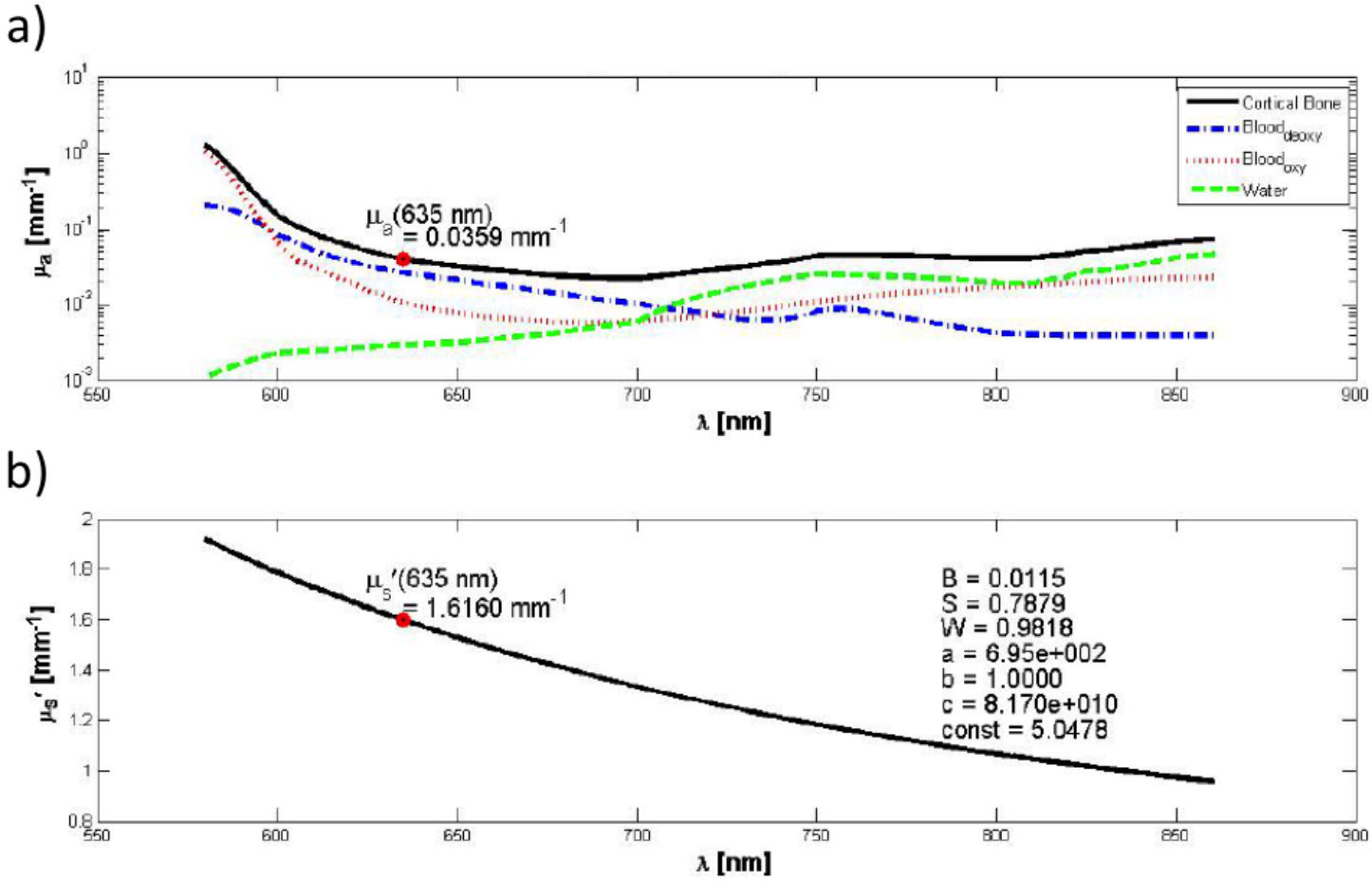

FIGURE 3.6: Average results from two porcine femurs. a) Wavelength dependence of absorption coefficients for water (green, dashed), oxygenated hemoglobin (red, dotted), deoxygenated hemoglobin (blue, dash-dot), and cortical bone (black, solid). The cortical bone curve is the sum of the other three curves, which have been scaled by their respective concentrations. A red circle denotes the absorption coefficient of cortical bone at $635nm$. b) The resulting wavelength dependence of the reduced scattering coefficient of cortical bone. A red circle denotes the reduced scattering coefficient of cortical bone at $635nm$. The average fitting parameters are listed in the lower right corner

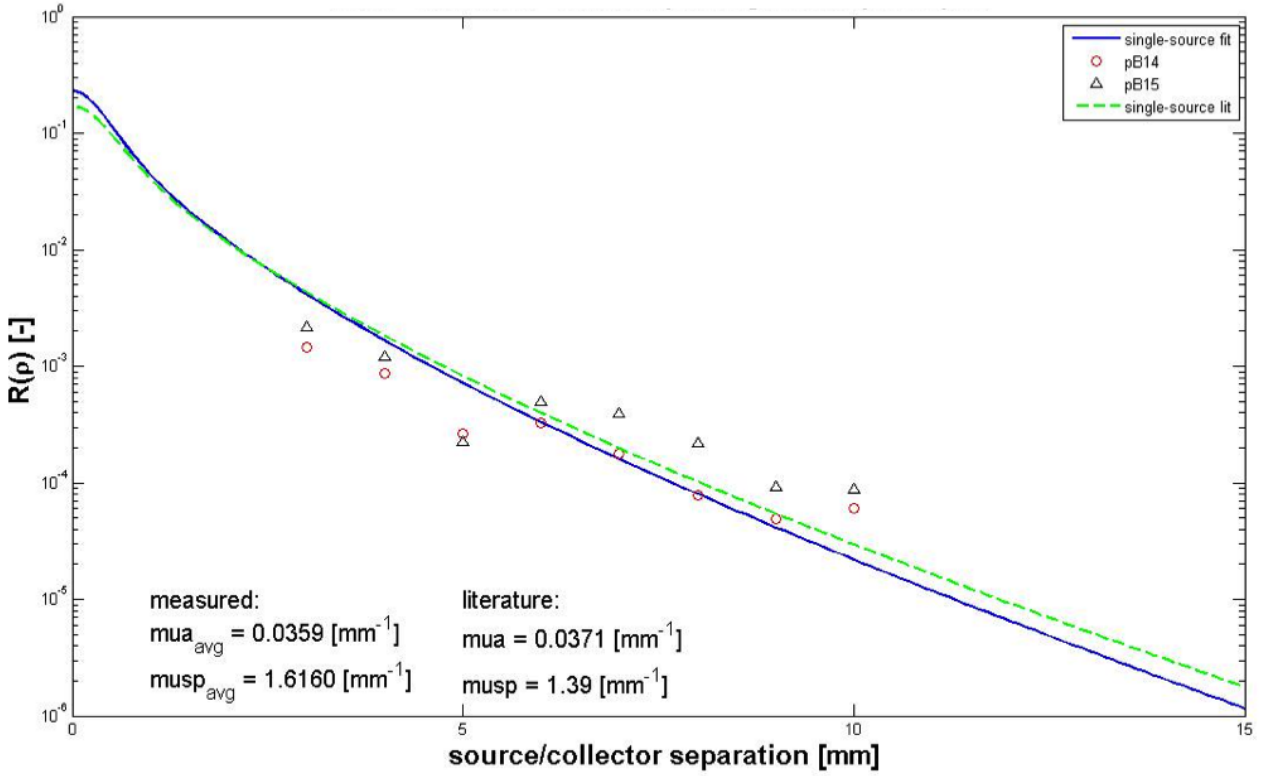

FIGURE 3.7: Reflectance measurements at $635nm$ for the two porcine femurs are depicted with circles (pb14) and triangles (pB15). The average absorption and reduced scattering coefficients at $635nm$ are listed in the lower left corner, and are compared to coefficients based on previous literature.[128] The blue plot (solid) represents the fit determined by the single source diffusion theory solution for diffuse reflectance (3.12). The green plot (dashed) represents the same plot for coefficients taken from previous literature.

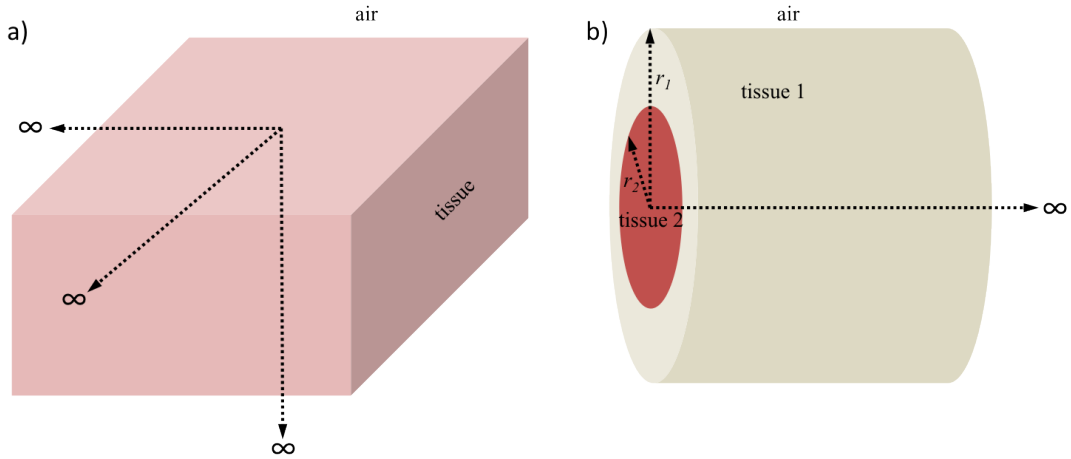

FIGURE 3.8: An illustration of a) the semi-infinite medium assumed via the Diffuse Reflectance Spectroscopy analysis versus b) the actual geometry of the medium.

In considering the issue of bone curvature with respect to these measurements, it should be noted that the geometry of the femur is not cylindrical as idealized, but in fact has regions of relative flatness. Diffuse Reflectance Spectroscopic measurements were taken centered about such flat regions of the porcine femurs in order to minimize any effects of bone curvature on the data. These flat regions were typically on the order of $1cm$ wide and $\sim 2-3cm$ long. Such distances should be sufficiently large compared to the e^{-1} penetration depth of $\sim 1.7mm$, such that bone curvatures should play no role in the data collection and consequently the analysis.

As justification for the assumption of a semi-infinite medium when applying the method of images to the diffusion equation, a Monte Carlo model (to be described in full detail in Chapter 4.) was run assuming a multi-layered medium with cylindrical symmetry. Using the absorption and scattering results determined via Diffuse Reflectance Spectroscopy for cortical bone, a cylindrical shell of cortical bone with inner radius of $r_{in} = 10mm$ and outer radius of $r_{out} = 14mm$ is filled with blood in order to approximate the optical properties of bone marrow. As this simulation is used to model the Diffuse Reflectance Spectroscopy experiement, the cortical bone is surrounded by air and the incident light is directed radially inward from the top surface of the bone.

Based on the energy deposition that results from this simulation (Figure 3.9), the light that passes through the cortical bone and reaches the marrow has decreased by some three or more orders of magnitude. With such a drastic drop off in the light that reaches the marrow, it is safe to assume that any light entering the marrow and scattering back towards the collecting fiber would therefore undergo another drop of three-plus orders of magnitude. Any light that were to reach the marrow and scatter back towards the collecting fiber would therefore carry one-millionth of the weight of the light scattered by the cortical shell alone. Therefore, this simulation clearly supports the assumption and

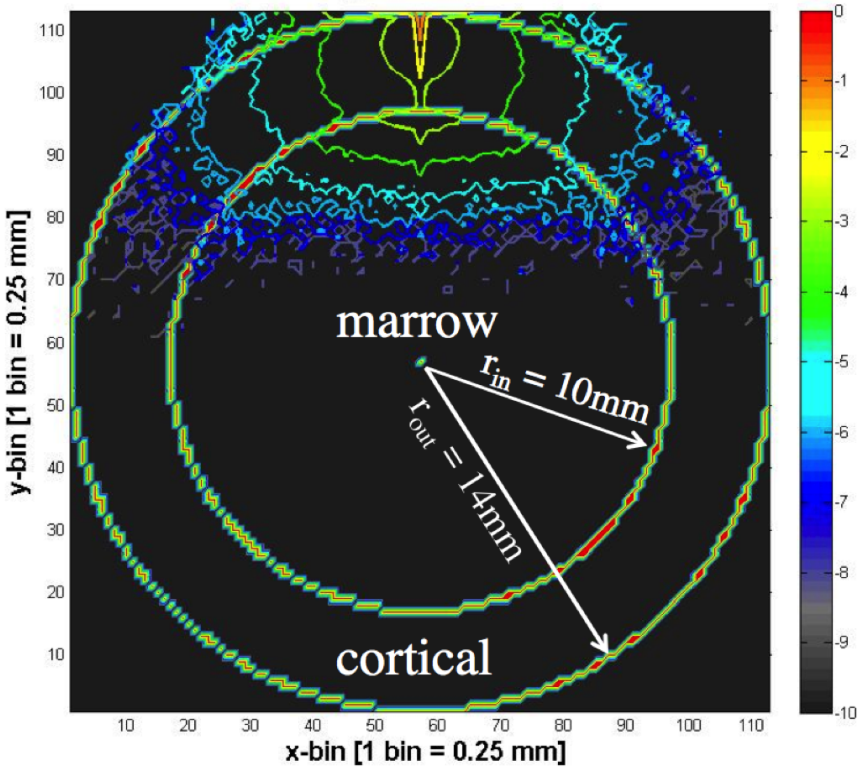

FIGURE 3.9: A Monte Carlo model of the Diffuse Reflectance Spectroscopy experiment. This view is a cross-section of a cylindrically symmetric bone model, with marrow at the core and surrounded by cortical bone. Incident light is directed radially inward at the surface (top, center of the image), as in the experiment. Based on the iso-curves (log_{10} scale) of energy deposition, it is clear that light reaching the marrow is attenuated by some 3 or more orders of magnitude. As such, the Monte Carlo model confirms the assumption that we can neglect any contribution to the measured reflectance from the deeper tissue.

use of a single layered medium in the analysis of the Diffuse Reflectance Spectroscopy measurements. The first of the assumptions made in the Diffuse Reflectance Spectroscopy analysis is upheld.

In order to test the validity of the second assumption made in analyzing the Diffuse Reflectance Spectroscopy data—that the curvature of the bone is slight enough as to be neglected and the surface can be considered flat in the analysis—Diffuse Reflectance Spectroscopy measurements were taken both along axial and angular directions along bone samples, centered around a flat region of bone (Figure 3.10). While differences are observed from sample to sample (red compared to green data points), source-collector separations along axial versus angular distances show similar results for a given sample. That angular and axial data points generally fall within the same range for a given sample and source-collector separation distance supports the assumption that bone curvature could be neglected in the analysis of experimental data.

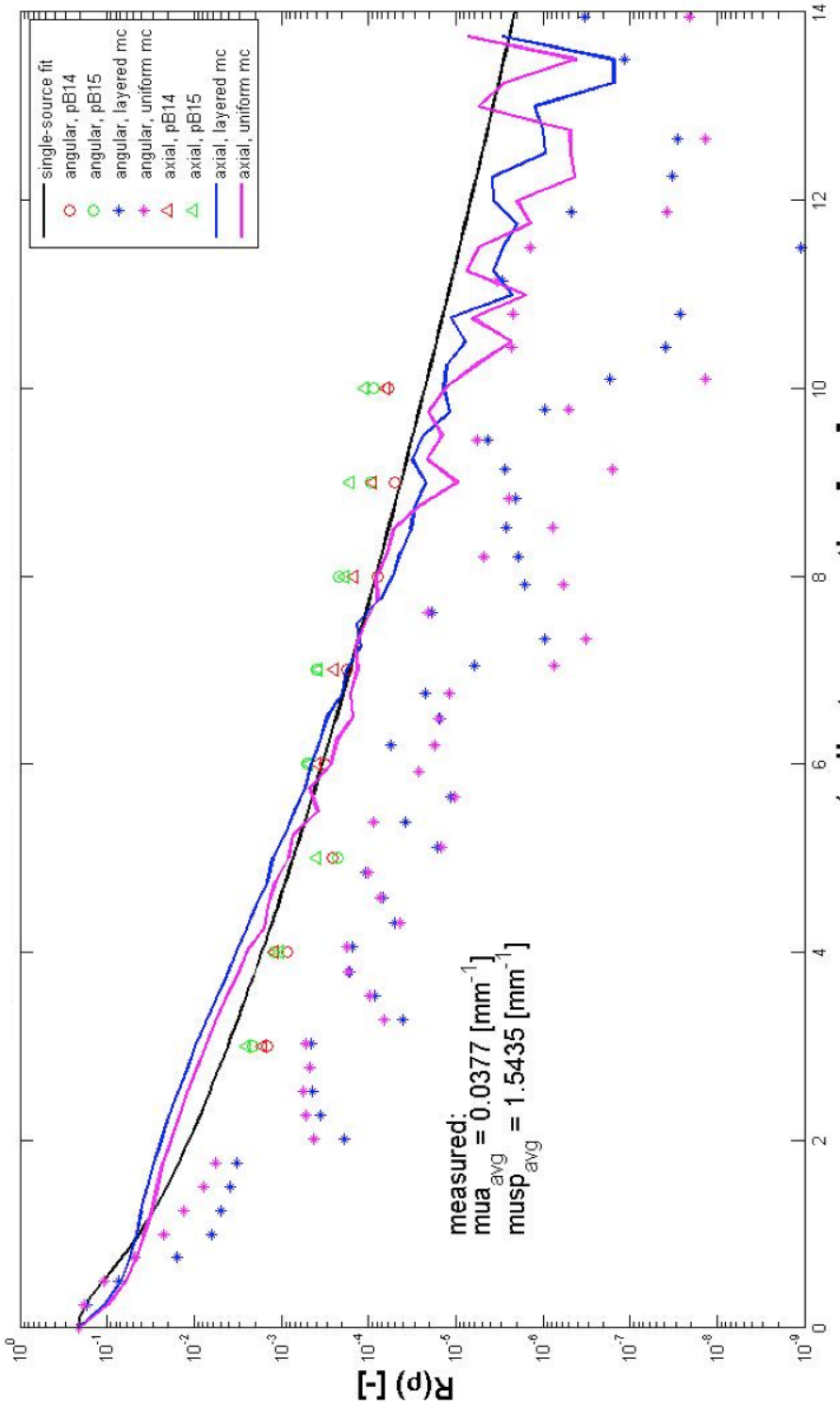

FIGURE 3.10: Additional results from the Monte Carlo model of the Diffuse Reflectance Spectroscopy experiment.

Data from the same Monte Carlo simulation can also be used as a further test of the validity of the assumption that bone curvature is negligible (Figure 3.10). Using the same layered cylindrical model of bone marrow surrounded by cortical bone as described previously, measurements of diffuse reflectance as predicted along both the axial (dark blue line) and angular (dark blue asterisks) directions by the simulation further support the assumption. We see that based on the Monte Carlo model, the predicted angular measurements are typically two or more orders of magnitude less than those measured along the axial direction of the cylindrical model. These predictions, in combination with the comparison of the actual measurements confirms the validity of this second assumption.

As a further, simultaneous test of both of these assumptions, the layered cylindrical shell applied in the Monte Carlo model is then assumed to be a solid cylinder of cortical bone only—thereby eliminating the multiple layered approach while still considering a system with curved geometry. The results from this model (Figure 3.10) are similar to those from the layered model for both the axial (magenta line) and angular (magenta asterisks) directions. These results confirm that the presence of a deeper, varying tissue is irrelevant for the Diffuse Reflectance Spectroscopic measurements, and again that the curvature was not observed to be relevant.

As a visual verification of these conclusions regarding the negligible effect of the multilayered bone tissue, cross sectional images of a porcine femur are taken with the lights on in order to mark the interface between tissue types and a second image was taken with the ambient lights off while illuminating the bone with the source fiber. Minding the margins of air-cortical bone and cortical bone-marrow interfaces indicated, the penetration of diffuse light can be observed. A negligible amount of light, if any, from the source fiber penetrates into the marrow. Any slight amount of light that might have possibly penetrated into the marrow would not have been able to contribute any noticeable or significant signal to the overall diffuse reflectance since it would have been attenuated by the same factor upon transmitting back towards the surface for detection.

Lastly, it was anticipated that a difference in slope of the semi-logarithmic plot of reflectance versus source-collector separation would be apparent between small and large source-collector separations. The slope of this plot would be directly indicative of a change in absorption and scattering coefficients, where the nearer measurements would be dominated by reflectance from cortical bone (the outer most layer). Measurements taken for greater source-collector separations would incorporate a greater influence of deeper penetrating photons that then scatter towards the surface. As such, the slope of the semi-logarithmic plot for greater source-collector separations was expected to change, reflecting a combination of absorption and scattering in the cortical layer as well as the marrow filled core.[129]

This was not observed (Figure 3.7), which further supports the findings that light didn't interact with the marrow core during diffuse reflectance spectroscopy measurements. As a result, we can be confident that the actual measured optical properties are indeed those of cortical bone alone and not compromised by deeper tissues.

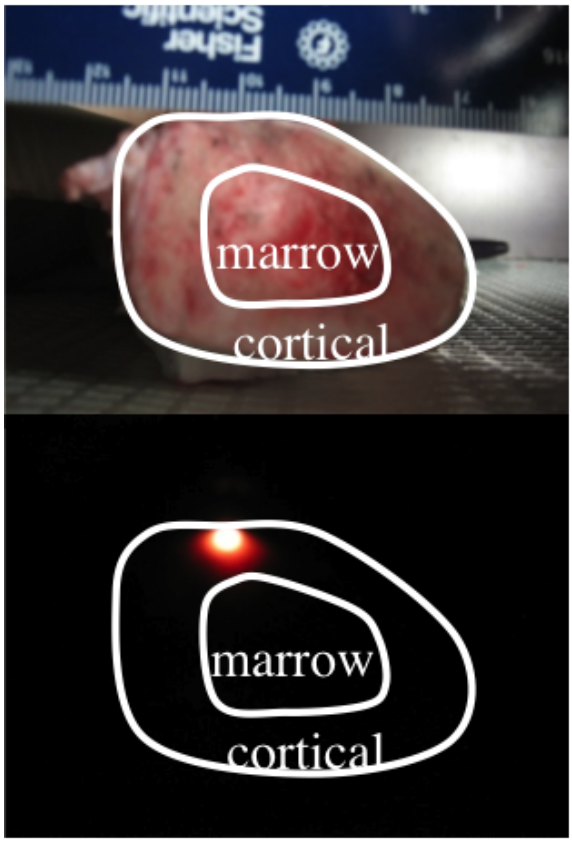

FIGURE 3.11: Cross sectional image of porcine femur, with margins of air-cortical bone and cortical bone-marrow interfaces indicated (top). Ambient lights are then turned off and the same image is captured while the source optical fiber is brought into contact with the surface of the cortical bone, such that the penetration of diffuse light can be observed (bottom). Clearly, little to no light from the source fiber penetrates into the marrow.

4. MODELING CLINICAL PDT OF OSTEOSARCOMA: A 3D MONTE CARLO SIMULATION

Experimentally determined absorption and scattering coefficients from the previous chapter (section 3.2.) are imported into a cylindrically symmetric Monte Carlo model, approximating the geometry of long bones. In using a series of coaxial cylindrical shells, the optical properties are varied by region in order to approximate the optical properties of a marrow core and cortical shell surrounded by tissue. Additionally, regions of osteosarcoma can be added to the model. Various geometries of light sources can be implemented to help predict light distributions in clinical applications of PDT. Results throughout this section will focus on the 635nm wavelength, which is typically applied in PDT induced through administering aminolevulinic acid (ALA) in order to facilitate production of protoporphyrin-IX (PpIX).

4.1. Cylindrically Symmetric Monte Carlo Model

A cylindrically symmetric Monte Carlo model was created using Matlab to approximate the geometry of long bones containing osteosarcoma in order to determine light dosimetry for PDT applications. This model was based on previous Monte Carlo simulations used to model slabs of layered tissues.[127] For this investigation, a cylindrical structure was created with inner radius of $7mm$ and $10mm$ outer radius, approximating the dimensions of the canine radius. This structure reflected the optical properties of red marrow and a cylindrical plug of osteosarcoma in the cylindrical core ($r < 7mm$), cortical bone in the cylindrical shell ($7mm < r < 10mm$), and surrounding tissue beyond ($r > 10mm$). The optical properties of importance for this model are index of refraction, anisotropy (g), and absorption (μ_a) and reduced scattering (μ_s') coefficients.

The key to Monte Carlo simulations is that the optical properties define attenuation in the tissue, which can be used to scale the probability of photon path lengths between scattering events.[127] The photon step size between scattering events is defined as

$$s = -\frac{ln\chi}{\mu_t}, \tag{4.1}$$

where the total attenuation coefficient is given by

$$\mu_t = \mu_a + \mu_s' \tag{4.2}$$

and χ is a random number in the range (0,1] as determined by a a random number generator in Matlab. Upon a scattering event, the photon is redirected along the direction

of scatter, defined by the scattering angle θ in the range [0,π]. The Henyey-Greenstein probability density function,

$$p(cos\theta) = \frac{1-g^2}{2(1+g^2-2gcos\theta)^{3/2}}, \tag{4.3}$$

describes the probability of scattering angle for Mie scattering and is generally adopted in tissue optics.[127] A random number (ζ) is generated and set equal to the integral of this probability distribution

$$\zeta = \int_{-1}^{cos\theta} \frac{1-g^2}{2(1+g^2-2gcos\theta)^{3/2}} d(cos\theta), \tag{4.4}$$

in order to solve for the weighed scattering angle

$$\theta = cos^{-1}\left(\frac{1}{2g}\left[1+g^2-\left(\frac{1-g^2}{1-g+2g\zeta}\right)^2\right]\right), \tag{4.5}$$

for $g \neq 0$. In the case that $g = 0$, the scattering probability distribution is 1/2, such that

$$\begin{aligned} \zeta &= \int_{-1}^{cos\theta} \frac{1}{2} dcos\theta \\ &= \frac{1}{2}(cos\theta + 1). \end{aligned} \tag{4.6}$$

Solving for θ in this case, we find that when $g = 0$,

$$\theta = cos^{-1}(2\chi - 1). \tag{4.7}$$

Similarly, the azimuthal scattering angle (ψ) needs be determined after each scattering event. The azimuthal scattering angle will be symmetrically distributed about the photon's initial axis of propagation, such that the corresponding probability density function is $1/2\pi$.[127] Another random number (ξ) is set equal to the integral of this distribution

$$\begin{aligned} \xi &= \int_0^{\psi} \frac{1}{2\pi} d\psi \\ &= \frac{\psi}{2\pi}, \end{aligned} \tag{4.8}$$

such that the randomly generated azimuthal scattering angle is

$$\psi = 2\pi\xi. \tag{4.9}$$

Based on the defined photon source and initially defined propagation vector, cylindrical structure, and random sampling of these propagation variables (grounded in the defined probability distributions), the Monte Carlo process entails launching a photon,

generating propagation variables (4.1), (4.7) and (4.9) and moving the photon accordingly. At each step, the program determines which region of tissue the photon is in and thereby applies the appropriate optical properties. At each step, the photon's energy, or weight (W, initially defined as unity), is decremented by the amount

$$dQ = W\frac{\mu_a}{\mu_t}, \tag{4.10}$$

which is deposited in the program's binning structure and the photon's weight is updated to reflect this loss.[127] The new propagation variables are again determined and the process repeats until the photon weight has fallen below a threshold limit. Upon dropping below the threshold weight, the photon is given a 1 in 2 chance of surviving, "roulette" is played in generating a new random number in the range (0,1] in order to determine whether the photon is extinguished or continues to propagate. When a photon is extinguished, the next photon is released from the source and the process repeats until all photons are depleted. A general flow chart of the Monte Carlo process is given in (Figure 4.1), which was adapted from "Monte Carlo Modeling of Light Transport in Tissues" by S.L. Jacques and L. Wang.[127]

We must also be mindful of when a photon reaches a boundary between tissue types (Figure 4.2). Since a discrete photon cannot be simultaneously refracted and reflected, the decision is made as to whether it passes into the other medium or reflects back into its current medium. The use of Fresnel's Law (1.11) can be used in order to determine the reflection and transmission coefficients based on the index of refraction mismatch at the boundary, as well as the incident angle. The photon can then be made to follow the weighed term of transmission or reflection.

This model can be adapted for a variety of photon source configurations. In this investigation, focus was made on modeling light distributions from a cylindrical diffusing source oriented along the central axis of a long bone (Figure 4.3). This source was defined with a length of $1cm$ within the structure of the program, broken into 40 discrete units (voxels). Each unit of the diffusing source was initialized with 10,000 photons to launch, for a total of 400,000 photons in each of these simulations. As a cylindrically symmetric diffusing source, the initial photon direction of propagation at launching from the source was also randomly generated as described above for scattering events, in order to assure a uniformly distributed source. Photons leaving the ends of the source were not permitted to launch along the central axis, reflecting actual cylindrical diffusers used in clinical settings.

Optical properties used in the Monte Carlo model were either determined via diffuse reflectance spectroscopy (section 3.2.), generated based on the physiology of the tissues, or else taken from the literature (Table 4.1).

Unable to measure the absorption coefficients of the marrow using diffuse reflectance spectroscopy, it was possible to determine the absorption coefficient of the marrow and tumor based upon the physiological properties of the tissues—namely their blood concentrations. Red bone marrow, found in medullary cavity of the epiphyses of long bones, is

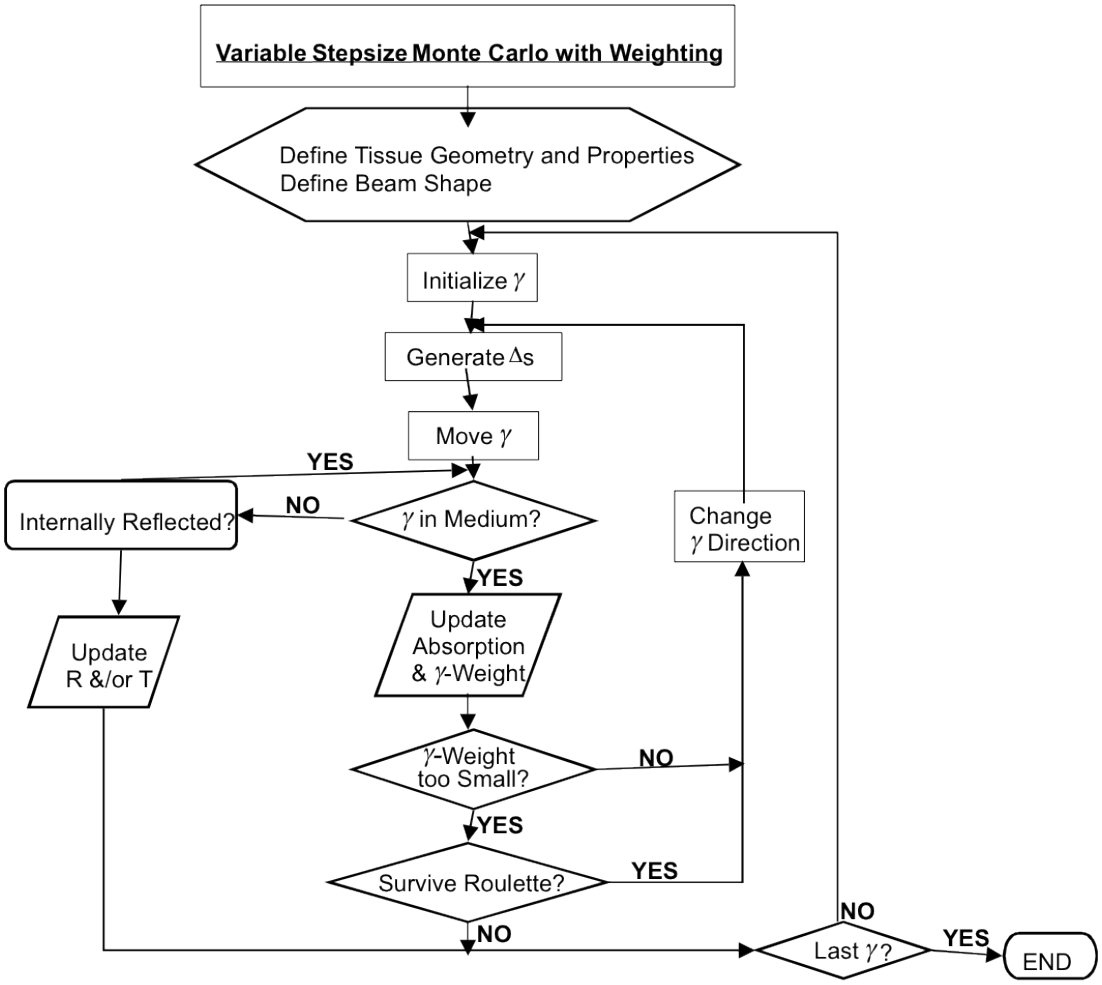

FIGURE 4.1: A flow chart of the Monte Carlo procedure. This figure is adapted from that found in "Monte Carlo Modeling of Light Transport in Tissues" by S.L. Jacques and L. Wang.[127]

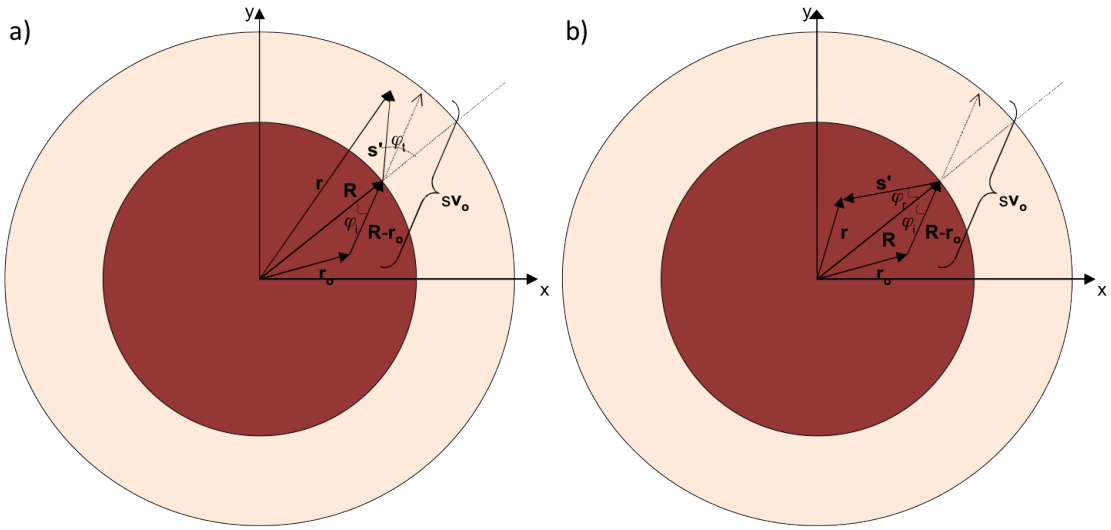

FIGURE 4.2: A cross-sectional display of the cylindrical geometry employed in the 3D Monte Carlo model. Photons incident from r_o reach a boundary between marrow and cortical bone at $R - r_o$. a) If the photon is propagated across the tissue interface, Snell's law must be accounted for as it refracts upon entry in the cortical bone. b) If the photon is instead reflected, the law of reflection must be obeyed. In either case, the step size is maintained for the overall process and the location of the next scattering/absorption event **r** is updated.

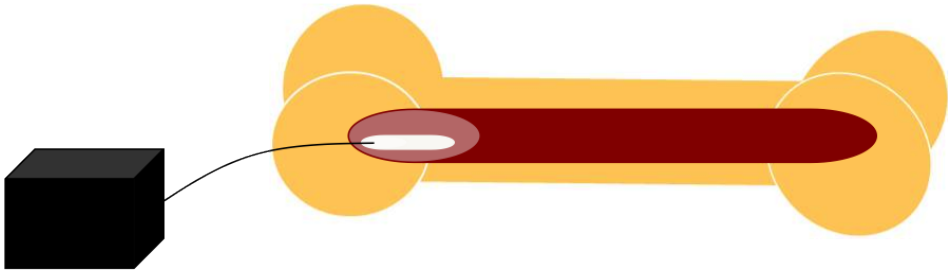

FIGURE 4.3: The diagram depicts what a clinical application of PDT for osteosarcoma would entail. The cortical bone surrounds the dark red marrow. Within the left epiphysis is a pink mass, representing an osteosarcoma tumor. Light is administered via an optical fiber and cylindrical diffusing tip through the end of the long bone.

predominantly composed of blood (B upwards of 0.8) and has an oxygen saturation of roughly 0.85. As such, the absorption coefficient of red marrow was calculated directly by (3.10). Scattering in the marrow will be dominated by cancellous bone in the cavity, so the reduced scattering coefficient within the medullary cavity was assumed the same as that determined for cortical bone.

As osteosarcoma grows within the medullary cavity it displaces the red marrow, lowering the blood concentration in the tumor as compared to the red marrow. Although osteosarcoma will have greater blood concentrations ($B \sim 0.2$) than healthy tissue, absorption due to blood in the osteosarcoma will be significantly less than the surrounding red marrow. Holding oxygen saturation at 0.85, absorption coefficients are plotted versus wavelength for varying blood concentrations, illustrating that absorption at 635nm in red marrow is nearly an order of magnitude greater than in osteosarcoma (Figure 4.4). Based on this reasoning, it is anticipated that light will penetrate deeper through osteosarcoma than through red marrow alone. A diffusion model of fluence versus depth of penetration is plotted to this affect for varying blood concentrations (Figure 4.5). Due to this, it is anticipated that sufficient light can be delivered to osteosarcoma in order to achieve the desired phototoxic effects in PDT. Upon penetrating beyond the boundaries of the osteosarcoma, incident light will quickly attenuate in the surrounding marrow due to greater absorption by blood, effectively minimizing the region of photochemical damage in healthy marrow and surrounding tissue. The reduced scattering coefficient within osteosarcoma is again assumed to be the same as in cortical bone, due to the presence of trabeculae.

TABLE 4.1: Optical Properties used in Monte Carlo Model

$\lambda = 635nm$	$r[mm]$	$n[-]$	$\mu_a[cm^{-1}]$	$\mu_s'[cm^{-1}]$	$g[-]$
marrow	< 7	1.35	7.0	1.616	0.95
osteosarcoma	< 7	1.35	1.4	1.616	0.95
cortical	$7 < r < 10$	1.45	0.15	1.616	0.95
$0.035\mu gPpIX/mL$	-	-	0.0008	-	-
$100\mu gPpIX/mL$	-	-	2.6	-	-

4.2. Results

The previously argued and experimentally determined absorption and reduced scattering coefficients at 635nm were then input into the cylindrically symmetric Monte Carlo

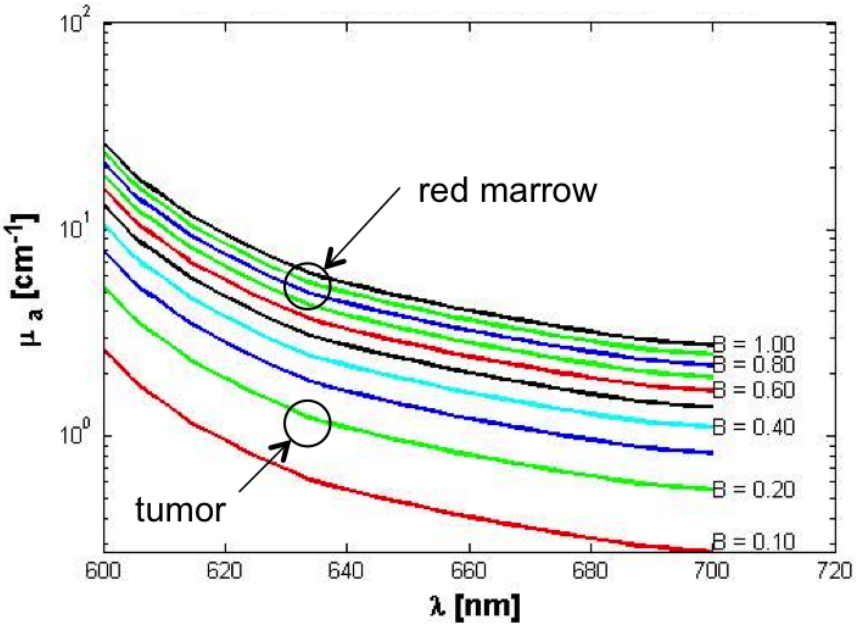

FIGURE 4.4: Absorption coefficient of oxygenated and deoxygenated hemoglobin (assumes $S = 0.85$) versus wavelength for varying blood concentrations. The absorption coefficient of red marrow is estimated to be nearly and order of magnitude larger than that of osteosarcoma.

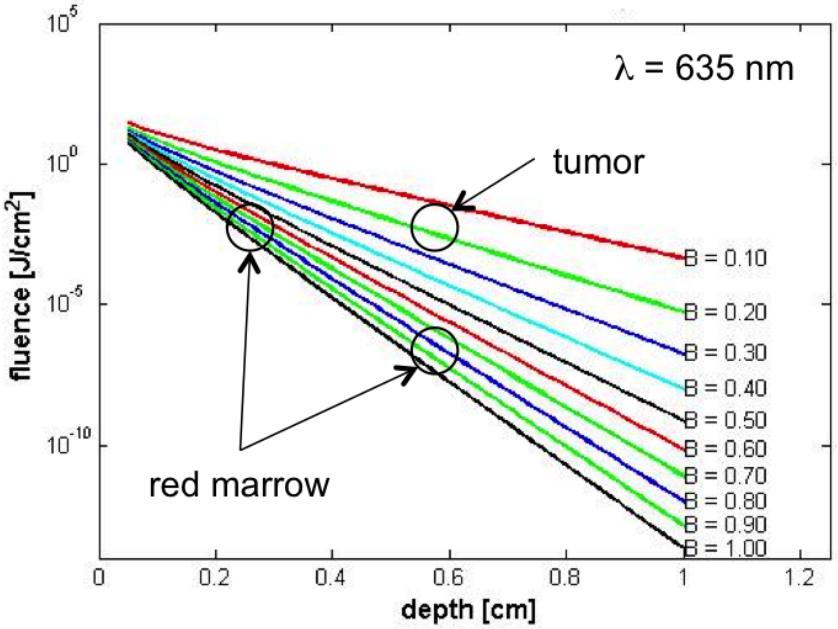

FIGURE 4.5: A diffusion model of fluence as a function of penetration depth at $635nm$ for varying blood concentrations. Neglecting scattering, the fluence found in red marrow would need to be increased by five orders of magnitude in order to achieve the same level of fluence found in osteosarcoma for the same penetration depth of $6mm$.

simulation in order to model light distributions in long bones, both with and without osteosarcoma present. The indices of refraction for marrow and osteosarcoma are assumed similar to that of soft tissue ($n_{m,ost} = 1.35$), while that of cortical bone is assumed to be similar to that of dentin ($n_{cort} = 1.45$). Both simulations used an inner radius of $7mm$, representing the medullary cavity, and outer radius of $10mm$, representing exterior of the cortical shell. The model including osteosarcoma assumed a cylindrical plug of osteosarcoma, filling a $10mm$ length of the medullary cavity.

A log_{10}-scale contour plot through a plane containing the central axis of each simulation is shown for a $10mm$ cylindrical diffusing source ($635nm$) located at the center of the medullary cavity (Figure 4.6). This source represents a cylindrical diffusing tip connected to a fiber-optic cable, inserted through the epiphysis and directly into the marrow or osteosarcoma. A cumulative exposure of $100Jcm^{-2}$ (the red contour line) is typically sought in order to achieve the desired phototoxic effect in ALA induced PDT.

In the marrow alone (Figure 4.6b), the exposure is attenuated to the order of $10Jcm^{-2}$ within the first $2mm$ beyond the source in the radial direction. Fluences on the order of only $\sim 1Jcm^{-2}$ penetrate along the axial direction and drop off by another order of magnitude within another millimeter.

When the osteosarcoma mass is present (Figure 4.6a), we see that the light does penetrate deeper through the tissue, as expected. A fluence of $100Jcm^{-2}$ is able to reach $\sim 3mm$ radially outward from the cylindrical diffuser. The fluence then drops another order of magnitude for roughly each $\sim 1mm$ that it propagates along the radial direction, such that it is nearly attenuated by the time it reached the cortical shell. In the absence of strong absorption, the small fraction of photons that do reach the cortical shell propagate throughout its depth and leave, such that a slight glow might be visible if the bone were exposed during treatment. The presence of the osteosarcoma, and therefore lesser blood concentrations than in the surrounding marrow, also allows the light to penetrate deeper along the axial direction, having a fluence as high as $100Jcm^{-2}$ within the first $\sim 1mm$ and then quickly attenuates again within another $\sim 3mm$ due to the high absorbance of blood in the marrow.

Concentrations of PpIX are added to the tumor, at similar levels observed *in vitro* for human osteosarcoma cells, $0.035\mu gPpIX/mL$ (section 5.2.). The measured concentrations were quite low, leading to a very low contribution to absorption for the Monte Carlo model. As such, absorption due to PpIX within the tumor mass was insignificant, and the light was able to maintain similar levels of fluence at similar depths as in the scenario without PpIX present.

In order to achieve attenuation of light within the osteosarcoma tumor similar to that of the blood in the marrow itself, some $100\mu g/mL$ concentration of PpIX would need be present (section 5.2.). While this is an excessive concentration of PpIX, it goes to demonstrate that for nominal levels of PpIX in the tumor, the light will still penetrate deep within the tumor to cause a phototoxic effect.

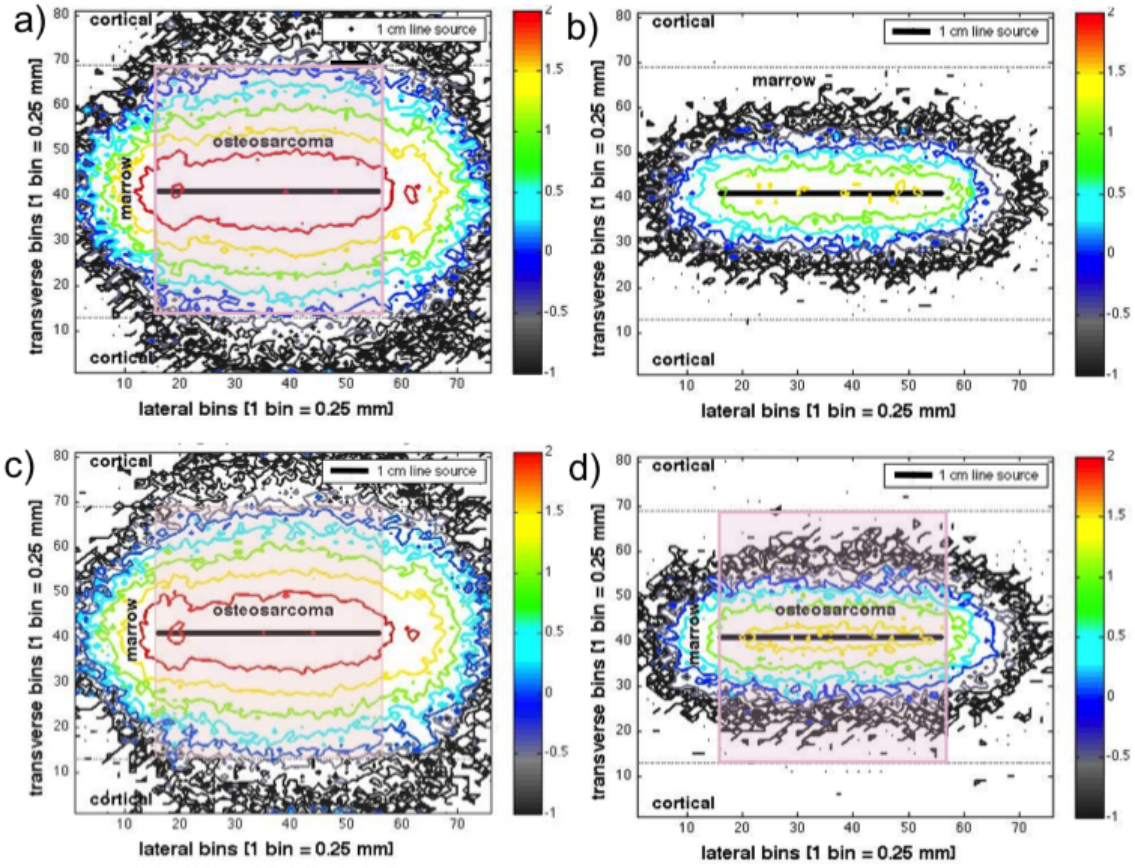

FIGURE 4.6: Lateral slices through the central axes of varied Monte Carlo simulations display isocurves for the log_{10}-scale fluence $[Jcm^{-1}]$. The thick black, central line represents the positioning of a $1cm$ cylindrically diffusing fiber tip along the central axis. The transparent, pink box centered in figures a, c and d represents the location of tumor masses within the respective bones. a) Cortical bone surrounding marrow and a $1cm$ long, cylindrical tumor which fills the medullary cavity in the radial direction. b) Cortical bone surrounding healthy marrow. c) The same physical scenario as (a), however absorption due to $0.035\mu gPpIX/mL$ is also added within the tumor mass. d) Concentrations of $100\mu gPpIX/mL$ would be needed to attenuate the light as efficiently as the absorption due to blood within the marrow.

4.3. Discussion

These simulations confirm the expectation that light will penetrate deeper through osteosarcoma while attenuating rapidly after reaching the surrounding red marrow. This should effectively increase the localization of PDT treatment to the desired region with minimal collateral damage to the surrounding marrow. As depicted in the simulation including osteosarcoma, light that reaches the cortical shell does not attenuate as rapidly. This is an effect of the low blood concentration in cortical bone ($B \sim 0.01$). Although light reaching the cortical bone may then create undesired phototoxic effects in the region during PDT, this exposure will be relatively minimal.

From these results including PpIX within the osteosarcoma tumor mass, we can gather that a phototoxic affect would be limited to within the first $\sim 1-2mm$ of the tumor along the axial direction. Some photodamage may result beyond that range, but widespread necrosis should be minimized. More interestingly, the Monte Carlo simulation predicts that the necrotic region within the tumor would extend $\sim 3mm$ radially outward from the diffusing tip, similar to the results seen in reported PDT of a porcine model of vertebral osteosarcoma using the photosensitizer BPD-MA.[48]

In order to achieve a necrotic effect throughout osteosarcoma tumors in clinical canine cases, a total fluence of $500Jcm^{-1}$ was reached in order to activate BPD-MA.[48,50] Using a $250mW/cm^2$ source as reported in that work, we can use (1.20) with the remaining parameters outlined for the $0.035\mu gPpIX/mL$ trial (Table 4.1) to determine that a modest exposure time of 1 hour and 21 minutes ($t_{exp} = 4,873s$) would be needed to accumulate a total fluence of $100Jcm^{-2}$ at the most distant reaches of the tumor margins ($z_{necrosis} = 7mm$). In employing (1.20), the backscatter term, k, has been set to unity since this trial illuminates the tumor internally and there would be no surface effects to attenuate the incident light prior to penetrating the tissue.

Measured and argued absorption and reduced scattering coefficients for bone tissues were applied to a cylindrically symmetric Monte Carlo simulation, approximating the geometry of long bones. These simulations compared light propagation in long bones both with and without the presence of osteosarcoma. Along with a diffusion model, the Monte Carlo model illustrated light as penetrating deeper through osteosarcoma, while attenuating quickly within the surrounding marrow. These effects are expected to add to the localization of phototoxic damage in applying PDT to treatment of osteosarcoma.

Although this work has focused on predicting how PDT can be used in treating cases of osteosarcoma, it can be adapted in the future towards broader clinical applications, including using PDT to treat secondary bone cancers that are the result of metastases originating in the lungs or breast. In all cases, a better understanding of the actual physiological accumulation and retention of PpIX (or any other PS) within the targeted tumor would help to further define and improve this model's predictive value.

5. PHOTODYNAMIC THERAPY OF OSTEOSARCOMA CELLS

This chapter looks at an *in vitro* study of photodynamic therapy (PDT) in the MG-63 line of human osteosarcoma cells, as mediated by aminolevulinic acid (ALA). While the previous chapter (sections 4.2. and 4.3.) looked at the optical transport necessary in order to reach sufficient levels of illumination in an osteosarcoma mass in silico, the primary goal of this chapter is to determine the feasibility and effectiveness of treating osteosarcoma through PDT based on an *in vitro* cell model.

The MG-63 cells are treated with increasing concentrations of ALA from $0.1 - 10mMALA$, leading to the accumulation of the photosensitizer protoporphyrin IX (PpIX) within the cells. After incubation periods of 4 and 24 hours in ALA, the cells are illuminated by $0 - 6Jcm^{-2}$ of $636nm$ light in order to activate the PpIX and induce oxidative damage to the cells. Light is administered by an 8×12 array of LEDs, which are controlled by an Arduino Duemilanove microcontroller board in order to assure ease of use along with accurate levels of exposure. Controls for this experiment include $0Jcm^{-2}$ of light exposure for all experimental concentrations of ALA, as well as illuminating cells that have not been incubated in ALA at all experimental levels of illumination. MG-63 cells are analyzed through MTT assays in order to determine the effectiveness of ALA mediated PDT of osteosarcoma.

The work represented in this chapter was done in collaboration with Paige Baugher, PhD and two undergraduate students at the time—Mariko Newton and Brad White—from the Pacific University Department of Biology. All optical work presented in this chapter is the direct work of the author, who also assisted with some of the tissue culture work and the application of PDT. The work on conversion of ALA to PpIX was done specifically by the author and Brad White. However, the majority of the tissue culture work was carried out by these collaborators, as well as the reported MTT assays post PDT.[56,130]

5.1. Experimental Design & Methodology

A spectrometer (Red Tide®, Ocean Optics, United States) was used to determine the absorption of PpIX versus concentration over the range of $380 - 950nm$. A $1mM$ stock solution of PpIX was created by diluting a PpIX disodium salt (Sigma-Aldrich, United States) in lysis buffer (1% SDS in $0.1MNaOH_{aq}$). Serial dilution of the $1mM$ stock solution was carried out in order to create $1 - 100\mu M$ concentrations of PpIX for spectral measurements. These results are then interpolated in order to determine the absorption of PpIX as a function of both wavelength and concentration (Figure 5.1). The intensity

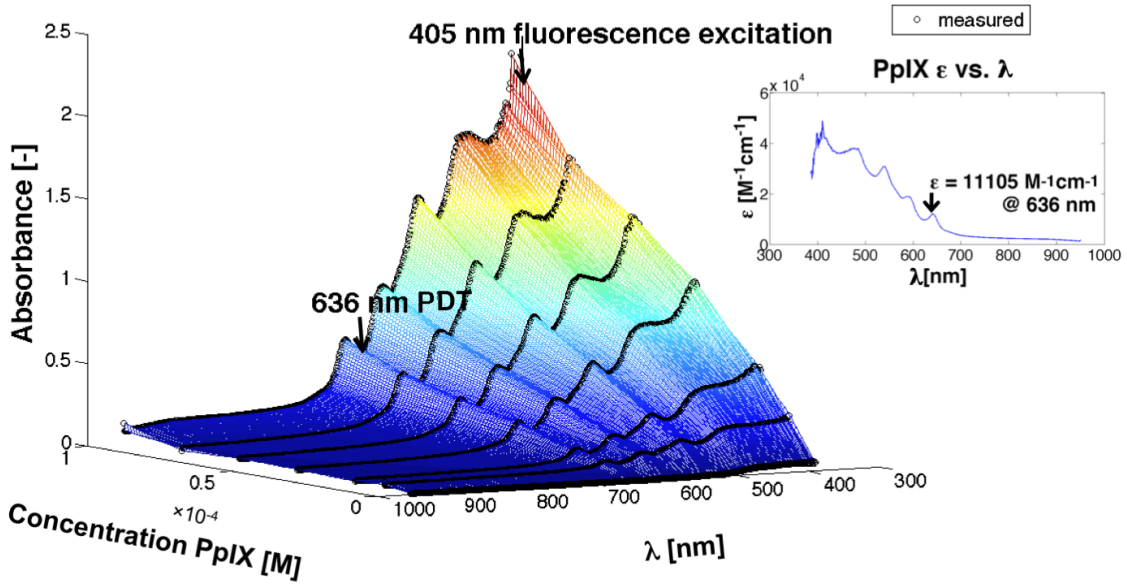

FIGURE 5.1: Absorption curves of PpIX versus wavelength for varying concentrations of PpIX. Experimental data is represented by black circles along lines of constant concentration. The colored contour plot is a fit of the absorption for all concentrations and wavelengths in this range. INLAY: The extinction coefficient of PpIX as a function of wavelength, as determined from the absorption measurements.

measured by the spectrometer in terms of absorption units (A_λ)

$$I = I_o 10^{-A_\lambda} \tag{5.1}$$

can also be expressed in terms of the extinction coefficient (ε_λ)

$$I = I_o e^{-\varepsilon_\lambda cl}, \tag{5.2}$$

where I is the measured intensity, I_o is the initial intensity of the source, c is the concentration of PpIX, and $l = 1cm$ is the length of the cuvette. The absorption and extinction coefficients are dependent upon wavelength and share the relationship

$$\varepsilon_\lambda = \frac{A_\lambda ln10}{cl} \tag{5.3}$$

which is determined by setting (5.1) and (5.2) equal. The extinction coefficient of PpIX versus wavelength is so determined over the range of the spectrometer (Figure 5.1, inlay). The excitation bands used in this chapter for fluorescence and photoactivation in PDT are indicated at $405nm$ and $636nm$, respectively. The $636nm$ wavelength has an extinction coefficient of $11105 M^{-1}cm^{-1}$. These results are employed later in order to determine the optical dosage absorbed by PpIX for *in vitro* PDT of MG-63 cells.

In order to quantify the conversion of ALA to PpIX after incubation in human MG-63 osteosarcoma cells, a spectrofluorometer (FluoroMax-4®, HORIBA Scientific, United

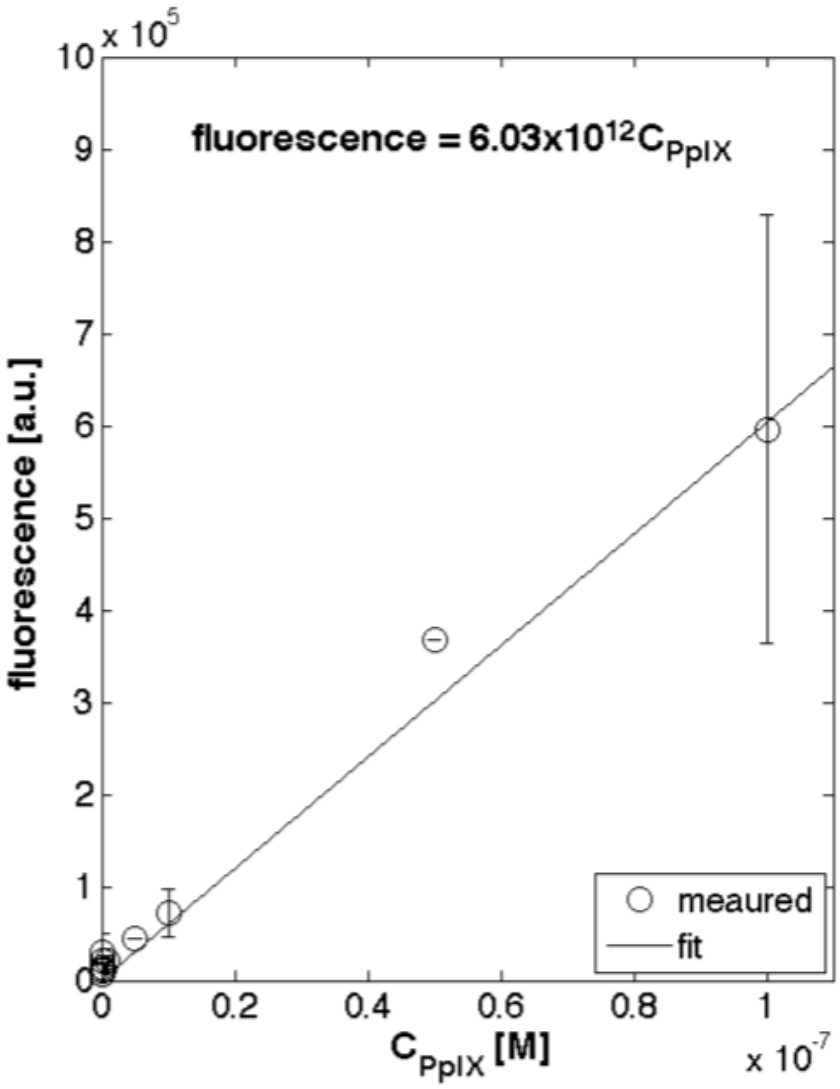

FIGURE 5.2: Fluorescence detected at the $650nm$ emission wavelength post $405nm$ illumination of PpIX is proportional to concentrations of PpIX.[56,130]

States) was used in order to determine a standard curve for PpIX fluorescence versus concentration (Figure 5.2). Serial dilution of the $1mMPpIX$ stock solution was carried out in order to create $10^{-12} - 10^{-6}M$ concentrations of PpIX for measurement. Fluorescence measurements were made using an excitation wavelength of $405nm$ while emission was detected at and above $650nm$. The fluorescence signal is linearly proportional to PpIX concentration, with a constant of proportionality of $6.03 \times 10^{12} M^{-1}$.[56,130]

An ALA hydrochloride salt (Sigma-Aldrich, United States) was diluted in phosphate buffer solution (PBS), creating a $100mMALA$ stock solution which was added to

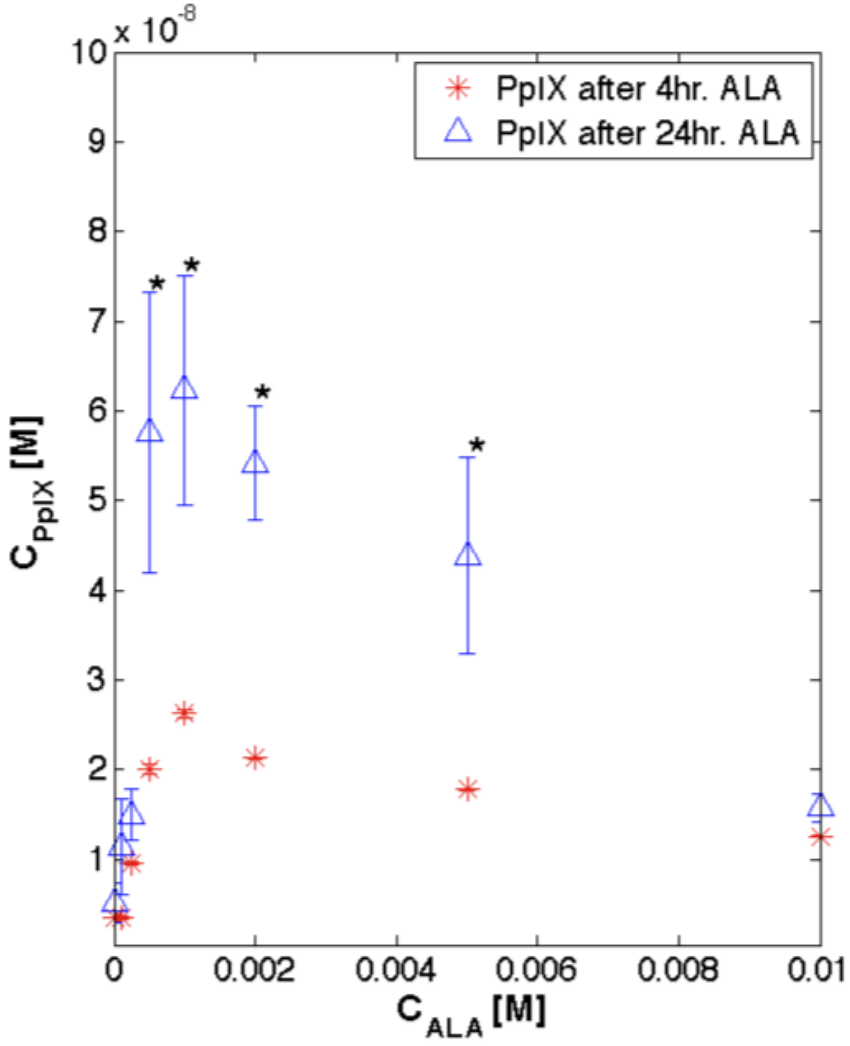

FIGURE 5.3: Measured fluorescence of PpIX after incubating known quantities of ALA in MG-63 cells indicates levels of accumulation of PpIX in these cells for concentrations of ALA. Error bars represent ± SEM. $* = p < 0.05$ compared to 4hr timepoints.[56, 130]

MG-63 cells for incubation in concentrations of $0.1 - 10mMALA$. Cells incubated for 4 and 24 hours at 37^oC in $5\%CO_2$ before lysing them with a lysis buffer solution (1% SDS in $0.1MNaOH$) in order to release accumulated PpIX for fluorescence measurements. The spectrofluorometer excites the solution with an excitation wavelength of $405nm$ in order to measure emission from accumulated PpIX at and above $650nm$. Resulting fluorescence measurements from MG-63 cells in known concentrations of ALA were then compared to the fluorescence versus PpIX concentration standard curve in order to determine a correlation between PpIX accumulation and ALA incubation concentrations (Figure 5.3).[56, 130]

As compared to 4 hours of incubation, PpIX accumulation is greater in cells after 24

hours of incubation in ALA. The increase in production of PpIX is particularly significant ($p < 0.05$) between the $0.5 - 5.0mM$ concentrations of ALA. For both the 4 and 24 hour incubation times, the PpIX accumulation in MG-63 cells reaches its maximum when cells are incubated in $1mMALA$. Instead of PpIX production increasing towards some limiting value as a function of ALA concentration, we found the levels of PpIX fall off beyond the $1mMALA$ concentrations. This response is likely tied to cellular toxicity of MG-63 cells in the presence of high concentrations of ALA. An example of this cytotoxicity can be seen in response to 24 hour incubation of MG-63 cells in $10mMALA$, as represented in (Figure 5.6) from (section 5.2.). However, further analysis of this response warrants further investigation before conclusive remarks can be made to this extent.

5.1.1 PDT of MG-63 Cells

The MG-63 cells were incubated at 37^oC in an atmosphere of 5% CO_2 in a flask of 500 μL of complete Dulbecco's Modified Eagle Medium (cDMEM). This medium was created by adding antibiotic LPS (l-glutamine, penicillin, and streptomyocin) and fetal bovine serum (FBS) to standard Dulbecco's Modified Eagle Medium (DMEM). While cells remained fixed to the bottom of their flask, the cDMEM was aspirated from the flask and $3mL$ of trypsin was added in order to break their bonds to the bottom of the flask. After allowing 2-3 minutes for the trypsin to release the cells from the bottom of the flask, $3mL$ of cDMEM was added back to the flask and rinsed repeatedly over the bottom in order to deactivate the trypsin and remove all of the cells from the bottom of the flask. The cells were then transferred in solution into a $15mL$ conical tube and centrifuged for 5 minutes in order to create a pellet of cells at the bottom of the tube to be separated from the medium. Once the cells were pulled out of suspension, the solution was aspirated and replaced again with pure cDMEM.

The cells were then transfered in solution to 96-well cell culture plates such that 3000 cells in $100\mu L$ of solution were plated in each well. Black plastic 96-well plates with clear bottoms were used for plating the MG-63 cells in preparation for PDT in order to prevent light contamination between wells during illumination. The clear bottoms of the wells allow the cells to be illuminated from below during PDT, as well as serving imaging and flourometry purposes. The plated cells then incubate at 37^oC in 5% CO_2 for 48 hours in order to give cells ample time to fix themselves to the bottoms of the plates prior to PDT.

Although cDMEM provides a positive growth environment for MG-63 cells, the presence of FBS in the medium blocks the uptake of ALA and therefore the production of PpIX.[131,132] As such, prior to introducing ALA to the plated cells, the cDMEM is aspirated from the wells and replaced with DMEM. Appropriate amounts of ALA are then added to the wells in order to reach the desired concentrations of $0.1 - 10mMALA$. From this time forward, care is taken to keep the cells in a dark environment in order to control the light dosimetry of the PDT process. The plates are then incubated for varying

drug-light intervals prior to illumination.

Upon reaching the targeted incubation period, the 96-well plates were then placed on top of the 8×12 LED array such that each well was illuminated by an individual LED. Light from the LED array was controlled using the Arduino microcontroller and interfacing software (section 5.1.2). The interfacing code was written such that the user need only update the desired cumulative fluence within the code. Upon uploading fluence changes to the microcontroller board, the activation time for each column of eight LED's is calculated based on their calibration. The time of exposure is also updated as the columns of LED's receiving stronger inputs time out and the signal to the remaining activated columns increases (Table 5.1). Once illumination of a 96-well plate is complete, the plate is again stored in a dark incubator at 37^oCin $5\%CO_2$.

TABLE 5.1: Exposure times for required fluence levels using LED array for PDT of 96-well plate

$E_o[Jcm^{-2}]$	t_{exp} [min:sec]
0	0:0
0.3	1:52
0.6	4:00
3	18:55
6	37:49

5.1.2 Light Source: Design and Protocol

An 8×12 array of $5.0mm$ red LEDs (Part No. 1586189, Jameco Electronics, United States) was created in order to control illumination in individual wells of black 96-well plates which were used for incubating MG-63 cells in ALA, PDT treatment, and MTT assays post PDT (Figure 5.4a). Grouped in columns of eight, the LED's were controlled by a microcontroller board (Arduino Duemilanove®, Arduino, Italy) and the associated Arduino open source software. Each of the twelve LED columns was connected to one of the digital output pins via a Darlington configuration of two transistors (Figures 5.4b and 5.5) in order to amplify the output of the digital pins.[133] The collectors of all of the transistors implemented were connected in parallel to the constant $5V$ output pin located on the Arduino board.

Although the digital output pins are rated at $5V$ and a maximum of $40mA$ (direct current) each, there were variations within these outputs depending on the number of pins activated at a given time. However, these variations were regular and overall signals

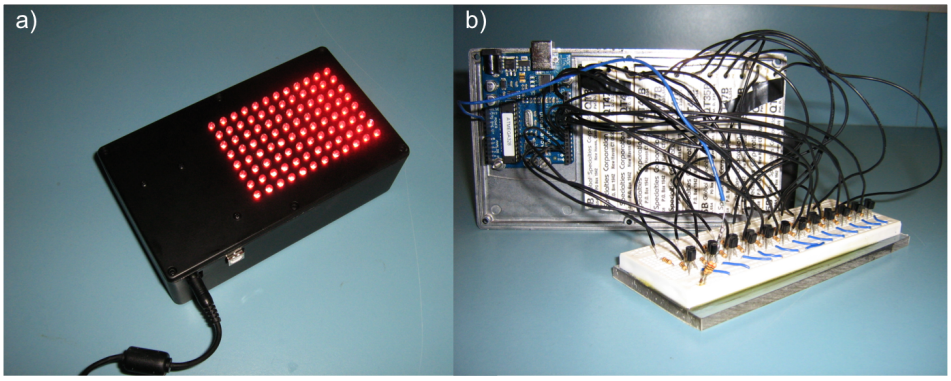

FIGURE 5.4: a) The functional 8×12 LED array used in irradiating MG-63 cells incubated in 96-well plates. b) Construction of the LED array, showing the Arduino Duemilanove microcontroller and each of the 12 Darlington transistor configurations.

generally decreased with increased pin number (I/O Pins 2-13). As such, once the LED's associated with the pin of greatest output had reached the specified cumulative irradiance output, they were automatically shut off and the remaining pins' outputs were recalculated at the resulting output levels. In this fashion, all of the output pins were controlled through the Arduino interfacing program such that they sequentially timed out upon achieving the desired light dosages. The LED's used were rated at a maximum forward voltage of $2.5V$ and forward currents of $20mA$. Given the parallel connection of each group of eight LED's, an individual LED was supplied by an average forward voltage of $1.96V$ and $6.9mA$ of forward current.

The LED array can be operated such that all wells receive equal levels of illumination (total energy incident per unit area), or these levels can be varied by column in order to treat different wells at different levels of illumination, depending on the experimental design. In addition, every third column of LED's can be left off in order to treat cells in 12-well plates. When treating cells in 12-well plates, four LED's (a 2×2 array) are used to illuminate an individual well. A diffusing plate is placed between the LED's and bottom of the well-plate in order to distribute the light evenly when using multiple LED's to treat larger surfaces, and the LED array is calibrated accordingly in order to account for attenuation.

Spectra were collected from each of the individual LED's in the array using a fiber optic cable (USB650 Red Tide Spectrometer®, Ocean Optics, Inc., United States). The peak wavelength of the LED's emission spectrum was at $636nm$ ($FWHM = 16nm$). Additionally, the output power was detected with a power meter calibrated to a $635nm$ wavelength (PM100D Power Meter®, ThorLabs, United States). In order to measure the power incident on the cells, measurements were taken at the same height above the LED's as the 96-well plate sits. Reflection at the bottom of the plastic well was also accounted for.

The spectral and power measurements collected were used in calibrating the array

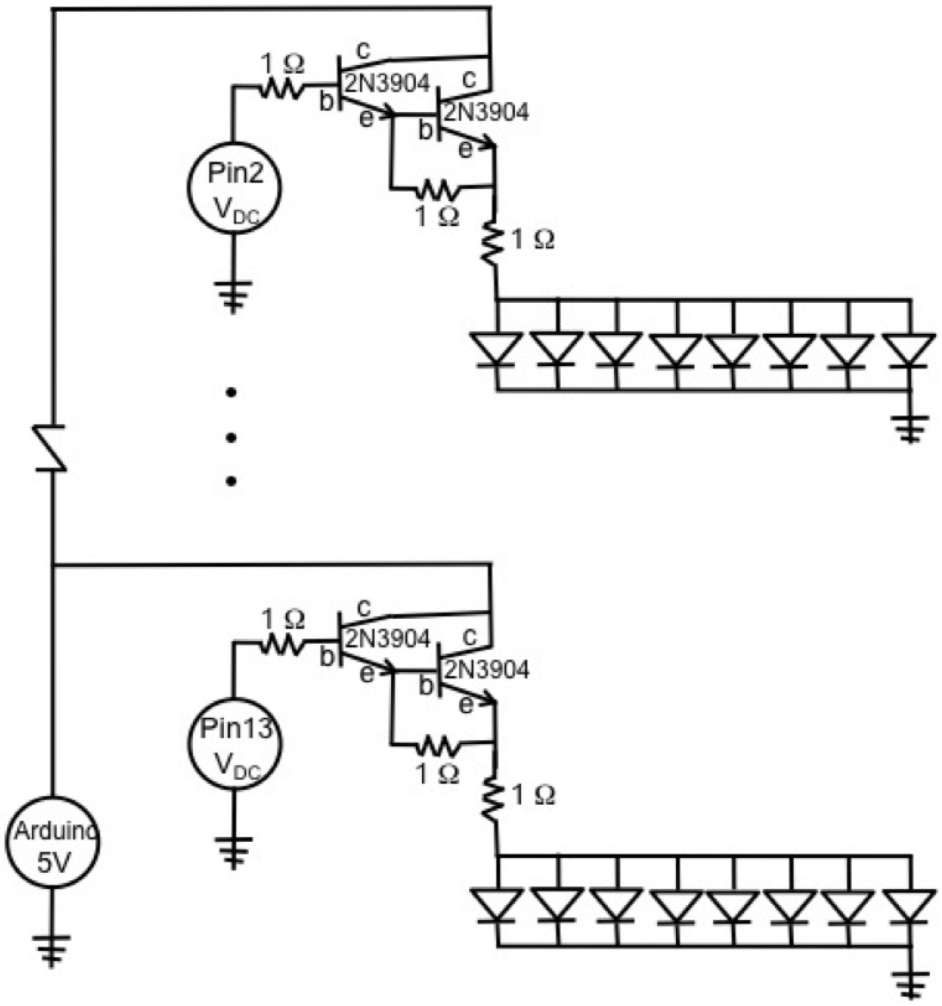

FIGURE 5.5: An electrical schematic of the LED array using the Darlington transistor configuration. Only a pair of Darlington transistor configurations are depicted in order to conserve space, however this configuration is repeated twelve times from Arduino Duemilanove microcontroller digital I/O pins 2-13—one for each column of eight LED's. All of the transistor collectors are connected in parallel to the board's $5V$ regulated power supply pin.

for control with the Arduino software. To begin, the spectrum was normalized by summing over the spectral measurements at each wavelength (S_λ) and dividing by the area of the fiber optic cable used to collect the spectra ($A_s = 3.14 \times 10^{-4} cm^2$),

$$N_\lambda = \sum_\lambda \frac{S(\lambda)}{A_s}, \tag{5.4}$$

rendering the normalization constant (N_λ). In this fashion, the normalized spectrum (S'_λ) can be achieved by dividing the measured spectra at a given wavelength by the normalization constant

$$S'(\lambda) = \frac{S(\lambda)}{N_\lambda}. \tag{5.5}$$

In order to relate the measured power measured (P_{LED}) to the normalized spectrum, we need to account for the area of the power meter ($A_p = 0.709 cm^2$)

$$\frac{P_{LED}}{A_p} = N_\lambda \cdot cal, \tag{5.6}$$

where the calibration constant (cal) is given in units of [W/counts],

$$cal = \frac{P_{LED}}{\sum_\lambda S(\lambda)} \cdot \frac{A_s}{A_p}. \tag{5.7}$$

Given this calibration constant, the irradiance (I) can be determined as a function of wavelength

$$I(\lambda) = \frac{S(\lambda)}{A_s} \cdot cal, \tag{5.8}$$

having units of Watts per unit area. Therefore, the power incident on a single 96-well (as a function of wavelength) is then determined by multiplying the wavelength dependent irradiance by the area of a single well,

$$P(\lambda) = I(\lambda) A_w, \tag{5.9}$$

where $A_w = 0.32 cm^2$ is the area of each well in a 96-well plate.

Using the calibrated power in conjunction with the concentration of PpIX accumulated in cells and its extinction coefficient as a function of wavelength, we can then integrate over the wavelength dependencies in order to determine the total power absorbed by PpIX during PDT,

$$P_{tot} = \int I(\lambda) A_w \varepsilon_{PpIX}(\lambda) c_{PpIX} d\lambda. \tag{5.10}$$

This total power absorbed can then be used to determine the equivalent power necessary to achieve the same results from a different light source by equating the integral (5.10) for the different source to these results. For instance, assuming a $633 nm$ helium-neon laser

with a negligible FWHM, the integral reduces to the product of the laser's power with the concentration and extinction coefficient of PpIX at that wavelength, such that

$$P_{633nm}\varepsilon_{PpIX,633nm}c_{PpIX} = \int I(\lambda)A_w\varepsilon_{PpIX}(\lambda)c_{PpIX}d\lambda. \tag{5.11}$$

Therefore, dividing both sides by the concentration and extinction coefficient of PpIX at $633nm$, we can determine the equivalent power necessary to achieve the same results as found using the LED array

$$P_{633nm} = \frac{\int I(\lambda)A_w\varepsilon_{PpIX}(\lambda)c_{PpIX}d\lambda}{\varepsilon_{PpIX,633nm}c_{PpIX}}. \tag{5.12}$$

For example, assuming an accumulation of $6.23\times10^{-8}MPpIX$ resulting from MG-63 cells incubating in $1mMALA$ for 24 hours (Figure 5.3), the absorbed power by PpIX using the LED array is $6\times10^{-7}W$. By (5.12), a $0.9mW$ $633nm$ helium-neon laser would have the same affect.[56]

5.2. Experimental Results

An MTT cell proliferation assay was used to determine the cytotoxicity of ALA-mediated PDT in MG-63 human osteosarcoma cells. MTT assays measure the activity of enzymes that reduce the yellow tetrazolium salt (MTT) to purple formazan crystals. This process occurs within the mitochondria and therefore can be used as a measure of viability and integrity of mitochondria in cells. Therefore, a high optical density (number of counts) measured in the micro-plate reader (SpectraMAX 190®, Molecular Devices, Inc., United States) will be suggestive of high levels of activity in mitochondria and therefore little cell death, whereas a low number of counts will suggest low activity and more cell death.

The MTT solution was prepared by adding $15mg$ of MTT to $3mL$ of PBS. In order to allow for sufficient time for apoptosis and necrosis to occur in treated cells, 48 hours post PDT $30\mu L$ of the MTT solution was added to each of the wells in a 96-well plate. The cells then incubate in this solution for three hours at 37^oC in $5\%CO_2$. After incubation, the media was aspirated from each well and replaced with $100\mu L$ of $0.4M$ HCl in isopropanol. The HCl-isopropanol solution solubilizes the formazan crystals for measurement (absorption at $595nm$) in the micro-plate reader.

While no significant correlation was apparent from MTT results for the ALA-mediated PDT of MG-63 cells after 4 hours of incubation in ALA (data not shown), significant cell death was observed in PDT after 24 hours of incubation in ALA. Results from this set of experiments are displayed plotting the optical density as a measure of cell activity versus incubating concentrations of ALA and total fluence (Figure 5.6). Measurements are grouped by incubated concentrations of ALA, with increasing fluence displayed

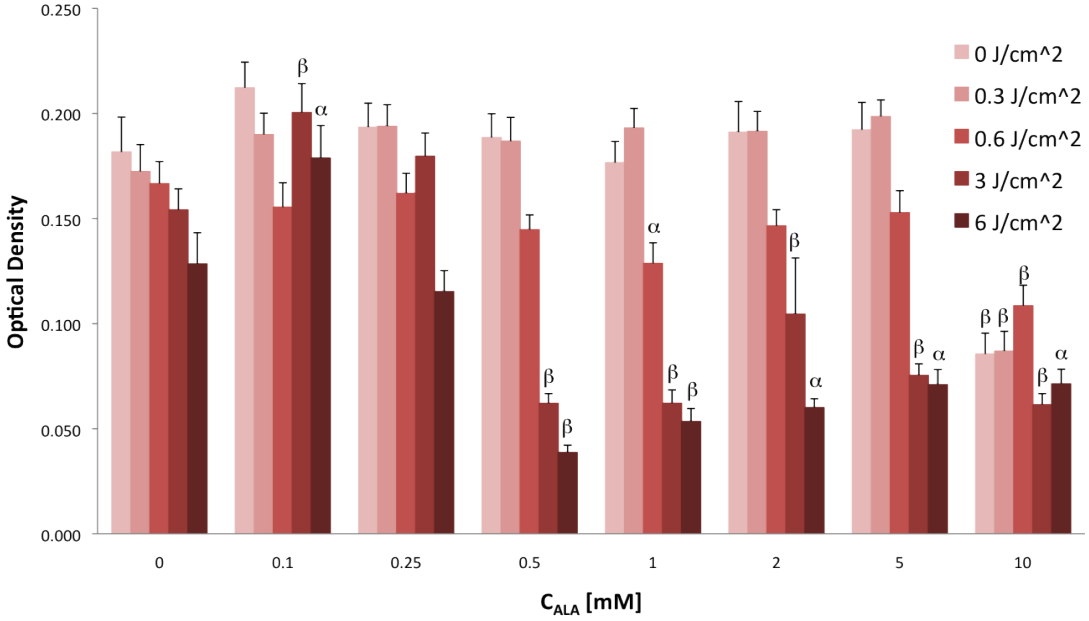

FIGURE 5.6: Cell viability post PDT (as measured by optical density) versus concentrations of ALA and fluence. Groups of columns are plotted along the horizontal axis for each concentration of ALA. Individual columns within these groupings represent varied light exposures. Results are shown for 24 hours of incubation in ALA. Cellular toxicity was evaluated with an MTT assay 48 hours post PDT treatment. The Optical Density of the MTT assay decreases with a loss of mitochondrial function and is therefore used as a measure of cell viability. Error bars represent +/- SEM. $^{\alpha} = p < 0.05$, $^{\beta} = p < 0.01$ as compared to the 0 mM ALA control.[56,130]

from left to right in each of those groups. Error bars are given using the standard error of the mean, and statistical significance is determined by comparing each fluence at a given concentration of ALA to the same fluence in the absence of ALA.

Plotting the results in this fashion gives the ability to test against two separate control groups—light exposure without the presence of ALA and then varied concentrations of ALA without irradiance. While the $0MALA$ group does appear to have a trend towards light toxicity at higher fluence levels, there was no statistical significance between these results. Comparing optical densities measured across the concentrations of ALA without illumination ($0Jcm^{-2}$) serves to test for cytotoxicity of ALA.

At and above $0.5mM$ of ALA, significant cell death was observed ($p < 0.05$ and $p < 0.01$ using the non-parametric Wilcoxon Signed-Rank Test) consistently for fluences of 3 and $6Jcm^{-2}$. All fluence levels at the $10mMALA$ concentration show significant differences from the $0mMALA$ control, however this is likely due to cytotoxicity of ALA and not from photochemical damage induced via PDT. This can be explained by reflecting on the significant cell death observed for the two lowest fluences (0 and $0.3Jcm^{-2}$) in the $10mMALA$ group, whereas no other concentrations of ALA saw significant cell

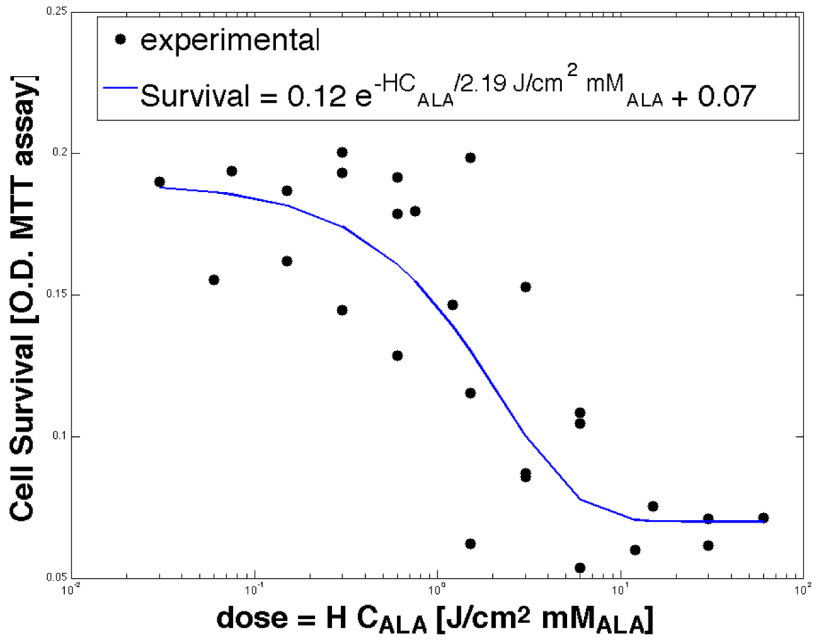

FIGURE 5.7: The cell survival data from the MTT assay results (Figure 5.6) is plotted again here, combining the radiant exposure (**H**) and concentration of ALA ($\mathbf{C}_{ALA}$) into a single dose parameter. Cell survival is again plotted on the vertical axis, as based on the Optical Density resulting from the MTT assay. As seen in the previous figure, the Optical Density decreases with increased dose. Cell survival decreases exponentially with dosage, as shown by the survival curve fit to the data via least squares fitting.

death at these fluence levels. No photochemical activation of PpIX will have occurred for the $0 Jcm^{-2}$ fluence, such that cell death will not be a result of PDT. With all other variables equal, this leaves cytotoxicity of ALA as the remaining explanation for cell death observed when MG-63 cells are incubated in $10 mM ALA$. If ALA is cytotoxic at $10 mM$, as explained, then it can be concluded that the resulting cell death for other fluences at this concentration will not be solely due to PDT and the cytotoxicity of ALA played a role in these results.

An alternative approach to displaying this data is to combine the radiant exposure and concentration of ALA in which cells were incubated into a single dose parameter. Cell survival is still determined by the optical density measurements from the MTT assay (Figure 5.6), but is now plotted against the single dose factor (Figure 5.7). In general, this figure emphasizes that cell death increases with dosage. An exponetial function can be fit to the survival curve in order to determine a quantitative, predictive function for future experiments.

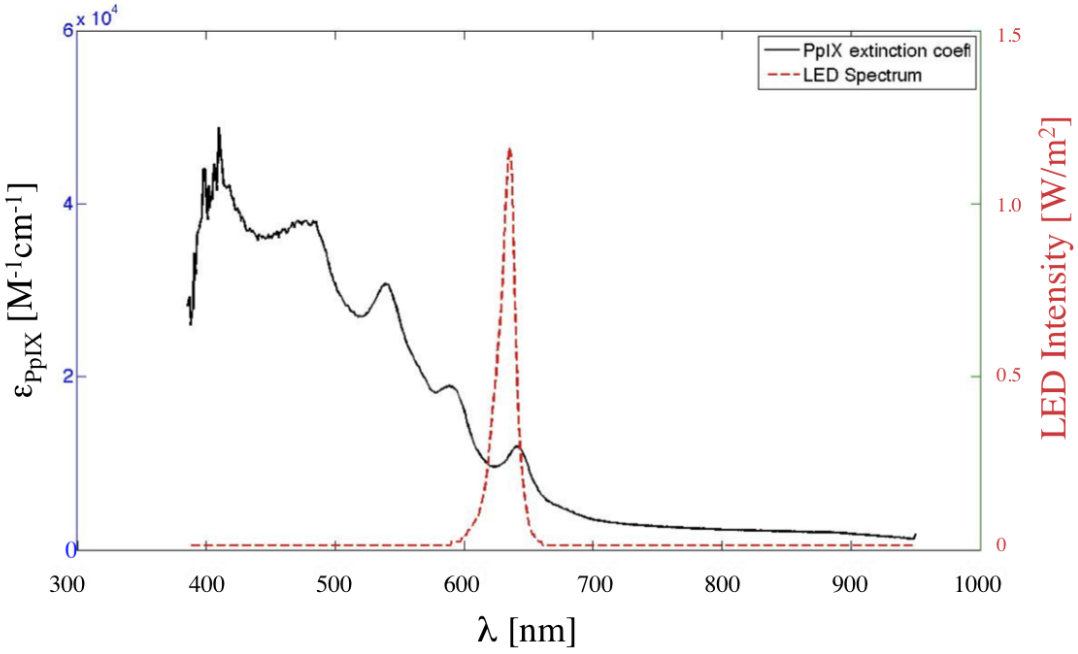

FIGURE 5.8: The PpIX extinction coefficient and illumination spectra are integrated over the visible spectrum in order to determine a photodynamic dose (the nubmer of photons absorbed by PpIX) achieved in the *in vitro* ALA mediated PDT of MG-63 human osteosarcoma cells.[56, 130]

5.3. Discussion

Knowing the concentration of PpIX that accumulates in MG-63 cells and the spectrum of the source used for illumination, it is possible to determine the photodynamic dose (number of photons absorbed by PpIX) for the *in vitro* experiments by integrating the PpIX extinction coefficient and illumination spectrum (Figure 5.8). The PDT dosage is determined via the integral

$$D_{PDT} = \int I(\lambda) t_{exp} \frac{\lambda}{hc} A_W \varepsilon_{PpIX}(\lambda) C_{PpIX} d\lambda, \tag{5.13}$$

where $I(\lambda)$ is the irradiance as a function of wavelength (λ), t_{exp} is the time of exposure, h is Planck's constant, c is the speed of light, A_W is the area of the well in which the cells were illuminated, $\varepsilon_{PpIX}(\lambda)$ is the extinction coefficient of PpIX as a function of wavelength, and C_{PpIX} is the accumulated concentration of PpIX. After plating 3000 cells per well in a 96-well plate ($A_W = 0.32$ cm^2), incubating in 1 mM ALA for 24 hours and a radiant exposure of 6 J/cm^2, the accumulated PDT dose was calculated to be on the order of 3×10^{15} photons absorbed.

The 3.4×10^{15} photons absorbed by PpIX in our example, as calculated from (5.13), is roughly two orders of magnitude less than the $10^{17} - 10^{20}$ photons that are typically

absorbed per gram of tissue in order to bring about sufficient photoactivation to achieve cell death.[57] Although the calculated number of photons absorbed in our example are only done so for a thin layer of MG-63 cells fixed to the bottom of the 96-well plate, extrapolating that scenario to a bulk tissue model still remains two orders of magnitude short of the $10^{17} - 10^{20}$ photons typically absorbed per gram of tissue in bulk models. This is a direct consequence of the low concentration of PpIX accumulated in MG-63 cells, which is two orders of magnitude less than reported levels accumulated in MTF7 cells.[134] While the accumulation of PpIX reported here and the total light absorbed by PpIX are considerably lower than expected, significant cell death was still observed in ALA-mediated PDT of the human MG-63 osteosarcoma cells when incubated in $0.5 - 5mMALA$ for 24 hours prior to illumination. Further investigation into the lower than expected PpIX production in human osteosarcoma MG-63 cells is warranted.

A qualitative review of Differential Contrast Microscopy images collected of treated and untreated MG-63 cells for the various experimental groups reported show a mix of both necrotic and apoptotic responses to ALA mediated PDT (Figure 5.9). This qualitative approach is based on morphological characteristics of apoptotic versus necrotic cells. Necrotic cell death is indicated when cells shows blebbing of its cytosol into the surrounding intercellular space. This process generally shows no general symmetry. Apoptotic cells tend to encapsulate themselves in preparation to break down into apoptotic bundles to be cleaned out via phagocytosis. During the early stages of apoptosis, cells tend to maintain a symmetric morphology.[135]

Initial work by collaborators has shown that there is no predominant response of either the necrotic or apoptotic pathways to ALA-mediated PDT of MG-63 cells. This may be due to a flaw in experimental design. The experiments were conducted in order to illuminate cells with a maximum concentration of PpIX, as determined via the spectrofluorometry data. The greatest concentrations were found for a drug-light interval of 24 hours between initial incubation in ALA and irradiance. This is no surprise—the greater concentrations of PpIX resulted from prolonged exposure to ALA. However, with this prolonged exposure also followed increased opportunity for the PpIX which was generated within the mitochondria to diffuse away from the mitochondria. This accumulation of ambient PpIX would lead to general, non-specific oxidative stress upon illumination, of which a general necrotic effect is characteristic. If the experiment were designed to bring about a predominantly apaoptotic effect, the drug-light interval would need to be much shorter, such that the PpIX is excited upon production within the mitochondria, which would then result in oxidative stress localized to the mitochondria, followed by a predominantly apoptotic response.

While further work should be done in quantitatively determining the relative mechanisms of cell death in these cells, studies have suggested that the unique combination of apoptotic and necrotic cell death resulting from PDT can activate an innate immune response, which can lead to tumor immunity.[136] Such an immunity would add to the advantages of PDT over systemic and traditional cancer therapies.

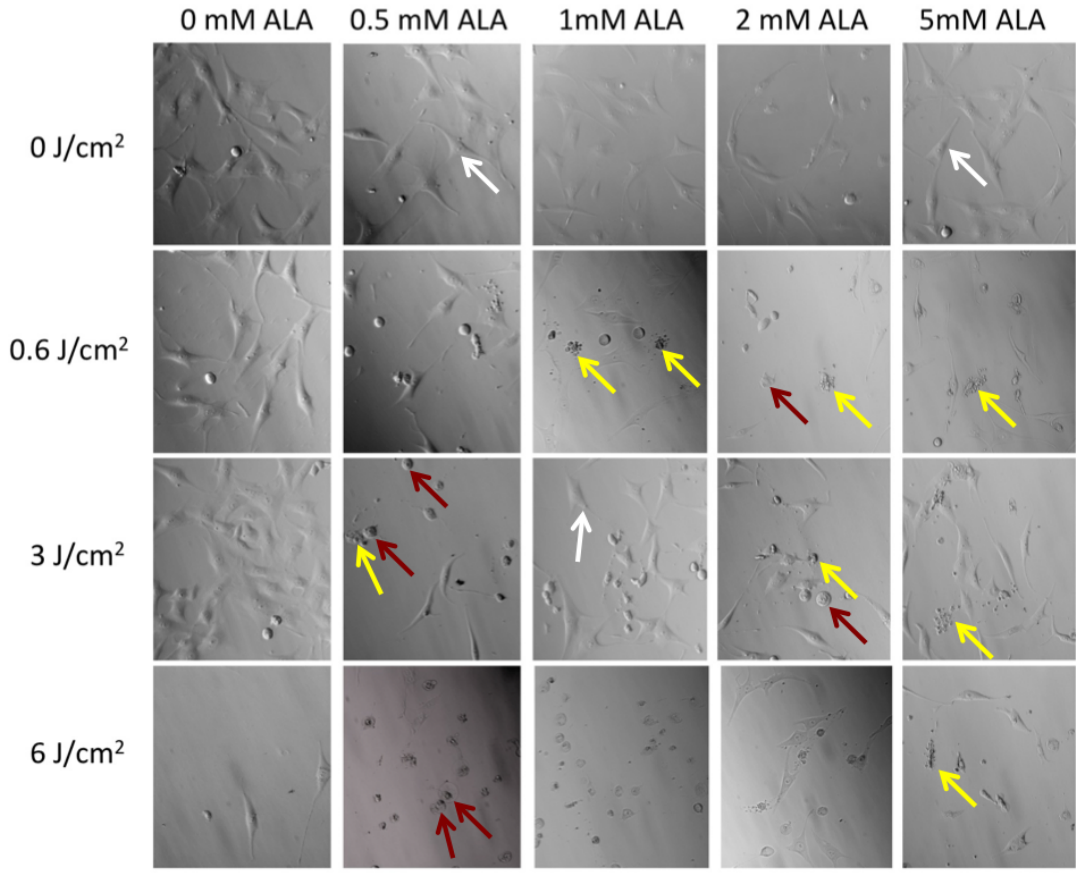

FIGURE 5.9: DIC images are displayed from the different control and experimental groups. The grid structure of these image tiles increases concentrations of ALA from left to right and total incident fluence from top to bottom. Examples of apoptotic (red arrows) and necrotic (yellow arrows) cell death are selected based on morphological indications. For reference, a few Mg-63 cells that don't appear to be undergoing either cell death pathway are indicated (white arrows). The DIC images were taken by Paige Buagher, PhD..[56,130]

We have demonstrated that ALA mediated PDT can effectively kill human osteosarcoma cells through an *in vitro* study using the MG-63 cell line (Figures 5.6 and 5.7).[56,130] PDT can result in both necrotic (general cell death) and apoptotic (programmed cell death) responses.

6. CONCLUSION

This work has outlined the basic principles behind light transport in tissues, including a brief description of scattering (Mie) theory. Moving beyond basic Biomedical Optics, a deeper look was taken at the applications and functionality of a digital Fourier holographic microscope and its use for optical scatter imaging. Computational models were used extensively as proof-of-principle simulations in explaining digital holography. The introduction then shifts from imaging concepts towards therapeutic application in the form of photodynamic therapy (PDT). An overview of PDT is given, followed by the specific application towards osteosarcoma. The principles of diffuse light spectroscopy and Monte Carlo modeling are then introduced as means of determining the optical properties of bone tissues and simulating a clinical application of PDT of osteosarcoma *in silico*.

The use of the digital Fourier holographic microscope (DFHM) is then demonstrated as a means of holographic imaging. The DFHM system gives a robust means of generating multimodal imaging, including optical scatter imaging (OSI), quantitative phase imaging (QPI) and 3D imaging. The advantage of this imaging modality over others is its ability to generate this diverse assortment of images from a single holographic exposure.

Prior to the generation of these multiple imaging modalities, this work gives an extensive and thorough description of the design and calibration of the DFHM. In particular, great effort was made in explaining the scaling of scattering angle space to the CCD pixel space at the conjugate Fourier plane of the DFHM. Both goniometric and ultimately OSI results are given for polystyrene microspheres of known diameter in mounting media in order to demonstrate the accuracy and effectiveness of this calibration.

Upon completing a description of the design and calibration of the DFHM, we then explore the multiple imaging modalities afforded by the DFHM. Imaging both cells in culture and thin slices of skin acquired post-biopsy demonstrates the ability of the system to discriminate between scattering objects within the respective samples. As applied to OSI, the DFHM is able to effectively pick out smaller collagen structures and bundles from larger structures within the dermis. This could be useful in exploring effects of hydration and aging on collagen bundling in the dermis. As we age, collagen structures break down in the skin, causing it to wrinkle, age and lose the elasticity that is generally associated with healthy skin.

OSI imaging of human osteosarcoma cells *in vitro* is also conducted in a pilot study to test for mitochondrial swelling during the onset of apoptosis, as initiated via exposure to staurosporine (STS). Cells were imaged in the DFHM over the course of an hour for both experimental (STS) and time control groups. Results from this experiment did generally show a decrease in the OSIR with time, which would suggest mitochondrial swelling during the onset of apoptosis. However, both the experimental and control groups show a similar decrease in the OSIR over the coarse of an hour in the DFHM. As such, we cannot make any claims with respect to mitochondrial swelling or the onset of apoptosis. We can however

claim that applying the DFHM towards OSI is sensitive to intracellular changes. While these results are suggestive, they are not conclusive, and a more rigorous and thorough investigation should be carried out. With respect to the use of the DFHM as an optical apoptosis assay, the experiment should be expanded to incorporate additional lines of interrogating the system such as apoptosis assays or electron microscopy. In addition, the time control group should be repeated a number of times and if the cells are indeed not viable for a long coarse of imaging in the DFHM system, adjustments will need to be made in order to keep cells viable in the DFHM under normal conditions. Ultimately, OSI has proven to be an effective optical assay in other systems, so it is anticipated that this should also be the case when applied via the DFHM.

Diffuse reflactance spectroscopy is then carried out in order to measure the absorption and scattering coefficiants of bone tissues. The application of diffuse reflectance spectroscopy is postulated on a semi-infinite medium without curvature. The application of diffuse reflectance spectroscopy for measuring the optical proberties of bulk bones poses two challenges. First, bones have a dynamic, multi layered structure. In addition, bones have curvature. Both of these factors break the idealized symmetries assumed in diffuse reflectance spectroscopy. As such, extensive modeling was done via diffusion theory and Monte Carlo in order to test the validity of diffuse reflectance spectroscopy for optical characterization of bulk bone tissues. All results indicate that the layered structure of bone—namely the deeper, medullary cavity—do not affect the measurements of optical properties of the superficial cortical layer. The analysis also shows that the curvature of the bone is slight as complared to the diffusion length of cortical bone, such that the application of diffuse reflectance spectroscopy is warranted for measuring the optical properties of bulk cortical bone.

The optical properties of bone determined via diffuse reflectance spectroscopy are then incorporated into a three dimensional Monte Carlo simulation of the clinical application pf PDT for treating osteosarcoma. This model assumes the use of a cylindrical diffusing fiber tip is inserted directly into the center of a bulk osteosarcoma tumor located in the medullary cavity of a long bone. The presence of protoporphyrin-IX (PpIX) as a result of application of aminolevulinic acid (ALA) is also assumed as the photosensitizer. After roughly an hour of illumination, this model shows depths of necrosis similar to those reported in similar clinical veterinary applications. This agreement goes to validate the predictive efficacy of this model, which can now be used applied towards predicting and guiding the design of additional clinical applications of PDT in treating osteosarcoma and bone tumors in general.

This work closes with a description of the *in vitro* experiment of ALA-mediated PDT of human osteosarcoma cells carried out in collaboration with the Biology Department at Pacific University, where the author taught for three years. The design of tissue culture and PDT protocols is explained and results demonstrate the efficacy of ALA-mediated PDT in killing the MG63 human osteosarcoma cell line *in vitro*. While we anticipated an apoptotic response by these cells in this experiment, results gave a mix of aopototic and necrotic

responses. The inability to detect a stronger apoptotic response in this experiment may not be indicative of the general response of these cells to ALA-mediated PDT, but may be attributed to the experimental design. The greatest accumulation of PpIX was found in the MG63 cells after incubation in ALA for 24 hours. This would have given ample time for the PpIX produced within the mitochondria to diffuse throughout intracellular space. Upon illumination, this would not elicit a targeted response, but instead a general oxidizing effect throughout the cell. This general oxidizing effect would then most likely result in a necrotic response. Were we to attempt to amplify the apoptotic response of the cells as a result of ALA-mediated PDT, it would be prudent to assure localization of PpIX within and in the immediate vicinity of the mitochondria, where it is produced. To assure localization of PpIX in and near the mitochondria, shorter drug-light intervals would be required, such that the cells are illuminated before the PpIX generated has had time to diffuse throughout the cell.

In all, the efficacy of the DFHM and PDT of osteosarcoma have been demonstrated throughout this work. This has been carried out via a combination of experimental and computational methods.

BIBLIOGRAPHY

1. H. van de Hulst, *Light Scattering by Small Particles*. New York: Dover, 1981.

2. C. Bohren and D. Huffman, *Absorption and Scattering of Light by Small Particles*. Weinheim, Germany: Wiley-VCH, 2004.

3. S. Prahl and OMLC, "Mie scattering calculator," 2012.

4. C. Matzler, "Matlab functions for mie scattering and absorption," Research Report 2002-08, Universitas Bernensis Institut fur Angewaandte Physik, matzler@iap.unibe.ch, June 2002.

5. J. Mourant, J. Freyer, A. Hielscher, A. Eick, D. Shen, and T. Johnson, "Mechanisms of light scattering from biological cells relevant to noninvasive optical-tissue diagnostics," *Appl. Opt.*, vol. 37, no. 16, pp. 3586–3593, 1998.

6. J. Mourant, M. Canpolat, C. Brocker, O. Esponda-Ramos, T. Johnson, A. Matanock, K. Stetter, and J. Freyer, "Light scattering from cells: the contribution of the nucleus and the effects of proliferative status," *J. Biomed. Opt.*, vol. 5, no. 2, pp. 131–137, 2000.

7. R. Drezek, A. Dunn, and R. Richards-Kortum, "Light scattering from cells: finite-difference time-domain simulations and goniometric measurements," *Appl. Opt.*, vol. 38, no. 16, pp. 3651–3661, 1999.

8. J. Wilson and T. Foster, "Mie theory interpretations of light scattering from intact cells," *Opt. Lett.*, vol. 30, pp. 2442–2444, September 2005.

9. N. Boustany, S. Kuo, and N. Thakor, "Optical scatter imaging: subcellular morphometry *in situ* with fourier filtering," *Opt. Lett.*, vol. 26, no. 14, pp. 1063–1065, 2001.

10. A. Welch and M. van Gemert, eds., *Optical-Thermal Response of Laser-Irradiated Tissue*. New York: Optical-Thermal Response of Laser-Irradiated Tissue, 1995.

11. A. Kramida, Y. Ralchenko, J. Reader, and and NIST ASD Team, "NIST Atomic Spectra Database (ver. 5.3)," 2015.

12. S. Prahl and OMLC, "Optical absorption of hemoglobin."

13. S. Prahl and OMLC, "Optical absorption of water compendium."

14. S. Jacques, "Laser-tissue interactions: photochemical, photothermal, and photomechanical," *Surg. Clin. North Am.*, vol. 72, pp. 531–558, 1992.

15. P. Bargo, S. Prahl, T. Goodell, R. Sleven, G. Koval, G. Blair, and S. Jacques, "In vivo determination of optical properties of normal and tumor tissue with white light reflectance and an empirical light transport model during endoscopy," *J. Biomed. Optics*, vol. 10, no. 3, p. 034018, 2005.

16. V. Rossi, S. Gustafson, and S. Jacques, "Characterizing light propagation in bone for photodynamic therapy of osteosarcoma," in *Proc. SPIE* (A. Mandelis, ed.), vol. 7166, pp. 716601 1–12, SPIE, 2009.

17. S. Jacques, "Simple optical theory for light dosimetry during PDT," *Proc. SPIE*, vol. 1645, pp. 155–165, 1992.

18. M. Kim, *Digital Holographic Microscopy: principles, techniques, and applications*. No. 162 in Springer Series in Optical Sciences, New York: Springer, 2011.

19. M. Kim, "Principles and techniques of digital holographic microscopy," *SPIE Reviews*, vol. 1, pp. 018005–1–50, 2010.

20. J. Goodman, *Introduction to Fourier Optics*. Englewood, CO: Roberts and Company, 3rd ed., 2005.

21. P. Picart and J. Li, *Digital Holography*. Hoboken, NJ: John Wiley and Sons, Inc., 2012.

22. P. Picart and J. Leval, "General theoretical formulation of image formation in digital fresnel holography," *J. Opt. Soc. Am. A*, vol. 25, no. 7, pp. 1744–1761, 2008.

23. E. Sanchez-Ortega, A. Doblas, G. Saavedra, M. MArtinez-Coral, and J. Garcia-Sucerquia, "Off-axis digital holographic microscopy: practical design parameters for operating at diffraction limit," *Appl. Opt.*, vol. 53, pp. 2058–2066, April 2014.

24. E. Cuche, P. Marquet, and C. Depeursinge, "Spatial filtering for zero-order and twin-image elimination in digital off-axis holography," *Appl. Opt.*, vol. 39, pp. 4070–4075, August 2000.

25. T. Kreis and W. Juptner, "Supression of the dc term in digital holography," *Opt. Eng.*, vol. 36, pp. 2357–2360, August 19997.

26. D. Ghiglia and M. Pritt, *Two-dimensional phase unwrapping: theory, algorithms, and software*. New York: John Wiley and Sons, Inc., 1998.

27. C. Mann, L. Yu, C. Lo, and M. Kim, "High-resolution quantitative phase-contrast microscopy by digital holography," *Opt. Exp.*, vol. 13, no. 22, pp. 8693–8698, 2005.

28. P. Marquet, B. Rappaz, P. Magistretti, E. Cuche, Y. Emery, T. Colomb, and C. Depeursinge, "Digital holographic microscopy: a noninvasive contrast imaging technique allowing quantitative visualization of living cells with subwavelength axial accuracy," *Opt. Lett.*, vol. 30, no. 5, pp. 468–470, 2005.

29. S. Grilli, P. Ferraro, S. DeNicola, A. Finizion, G. Pierattini, and R. Meucci, "Whole optical wavefields reconstruction by digital holography," *Opt. Exp.*, vol. 9, no. 6, pp. 294–302, 2001.

30. D. Nolte, *Optical Interferrometry for Biology and Medicine*. Bioanalysis: advanced materials, methods, and devices, New York: Springer, 2012.

31. J. Mertz, *Introduction to Optical Microscopy*. Greenwood Village, CO: Roberts and Company, 2010.

32. E. Hecht, *Optics*. San Francisco, CA: Addison-Wesley, 4th ed., 2002.

33. D. Voelz, *Computational Fourier Optics: a Matlab Tutorial*, vol. TT89 of *Tutorial Texts in Optical Engineering*. Bellingham, WA: SPIE Press, 2011.

34. M. Molaei and J. Sheng, "Imaging bacterial 3D motion using digital in-line holographic microscopy and correlation-based de-noising algorithm," *Opt. Exp.*, vol. 22, pp. 32119–32137, December 2014.

35. H. Liu, E. Jonas, L. Tian, J. Zhong, B. Recht, and L. Waller, "3D imaging in volumetric scattering media using phase-space measurements," *Opt. Exp.*, vol. 23, pp. 14461–14471, June 2015.

36. P. Prasad, *Introductino to Biophotonics*. Hoboken, NJ: John Wiley and Sons, Inc., 2003.

37. N. Boustany, R. Drezek, and N. Thakor, "Calcium-induced alterations in mitochondrial morphology quantified in situ with optical scatter imaging," *Biophys. J.*, vol. 83, no. 3, pp. 1697–1700, 2002.

38. N. Boustany, Y. Tsai, B. Pfister, W. Joiner, and G. Oyler, "$BCL-x_L-$dependent light scattering by apoptotic cells," *Biophys. J.*, vol. 87, pp. 4163–4171, 2004.

39. J. Zheng, R. Pasternack, and N. Boustany, "Optical scatter imaging with a digital micromirror device," *Opt. Exp.*, vol. 17, pp. 20401–20414, October 2009.

40. N. Boustany, "Personal communication with N. Boustany." email correspondence, March 2011.

41. K. Seet, P. Blazkiewicz, P. Meredith, and A. Zvyagin, "Optical scatter imaging using digital fourier microscopy," *J. Phys. D: Appl. Phys.*, vol. 38, pp. 3590–3598, 2005.

42. B. Henderson and T. Dougherty, eds., *Photodynamic Therapy: Basic Principles and Clinical Applications*. New York: Marcel Dekker, Inc., 1992.

43. M. Hamblin and P. Mroz, eds., *Advances in Photodynamic Therapy: Basic, Translational, and Clinical*. Engineering in Medicine and Biology Series, Boston, MA: Artech House, 2008.

44. R. Bonnett, *Chemical Aspects of Photodynamic Therapy*, vol. 1 of *Advanced Chemistry Texts*. Australia: Gordon and Breach Science Publishers, 2000.

45. T. Hasan, A. Moore, and B. Ortel, *Cancer Medicine*, ch. Photodynamic Theraphy of Cancer, pp. 489–502. BC Decker Inc, 5th ed., 2000.

46. S. Burch, S. Bisland, A. Bogaards, A. Yee, C. Whyne, J. Finkelstein, and B. Wilson, "Photodynamic therapy for the treatment of vertebral metastases in a rat model of human breast carcinoma," *J. Orthop. Res.*, vol. 23, pp. 995–1003, 2005.

47. S. Burch, A. Bogaards, J. Siewerdsen, D. Moseley, A. Yee, J. Finkelstein, R. Weersink, B. Wilson, and S. Bisland, "Photodynamic therapy for the treatment of metastatic lesions in bone: Studies in rat and porcine models," *J. BioMed. Optics*, vol. 10, no. 3, p. 034011, 2005.

48. S. Bisland and S. Burch, "Photodynamic therapy of diseased bone," *Photodiagnosis and Photodynamic Therapy*, vol. 3, pp. 147–155, 2006.

49. M. Akens, A. Yee, B. Wilson, S. Burch, C. Johnson, L. Lilge, and S. Bisland, "Photodynamic therapy of vertebral metastases: Evaluationg tumor-to-neural tissue uptake of BPD-MA and ALA-PpIX in a murine model of metastatic himan breast carcinoma," *Photochem. Photobiol.*, vol. 83, pp. 1034–1039, 2007.

50. S. Burch, C. London, B. Seguin, C. Rodriguez, B. Wilson, and S. Bisland, "Treatment of canine osseous tumors with photodynamic therapy," *Clin. Orthop. Relat. Res.*, vol. 467, pp. 1028–1034, 2009.

51. M. Ochsner, "Photophysical and photobiological processes in the photodynamic therapy of tumors," *Photochem. Photobiol. B: Biol.*, vol. 39, pp. 1–18, 1997.

52. N. Oleinick and H. Evans, "The photobiology of photodynamic therapy: cellular targets and mechanisms," *Radiat. Res.*, vol. 150, pp. S146–S156, 1998.

53. G. Peavy, "Lasers and laser–tissue interaction," *Vet. Clin. Small Anim.*, vol. 32, no. 3, pp. 517–534, 2002.

54. M. Wainwright, "Photodynamic antimicrobial chemotherapy (PACT)," *J. Antimicrob. Chemother*, vol. 42, pp. 13–28, 1998.

55. J. Mata, L. Dyal, V. Rossi, and S. Gustafson, *Cancer Nanotechnology*, ch. 14, "Solid Tumor Physiology as a Target for Nanomedicines". American Scientific Publishers, 2006.

56. V. M. Rossi, B. M. White, M. J. Newton, S. L. Jacques, and P. J. Baugher, "*In vitro* photodynamic therapy of MG-63 osteosarcoma cells mediated by aminolevulinic acid," in *Proc. of SPIE* (D. H. Kessel and T. Hasan, eds.), vol. 7886, pp. 78860T 1–12, SPIE, 2011.

57. S. Jacques, "Photodynamic therapy," tissue optics course notes, OHSU Biomedical Engineering Dept., 2008.

58. S. Jacques, "How tissue optics affect dosimetry of photodynamic therapy," *JBO*, vol. 15, no. 5, pp. 0515081–6, 2010.

59. S. Hatz, L. Poulsen, and P. Ogilby, "Time-resolved singlet oxygen phosphorescence measurements from photosensitized experiments in single cells: Effects of oxygen diffusion and oxygen concentration," *Photochem. Photobiol.*, vol. 84, pp. 1284–1290, 2008.

60. J. Crank, *The Mathematics of Diffusion.* Oxford: Oxford University Press, 2nd ed., 1975.

61. T. Finkel and N. Holbrook, "Oxidants, oxidative stress and the biology of ageing," *Nature*, vol. 408, pp. 239–247, November 2000.

62. J. Martindale and N. Holbrook, "Cellular response to oxidative stress: Signaling for suicide and survival," *J. Cell. Phys.*, vol. 192, pp. 1–15, 2002.

63. J. Turrens, "Mitochondrial formation of reactive oxygen species," *JPhysiol*, vol. 552, no. 2, pp. 335–344, 2003.

64. A. Pisoschi and A. Pop, "The role of antioxidants in the chemistry of oxidative stress: A review," *Euro. J. Med. Chem.*, vol. 97, pp. 55–74, 2015.

65. K. Apel and H. Hirt, "Reactive oxygen species: Metabolism, oxidative stress, and signal transduction," *Annu. Rev. Plant Biol.*, vol. 55, pp. 373–399, 2004.

66. J. Sakurai, *Modern Quantum Mechanics.* Addison-Wesley, revised ed. ed., 1994.

67. R. Liboff, *Introductory Quantum Mechanics.* Reading, MA: Addison-Wesley, 3rd ed., 1998.

68. D. Beljonne, Z. Shuai, G. Pourtois, and J. Bredas, "Intersystem crossing in conjugated polymers: A configuration interaction description," *J. Phys. Chem. A*, vol. 105, no. 15, pp. 3899–3907, 2001.

69. D. Dexter, "A theory of sensitized luminescence in solids," *J. Chem. Phys.*, vol. 21, pp. 836–850, 1953.

70. U. Davis, "Dexter energy transfer."

71. N. Kollias and W. Gratzer, "Tabulated molar extinction coefficient for hemoglobin in water." Wellman Laboratories, Harvard Medical School, Boston, 1999.

72. G. M. Hale and M. R. Querry, "Optical constants of water in the 200nm to 200m wavelength region," *Appl. Opt.*, vol. 12, pp. 555–563, 1973.

73. E. Rud, O. Gederaas, A. Hogset, and K. Berg, "5-aminolevulinic acid, but not 5-aminolevulinic acid esters, is transported into adenocarcenoma cells by system BETA transporters," *Photochem. Photobiol.*, vol. 71, pp. 640–647, 2000.

74. F. Doring, J. Waller, J. Will, M. Focking, M. Boll, S. Amasheh, W. Clauss, and H. Daniel, "Delta-aminolevulinic acid transport by intestinal and renal peptide transporters and its physiological and clinical implications," *J. Clin. Invest.*, vol. 101, pp. 2761–2767, 1998.

75. T. Ishikawa, K. Takahashi, N. Ikeda, Y. Kajimoto, Y. Hagiya, S. Ogura, S. Miyatake, and T. Kuroiwa, "Transporter-mediated drug interaction strategy for 5-aminolevulinic acid (ALA)-based photodynamic diagnosis of malignant brain tumor: Molecular design of ABCG2 inhibitors," *Pharemaceutics*, vol. 3, pp. 615–635, 2011.

76. R. Donnelly, P. McCarron, and A. Woolfson, "Derivatives of 5-aminolevulinic acid for photodynamic therapy," *Perspectives in Medicinal Chemistry*, vol. 1, pp. 49–63, 2007.

77. J. Moan, L. Ma, and V. Iani, "On the pharmokinetics of topically applied 5-aminolevulinic acid and two of its esters," *Int. J. Cancer*, vol. 92, pp. 139–143, 2001.

78. K. Berg, H. Anholt, O. Bech, and J. Moan, "The influence of iron chelators on the accumulation of protoporphyrin ix in 5-aminolevulinic acid-treated cells," *Br. J. Cancer*, vol. 74, pp. 688–697, 1996.

79. T. Kriska, W. Korytowski, and A. Giroti, "Role of mitochondrial cardiolipin peroxidation in apoptotic photokilling of 5-aminolevulinate-treated tumor cells," *Arch. Biochem. Biophys.*, vol. 433, pp. 435–446, 2005.

80. D. Green, *Means to an End: Apoptosis and Other Cell Death Mechanisms*. New York: Cold Spring Harbor Laboratory Press, 2011.

81. M. C. Support, "Secondary cancer in the bone," December 2012.

82. Cancer.org, "What are the key statistics about bone metastases?," February 2014.

83. A. S. of Clinical Oncology, "Osteosarcoma—childhood," July 2010.

84. A. C. Society, "Cancer facts & figures 2010," 2010.

85. Cancer.org, "What are the key statistics about osteosarcoma?," January 2015.

86. Cancer.org, "What are the risk factors for osteosarcoma?," January 2015.

87. Cancer.org, "What are the survival rates for osteosarcoma?," January 2015.

88. Cancer.org, "How is osteosarcoma treated?," January 2015.

89. S. LaRue and S. Withrow, *Clinical Veterinary Oncology*, ch. Tumors of the Skeletal System, p. 234. J.B. Lippincott Company, 1989.

90. S. Burch, S. Bisland, and A. Yee, "Photodynamic therapy for bone metastases," *Onc. Exch.*, vol. 4, pp. 6–12, June 2005.

91. M. Meyer and P. S. andS.G. Bown, "A study of the effects of photodynamic therapy on the normal tissues of the rabbit jaw," *Br. J. Cancer*, vol. 64, pp. 1093–1097, 1991.

92. C. Mulroney, S. Gluck, and A. Ho, "The use of photodynamic therapy in bone marrow purging," *Sem. Onc.*, vol. 6, pp. 24–27, December 1994.

93. K. Kusuzaki, K. Aomori, T. Suginoshita, G. Minami, H. Takeshita, H. Murata, S. Hashiguchi, T. Ashihara, and Y. Hirasawa, "Total tumor cell elimination with minimum damage to normal tissues in musculoskeletal sarcomas following photodynamic therapy with acridine orange," *Oncology*, vol. 59, pp. 174–180, 2000.

94. K. Kusuzaki, G. Minami, H. Takeshita, H. Murata, S. Hashiguchi, T. Nozaki, T. Ashihara, and Y. Hirasawa, "Photodynamic inactivation with acridine orange on a multidrug-resistant mouse osteosarcoma cell line," *Jpn. J. Cancer Res.*, vol. 91, pp. 439–445, 2000.

95. S. Hashiguchi, S. Kusuzaki, H. Murata, H. Takeshita, M. Hashiba, T. Nishimura, T. Ashihara, and Y. Hirasawa, "Acridine orange excited by low-dose radiation has a strong cytocidal effect on mouse osteosarcoma," *Oncology*, vol. 62, pp. 85–93, 2002.

96. J. Nomura, S. Yanase, Y. Matsumura, K. Nagai, and T. Tagawa, "Efficacy of combined phhotodnamic and hyperthermic therapy with a new light source in an *in vivo* osteosarcoma tumor model," *J. Clin. Laser Med. Surg.*, vol. 22, no. 1, pp. 3–8, 2004.

97. S. Yanase, J. Nomura, Y. Matsumura, T. Nagata, T. Fujii, and T. Tagawa, "Synergistic interaction of 5-aminolevulinic acid-based photodynamic therapy with simultaneous hyperthermia in an osteosarcoma tumor model," *Int. J. Oncol.*, vol. 29, pp. 365–373, 2006.

98. K. Reidy, C. Campanile, R. Muff, W. Born, and B. Fuchs, "mTHPC-mediated photodynamic therapy is effective in the metastatic human 143B osteosarcoma cells," *Photochem. Photobiol.*, vol. 88, pp. 721–727, 2012.

99. R. Gonzalez and R. Woods, *Digital Image Processing.* New Jersey: Prentice Hall, 3rd ed., 2007.

100. *Image Processing Toolbox for use with MATLAB.* Natick, MA: The MathWorks, 4th ed., 2003.

101. H. Ding, Z. Wang, F. Nquyen, S. Boppart, and G. Popescu, "Fourier transform light scattering of inhomogenious and dynamic structures," *Phys. Rev. Lett.*, vol. 101, p. 238102(4), December 2008.

102. K. Kim and Y. Park, "Fourier transform light scattering angular spectroscopy using digital inline holography," *Opt. Lett.*, vol. 37, pp. 4161–4163, October 2012.

103. J. Ramella-Roman, P. Bargo, S. Prahl, and S. Jacques, "Evaluation of spherical particle sizes with an asymmetric illumination microscope," *IEEE J. Select. Topics Quantum Electron*, vol. 9, pp. 301–306, March/April 2003.

104. H. Ding, F. Ngyuen, S. Boppart, and G. Popescu, "Optical properties of tissues quantified by fourier-transform light scattering," *Opt. Lett.*, vol. 34, no. 9, pp. 1372–1374, 2009.

105. S. Urayama, A. Kawakami, T. Namashima, M. Tsuboi, S. Yamasaki, A. Hida, Y. Ichinose, H. Nakamura, E. Ejima, T. Aoyagi, T. Nakamura, K. Migita, Y. Kawabe, and K. Eguchi, "Effect of vitamin k2 on osteoblast apoptosis: Vitamin k2 inhibits apoptotic cell death of human osteoblasts induced by Fas, proteasome inhibitor, etoposide, and staurosporine," *J. Lab. Clin. Med.*, vol. 136, no. 3, pp. 181–193, 2000.

106. S. Alexandrov, T. Hillman, and D. Sampson, "Spatially resolved fourier holographic light scattering angular spectroscopy," *Opt. Lett.*, vol. 30, no. 24, pp. 3305–3307, 2005.

107. S. Alexandrov, T. Hillman, T. Gutzler, M. Same, and D. Sampson, "Particle sizing with spatially-resolved fourier-holographic light scattering angular spectroscopy," in *Multimodal Biomedical Imaging* (F. Azar and D. Metaxas, eds.), vol. 6081, pp. 6081041–11, SPIE, 2006.

108. T. Hillman, S. Alexandrov, T. Gutzler, and D. Sampson, "Microscopic particle discrimination using spatially-resolved fourier-holographic light scattering angular spectroscopy," *Opt. Exp.*, vol. 14, no. 23, pp. 11088–11102, 2006.

109. F. Dubois, C. Schockaert, N. Callens, and C. Yourassowsky, "Focus plane detection criteria in digital holography microscopy by amplitude analysis," *Opt. Exp.*, vol. 14, pp. 5895–5908, June 2006.

110. C. Trujillo and J. Garcia-Sucerquia, "Automatic method for focusing biological specimens in digital lensless holographic microscopy," *Opt. Lett.*, vol. 39, pp. 2569–2572, May 2014.

111. Y. Yang, B. Kang, and Y. Choo, "Application of the correlation coefficient method for determination of the focal plane to digital particle holography," *Appl. Opt.*, vol. 47, pp. 817–824, February 2008.

112. M. Tachiki, M. Itoh, and T. Yatagai, "Simultaneous depth determination of multiple objects by focus analysis in digital holography," *Appl. Opt.*, vol. 47, pp. D144–D153, July 2008.

113. E. Cuche, F. Bevilacqua, and C. Depeursinge, "Digital holography for quantitative phase-contrast imaging," *Opt. Lett.*, vol. 24, pp. 291–293, March 1999.

114. U. Schnars, "Direct phase determination on hologram interferometry with the use of digitally recorded holograms," *J. Opt. Soc. Am. A*, vol. 11, pp. 2011–2015, July 1994.

115. B. Spottiswoode, "Qualityguidedunwrap2d.m."

116. P. Ferraro, S. DeNicola, A. Finizion, G. Coppola, S. Grilli, C. Margo, and G. Pierattini, "Compensation of the inherent wave front curvature in digital holographic coherent microscopy for quantitative phase-contrast imaging," *Appl. Opt.*, vol. 42, pp. 1938–1946, April 2003.

117. W. Snyder, M. Cook, E. Nasset, L. Karhausen, G. Howells, and I. Tipton, "Report of the task group on reference man," Report 23, The International Commission on Radiological Protection, Pergaman Press, Oxford, 1975.

118. N. Zakharov, I. A. Polunin, K. Polunin, N. Rakitina, E. Kochetkova, N. Sokolova, and V. Kalinnikov, "Calcium hydroxyapatite for medical applications," *Inorg. Mat.*, vol. 40, no. 6, pp. 641–648, 2004.

119. R. Rithcie, M. Buehler, and P. Hansma, "Plasticity and toughness in bone," *Phys. Today*, pp. 41–46, June 2009.

120. L. Bachmann, A. Gomes, and D. Zezell, "Collagen absorption bands in heated and rehydrated dentine," *SpectroChem Acta PartA*, vol. 62, pp. 1045–1049, 2005.

121. T. Farrell, M. Patterson, and B. Wilson, "A diffusion theory model of spatially resolved, steady-state diffuse reflectance for the noninvasive determination of tissue optical properties in vivo," *Med. Phys.*, vol. 19, no. 4, pp. 879–888, 1992.

122. D. Fried, R. Glena, J. Featherstone, and W. Seka, "Nature of light scattering in dental enamel and dentin at visible and near-infrared wavelengths," *Applied Optics*, vol. 34, no. 7, pp. 1278–1285, 1995.

123. J. Zijp and J. ten Bosch, "Theoretical model for the scattering of light by dentin and comparison with measurements," *Applied Optics*, vol. 32, no. 4, pp. 411–415, 1993.

124. O. Ugnell and P. Oberg, "The optical properties of the cochlear bone," *Med. Eng. Phys.*, vol. 19, no. 7, pp. 630–636, 1997.

125. S. Kanick, D. Robinson, H. J. Sterenborg, and A. Amelink, "Semi-empirical model of the effect of scattering on single fiber fluorescence intensity measured on a turbid medium," *Biomed. Opt. Expr.*, vol. 3, no. 1, pp. 137–152, 2012.

126. S.C.Kanick, D. M. III, V. Krishnaswamy, J. Elliott, K. Paulsen, and B. Pogue, "Sub-diffusive scattering parameter maps recovered using wide-field high-frequency structured light imaging," *Biomed. Opt. Expr.*, vol. 5, no. 10, pp. 3376–3390, 2014.

127. S. Jacques and L. Wang, *Optical-Thermal Response of Laser-Irradiated Tissue*, ch. Monte Carlo Modeling of Light Transport in Tissues, pp. 73–100. New York: Plenum Press, 1995.

128. S. Tauber, R. Baumgartner, K. Schorn, and W. Beyer, "Lightdosimetric quantitative analysis of the human petrous bone: Experimental study for laser irradiation of the cochlea," *Lasers Surg. Med.*, vol. 28, pp. 18–26, 2001.

129. J. Schmitt, G. Zhou, and E. Walker, "Multilayer model of photon diffusion in skin," *J. Opt. Soc. Am. A*, vol. 7, no. 11, pp. 2141–2153, 1990.

130. M. Newton, B. White, V. Rossi, and P. Baugher, "Aminolevulinic acid-mediated photodynamic therapy induces cell death in human osteosarcoma cells," in *Proc. AACR*, vol. 72, p. 3464, AACR, 2012.

131. J. Bartosova and Z. Hrkal, "Accumulation of protoporphyrin-IX (PpIX) in leukemic cell lines following induction by 5-aminolevulinic acid (ALA)," *Comp. Biochem. Physiolo. C Toxicol. Pharmacol.*, vol. 126, no. 3, pp. 245–252, 2000.

132. J. Berlanda, T. Kiesslicj, V. Engelhardt, B. Krammer, and K. Plaetzer, "Comparative in vitro study on the characteristics of different photosensitizers employed in PDT," *J. Photochem. Photobiol. B: Biol.*, vol. 100, pp. 173–180, 2010.

133. P. Horowitz and W. Hill, *The Art of Electronics*. New York: Cambridge University Press, 2nd ed. ed., 1989.

134. S. Jacques, X. He, and G. Gofstein, "Desing of PDT protocols using δ-aminolevulinic acid (5ALA)," *Proc. SPIE*, vol. 1881, pp. 99–108, 1993.

135. A. Edinger and C. Thompson, "Death by design: apoptosis, necrosis and autophagy," *Curr. Op. Cell Biol.*, vol. 16, pp. 663–669, 2004.

136. A. Castano, P. Mroz, and M. Hamblin, "Photodynamic therapy and anti-tumor immunity," *Nat. Rev. Cancer*, vol. 6, no. 7, pp. 535–545, 2006.